MEASUREMENT AND CONTROL OF TRANSVERSE PHOTONIC DEGREES OF FREEDOM VIA PARITY SORTING AND SPIN-ORBIT INTERACTION

by

CODY COLLIN LEARY

A DISSERTATION

Presented to the Department of Physics
and the Graduate School of the University of Oregon
in partial fulfillment of the requirements
for the degree of
Doctor of Philosophy

June 2010

University of Oregon Graduate School

Confirmation of Approval and Acceptance of Dissertation prepared by:

Cody Leary

Title:

"Measurement and Control of Transverse Photonic Degrees of Freedom via Parity Sorting and Spin-Orbit Interaction"

This dissertation has been accepted and approved in partial fulfillment of the requirements for the degree in the Department of Physics by:

Daniel Steck, Chairperson, Physics
Michael Raymer, Member, Physics
Jens Noeckel, Member, Physics
Steven van Enk, Member, Physics
Andrew Marcus, Outside Member, Chemistry

and Richard Linton, Vice President for Research and Graduate Studies/Dean of the Graduate School for the University of Oregon.

June 14, 2010

Original approval signatures are on file with the Graduate School and the University of Oregon Libraries.

An Abstract of the Dissertation of

Cody Collin Leary   for the degree of   Doctor of Philosophy

in the Department of Physics   to be taken   June 2010

Title: MEASUREMENT AND CONTROL OF TRANSVERSE

PHOTONIC DEGREES OF FREEDOM VIA PARITY SORTING

AND SPIN-ORBIT INTERACTION

Approved: _____

Dr. Michael G. Raymer

In this dissertation, several new methods for the measurement and control of transverse photonic degrees of freedom are developed. We demonstrate a mode sorter for two-dimensional (2-D) parity of transverse spatial states of light based on an out-of-plane Sagnac interferometer. The first experimental 2-D parity sorting measurements of Hermite-Gauss transverse spatial modes are presented. Due to the inherent phase stability of this type of interferometer, it provides a promising tool for the manipulation of higher order transverse spatial modes for the purposes of quantum information processing. We propose two such applications: the production of both spatial-mode entangled Bell states and heralded single photons, tailored to cover the entire Poincaré sphere of first-order transverse modes.

In addition to the aforementioned transverse spatial manipulation based on free-space parity sorting, we introduce several more such techniques involving photons propagating in optical fibers. We show that when a photon propagates in a cylindrically symmetric waveguide, its spin angular momentum and its orbital angular momentum (OAM) interact. This spin-orbit interaction (SOI) leads to the prediction of several novel rotational effects: the spatial or time evolution of the photonic polarization vector is controlled by its OAM quantum number or, conversely, its spatial wave function is controlled by its spin. We demonstrate how these phenomena can be used to reversibly transfer entanglement between the spin and OAM degrees of freedom of two-particle states.

In order to provide a deeper insight into the cause of the SOI for photons, we also investigate an analogous interaction for electrons in a cylindrical waveguide and find that each of the SOI effects mentioned above remain manifest for the electron case. We show that the SOI dynamics are quantitatively described by a single expression applying to both electrons and photons and explain their common origin in terms of a universal geometric phase associated with the interplay between either particle's spin and OAM. This implies that these SOI-based effects occur for any particle with spin and thereby exist independently of whether or not the particle has mass, charge, or magnetic moment.

CURRICULUM VITAE

NAME OF AUTHOR: Cody Collin Leary

PLACE OF BIRTH: Anchorage, Alaska

DATE OF BIRTH: June 14, 1981

GRADUATE AND UNDERGRADUATE SCHOOLS ATTENDED:

>   University of Oregon, Eugene, Oregon
>   University of Puget Sound, Tacoma, Washington

DEGREES AWARDED:

>   Doctor of Philosophy in Physics, 2010, University of Oregon
>   Bachelor of Arts in Physics, 2003, University of Puget Sound
>   Bachelor of Arts in Mathematics, 2003, University of Puget Sound

AREAS OF SPECIAL INTEREST:

>   Quantum Mechanics, Optics, and Information
>   General Relativity

PROFESSIONAL EXPERIENCE:

>   Graduate Research Assistant, University of Oregon, 2006 – 2010
>
>   GK-12 Teaching Fellow, University of Oregon, 2004 – 2006
>
>   Graduate Teaching Assistant, University of Oregon, 2003 – 2004
>
>   Teaching Assistant, University of Puget Sound, 2002 – 2003

Physics and Mathematics Tutor, Writing and Learning Center, University of Puget Sound, 2002 – 2003

GRANTS, AWARDS AND HONORS:

Peter K. Wallerich Science Scholarship, University of Puget Sound, Tacoma, Washington, 2002 – 2003

Admitted to Los Alamos Summer School in Physics, Los Alamos, New Mexico, 2002

Seward Memorial Physics Scholarship, University of Puget Sound, Tacoma, Washington, 2001 – 2002

Murdock Foundation Summer Research Award, University of Puget Sound, Tacoma, Washington, 2001

Leonard Howarth Science Scholarship, University of Puget Sound, Tacoma, Washington, 1999 – 2003

PUBLICATIONS:

Yoonshik Kang, Kiyoung Cho, Jaewoo Noh, Dash Vitullo, Cody Leary, Michael G. Raymer, "Remote preparation of complex spatial states of single photons and verification by two-photon coincidence experiment," Opt. Express, **18**, 2 (2010).

C. C. Leary, M. G. Raymer, and S. J. van Enk, "Spin and orbital rotation of electrons and photons via spin-orbit interaction," Phys. Rev. A, **80**, 061804 (2009).

C. C. Leary, L. A. Baumgardner, and M. G. Raymer, "Stable mode sorting by two-dimensional parity of photonic transverse spatial states," Opt. Express, **17**, 4 (2009).

C. C. Leary, D. Reeb, and M. G. Raymer, "Self-spin-controlled rotation of spatial states of a Dirac electron in a cylindrical potential via spin-orbit interaction," New J. Phys. **10**, 103022 (2008).

C. C. Leary and M. G. Raymer, "Single-photon spin-orbit coupling and LOQC," in Conference on Laser and Electro Optics 2008 and 2008 Quantum Electronics and Laser Science Conference (CLEO/QELS), San Jose, CA, May 4–9, 2008.

C. C. Leary and M. G. Raymer, "Cluster State LOQC with Entangled Spatial Modes," in The Ninth Conference on Coherence and Quantum Optics 2007 (CQO9), Rochester, New York, June 10–13, 2007.

ACKNOWLEDGEMENTS

First of all I thank my advisor Professor Michael Raymer, who made his support continually available throughout my time at the University of Oregon. I have learned many valuable things through your example and insight, which has challenged me toward both academic and personal growth. I appreciate each of the opportunities that you have given me. I would also like to thank Professor Konrad Banaszek at the University of Warsaw, Poland, and Professor Ian Walmsley at the University of Oxford, United Kingdom, for helpful discussions and their generous hospitality when I visited for collaborative research. I thank Professor Jaewoo Noh at Inha University, Korea, for his experimental help and fruitful discussions while collaborating with us here in Oregon. Finally, I would like to acknowledge University of Oregon Professors Daniel Steck, Jens Nöckel, Miriam Deutsch, and Hailin Wang for their willingness to talk physics with me when I needed a hand, and David Reeb, Ashleigh Baumgardner, Zachary Bond, and Professor Steven van Enk for their helpful collaboration.

I have benefited from countless discussions and collaborations with all my peers who have temporally overlapped with me in the Raymer lab. Specifically, I thank Dr. Guoqiang Cui, Dr. Wenhai Ji, Dr. Justin Hannigan, Chunbai Wu, Erin Mondloch, and Anna Smith, while giving special thanks to Dr. Brian Smith, Hayden McGuinness, and Dash Vitullo, with whom I worked most closely—you are to be commended for putting up with me.

τω δυναμενω υμας στηριξαι κατα το ευαγγελιον μου και το κηρυγμα ιησου χριστου κατα

αποκαλυψιν μυστηριου χρονοις αιωνιοις σεσιγημενου φανερωθεντος δε νυν δια τε γραφων

προφητικων κατ επιταγην του αιωνιου θεου εις υπακοην πιστεως εις παντα τα εθνη γνωρισ-

θεντος μονω σοφω θεω δια ιησου χριστου ω η δοξα εις τους αιωνας αμην

Rom 16:25-27

TABLE OF CONTENTS

LIST OF FIGURES

CHAPTER I

INTRODUCTION

Photons have four degrees of freedom. In typical optics experiments involving paraxial laser beams, they may be described as follows: One spectral (energy) degree of freedom (DOF), one polarization (spin) DOF, and two transverse spatial DOFs. Due to recent advances in the measurement and control of each of these DOFs, the study of quantum optics has entered a truly exciting era. As far back as the 1930's it was understood that entanglement, the quantum phenomenon which allows for two spatially separated objects to posses more strongly correlated properties than similarly separated classical systems, lies at the heart of what makes quantum theory so intuitively distinct from the notions of classical physics [1]. Today, it is possible to generate and characterize quantum states of light consisting of either heralded single photons or small numbers of photons with entangled field modes. This has resulted in a series of impressive achievements, such as the practical production and analysis of two-photon states exhibiting maximal entanglement in each photonic degree of freedom, including spectral [2], polarization [3], and transverse spatial [4–9]. Simultaneous entanglement in all of these degrees of freedom has also been realized [10], as well as multimode two-photon (Hong-Ou-Mandel) interference involving photonic transverse spatial and polarization DOFs [11] and two-photon "ghost" imaging of the transverse DOFs [12]. Various multi-photon entangled states have been generated [13–17], in addition to

the engineering of pure two-photon product states which are completely *unentangled* in the spectral degree of freedom, leading to spectrally pure heralded single-photon states [18, 19]. Most recently, the successful transfer of entanglement *between* DOFs has been realized, including entanglement transfer from the polarization to the spectral DOF [20], and from the polarization (spin angular momentum) to the spatial (orbital angular momentum) DOF [21].

At the heart of many of the aforementioned advances are several experimental tools which have recently been developed for manipulating the transverse spatial degree of freedom of light, including mode-sorting holograms (cf. [4, 6]), astigmatic mode converters [22], one-dimensional (1-D) parity sorters [8, 9, 23], and inhomogeneous anisotropic birefringent "q-plates" [21, 24]. In this dissertation, we develop several new methods for the measurement and control of transverse spatial photonic degrees of freedom. We demonstrate a mode sorter for two-dimensional (2-D) parity of transverse spatial states of light based on an out-of-plane Sagnac interferometer. The first experimental 2-D parity sorting measurements of Hermite-Gauss transverse spatial modes are presented. Due to the inherent phase stability of this type of interferometer, it provides a promising tool for the manipulation of higher-order transverse spatial modes for the purposes of quantum information processing. We propose two such applications: the production of both spatial-mode entangled Bell states and heralded single photons, tailored to cover the entire Poincaré sphere of first-order transverse modes [25].

In addition to the aforementioned transverse spatial manipulation based on free-space parity sorting, we introduce several more such techniques involving photons propagating in optical fibers. We show that when a photon propagates in a cylindrically symmetric

waveguide, its spin angular momentum (SAM) and its orbital angular momentum (OAM) interact. This spin-orbit interaction (SOI) leads to the prediction of several novel rotational effects: the spatial or time evolution of the photonic polarization vector is controlled by its OAM quantum number or, conversely, its spatial wave function is controlled by its spin. We propose several experiments to characterize these phenomena, and demonstrate how they can be used to reversibly transfer entanglement between the spin and OAM degrees of freedom of two-particle states. In order to provide a deeper insight into the cause of the SOI for photons, we also investigate an analogous interaction for electrons in a cylindrical waveguide and find that each of the SOI effects mentioned above remain manifest for the electron case. We show that the SOI dynamics are quantitatively described by a single expression applying to both electrons and photons, and explain their common origin in terms of a universal geometric phase associated with the interplay between either particle's spin and OAM. This implies that these SOI-based effects occur for any particle with spin, and thereby exist independently of whether or not the particle has mass, charge, or magnetic moment.

The remaining chapters of this dissertation are outlined as follows: in Chapter II, we consider the general case of a paraxial quantum particle (i.e., either an electron or a photon) in a beam-like wave packet with well-defined values for both its intrinsic spin and orbital angular momentum. When such a "spin-orbit" wave packet propagates in an inhomogeneous medium with reasonably well-defined and cyclically varying linear momentum, we find that in a single momentum cycle the particle's wave function accumulates an overall geometric (Berry) phase of the form

$$\Phi_B = -\left(\lambda\sigma + m_\ell\right)\Omega, \tag{1.1}$$

where λ is the particle helicity magnitude (i.e., the absolute value of the particle spin), σ and m_ℓ are the respective SAM and OAM quantum numbers of the spin-orbit wave packet, and Ω is the momentum-space solid angle subtended by the cyclical loop. This result plays a central role in both the design of our 2-D parity sorting interferometer and to understanding the physics of the spin-orbit interaction.

In Chapter III, we discuss in detail the properties of interferometric devices based on the transverse mode parity of photons, by presenting a theoretical treatment of the 1-D and 2-D spatial parity properties of paraxial Hermite-Gauss (HG) and Laguerre-Gauss (LG) modes. We then use this theoretical description to describe a new type of interferometric 2-D parity sorter, which has substantially superior stability properties as compared to previously realized devices. Our improved mode sorter is an out-of-plane Sagnac interferometer whose 2-D sorting capabilities are based on a spatial rotation effect caused by the geometric phase discussed in Chapter II, which is in turn induced by an out-of-plane mirror reflection. We discuss this geometric phase, and explain how one may exploit it to realize a 2-D parity operation on the transverse mode space.

In Chapter IV, we present experimental results demonstrating the measurement and control of photonic transverse spatial modes, employing interferometers based on both 1-D and 2-D parity as described in Chapter III. In the case of the interferometer based on 1-D parity, we observed its predicted behavior as both a 1-D parity sorter and an HG-to-LG

mode converter. In the case of the interferometer based on 2-D parity, we present the first 2-D parity measurements of Hermite-Gauss transverse spatial modes, and demonstrate the stable sorting of these modes according to their 2-D parity. Additionally, we employ the 2-D sorter to sort the output modes of a "three-mode" optical fiber, show how the 2-D sorter can be made to work at nearly 100% efficiency, and perform a detailed loss and efficiency analysis of the device. We also propose several applications of this interferometer, including its use as an alternative to holograms in spatial mode filtering, the measurement of the OAM of single photons, the production of Bell states entangled in first-order transverse spatial modes, and the production of heralded single photons in first-order transverse spatial states corresponding to an arbitrary point of the first-order spatial mode Poincaré sphere.

In Chapter V, we provide the first unified treatment of the spin-orbit interaction for both electrons and photons in the "wave function" picture, in which the full wave nature of each particle is taken into account. We restrict our analysis to particle propagation in a straight cylindrically symmetric waveguide, solving both the Dirac and Maxwell equations perturbatively for this geometry. Remarkably, we find in this case that the SOI is quantitatively described by a single expression applying to either an electron or a photon, which predicts that both particles pick up a phase Φ due to the SOI of the general form

$$\Phi \propto \sigma m_\ell z, \tag{1.2}$$

where z is the longitudinal distance the particle has propagated down the waveguide. This result leads to the prediction of several rotational effects for both particle types, in which the

particle's spin and orbital degrees of freedom influence one another as it propagates down the waveguide. We show that these rotational phenomena allow for the reversible transfer of entanglement between the SAM and OAM degrees of freedom of two-particle states.

In Chapter VI, we focus on the special case of SOI in a waveguide with a step-profile for the electronic potential or the photonic permittivity. Using (1.1), we show that in this case the common origin of the SOI effects in electrons and photons is a universal geometric phase associated with the interplay between either particles spin and OAM.

CHAPTER II

ANGULAR MOMENTUM AND THE GEOMETRIC PHASE

Introduction

As discussed in Chapter I, the four physical degrees of freedom (DOFs) available to a freely-propagating quantum particle with spin may be given a particularly simple interpretation when the particle is constrained to a paraxial beam, such that the particle momentum is directed predominantly along the propagation axis of the wave function. Specifically, for a monoenergetic photon (or a monoenergetic, nonrelativistic electron) propagating paraxially down the z axis, these DOFs may be associated with four quantum numbers representing the following physical quantities: the energy $\hbar\omega$, the momentum z-component $\hbar\beta$, the spin angular momentum (SAM) z-component $\hbar\lambda\sigma$, and the orbital angular momentum (OAM) z-component $\hbar m_\ell$. Here, the angular frequency ω and propagation constant β may take continuous values, while the SAM $\sigma = \pm 1$ and OAM $m_\ell = 0, \pm 1, \pm 2, \ldots$ take on discrete values, with λ being the magnitude of the particle helicity (i.e., the particle spin) such that $\lambda = \dfrac{1}{2}$ for electrons and $\lambda = 1$ for photons.

For both particle types, the quantum numbers $(\omega, \beta, \sigma, m_\ell)$ reflect the conserved quantities arising from the Poincaré group symmetries present in their respective free-space Hamiltonians [26–28]. In this way, ω and β together reflect the conservation of energy-momentum

due to time translation symmetry and space translation symmetry with respect to the z axis, respectively. Similarly, σ and m_ℓ together reflect the conservation of the z-component of *total* angular momentum—represented by the quantum number $m_j \equiv \lambda\sigma + m_\ell$—due to spatial rotation symmetry about the z axis. The monoenergetic, paraxial wave function of either particle is proportional to the traveling wave exponential phase factor $e^{i(\beta z - \omega t)}$, which contains the entirety of the dependence of the wave function on the variables z and t. As we will show, if the beam-like wave function is expressed in cylindrical coordinates (ρ, ϕ, z), the SAM and OAM contributions to the wave function are proportional to an exponential phase factor of the form $e^{im_j\phi}$, which depends only upon the total angular momentum quantum number m_j.

Suppose now that an electron (photon) travels from free space into an inhomogeneous potential (permittivity) that is slowly varying in space. Due to the nonzero potential (permittivity) gradient, its momentum will then begin to change adiabatically as the particle propagates, resulting in a curvilinear path (see Fig. 2.1). If we transform to the reference frame of the particle, and continually rotate our spatial coordinate axes in time such that the z-axis remains aligned with the adiabatically changing particle momentum, then the particle wave function remains proportional to the phase factor $e^{im_j\phi} \times e^{i(\beta z - \omega t)}$. A question, however, arises: how should the x and y axes be reoriented (about the z-axis) as the particle is transported along the continuously varying z direction in order to properly account for the orientation of the particle's transverse wave function $\psi_T(\rho, \phi, z) \propto e^{im_j\phi}$? This question turns out to be more than merely academic, because the choice of how to "transport"
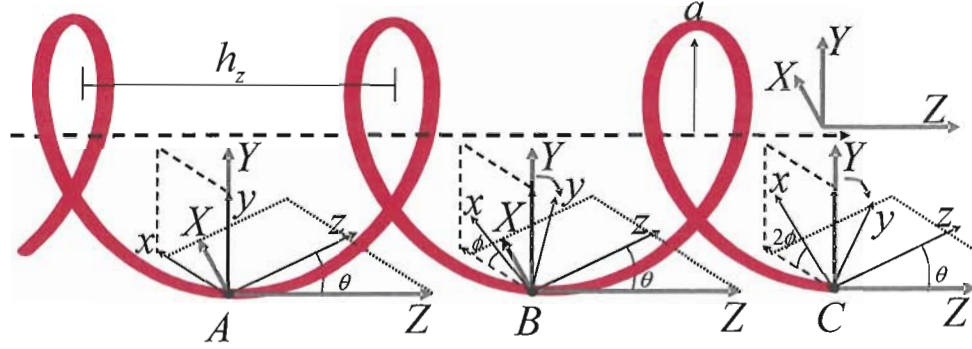
Figure 2.1. Transport of the coordinate frame (x, y, z) attached to a particle propagating along a curvilinear path where the z axis is fixed to the direction of the particle momentum by construction. In the example shown, the particle path is a circular helix with constant radius a and pitch h_z, such that the helix's axis of symmetry is coaxial with the Z axis of a (fixed) coordinate system (X, Y, Z), displayed in gray. The z axis (particle momentum vector) therefore makes a constant angle θ with the Z axis, and lies instantaneously in the $X - Z$ plane at points A, B, and C, as shown. As the particle propagates from point A to point B in time τ, it accumulates a dynamical phase $\beta \zeta - \omega \tau$, where $\zeta = \sqrt{(2\pi a)^2 + h_z^2}$ is the path length between A and B along the helix. Furthermore, at the same time the $x - y$ plane, which is always transverse to the particle motion, experiences a transverse rotation through an angle ϕ about the z axis as the particle propagates. This coordinate rotation manifests itself as an additional geometric phase factor for particle wave functions with a well-defined value of their total angular momentum m_j. Unlike the dynamical phase, which depends only upon the path length, this geometric phase depends on both the quantum number m_j and the geometric characteristics of the path taken by the particle. See text for further details.

the orientation of the x and y axes affects the value of the ϕ coordinate of $\psi_T(\rho, \phi, z)$, as shown in Fig. 2.1.

Over a time interval τ, the particle will propagate through some distance d along the curvilinear path, corresponding to "optical" path length $\zeta = \int_0^d n(z)\, dz$, where $n(z)$ is the refractive index as seen from the particle frame. As is well known, the traveling wave phase factor $e^{i(\beta z - \omega t)}$ gives rise to a dynamical phase accumulation over the time interval τ

equal to $\beta\zeta - \omega\tau$, which depends only on the optical path length ζ and not upon any other details of the particular history of the curvilinear path take by the particle. However, it is perhaps surprising to note that the angular momentum phase factor $e^{im_j\phi}$ also accumulates an additional, distinct phase during the time τ, the precise value of which depends upon the total angular momentum quantum number m_j and the *history of the specific path taken by the particle*. This second mechanism of phase accumulation is an example of a phenomenon known as the geometric phase, since it depends upon the geometric characteristics of the particle's path.

The geometric (Berry) phase was discovered by Berry in 1984 in the context of general quantum systems undergoing adiabatic changes in the parameters of their associated Hamiltonians [29]. However, various manifestations of this phenomenon had been known previously, including the Rytov polarization rotation [30] and the Pancharatnam phase [31] for photons, and the Aharonov-Bohm effect [32] for electrons. Shortly after Berry's important work, it was shown that any unitary cyclic evolution in the (projective) Hilbert space of a quantum system generates a geometric phase independently of any adiabaticity requirements on the Hamiltonian parameters as imposed by Berry [33]. Subsequently, even the requirements that the evolution be unitary and cyclic were both relaxed [34].

In this chapter, we develop the aforementioned relationship between the angular momentum of a quantum particle and the geometric phase, treating the electron and photon cases simultaneously throughout. We begin by finding the appropriate description of a paraxial quantum particle in a beam-like wave packet propagating in an inhomogeneous medium with

reasonably well-defined and cyclically varying linear momentum, such that the wave packet also has well-defined values for its intrinsic spin and orbital angular momentum. We then develop the principal result of [33]—an explicit expression for the geometric phase for a general quantum system—before adapting it in order to calculate the Berry phase accumulated by our beam-like wave packet with SAM and OAM. We will make use of this important result throughout the remainder of this work, as it forms the basis for understanding both the operation of our interferometric two-dimensional (2-D) parity sorter and the spin-orbit interaction phenomenon.

Beam-like Wave Packet with Spin and Orbital Angular Momentum

Consider first a monoenergetic beam-like electron in free space, such that its wave function propagates in a well-defined direction with phase velocity $\frac{\omega}{\beta}$. Taking the propagation direction to be the z-direction, the electron wave function Ψ_ω assumes under these conditions the traveling-wave form

$$\Psi_\omega = \Psi\left(\rho, \phi, z\right) e^{i(\beta z - \omega t)} \tag{2.1}$$

where we have used cylindrical coordinates (ρ, ϕ, z), and where β is known as the propagation constant. Furthermore, without loss of generality we may assume that $\Psi\left(\rho, \phi, z\right) \to \Psi\left(\rho, \phi\right)$ is independent of z, since the resulting non-diffracting beams (the so-called Bessel beams, cf. [35, 36]) form a complete basis set for an arbitrary diffracting wave $\Psi\left(\rho, \phi, z\right)$.

For a nonrelativistic electron in a state of the form (2.1), the appropriate wave equation is the free-space Pauli equation [37], which may be written as a two-component Schrödinger-type wave equation,

$$\left[\nabla_T^2 + \frac{2m\omega}{\hbar}\right]\Psi_\omega = \beta^2\Psi_\omega,\tag{2.2}$$

where $\nabla_T^2 \equiv \nabla^2 - \partial_z^2$ with $\partial_z^2 \equiv \dfrac{\partial^2}{\partial_z^2}$, and

$$\Psi_\omega = \psi\left(\rho,\phi\right)e^{i(\beta z - \omega t)}\hat{\mathbf{e}}_\sigma,\tag{2.3}$$

such that $\hat{\mathbf{e}}_\sigma \equiv \begin{pmatrix} \delta_{\sigma+} \\ \\ \delta_{\sigma-} \end{pmatrix}$ is a normalized two-component spinor denoting the electron spin state along the z-axis as determined by $\sigma = \pm 1$. The $\delta_{\sigma+}$ and $\delta_{\sigma-}$ are Kronecker delta functions, so that $\delta_{\sigma+} = 1$ for $\sigma = +1$, and $\delta_{\sigma+} = 0$ for $\sigma = -1$, etc.

In Appendix A, we derive the analogous wave equation for a monoenergetic beam-like photon in free space, propagating along the z axis with phase velocity $\dfrac{\omega}{\beta}$. There we also show that when the photon propagates paraxially, this general free-space photon wave equation (A.2) reduces to a paraxial photon wave equation (A.23), which for practical purposes may be expressed entirely in terms of the transverse electric field $\mathbf{E}_T$ as a two-component Helmholtz type wave equation,

$$\left[\nabla_T^2 + \omega^2\epsilon_0\mu_0\right]\mathbf{E}_T = \beta^2\mathbf{E}_T,\tag{2.4}$$

with

$$\mathbf{E}_T = E_T \left(\rho, \phi \right) e^{i(\beta z - \omega t)} \hat{\mathbf{e}}_\sigma, \tag{2.5}$$

where in this case $\hat{\mathbf{e}}_\sigma \equiv \dfrac{1}{\sqrt{2}} \left(\hat{\mathbf{x}} + i \sigma \hat{\mathbf{y}} \right)$ is not a spinor but a two-component unit vector denoting the circular polarization (helicity) state of the photon in the transverse plane with respect to the z axis, as determined by $\sigma = \pm 1$.

Comparing the above free-space equations (2.2)–(2.5) for nonrelativistic electrons and paraxial photons, one can see that they have intriguingly analogous forms. This suggests that we interpret the monoenergetic transverse electric field $\mathbf{E}_T$ as a photon wave function Ψ_ω such that $\mathbf{E}_T \to \Psi_\omega$, which may indeed be consistently done as we show in Appendix A. In this way, the wave function dynamics of the electron and photon become completely analogous, and we may write a single wave equation that applies to both particles,

$$\left[\nabla_T^2 + k^2 \right] \Psi_\omega = \beta^2 \Psi_\omega, \tag{2.6}$$

where $k^2 \equiv \dfrac{2m}{\hbar^2} \hbar \omega$ for electrons and $k^2 \equiv \omega^2 \epsilon_0 \mu_0$ for photons. The solutions to (2.6), denoted as $\Psi_{\omega \beta \sigma m_\ell}$, which are examples of non-diffracting Bessel beams [35, 36], have the general form

$$\Psi_{\omega \beta \sigma m_\ell} = N J_{m_\ell} \left(\kappa \rho \right) e^{i m_\ell \phi} e^{i \beta z - \omega t} \hat{\mathbf{e}}_\sigma, \tag{2.7}$$

where the radial wave function $J_{m_\ell} \left(\kappa \rho \right)$ is a Bessel function of the first kind of order m_ℓ, with $\kappa \equiv \sqrt{k^2 - \beta^2}$ being the transverse wave number. The states $\Psi_{\omega \beta \sigma m_\ell}$ are characterized by the four quantum numbers $\omega, \beta, \sigma, m_\ell$ as defined above, and therefore have well-defined

values for both their SAM and OAM. We note here that while only paraxial photons can be described by the wave functions (2.7), even non-paraxial electrons may take that form. However, in this Dissertation we are concerned primarily with analogies between electrons and photons in which their wave functions have similar properties, so that we henceforth assume that both electrons and photons are propagating paraxially with momentum directed primarily along the z axis.

Our stated task is to construct a traveling wave packet from the fundamental Bessel beam solutions (2.7). In view of this, we consider the integral representation of the Bessel function $J_{m_\ell}(\kappa\rho)$ [38],

$$J_{m_\ell}(\kappa\rho) = \frac{1}{2\pi}\int_{-\pi}^{\pi} e^{i(m\alpha - \kappa\rho\sin\alpha)}d\alpha, \tag{2.8a}$$

$$= \frac{(-i)_\ell^m}{2\pi}\int_{-\pi}^{\pi} e^{im_\ell\phi'}e^{i\kappa\rho\cos(\phi'-\phi)}d\phi'e^{-im_\ell\phi}, \tag{2.8b}$$

where the substitution $\alpha \to \phi' - \phi - \dfrac{\pi}{2}$ has been made in (2.8b). Therefore, by (2.7) and (2.8b), the state $\Psi_{\omega\beta\sigma m_\ell}$ may be written as

$$\Psi_{\omega\beta\sigma m_\ell} = \frac{(-i)^{m_\ell}N}{2\pi}\int_{-\pi}^{\pi} e^{im_\ell\phi'}e^{i\kappa\rho\cos(\phi'-\phi)+\beta z-\omega t}d\phi'\hat{\mathbf{e}}_\sigma, \tag{2.9a}$$

$$= \tilde{N}\int_{-\pi}^{\pi} e^{im_\ell\phi'}e^{i\mathbf{k}(\theta',\phi')\cdot\mathbf{r}-\omega t}d\phi'\hat{\mathbf{e}}_\sigma, \tag{2.9b}$$

where

$$\mathbf{k}\left(\theta', \phi'\right) \cdot \mathbf{r} = kr \begin{pmatrix} \sin\theta'\cos\phi'\hat{\mathbf{x}} \\ \sin\theta'\sin\phi'\hat{\mathbf{y}} \\ \cos\theta'\hat{\mathbf{z}} \end{pmatrix} \cdot \begin{pmatrix} \sin\theta\cos\phi\hat{\mathbf{x}} \\ \sin\theta\sin\phi\hat{\mathbf{y}} \\ \cos\theta\hat{\mathbf{z}} \end{pmatrix}, \tag{2.10a}$$

$$= k\sin\theta' r\sin\theta\left(\cos\phi'\cos\phi + \sin\phi'\sin\phi\right) + k\cos\theta' r\cos\theta', \tag{2.10b}$$

$$= \kappa\rho\cos\left(\phi' - \phi\right) + \beta z, \tag{2.10c}$$

has been used in (2.9b), along with the indentity $\cos\phi'\cos\phi + \sin\phi'\sin\phi = \cos\left(\phi' - \phi\right)$ and the relations $k\sin\theta' \equiv \kappa$, $k\cos\theta' \equiv \beta$, $r\sin\theta \equiv \rho$, and $r\cos\theta \equiv z$. Also in (2.9) and (2.10), spherical coordinates $\mathbf{r}\left(r, \theta, \phi\right)$ and $\mathbf{k}\left(k, \theta', \phi'\right)$ have been employed, and $\tilde{N} \equiv \dfrac{(-i)^{m_\ell} N}{2\pi}$.

It is explicitly apparent from (2.9) that the Bessel beams $\Psi_{\omega\beta\sigma m_\ell}$ are simply a linear superposition of plane waves oriented at a fixed polar angle θ' with respect to the z axis, but with all possible values of ϕ' included, weighted by the $m\phi'$-dependent phase factor $e^{im_\ell\phi'}$. Therefore, to construct a monoenergetic paraxial wave packet from the states $\Psi_{\omega\beta\sigma m_\ell}$ that retains its non-diffracting character, we may compose a superposition state $\Psi_{k\theta_0\sigma m_\ell}$ in the θ' polar momentum angle such that the weight function $W_{\theta_0}\left(\theta'\right)$ is sharply peaked about some value $\theta_0 \ll 1$,

$$\Psi_{k\theta_0\sigma m_\ell} \equiv \int W_{\theta_0}\left(\theta'\right) \Psi_{\omega\beta\sigma m_\ell} \sin\theta' d\theta', \tag{2.11a}$$

$$= \tilde{N} \int W_{\theta_0}\left(\theta'\right) \left[J_{m_\ell}\left(\kappa\rho\right) e^{im_\ell\phi} e^{i\beta z - \omega t}\right] \sin\theta' d\theta' \hat{\mathbf{e}}_\sigma, \tag{2.11b}$$

$$= e^{im_\ell\phi}\hat{\mathbf{e}}_\sigma \left[\tilde{N} \int W_{\theta_0}\left(\theta'\right) J_{m_\ell}\left(k\rho\sin\theta'\right) e^{ik(z\cos\theta' - ct)} \sin\theta' d\theta'\right]. \tag{2.11c}$$

where (2.7) has been used in (2.11b), while $\kappa = k\sin\theta'$, $\beta = k\cos\theta'$, and $\omega = kc$ have been used in (2.11c).

By inspection of (2.11c), we see that the term in square brackets is independent of the SAM and OAM quantum numbers σ and m_ℓ, so that these paraxial, monoenergetic, "polar-angle" wave packets retain well-defined values for σ and m_ℓ. This is why we have included σ and m_ℓ as subscripts in the wave packet function $\Psi_{k\,\theta_0\,\sigma\,m_\ell}$. Although ω remains a good quantum number for the wave packet, we have replaced it with the equivalent quantum number $k = \dfrac{\omega}{c}$ since explicit appearances of k are dominant in (2.11b). In making the above angular superposition, however, we have lost $\beta = k\cos\theta'$ as a good quantum number, and we instead have included the subscript θ_0, which acts to characterize the angular distribution of the wave packet.

Since SAM and OAM terms $e^{im_\ell\phi}\hat{\mathbf{e}}_\sigma$ not only factor out of the θ' integrand, but are also independent of k, we may construct a superposition of the wave packets $\Psi_{k\,\theta_0\,\sigma\,m_\ell}$ with different k values which retain well-defined values of σ and m_ℓ. We therefore compose such a superposition in k such that the weight function $W_{k_0}(k)$ is sharply peaked about some value k_0,

$$\Psi_{k_0\,\theta_0\,\sigma\,m_\ell} \equiv \int W_{k_0}(k)\,\Psi_{k\,\theta_0\,\sigma\,m_\ell}k^2 dk, \tag{2.12a}$$

$$= \int W_{k_0}(k) \int W_{\theta_0}(\theta') \int e^{im_\ell\phi'} \times e^{i\mathbf{k}(\theta',\phi')\cdot\mathbf{r}-\omega t}d\phi'\sin\theta' d\theta' k^2 dk\,\hat{\mathbf{e}}_\sigma, \tag{2.12b}$$

$$= e^{im_\ell\phi}\hat{\mathbf{e}}_\sigma \int W_{k_0}(k) \int W_{\theta_0}(\theta')\,J_{m_\ell}(k\rho\sin\theta')\,e^{ik(\cos\theta'\hat{\mathbf{z}}\cdot\mathbf{r}-ct)}\sin\theta' d\theta' k^2 dk, \tag{2.12c}$$

$$\approx e^{im_\ell \phi} \hat{\mathbf{e}}_\sigma \left[\int W_{k_0}(k) \int W_{\theta_0}(\theta') J_{m_\ell}(k\rho \sin \theta') \sin \theta' d\theta' e^{i\delta k(\hat{\mathbf{z}} \cdot \mathbf{r} - ct)} k^2 dk \right] e^{ik_0(\hat{\mathbf{z}} \cdot \mathbf{r} - ct)},$$

$$\tag{2.12d}$$

$$\equiv e^{im_\ell \phi} \hat{\mathbf{e}}_\sigma \Phi_{k_0 \theta_0}(\rho, z, t) e^{i(\mathbf{k}_c \cdot \mathbf{r} - \omega t)}, \tag{2.12e}$$

$$\equiv |\psi(\mathbf{k}_c)\rangle. \tag{2.12f}$$

In (2.12b), we have for completeness written out the full expansion of $\Psi_{k_0 \theta_0 \sigma m_\ell}$ in terms of plane waves $e^{i\mathbf{k}(\theta', \phi') \cdot \mathbf{r} - \omega t}$, while in (2.12c) we have performed the ϕ' integration using $\mathbf{k}(\theta', \phi') \cdot \mathbf{r} = k \sin \theta' \rho \cos \phi' - \phi + k \cos \theta' \hat{\mathbf{z}}$, $\omega = kc$, and (2.8b). In (2.12d) we have used the paraxial approximation $\theta_0 \ll 1$ to write $k \cos \theta' \approx k$, let $k \equiv k_0 + \delta k$, and factored the constant term $e^{ik_0(\hat{\mathbf{z}} \cdot \mathbf{r} - ct)}$ out of the θ' and k integrands.

The construction of the desired states $\Psi_{k_0 \theta_0 \sigma m_\ell} \equiv |\psi(\mathbf{k})\rangle$ is now complete. These wave packets are polyenergetic paraxial beams, constructed such that their momentum distribution is characterized by sharp peaks about the central wave number k_0 and the central spherical polar angle $\theta_0 \ll 1$ in k-space, which enforces the paraxial condition. And, most importantly for our purposes, they carry well-defined values of SAM and OAM, have a well defined propagation direction as determined by the central momentum vector $\mathbf{k}_c = k_0 \cos \theta_0 \hat{\mathbf{z}} \approx k_0 \hat{\mathbf{z}}$, and describe physical wave functions associated with both electrons and photons. Due to their SAM and OAM, we will henceforth call such states spin-orbit wave packets.

Spin-Orbit Wave Packet in a Weakly Inhomogeneous Medium

The spin-orbit wave packets $|\psi(\mathbf{k}_c)\rangle$ defined in (2.12f) are freely propagating, so that their central wave vector $\mathbf{k}_c$ is constant and points in the $\hat{\mathbf{z}}$ direction. Furthermore, recall that the magnitude of a free-space wave vector $\mathbf{k}$ is given under (2.6) via the relation $k^2 \equiv \frac{2m}{\hbar^2} E_0$ for electrons and $k^2 \equiv \omega^2 \mu_0 \epsilon_0$ for photons, where $E_0 = \hbar \omega$ has been used. For a particle traveling in a homogeneous medium (i.e., a homogeneous potential energy U for electrons or a medium with homogeneous permitivity ϵ for photons), these relations must be modified by substituting $E_0 \rightarrow E = E_0 \left(1 - \frac{U_{e^-}}{E_0} \right)$ for electrons and $\epsilon_0 \rightarrow \epsilon = \epsilon_0 \left(1 + \frac{U_\gamma}{\epsilon_0} \right)$ for photons, where $U_{e^-} = -eV$ is the electron's difference in potential energy from the zero point, while $U_\gamma = \epsilon - \epsilon_0$ is the photon's difference in permitivity from the vacuum value. For both particles, these substitutions result in the modification of the wave number k by $k \rightarrow kn$, where n is the refractive index for the particle wave function such that $n \equiv \sqrt{\frac{E}{E_0}} = \sqrt{1 - \frac{U_{e^-}}{E_0}}$ for electrons and $n \equiv \sqrt{\frac{\epsilon}{\epsilon_0}} = \sqrt{1 + \frac{U_\gamma}{\epsilon_0}}$ for photons. Therefore, one may construct wave packets of the form $|\psi(\mathbf{k}_c)\rangle$ which propagate in a homogeneous media, provided the substitution $k \rightarrow kn$ is made in (2.12), such that the central wave number in particular is modified by $k_0 \rightarrow k_0 n$.

Although the wave number of a quantum particle propagating in a homogeneous medium is modified from the free-space wave number as discussed above, the direction of the wave vector remains constant in both the free space and homogeneous cases. Since we are interested in the case in which an electron or photon wave packet propagates along a curvilinear

path S such that the direction of the wave vector will vary, we must consider an inhomogeneous medium characterized by a spatially dependent refractive index $n(\mathbf{r})$ which varies slowly compared to an optical wavelength $\lambda = \dfrac{2\pi}{k_0}$. In such a medium, the central wave vector of the wave packet $|\psi(\mathbf{k}_c)\rangle$ becomes spatially dependent, assuming the general form $\mathbf{k}_c \to k_0 n(\mathbf{r}_c)\,\hat{\mathbf{u}}(\mathbf{r}_c)$, such that both the wave vector magnitude $k_0 n(\mathbf{r}_c)$ and direction $\hat{\mathbf{u}}(\mathbf{r}_c)$ depend upon the location $\mathbf{r}_c$ of the wave packet center in the medium. Furthermore, letting s parameterize the curve S such that $\mathbf{r}_c \to \mathbf{r}_c(s)$, we note that the unit wave vector $\hat{\mathbf{u}}(\mathbf{r}_c(s))$ is also the unit tangent vector to the curve S. Therefore, treating the particle as a ray with position $\mathbf{r}_c(s)$ and tangent vector $\hat{\mathbf{u}}(\mathbf{r}_c(s))$, which experiences the local refractive index $n(\mathbf{r}_c(s))$ as it propagates along the curve S, allows us to invoke the ray equation [39],

$$\partial_s n(\mathbf{r}_c(s))\,\partial_s \mathbf{r}_c(s) = \nabla n(\mathbf{r}_c(s)), \tag{2.13}$$

where $\partial_s \equiv \hat{\mathbf{u}}(\mathbf{r}_c(s)) \cdot \nabla$ is the directional derivative along the curve.

For concreteness, we consider first the simple case of a cylindrically symmetric medium coaxial with the z axis with a weakly varying parabolic refractive index of the cylindrically symmetric form $n(\mathbf{r}_c(s)) = n(\rho_c(s)) = n(0)\sqrt{1 - \Delta\rho_c^2(s)}$, with $\Delta \ll 1$, such that $n(\rho_c(z)) \approx n(0)\left(1 - \dfrac{1}{2}\Delta\rho_c^2(z)\right)$. Furthermore, to simplify the analysis we further assume that the trajectory $\mathbf{r}_c(s)$ remains approximately parallel with the z axis for all s, so that $s \approx z$ and $\hat{\mathbf{u}}(\mathbf{r}_c(s)) \approx \hat{\mathbf{z}}$, which implies $\partial_s \approx \partial_z$. Under this paraxial trajectory approximation, (2.13) therefore reduces to the paraxial ray equation,

$$\partial_z n\left(\mathbf{r}_c\left(z\right)\right)\partial_z \mathbf{r}_c\left(z\right) = \nabla n\left(\mathbf{r}_c\left(z\right)\right), \tag{2.14a}$$

$$\rightarrow \partial_z^2 \mathbf{r}_c\left(z\right) = \nabla \ln n\left(\rho_c\left(z\right)\right), \tag{2.14b}$$

$$\rightarrow \partial_z^2 \mathbf{r}_c\left(z\right) \approx -\Delta \mathbf{r}_{Tc}\left(z\right), \tag{2.14c}$$

where we have replaced $n\left(\mathbf{r}_c\left(z\right)\right) \rightarrow n\left(\rho_c\left(z\right)\right)$ in (2.14b), and where $\mathbf{r}_{T_c}\left(z\right) \equiv x_c\left(z\right)\hat{\mathbf{x}} + y_c\left(z\right)\hat{\mathbf{y}}$ is the transverse part of the ray position vector $\mathbf{r}_c\left(z\right)$ in (2.14c). Also in (2.14c), we have used $\nabla \ln n\left(\rho_c\left(z\right)\right) = \dfrac{\nabla n\left(\rho_c\left(z\right)\right)}{n\left(\rho_c\left(z\right)\right)} \approx \nabla\left(1 - \dfrac{1}{2}\Delta\rho_c^2\left(z\right)\right) = -\dfrac{\Delta}{2}\nabla\left(x_c^2\left(z\right) + y_c^2\left(z\right)\right) = -\Delta \mathbf{r}_{Tc}\left(z\right)$.

The general solutions to (2.14c) are

$$\mathbf{r}_{Tc}\left(z\right) = \begin{pmatrix} x_0 \cos\left(\sqrt{\Delta}z\right) + \dfrac{\theta_{x_0}}{\sqrt{\Delta}}\sin\left(\sqrt{\Delta}z\right) \\ y_0 \cos\left(\sqrt{\Delta}z\right) + \dfrac{\theta_{y_0}}{\sqrt{\Delta}}\sin\left(\sqrt{\Delta}z\right) \end{pmatrix} \tag{2.15}$$

where x_0 and y_0 are the initial x and y coordinates of the ray $\mathbf{k}_c$, and θ_{x_0} and θ_{y_0} are its initial angle in the x–z and y–z planes, respectively. The curves traced out by the trajectories $\mathbf{r}_{Tc}$ are in general elliptical helices. However, for $x_0 = 0$, $\theta_{y_0} = 0$, and $\theta_{x_0} = y_0\sqrt{\Delta}$, $\mathbf{r}_{Tc}$ assumes the simpler form

$$\mathbf{r}_{Tc}\left(z\right) = \begin{pmatrix} y_0 \sin\left(\sqrt{\Delta}z\right) \\ y_0 \cos\left(\sqrt{\Delta}z\right) \end{pmatrix} \tag{2.16}$$

so that the trajectories become circular helices with pitch $\dfrac{2\pi}{\sqrt{\Delta}}$ and radius y_0.
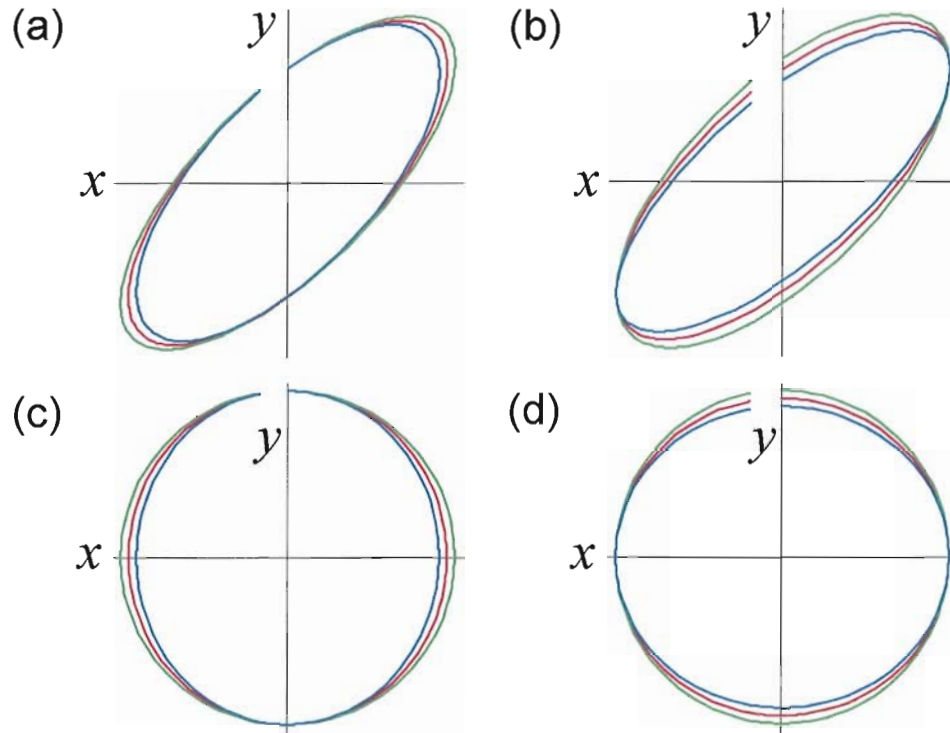
Figure 2.2. Projections of helical trajectories of rays in a gradient index medium with a weakly parabolic index profile with $\Delta = 0.05$. The rays are propagating paraxially with respect to the z direction, and their paths are projected into the x–y plane. For purposes of illustration, 97% of a single full helical cycle is shown. The initial condition $x_0 = 0$ holds for all plots. See text for further discussion. (a) Elliptical helical rays with slightly different initial angular coordinates: $\theta_{x_0} = \theta_{y_0} = y_0\Delta$ (red), $\theta_{x_0} = \theta_{y_0} = 1.05y_0\Delta$ (green), and $\theta_{x_0} = \theta_{y_0} = 0.95y_0\Delta$ (blue). (b) Elliptical helical rays with different initial transverse coordinates: y_0 (red), $1.05y_0$ (green), and $0.95y_0$ (blue). (c) Circular helical rays ($x_0 = 0$, $\theta_{y_0} = 0$, and $\theta_{x_0} = y_0\sqrt{\Delta}$) with slightly different initial angular coordinates: $\theta_{x_0} = y_0\Delta$ (red), $\theta_{x_0} = 1.05y_0\Delta$ (green), and $\theta_{x_0} = 0.95y_0\Delta$ (blue). (d) Circular helical rays ($x_0 = 0, \theta_{y_0} = 0$) with different initial transverse coordinates: y_0 (red), $1.05y_0$ (green), and $0.95y_0$ (blue).

Projections of the helical trajectories of various rays onto the x–y plane are plotted in Fig. 2.2. In Fig. 2.2(a), the solutions (2.15) are plotted for slightly different initial angular coordinates θ_{x_0} and θ_{y_0}, while in Fig. 2.2(b) they are plotted for slightly different initial transverse coordinates y_0 (due to the cylindrical symmetry of the problem, we set $x_0 = 0$ throughout without loss of generality.) Similarly, in Fig. 2.2(c), the solutions (2.16) are plotted for slightly different initial angular coordinates, while in Fig. 2.2(d) they are plotted for slightly different initial transverse coordinates. In each plot, 97% of a single full helical cycle is shown for purposes of illustration. Comparing now (2.15) and (2.16) with Fig. 2.2, we may see that each individual ray is cyclic—that is, each ray follows a repreated periodic path. Specifically, if the rays start out at the same position but at different angles, they will take slightly difference paths, but will all return to the same position after each cycle (see Fig. 2.2(a),(c)). Similarly, if the rays start out with different transverse positions but are at the same initial angle, they will again take seperate paths, but their separation distance will not be distorted at the completion of each cycle (see Fig. 2.2(b),(d)).

From the above analysis we may make two important conclusions: First, in a weakly varying parabolic medium such that Δ is sufficiently small, a paraxial beam of rays neither diverges nor is distorted. Also, since the optical path lengths of the different rays of Fig. 2.2 are approximately equal, each paraxial ray will accumulate approximately the same phase, at least for a reasonably small number of cycles. It follows from these that a paraxial spin-orbit wave packet $|\psi(\mathbf{k}_c)\rangle$, which decomposes into plane waves according to (2.12), retains its approximate form when propagating in such a parabolic medium with $\Delta \ll 1$, with

its central momentum wave vector $\mathbf{k}_c$ following the central trajectories given in red in Fig. 2.2 (the other contributing wave vectors follow nearby trajectories in Fig. 2.2 such as the outlying blue and green ones). Furthermore, from this example it is clear that in any medium with a sufficiently weakly varying refractive index profile $n(\mathbf{r}) = n(0)\sqrt{1 - \Delta\chi(\mathbf{r})}$ such that $\Delta \ll 1$ and $\chi(\mathbf{r})$ arbitrary, $|\psi(\mathbf{k}_c)\rangle$ will approximately retain its form, provided that the central wave vector $\mathbf{k}_c$ undergoes cyclic variations as in the example above.

From the above arguments, we conclude that if the central wave vector $\mathbf{k}_c$ of the spin-orbit wave packet $|\psi(\mathbf{k}_c)\rangle$ traverses a single cycle of a cyclic path in some time interval τ, then the wave packet evolves back into the same state, up to an overall phase:

$$|\psi(\mathbf{k}_c(\tau))\rangle = e^{i\Phi}\,|\psi(\mathbf{k}_c(0))\rangle. \tag{2.17}$$

What is this overall phase? One component of it is the dynamical phase Φ_D, which is given by the line integral of the wave number along the path S with parameter s:

$$\Phi_D \equiv \int \mathbf{k}_c \cdot \hat{\mathbf{u}}(s)\,ds = \int k_0 n(s)\,ds, \tag{2.18}$$

where $\mathbf{k}_c = k_0 n(s)\,\hat{\mathbf{u}}(s)$ has been used. We focus now on the simple case of the red circular helical trajectory in Figs. 2.2(c),(d), of which a rendering of the three-dimensional trajectory has already been given in Fig. 2.1. In this special case, the refractive index is constant for a trajectory of constant radius y_0 due to the cylindrical symmetry of the medium, so that

$$\Phi_D = k_0\,n(\rho)|_{\rho=y_0}\int ds = 2\pi k_0 n(y_0)\sqrt{y_0^2 + \frac{1}{\Delta}}, \tag{2.19}$$

is the dynamical phase accumulated by the spin-orbit wave packet, where $2\pi\sqrt{y_0^2 + \dfrac{1}{\Delta}}$ is the helical path length for a single helical cycle. As we have already discussed, however, there is in general another geometrical contribution to the phase factor $e^{i\Phi}$ in (2.17), which depends not simply on the total optical path length, but on the geometry of the path S. It is to this geometric phase that we now turn.

Geometric Phase of a General Quantum System

Consider a normalized quantum state $|\psi(t)\rangle$ in a Hilbert space $\mathcal{H}$, which evolves according to the Schrödinger equation

$$\hat{H}(t)|\psi(t)\rangle = i\hbar\partial_t |\psi(t)\rangle, \tag{2.20}$$

such that the original state $|\psi(0)\rangle$ at time $t = 0$ evolves back into itself—up to a unitary phase factor $e^{i\Phi}$—at some later time τ:

$$|\psi(\tau)\rangle = e^{i\Phi}|\psi(0)\rangle. \tag{2.21}$$

Although the states $|\psi(0)\rangle$ and $|\psi(\tau)\rangle$ are distinct vector in the Hilbert space $\mathcal{H}$, one may define a "projective" Hilbert space $\mathcal{P}$ where these states (and all other states related by a complex phase factor such as $e^{i\Phi}$) are identified as the same element of that space. Formally, given some vector $e^{i\Phi}|\psi'\rangle$ in $\mathcal{H}$, let the set $\{|\psi'\rangle\}$ be defined as the set of all vectors $|\bar{\psi}\rangle$ in $\mathcal{H}$ such that $|\bar{\psi}\rangle = e^{i\Phi}|\psi'\rangle$. Then the projective Hilbert space $\mathcal{P}$ is defined as the vector space

whose elements consist of all possible sets of the form $\{|\psi'\rangle\}$ that may be constructed from vectors in $\mathcal{H}$. using this language, we may say that the condition (2.21) means that $|\psi(t)\rangle$ has traversed a closed loop (i.e., a cyclic evolution) in the projective Hilbert space $\mathcal{P}$.

Note that we may carry out a unitary transformation on the state $|\psi(t)\rangle$ without affecting the value of the observable $\langle\psi(t)|\hat{H}|\psi(t)\rangle$. With this in mind, we now carry out a unitary (gauge) transformation upon $|\psi(t)\rangle$,

$$|\tilde{\psi}(t)\rangle \equiv \hat{U}(t)|\psi(t)\rangle = e^{-i\tilde{\Phi}(t)}|\psi(t)\rangle, \tag{2.22}$$

such that $\tilde{\Phi}(\tau) - \tilde{\Phi}(0) = \Phi$. The transformed state $|\tilde{\psi}(t)\rangle$ then satisfies

$$|\tilde{\psi}(\tau)\rangle = |\tilde{\psi}(0)\rangle, \tag{2.23}$$

which is not true for $|\psi(t)\rangle$, see (2.21). We are interested in the evolution of $|\tilde{\psi}(t)\rangle$ with respect to the time translation operator $i\partial_t$, which by the chain rule may be expressed as:

$$i\partial_t|\tilde{\psi}(t)\rangle = i\partial_t e^{-i\tilde{\Phi}(t)}|\psi(t)\rangle = \left[i\partial_t e^{-i\tilde{\Phi}(t)}\right]|\psi(t)\rangle + e^{-i\tilde{\Phi}(t)}i\partial_t|\psi(t)\rangle, \tag{2.24}$$

where the square brackets emphasize that the derivative is acting only on the phase factor $e^{-i\tilde{\Phi}(t)}$ in (2.24), and not the state $|\psi(t)\rangle$. "Dotting" both sides of (2.24) by the bra $\langle\tilde{\psi}(t)|$ and integrating from time zero to time τ then gives

$$\int_0^\tau \langle \tilde{\psi}(t) | i\partial_t | \tilde{\psi}(t) \rangle \, dt = \int_0^\tau \langle \psi(t) | \left[e^{i\tilde{\Phi}(t)} i\partial_t e^{-i\tilde{\Phi}(t)} \right] | \psi(t) \rangle \, dt$$

$$+ \int_0^\tau \langle \psi(t) | e^{i\tilde{\Phi}(t)} e^{-i\tilde{\Phi}(t)} i\partial_t | \psi(t) \rangle \, dt, \qquad (2.25\text{a})$$

$$= \int_0^\tau \left[e^{i\tilde{\Phi}(t)} i\partial_t e^{-i\tilde{\Phi}(t)} \right] \, dt$$

$$+ \frac{1}{\hbar} \int_0^\tau \langle \psi(t) | \hat{H}(t) | \psi(t) \rangle \, dt, \qquad (2.25\text{b})$$

$$= \int_0^\tau \partial_t \tilde{\Phi}(t) \, dt + \frac{1}{\hbar} \int_0^\tau \langle \psi(t) | \hat{H}(t) | \psi(t) \rangle \, dt, \qquad (2.25\text{c})$$

$$= \Phi + \Phi_D, \qquad (2.25\text{d})$$

where (2.20) has been used in (2.25b). In (2.25d), $\Phi \equiv \tilde{\Phi}(\tau) - \tilde{\Phi}(0)$ is the total phase accumulated over time τ as defined in (2.21) and below (2.22), and

$$\Phi_D \equiv \frac{1}{\hbar} \int_0^\tau \langle \psi(t) | \hat{H}(t) | \psi(t) \rangle \, dt, \qquad (2.26)$$

which simplifies to $\Phi_D = \frac{E}{\hbar} t$ in the case where $| \psi(t) \rangle$ is an eigenstate of $\hat{H}(t)$, is the so-called dynamical part of the phase accumulated over time τ.

From (2.25d), we therefore see that the total phase Φ is made up of two contributions: a dynamical phase contribution Φ_D and the Berry phase contribution

$$\Phi_B \equiv \int_0^\tau \langle \tilde{\psi}(t) | i\partial_t | \tilde{\psi}(t) \rangle \, dt = \int_0^\tau \langle \psi(t) | e^{+i\tilde{\Phi}(t)} i\partial_t e^{-i\tilde{\Phi}(t)} | \psi(t) \rangle \, dt, \qquad (2.27)$$

so that

$$\Phi = \Phi_B - \Phi_D. \tag{2.28}$$

Equation (2.27) is the general expression for the Berry phase derived in [33].

However, hereafter we will make exclusive use of a simplified form of this expression: we substitute $\tilde{\Phi}(t) \equiv \tilde{\Phi}_B(t) - \tilde{\Phi}_D(t)$ into the right hand side of (2.25b), and use the definitions (2.27) and (2.26) in order to write the Berry phase as

$$\Phi_B = \int_0^\tau \left[e^{i\tilde{\Phi}_B(t)} i\partial_t e^{-i\tilde{\Phi}_B(t)} \right] dt + \int_0^\tau \left[e^{-i\tilde{\Phi}_D(t)} i\partial_t e^{i\tilde{\Phi}_D(t)} \right] dt + \Phi_D, \tag{2.29}$$

where the chain rule $i\partial_t e^{-i\left(\tilde{\Phi}_B(t) - \tilde{\Phi}_D(t)\right)} = e^{i\tilde{\Phi}_D(t)} i\partial_t e^{-i\tilde{\Phi}_B(t)} + e^{-i\tilde{\Phi}_B(t)} i\partial_t e^{i\tilde{\Phi}_D(t)}$ has been used. Carrying out the differentiation of the second term yields the expression $e^{-i\tilde{\Phi}_D(t)} i\partial_t e^{+i\tilde{\Phi}_D(t)} = -e^{-i\tilde{\Phi}_D(t)} e^{i\tilde{\Phi}_D(t)} \partial_t \tilde{\Phi}_D(t) = -\partial_t \tilde{\Phi}_D(t)$, so that upon performing the subsequent integration we have, $-\int_0^\tau \partial_t \tilde{\Phi}_D(t) \, dt = -\tilde{\Phi}_D(t) \Big|_0^\tau = -\left(\tilde{\Phi}_D(\tau) - \tilde{\Phi}_D(0)\right) = -\Phi_D$ which gives rise to the cancellation of the Φ_D term in (2.29). This results in the following expression for the Berry phase:

$$\Phi_B = \int_0^\tau \left[e^{i\tilde{\Phi}_B(t)} i\partial_t e^{-i\tilde{\Phi}_B(t)} \right] dt. \tag{2.30}$$

We note that this expression may seem trivial, since performing the differentiation $i\partial_t e^{-i\tilde{\Phi}_B(t)} = \partial_t \tilde{\Phi}_B(t)$, canceling the complex exponential factors, and integrating the resulting integrand $\partial_t \tilde{\Phi}_B(t)$ yields the trivial relation $\tilde{\Phi}_B(t) = \tilde{\Phi}_B(t)$. However, as we will see, the right hand side of (2.30) has a geometrical interpretation which will allow its straightforward use in calculating the Berry phase Φ_B.

Geometric Phase of a Spin-Orbit Wave Packet

In order to adapt the general expression (2.30) to calculate the Berry phase accumulated by a spin-orbit wave packet of the form $|\psi(\mathbf{k}_c)\rangle$ propagating in an weakly inhomogeneous medium, we note that (2.17) has the same form as the general equation (2.21):

$$|\psi(\tau)\rangle = e^{i\Phi}|\psi(0)\rangle, \tag{2.31a}$$

$$\Leftrightarrow |\psi(\mathbf{k}_c(\tau))\rangle = e^{i\Phi}|\psi(\mathbf{k}_c(0))\rangle, \tag{2.31b}$$

$$\Leftrightarrow |\psi(\mathbf{k}_f)\rangle = e^{i\Phi}|\psi(\mathbf{k}_i)\rangle, \tag{2.31c}$$

Since the time dependence of the state is completely contained within the wave vector $\mathbf{k}_c(t)$ in this case, the time dependence of the momentum has been dropped in (2.31c), where the initial momentum $\mathbf{k}_i$ and final momenta $\mathbf{k}_f$ are equal by construction (in what follows we also temporarily drop the subscript c to simplify the notation). As before in (2.21), the constraint (2.31c) implies that $|\psi(\mathbf{k}_i)\rangle$ has undergone a cyclic evolution in the projective Hilbert space.

After carrying out a gauge transformation on $|\psi(\mathbf{k})\rangle$ analogously to (2.22),

$$|\tilde{\psi}(\mathbf{k})\rangle \equiv \hat{U}(\mathbf{k})|\psi(\mathbf{k})\rangle = e^{-i\tilde{\Phi}(\mathbf{k})}|\psi(\mathbf{k})\rangle, \tag{2.32}$$

we are prepared to consider—analogously to (2.24)—the evolution of $|\tilde{\psi}(\mathbf{k})\rangle$ with respect to the momentum-space translation operator $\partial_{\mathbf{k}}$ (which is, of course, the position operator

$\hat{\mathbf{r}}$) . Note however that equations (2.23)–(2.30) follow directly from the assumption (2.21) and the definition (2.22), if the Schrödinger equation (2.20) is also used. Therefore, since (2.31) and (2.32) are the direct momentum-space analogues to (2.21) and (2.22), and the definition of the position operator in momentum space $\hat{\mathbf{r}} |\psi(\mathbf{k})\rangle = -i\partial_{\mathbf{k}} |\psi(\mathbf{k})\rangle$ acts as a direct analogy to the Schrödinger equation (2.20), we conclude that an analogous version of (2.30) applies to the present case of momentum space with $t \rightarrow \mathbf{k}$, so that $\partial_t \rightarrow \partial_{\mathbf{k}}$, $dt \rightarrow d\mathbf{k}$, $t = 0 \rightarrow \mathbf{k} = \mathbf{k}_i$, and $t = \tau \rightarrow \mathbf{k} = \mathbf{k}_f$:

$$\Phi_B = \int_{\mathbf{k}_i}^{\mathbf{k}_f} \left[e^{i\tilde{\Phi}_B(\mathbf{k})} i\partial_{\mathbf{k}} e^{-i\tilde{\Phi}_B(\mathbf{k})} \right] \cdot d\mathbf{k}. \tag{2.33}$$

Furthermore, we again have the general relationship

$$\Phi = \Phi_B - \Phi_D, \tag{2.34}$$

where the dynamical phase Φ_D now takes the form

$$\Phi_D = - \int_{\mathbf{k}_i}^{\mathbf{k}_f} \langle \psi(\mathbf{k})| \hat{\mathbf{r}} |\psi(\mathbf{k})\rangle \cdot d\mathbf{k}, \tag{2.35}$$

analogously to (2.26). For a wave packet with a sufficiently well-defined position $\mathbf{r} = \langle \psi(\mathbf{k})| \hat{\mathbf{r}} |\psi(\mathbf{k})\rangle$, such that the refractive index of the medium does not vary appreciably over the length scale associated with the wave packet, we may express (2.35) as

$$\Phi_D = -\int_{\mathbf{k}_i}^{\mathbf{k}_f} \mathbf{r} \cdot d\mathbf{k}, \tag{2.36a}$$

$$= -\mathbf{r} \cdot \mathbf{k}\Big|_{\mathbf{k}_i}^{\mathbf{k}_f} + \int_{\mathbf{r}_i}^{\mathbf{r}_f} \mathbf{k} \cdot d\mathbf{r}, \tag{2.36b}$$

$$= \int_{s_i}^{s_f} k_0 n\,(s)\,ds. \tag{2.36c}$$

Here, integration by parts has been used in (2.36b) with the "boundary term" $\mathbf{r} \cdot \mathbf{k}$ being zero since the line integral is over a closed path C in momentum space ($\mathbf{k}_i = \mathbf{k}_f$). In (2.36c), $\mathbf{k} = k_0 n\,(\mathbf{r}\,(s))\,\hat{\mathbf{u}}\,(\mathbf{r}\,(s)) = k_0 n\,(s)\,\hat{\mathbf{u}}\,(s)$ and $d\mathbf{r} = \hat{\mathbf{u}}\,(\mathbf{r}\,(s))\,ds = \hat{\mathbf{u}}\,(s)\,ds$ have been used, where s parameterizes the particle trajectory S as in (2.13). Note that equation (2.36) for the dynamical phase Φ_D gives the same form as (2.18), as is to be expected.

Armed with (2.33), we are now in a position to calculate the Berry phase accumulated by the spin-orbit wave packet $|\psi\,(\mathbf{k}_c)\rangle \propto e^{im_\ell \phi}\hat{\mathbf{e}}_\sigma$ (see equation (2.12e)). As already discussed in and around Fig. 2.1, as the wave packet propagates between two points along a curvilinear trajectory S such that its initial and final wave vectors $\mathbf{k}_i$ and $\mathbf{k}_f$ are collinear, the plane transverse to the particle motion (the x–y plane in Fig. 2.1) may experience a rotation about the propagation (z) axis through an angle $\phi\,(\mathbf{k}_c)$ which depends upon the geometry of the curve S via the wave vector $\mathbf{k}_c$. This rotation manifests itself in two ways: the cylindrical ϕ coordinate effectively undergoes the transformation $\phi \to \phi - \phi\,(\mathbf{k}_c)$, and the spin (polarization) state of the electron (photon) undergoes a rotation through the same angle $\phi\,(\mathbf{k}_c)$, where the rotation angle $\phi\,(\mathbf{k}_c)$ depends upon the geometry of the curve S via the wave vector $\mathbf{k}_c$.

As a result of this ϕ coordinate rotation, the OAM term $e^{im_\ell\phi}$ in $|\psi(\mathbf{k}_c)\rangle$ undergoes the transformation

$$e^{im_\ell\phi} \to e^{im_\ell(\phi-\phi(\mathbf{k}_c))} = e^{-im_\ell\phi(\mathbf{k}_c)}e^{im_\ell\phi}, \tag{2.37}$$

so that the geometric phase accumulated from the OAM term is proportional to the OAM quantum number m_ℓ for both electrons and photons. In contrast, the SAM term $\hat{\mathbf{e}}_\sigma$ transforms differently for the two particle types: for electrons, $\hat{\mathbf{e}}_\sigma$ is a two component spinor which in the $\hat{S}_z$ basis take the form

$$\hat{\mathbf{e}}_\sigma = \begin{pmatrix} \delta_{\sigma+} \\ \delta_{\sigma-} \end{pmatrix}, \tag{2.38}$$

so that the proper matrix representation for a rotation $\hat{R}_z(\phi(\mathbf{k}_c))$ through a angle $\phi(\mathbf{k}_c)$ about the z axis is the so-called $D_{\frac{1}{2}}$ representation [40],

$$D_{\frac{1}{2}}\left[\hat{R}_z(\phi(\mathbf{k}_c))\right]\hat{\mathbf{e}}_\sigma = \left[I\cos\frac{\phi(\mathbf{k}_c)}{2} - i(\hat{\sigma}\cdot\hat{\mathbf{z}})\sin\frac{\phi(\mathbf{k}_c)}{2}\right]\hat{\mathbf{e}}_\sigma, \tag{2.39a}$$

$$= \begin{pmatrix} \cos\dfrac{\phi(\mathbf{k}_c)}{2} - i\sin\dfrac{\phi(\mathbf{k}_c)}{2} & 0 \\ 0 & \cos\dfrac{\phi(\mathbf{k}_c)}{2} + i\sin\dfrac{\phi(\mathbf{k}_c)}{2} \end{pmatrix}\begin{pmatrix} \delta_{\sigma+} \\ \delta_{\sigma-} \end{pmatrix},$$

$$\tag{2.39b}$$

$$= \begin{pmatrix} e^{-i\frac{\phi(\mathbf{k}_c)}{2}} & 0 \\ 0 & e^{i\frac{\phi(\mathbf{k}_c)}{2}} \end{pmatrix}\begin{pmatrix} \delta_{\sigma+} \\ \delta_{\sigma-} \end{pmatrix}, \tag{2.39c}$$

$$= e^{-i\lambda\sigma\phi(\mathbf{k}_c)}\hat{\mathbf{e}}_\sigma, \tag{2.39d}$$

where $\lambda = \dfrac{1}{2}$ is the magnitude of the electron helicity. For photons, however, $\hat{\mathbf{e}}_\sigma$ is a two component polarization vector in the transverse $(x\text{–}y)$ plane which in the linearly polarized basis takes the form

$$\hat{\mathbf{e}}_\sigma = \frac{1}{\sqrt{2}}\left(\hat{\mathbf{x}} + i\sigma\hat{\mathbf{y}}\right) = \begin{pmatrix} 1 \\ i\sigma \end{pmatrix}, \tag{2.40}$$

so that the proper matrix representation for the rotation $\hat{R}_z\left(\phi\left(\mathbf{k}_c\right)\right)$ is the D_1 (faithful) representation for three-dimensional vectors,

$$D_1\left[\hat{R}_z\left(\phi\left(\mathbf{k}_c\right)\right)\right]\hat{\mathbf{e}}_\sigma = \begin{pmatrix} \cos\phi\left(\mathbf{k}_c\right) & -\sin\phi\left(\mathbf{k}_c\right) \\ \sin\phi\left(\mathbf{k}_c\right) & \cos\phi\left(\mathbf{k}_c\right) \end{pmatrix}\begin{pmatrix} 1 \\ i\sigma \end{pmatrix} = e^{-i\lambda\sigma\phi(\mathbf{k}_c)}\hat{\mathbf{e}}_\sigma. \tag{2.41}$$

where $\lambda = 1$ is now the magnitude of the photon helicity. From (2.37), (2.39d), and (2.41), we may thereby express in a single equation the effects of the transverse rotation $\hat{R}_z\left(\phi\left(\mathbf{k}_c\right)\right)$ on the spin-orbit wave packet $|\psi\left(\mathbf{k}_c\right)\rangle$ for both particles:

$$\hat{R}_z\left(\phi\left(\mathbf{k}_c\right)\right)|\psi\left(\mathbf{k}_c\right)\rangle = e^{-i(\lambda\sigma+m_\ell)\phi(\mathbf{k}_c)}|\psi\left(\mathbf{k}_c\right)\rangle. \tag{2.42}$$

From (2.42), we see that this momentum-dependent transverse rotation acts on the state $|\psi\left(\mathbf{k}_c\right)\rangle$ as a momentum-dependent unitary transformation of the general form (2.32), with $\tilde{\Phi}\left(\mathbf{k}\right) = \left(\lambda\sigma + m_\ell\right)\phi\left(\mathbf{k}_c\right)$. As discussed earlier, it follows from this that the particle accumulates a geometric phase Φ_B which is given by (2.33):

$$\Phi_B = \int_{\mathbf{k}_i}^{\mathbf{k}_f} \left[e^{-i(\lambda\sigma+m_\ell)\phi(\mathbf{k}_c)} i\partial_{\mathbf{k}_c} e^{i(\lambda\sigma+m_\ell)\phi(\mathbf{k}_c)} \right] \cdot d\mathbf{k}. \tag{2.43}$$

This expression may be simplified by taking the derivative of the exponential,

$$i\partial_{\mathbf{k}_c} e^{i(\lambda\sigma+m_\ell)\phi(\mathbf{k}_c)} = i\partial_{\mathbf{k}_c} \left(e^{i\phi(\mathbf{k}_c)} \right)^{\lambda\sigma+m_\ell} = (\lambda\sigma + m_\ell) \left(e^{i\phi(\mathbf{k}_c)} \right)^{\lambda\sigma+m_\ell-1} i\partial_{\mathbf{k}_c} e^{i\phi(\mathbf{k}_c)}, \tag{2.44}$$

so that substitution of (2.44) into (2.43) yields

$$\Phi_B = (\lambda\sigma + m_\ell) \int_{\mathbf{k}_i}^{\mathbf{k}_f} \left[e^{-i\phi(\mathbf{k}_c)} i\partial_{\mathbf{k}_c} e^{i\phi(\mathbf{k}_c)} \right] \cdot d\mathbf{k}. \tag{2.45}$$

In Appendix B, following the work of Białynicki-Birula and Białynicka-Birula [28] and Bliokh and Freilikher [41], we show for both electrons and photons that the quantity $\left[e^{-i\phi(\mathbf{k}_c)} i\partial_{\mathbf{k}_c} e^{i\phi(\mathbf{k}_c)} \right] \equiv \mathbf{A}(\mathbf{k}_c)$ is a three-dimensional momentum-dependent vector with curl

$$\nabla \times \mathbf{A}(\mathbf{k}_c) = -\frac{\hat{\mathbf{k}}_c}{k_c^2}, \tag{2.46}$$

where momentum-space spherical coordinates are being used, with k_c being the radial coordinate and $\hat{\mathbf{k}}_c \equiv \dfrac{\mathbf{k}_c}{|\mathbf{k}_c|}$ being the radial unit vector. This result allows us to use Stokes' theorem in order to convert the line integral in (2.45) about the closed momentum-space curve C into a surface integral over a surface spanning C,

$$\oint_C \mathbf{A}(\mathbf{k}_c) \cdot d\mathbf{k} = \int_C \nabla \times \mathbf{A}(\mathbf{k}_c) \cdot d\mathbf{A}, \tag{2.47}$$

where $d\mathbf{A} = dA\hat{\mathbf{n}}$, with $\hat{\mathbf{n}}$ being a unit vector normal to the differential momentum-space surface area element dA. Substituting (2.46) into (2.47), we see that (2.45) may be expressed as

$$\Phi_B = -\left(\lambda\sigma + m_\ell\right) \int_C \frac{\hat{\mathbf{k}}_c}{k_c^2} \cdot d\mathbf{A}, \tag{2.48a}$$

$$= -\left(\lambda\sigma + m_\ell\right) \int_C \frac{\hat{\mathbf{n}}}{k_c^2} \cdot k_c^2 d\Omega\hat{\mathbf{n}}, \tag{2.48b}$$

$$= -\left(\lambda\sigma + m_\ell\right) \int_C d\Omega, \tag{2.48c}$$

$$= -\left(\lambda\sigma + m_\ell\right) \Omega, \tag{2.48d}$$

where $\hat{\mathbf{k}}_c = \hat{\mathbf{n}}$ and $dA = k_c^2 d\Omega$ have been used in (2.48b), with $d\Omega$ being the differential momentum-space element of solid angle. In (2.48c) we see that all factors of the momentum-space radial coordinate k_c cancel and that the dot product is trivial, so that the integral reduces to $\int_C d\Omega = \Omega$, which is the total solid angle subtended by the momentum-space curve C as seen from the origin.

This important result states in words that a spin-orbit wave packet of the form $|\psi(\mathbf{k}_c)\rangle$ with SAM σ and OAM m_ℓ as given in (2.12) will accumulate a geometric phase of the form $\Phi_B = -\left(\lambda\sigma + m_\ell\right)\Omega$ upon propagating around a single closed loop in momentum space, where λ is the particle helicity magnitude and Ω is the solid angle subtended by the loop. For a simple example, consider the case where the particle's curvilinear trajectory S marks out a circular helix as shown in Fig. 2.3(a), such that the momentum-space curve C becomes a circle on the Poincaré (unit) sphere, as shown in Fig. 2.3(b). In this case (which was also
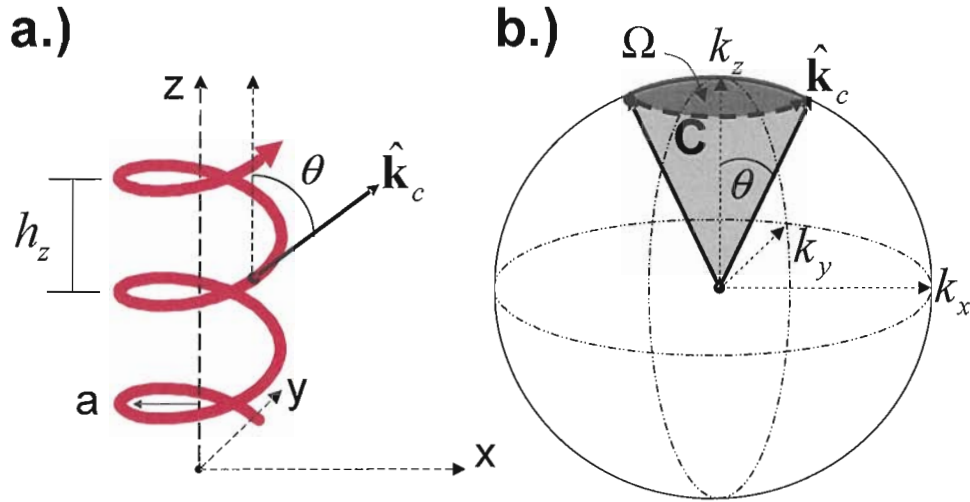
Figure 2.3. (a) Helical particle trajectory S with constant radius a, helixt pitch h_z, and pitch angle θ. (b) The helical path S corresponds to a circular curve C traced out by the unit momentum vector $\hat{\mathbf{k}}_c$ in momentum space, which subtends solid angle $\Omega = 4\pi \sin^2 \frac{\theta}{2}$ as seen from the origin. This solid angle is proportional to the accumulated geometric phase.

considered in Fig. 2.1), the solid angle Ω is given by the simple formula $\Omega = 4\pi \sin^2 \frac{\theta}{2}$ so that the accumulated geometric phase is

$$\Phi_B = -\left(\lambda\sigma + m_\ell\right) 4\pi \sin^2 \frac{\theta}{2}, \tag{2.49}$$

where θ is the angle that the particle's central wave vector $\mathbf{k}_c$ makes with the rotation axis of the helix (i.e., the helix pitch angle, see Figs. 2.1 and 2.3).

The OAM-dependence of the result (2.48d) was first presented in the context of spin-orbit wave packets by Bliokh [41–44], while its SAM-dependence was first discussed in a unified manner for both particles by Białynicki-Birula and Białynicka-Birula in the context of Poincaré group transformations of plane waves [28]. As we will see in subsequent chapters,

(2.48d) plays a central role in both the design of our 2-D parity sorting interferometer and in understanding the physics of the spin-orbit interaction.

CHAPTER III

TRANSVERSE SPATIAL PARITY SORTING OF PHOTONS

Introduction

In recent years, several studies have focused on the problem of sorting higher-order photonic transverse spatial modes by their spatial symmetry properties. In particular, several different interferometers of the Mach-Zehnder type have been proposed and employed to this end. For Laguerre-Gauss (LG) modes, an orbital angular momentum (OAM) sorter was demonstrated at the single-photon level which sorted modes with even OAM values, which exited one port of the interferometer, from those with odd OAM values, which exited the other port [45, 46]. For the Hermite-Gauss (HG) modes, a mode index sorter was theoretically proposed to measure the value of a single HG index n or m [47], while a different setup experimentally distinguished the HG_{10} and HG_{01} modes, thereby acting as a transverse-mode beam splitter for first-order HG modes, in analogy with a polarizing beam splitter [23]. A similar setup was later used to perform various spatial parity manipulations on photonic qubits [8].

In this chapter, we discuss in detail the properties of the two aforementioned sorters which have been experimentally implemented (see [23] and [46]), and build off of this groundwork by describing a new type of interferometric two-dimensional (2-D) parity sorter, which has

substantially superior stability properties as compared to those of the Mach-Zehnder type. The interferometers first demonstrated in [23] and [46] perform physically distinct parity operations on the transverse mode space; the scheme in [23] is based upon a one-dimensional (1-D) parity operation, while that of [45] is based on 2-D parity. This distinction seems to have been overlooked in the context of mode sorting prior to our recent work [48], so that the difference between the two sorters had not been previously emphasized.

In order to properly describe these devices, we begin the chapter by presenting a theoretical treatment of the 1-D and 2-D spatial parity properties of paraxial HG and LG modes, and subsequently apply this framework to explain the operation of the 1-D and 2-D sorters. We then describe our improved mode sorter, an out-of-plane Sagnac interferometer whose 2-D sorting capabilities are based on a spatial rotation effect caused by a geometric phase, which is in turn induced by an out-of-plane mirror reflection. We discuss this geometric phase, and explain how one may exploit it to realize a 2-D parity operation on the transverse mode space.

The Paraxial Description of the Electromagnetic Field

In typical optical experiments, the electromagnetic radiation emitted from lasers is confined to a beam-like geometry. Furthermore, in free space the electric and magnetic fields are not independent, so that the one such field may be calculated once the other is known. Therefore, since the response of most laboratory photo detectors depends negligibly on the magnetic field, in what follows we will focus entirely on the electric field. These considera-

tions motivate the use of a beam-like description of the electric field known as the paraxial approximation.

In free space, the electric field $\mathbf{E}(\mathbf{r}, t)$ is a solution of the vector wave equation,

$$\nabla^2 \mathbf{E}(\mathbf{r}, t) - \frac{1}{c^2} \partial_t^2 \mathbf{E}(\mathbf{r}, t) = 0. \tag{3.1}$$

Here, $\mathbf{r} = x\hat{\mathbf{x}} + y\hat{\mathbf{y}} + z\hat{\mathbf{z}}$ is the Cartesian position vector, and the notation ∂ denotes a partial derivative with respect to the coordinate in the subscript position, such that ∂_t^2 denotes a second partial derivative with respect to t. In order to model beam-like radiation, we choose the z-axis as the beam propagation direction, and we express $\mathbf{E}(\mathbf{r}, t)$ as a product of a transverse field distribution $\mathcal{E}_T(\mathbf{r}_T, z)$ and a longitudinal field distribution $\mathcal{E}_L(z, t)$:

$$\mathbf{E}(\mathbf{r}, t) = \mathcal{E}_T(\mathbf{r}_T, z) \times \mathcal{E}_L(z, t)\,\hat{\mathbf{e}}. \tag{3.2}$$

In (3.2), $\mathbf{r}_T = x\hat{\mathbf{x}} + y\hat{\mathbf{y}}$ denotes the Cartesian position vector in the plane transverse to the propagation direction, while $\hat{\mathbf{e}}$ denotes a constant unit vector. The longitudinal function $\mathcal{E}_L(z, t)$ may generally be expressed in the form of a wave packet,

$$\mathcal{E}_L(z, t) = \int \mathcal{E}(\beta)\, e^{i(\beta z - \omega t)} d\beta, \tag{3.3a}$$

$$= \int \mathcal{E}(\beta)\, e^{i[(\beta - k_c)z - (\omega - \omega_c)t]} d\beta \times e^{i(k_c z - \omega_c t)}, \tag{3.3b}$$

$$\equiv F(z, t) \times e^{i(k_c z - \omega_c t)}, \tag{3.3c}$$

where β denotes the z-component of the wave vector, which is also known as the propagation constant for beam-like geometries, and ω denotes angular frequency. In (3.3b), the central monochromatic contribution to the wave packet (known as the carrier wave) has been factored out of the integral, so that k_c and ω_c are the carrier wave propagation constant and angular frequency, respectively. In (3.3c), $F(z,t)$ is known as the longitudinal envelope function.

We now likewise split the Laplacian into its respective transverse and longitudinal parts, such that $\nabla^2 = \nabla_T^2 + \partial_z^2$. Substituting this expression along with (3.2) and (3.3c) into (3.1) leads to the following (exact) equation,

$$\left[\nabla_T^2 + \left(2ik_c\partial_z + 2i\frac{\omega_c}{c^2}\partial_t\right) + \left(\partial_z^2 - \frac{1}{c^2}\partial_t^2\right) - \left(k_c^2 - \frac{\omega_c^2}{c^2}\right)\right]\mathcal{E}_T(\mathbf{r}_T, z)\,F(z,t) = 0, \quad (3.4a)$$

$$\Rightarrow \left[\nabla_T^2 + 2ik_c\left(\partial_z + \frac{1}{c}\partial_t\right) + \left(\partial_z^2 - \frac{1}{c^2}\partial_t^2\right)\right]\mathcal{E}_T(\mathbf{r}_T, z)\,F(z,t) = 0, \quad (3.4b)$$

where the free-space condition $\omega_c = k_c c$ has been used in (3.4b). The paraxial approximation can be made from (3.4) by assuming that the transverse field $E_T(\mathbf{r}_T, z)$ is sufficiently slowly varying with respect to z such that its second derivative is small compared to its first derivative:

$$\partial_z^2 \mathcal{E}_T(\mathbf{r}_T, z) \ll 2k_c\partial_z\mathcal{E}_T(\mathbf{r}_T, z). \quad (3.5)$$

Under this assumption, the term $\partial_z^2 \mathcal{E}_T(\mathbf{r}_T, z)$ in (3.4b) be may neglected, so that (3.4b) may be readily expressed in terms of separate longitudinal and transverse equations,

$$\left[2ik_c \left(\partial_z + \frac{1}{c}\partial_t \right) + \left(\partial_z^2 - \frac{1}{c^2}\partial_t^2 \right) \right] F(z,t) = 0, \tag{3.6a}$$

$$\left(\nabla_T^2 + 2ik_c\partial_z \right) \mathcal{E}_T(\mathbf{r}_T, z) = 0, \tag{3.6b}$$

In what follows we will be interested only in the paraxial transverse field, so we will henceforth

focus on (3.6b), which is known as the paraxial wave equation.

In Cartesian coordinates (x, y, z), the general solutions to (3.6b) are known as the

Hermite-Gaussian (HG_{nm}) modes and take the form [49]

$$\mathcal{E}_T(x,y,z) = \frac{A_{nm}}{w(z)} H_n \left(\frac{\sqrt{2}x}{w(z)} \right) H_m \left(\frac{\sqrt{2}y}{w(z)} \right) e^{-\frac{x^2+y^2}{w^2(z)}} e^{-i\left[(m+n+1)\tan^{-1}\frac{z}{z_0} + \frac{k_c}{2R(z)}(x^2+y^2) \right]}, \tag{3.7}$$

where $A_{nm} = \sqrt{\dfrac{2^{-(n+m-1)}}{\pi n! m!}}$ is a normalization constant, $w(z) = w_0\sqrt{1 + \dfrac{z^2}{z_0^2}}$ parameterizes

the beam width, $H_q(u) = (-1)^q e^{u^2} \dfrac{d^q}{du^q}\left(e^{-u^2} \right)$ denotes a qth-order Hermite polynomial,

$R(z) = z\left(1 + \dfrac{z_0^2}{z^2} \right)$ characterizes the phase curvature, $z_0 = \dfrac{\omega}{2c}w_0^2$ is the Raleigh range, and

w_0 is the minimum beam width, or beam waist. Also in (3.7), n and m are nonnegative

integers which provide a distinct label for orthogonal transverse modes. In cylindrical coor-

dinates (ρ, ϕ, z), the solutions to (3.6b) are known as the Laguerre-Gaussian (LG_p^ℓ) modes,

$$\mathcal{E}_T(\rho, \phi, z) = \frac{A_p^{|\ell|}}{w(z)} \left(\frac{\rho}{w(z)} \right)^{|\ell|} L_p^{|\ell|} \left(\frac{2\rho^2}{w^2(z)} \right) e^{-\frac{\rho^2}{w^2(z)}} e^{-i\left[\ell\phi - (2p+\ell+1)\tan^{-1}\left(\frac{z}{z_0} \right) + \frac{k_c\rho^2}{2R(z)} \right]}, \tag{3.8}$$

where $A_p^{|\ell|} = \sqrt{\dfrac{2^{|\ell|+1}p!}{\pi(|\ell|+p)!}}$, and $L_p^{|\ell|}(u) = \dfrac{u^{-|\ell|}e^u}{p!}\dfrac{d^p}{du^p}\left(e^{-u}u^{p+|\ell|} \right)$ denotes a generalized La-
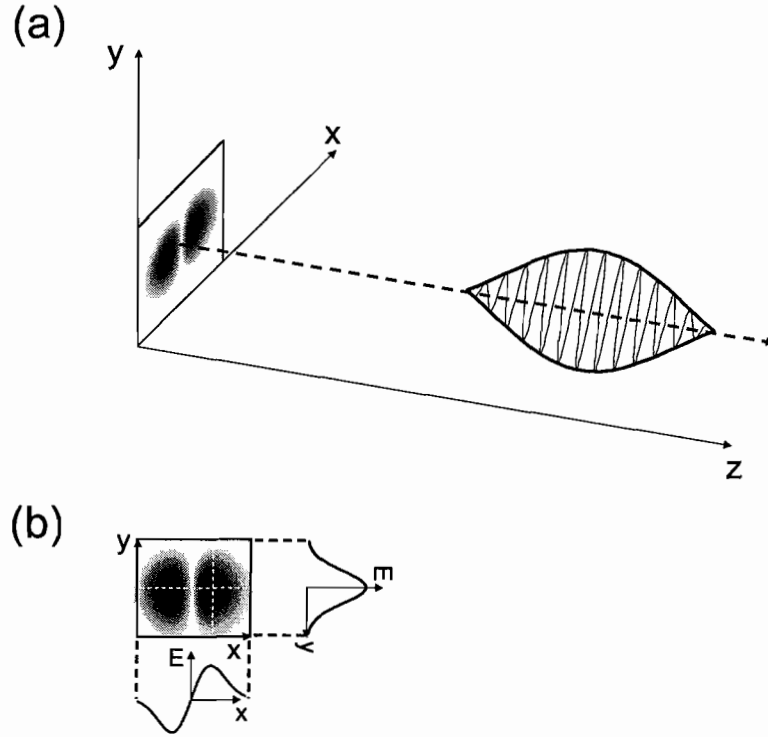
Figure 3.1. (a) Diagram of the electric field of a linearly polarized paraxial beam of the form $E\left(\mathbf{r}, T\right) = \mathcal{E}_T\left(\mathbf{r}_T, z\right) \times F\left(z, T\right) \times e^{i\left(k_c z - \omega_c T\right)}$, at some constant time T. The coordinate axes are displaced from the origin for visibility purposes, such that the dashed arrow emanates from the coordinate origin $(x, y) = (0, 0)$. See text for further discussion. (b) The spatial dependence of the transverse field—chosen to be an HG_{10} mode. In the x vs. y plot, darker shading represents higher field intensity. The dashed white lines indicate slices in the x and y directions along which one-dimensional transverse field profiles are given, which plot x and y vs. the field amplitude E, respectively.

guerre polynomial. Also in (3.8), p is an nonnegative integer and ℓ is an integer, which label distinct orthogonal LG modes.

A temporal "snapshot" of a paraxial beam at time T—that is, an electric field distribution of the form $E\left(\mathbf{r}, T\right) = \mathcal{E}_T\left(\mathbf{r}_T, z\right) \times F\left(z, T\right) \times e^{i\left(k_c z - \omega_c T\right)}$ obeying equations (3.6)—is given

as Fig. 3.1. The longitudinal envelope function is given by the bold curve in Fig. 3.1(a), and the longitudinal field amplitude is given by the height of the curve. The rapidly varying carrier wave is shown inside the envelope function. We have chosen the transverse intensity distribution $|\mathcal{E}_T(\mathbf{r}_T, z)|^2$ to be that of an HG_{10} mode (i.e., an Hermite-Gaussian mode of order $(n, m) = (1, 0)$ as given by (3.7)) which lies entirely in the transverse plane as shown, where darker shading represents higher field intensity. Fig. 3.1(b) shows the spatial dependence of the transverse field $\mathcal{E}_T(\mathbf{r}_T, z)$ along one-dimensional slices in the x and y directions, which are given by the dashed white lines.

<div style="text-align:center">Hermite and Laguerre-Gaussian Transverse Modes</div>

In what follows we are predominantly interested in the transverse properties of the solutions (3.7) and (3.8), so that without loss of generality we may consider a cross-section of these modes at their waist, where $z = 0$. We therefore take the limit as z approaches zero in (3.7) and (3.8), which yield the following formulas for the HG and LG modes:

$$\mathcal{E}_T(x, y, 0) \equiv |HG_{nm}\rangle = \frac{A_{nm}}{w_0} H_n\left(\frac{\sqrt{2}x}{w_0}\right) H_m\left(\frac{\sqrt{2}y}{w_0}\right) e^{-\frac{x^2+y^2}{w_0^2}}, \qquad (3.9a)$$

$$\mathcal{E}_T(\rho, \phi, 0) \equiv |LG_p^\ell\rangle = \frac{A_p^{|\ell|}}{w_0} \left(\frac{\rho}{w_0}\right)^{|\ell|} L_p^{|\ell|}\left(\frac{2\rho^2}{w_0^2}\right) e^{-\frac{\rho^2}{w_0^2}} e^{-i\ell\phi}. \qquad (3.9b)$$

The solutions (3.9a) and (3.9b) (or equivalently, (3.7) and (3.8)) are interchangeable in the sense that each form a complete basis for the transverse mode space, and that any mode from one such basis may be described by a linear combination of modes from the other.

Specifically, a $LG_p^{\pm|\ell|}$ mode may be expressed as a combination of HG_{nm} modes via the following relation [22],

$$\left(\frac{\rho}{w_0}\right)^{|\ell|} L_p^{|\ell|}\left(\frac{2\rho^2}{w_0^2}\right) e^{\mp i\ell\phi} = \frac{w_0}{A_p^{|\ell|}} \left|LG_p^{\pm|\ell|}\right\rangle e^{+\frac{\rho^2}{w_0^2}}$$

$$= (-1)^p \frac{2^{-(2p+|\ell|)}}{p!} \sum_{k=0}^{2p+|\ell|} (2i)^k P_k^{(p+|\ell|-k,\, p-k)}(0)\, H_{2p+|\ell|-k}\left(\frac{\sqrt{2}x}{w_0}\right) H_k\left(\frac{\sqrt{2}y}{w_0}\right),$$

$$(3.10)$$

where $P_k^{(p+|\ell|-k,\, p-k)}(0) = \left.\dfrac{(-1)^k}{2^k k!}\dfrac{d^k}{dt^k}\left[(1\pm t)^{(p+|\ell|)}(1\mp t)^p\right]\right|_{t=0}$. Similarly, an HG_{nm} mode azimuthally rotated by 45°—denoted as $\left|HG_{nm}^{\pm45°}\right\rangle$—so that $x \to \dfrac{x\pm y}{\sqrt{2}}$ and $y \to \dfrac{x\mp y}{\sqrt{2}}$ in (3.9a), may be expressed as a combination of HG_{nm} modes by [22],

$$H_n\left(\frac{x\pm y}{w_0}\right) H_m\left(\frac{x\mp y}{w_0}\right) = \frac{w_0}{A_{nm}}\left|HG_{nm}^{\pm45°}\right\rangle e^{+\frac{\rho^2}{w_0^2}}$$

$$= 2^{-\frac{1}{2}(n+m)} \sum_{k=0}^{n+m} (-2)^k P_k^{(n-k,\, m-k)}(0)\, H_{n+m-k}\left(\frac{\sqrt{2}x}{w_0}\right) H_k\left(\frac{\sqrt{2}y}{w_0}\right), \quad (3.11)$$

where $P_k^{(n-k,\, m-k)}(0) = \left.\dfrac{(-1)^k}{2^k k!}\dfrac{d^k}{dt^k}\left[(1\pm t)^n(1\mp t)^m\right]\right|_{t=0}$.

Now, note that the sums in (3.10) are (3.11) are quite similar in form. In fact, if the integer quantities n and m are respectively identified with $p+|\ell|$ and p throughout, it is seen that these sums are nearly identical except for a phase factor $(-i)^k$ associated with the kth-order Hermite polynomial $H_k\left(\dfrac{\sqrt{2}y}{w_0}\right)$ in each sum. To illustrate this connection between the HG_{nm}, $HG_{nm}^{\pm45°}$, and LG_p^ℓ modes, we have shown in Fig. 3.2 the cases of (3.10) and (3.11) where the sums terminate at $n+m = 2p+|\ell| = 1$. Each of the linear combinations
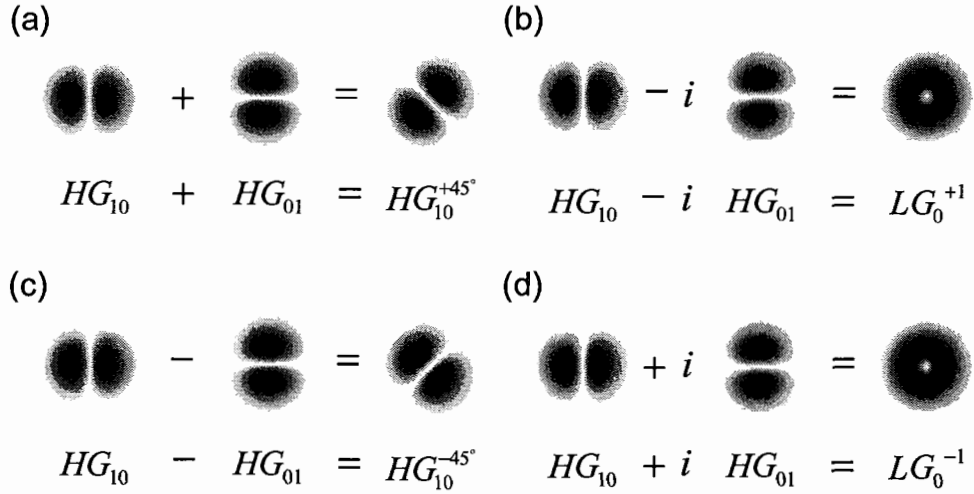
Figure 3.2. Transverse mode intensity distributions showing the decomposition of $HG_{10}^{\pm 45°}$ and $LG_0^{\pm 1}$ modes in terms of HG_{10} and HG_{10} modes. Each mode decomposition is of the form $HG_{10} + e^{i\Phi}HG_{01}$, with $e^{i\Phi}$ taking the values $(1, -i, -1, +i)$ in Figs. (a), (b), (c), and (d) respectively, thereby demonstrating the simple phase relationship between first-order modes.

of transverse fields in Fig. 3.2 has the form $HG_{10} + e^{i\Phi}HG_{01}$, with the relative phase factor $e^{-i\Phi}$ between the HG_{10} and HG_{10} modes changing by increments of $e^{-i\frac{\pi}{2}} = -i$. In this way, the $HG_{10}^{\pm 45°}$ and $LG_0^{\pm 1}$ modes are simply related by a relative phase factor of $-i$.

1-D vs. 2-D Parity Transformations of HG and LG Modes

We now proceed to study the properties of the HG and LG transverse modes of (3.9) under one-dimensional (1-D) and two-dimensional (2-D) spatial parity transformations, which will provide a theoretical basis for our mode-sorting experiments.

1-D Parity

One may define two independent 1-D spatial parity transformation operators $\hat{\Pi}_x$ and $\hat{\Pi}_y$, which respectively act on the x and y coordinates of the transverse HG modes as follows:

$$\hat{\Pi}_x \left[\mathcal{E}_T \left(x, y, 0 \right) \right] \to \mathcal{E}_T \left(-x, y, 0 \right), \tag{3.12a}$$

$$\hat{\Pi}_y \left[\mathcal{E}_T \left(x, y, 0 \right) \right] \to \mathcal{E}_T \left(x, -y, 0 \right). \tag{3.12b}$$

In other words, $\hat{\Pi}_x$ takes x to $-x$ but does not act on y, while $\hat{\Pi}_y$ takes y to $-y$ but does not act on x. Note however that electric fields are vector-valued functions, so that $\hat{\Pi}_x$ and $\hat{\Pi}_y$ transform not only the functional coordinates (x, y) of the fields, but also the field vectors. The actions of the 1-D parity operators on the unit vectors $\hat{\mathbf{x}}$ and $\hat{\mathbf{y}}$ are given by

$$\hat{\Pi}_x \hat{\mathbf{u}}_\pm = \pm \hat{\mathbf{u}}_\pm, \tag{3.13a}$$

$$\hat{\Pi}_y \hat{\mathbf{u}}_\pm = \mp \hat{\mathbf{u}}_\pm, \tag{3.13b}$$

where $\hat{\mathbf{u}}_+ \equiv \hat{\mathbf{y}}$ and $\hat{\mathbf{u}}_- \equiv \hat{\mathbf{x}}$, so that $\hat{\mathbf{x}} \to -\hat{\mathbf{x}}$ under $\hat{\Pi}_x$ and $\hat{\mathbf{y}} \to -\hat{\mathbf{y}}$ under $\hat{\Pi}_y$. Equations (3.12) and (3.13) completely define the actions of $\hat{\Pi}_x$ and $\hat{\Pi}_y$ on transverse fields.

Using the cylindrical coordinate definitions $\rho = \sqrt{x^2 + y^2}$ and $\phi = \tan^{-1} \left(\dfrac{y}{x} \right)$, one finds that $\rho \to \rho$ and $\phi \to -\phi$ under the action of both $\hat{\Pi}_x$ and $\hat{\Pi}_y$. Therefore, $\hat{\Pi}_x$ and $\hat{\Pi}_y$ act on the ρ and ϕ coordinates of the transverse LG modes as

$$\hat{\Pi}_x \left[\mathcal{E}_T \left(\rho, \phi, 0 \right) \right] \rightarrow \mathcal{E}_T \left(\rho, -\phi, 0 \right), \tag{3.14a}$$

$$\hat{\Pi}_y \left[\mathcal{E}_T \left(\rho, \phi, 0 \right) \right] \rightarrow \mathcal{E}_T \left(\rho, -\phi, 0 \right). \tag{3.14b}$$

Substituting (3.9a) and (3.9b) into (3.12)-(3.14) then gives the transformation properties of the HG and LG modes under the action of the 1-D parity operators $\hat{\Pi}_x$ and $\hat{\Pi}_y$:

$$\hat{\Pi}_x \left| HG_{nm} \right\rangle \hat{\mathbf{u}}_\pm = \pm \left(-1 \right)^n \left| HG_{nm} \right\rangle \hat{\mathbf{u}}_\pm, \tag{3.15a}$$

$$\hat{\Pi}_y \left| HG_{nm} \right\rangle \hat{\mathbf{u}}_\pm = \mp \left(-1 \right)^m \left| HG_{nm} \right\rangle \hat{\mathbf{u}}_\pm, \tag{3.15b}$$

$$\hat{\Pi}_x \left| LG_p^\ell \right\rangle \hat{\mathbf{u}}_\pm = \pm \left| LG_p^{-\ell} \right\rangle \hat{\mathbf{u}}_\pm, \tag{3.15c}$$

$$\hat{\Pi}_y \left| LG_p^\ell \right\rangle \hat{\mathbf{u}}_\pm = \mp \left| LG_p^{-\ell} \right\rangle \hat{\mathbf{u}}_\pm. \tag{3.15d}$$

In deriving (3.15a) and (3.15b) the following property of the Hermite polynomials has been used, $H_q \left(-u \right) = \left(-1 \right)^q H_q \left(u \right)$, where $u = x$ or $u = y$. Due to the relationship in (3.15a) and (3.15b), we say that a transverse mode of the form $\left| HG_{nm} \right\rangle \hat{\mathbf{u}}_\pm$ acts as an "even" mode under a 1-D parity flip $\hat{\Pi}_v$ if $\hat{\Pi}_v \left| HG_{nm} \right\rangle \hat{\mathbf{u}}_\pm = + \left| HG_{nm} \right\rangle \hat{\mathbf{u}}_\pm$, and as an "odd" mode under $\hat{\Pi}_v$ if $\hat{\Pi}_v \left| HG_{nm} \right\rangle \hat{\mathbf{u}}_\pm = - \left| HG_{nm} \right\rangle \hat{\mathbf{u}}_\pm$, where $v = x$ or $v = y$. Furthermore, from (3.15c) and (3.15d) it is clear that the action of $\hat{\Pi}_u$ on an LG mode $\left| LG_p^\ell \right\rangle$ simply changes the sign of ℓ.

2-D Parity

It is straightforward to generalize the above results to the case of the 2-D parity transformation $\hat{\Pi}_{xy}$, which is the operator product of $\hat{\Pi}_x$ and $\hat{\Pi}_y$:
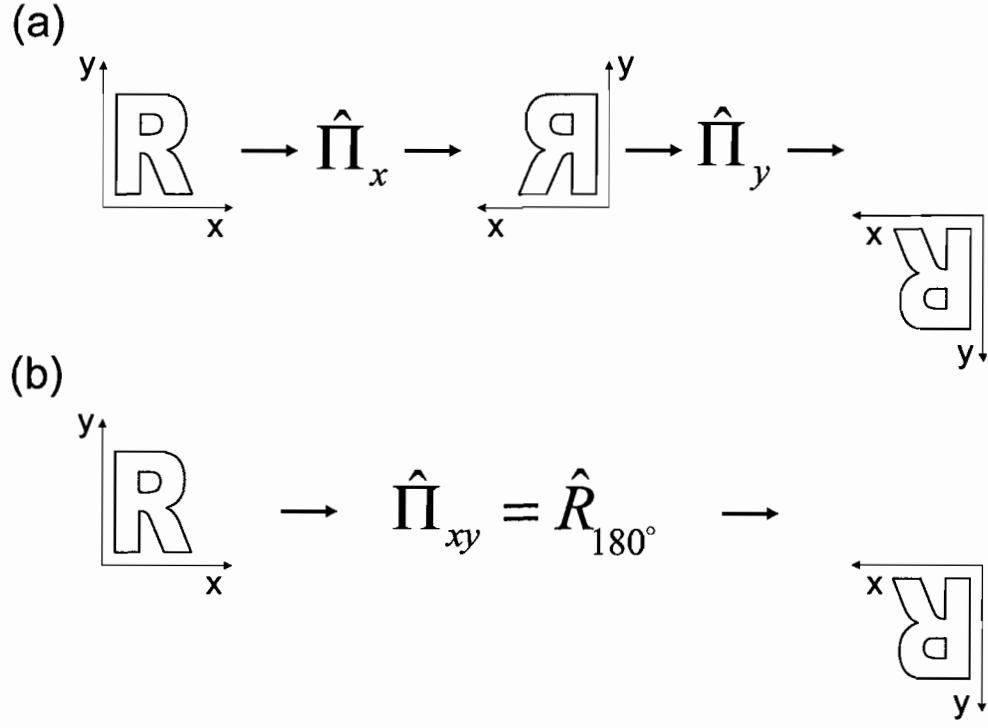
Figure 3.3. (a) The successive action of 1-D parity operators $\hat{\Pi}_x$ and $\hat{\Pi}_y$ upon a two-dimensional image. (b) The action of a 180° azimuthal rotation about the z-axis upon the same image. The transformations (a) and (b) yield identical results.

$$\hat{\Pi}_{xy} \equiv \hat{\Pi}_y \hat{\Pi}_x. \tag{3.16}$$

From (3.16) and (3.13), we find that the vectorial part of a transverse field is transformed by 2-D parity according to

$$\hat{\Pi}_{xy} \hat{\mathbf{u}}_\pm = -\hat{\mathbf{u}}_\pm \tag{3.17}$$

which amounts to a trivial overall phase factor $e^{i\pi} = -1$ for both $\hat{\mathbf{u}}_+$ and $\hat{\mathbf{u}}_-$, in contrast to the case of the 1-D parity flip operation (see (3.13)).

The 2-D parity operator thus takes x to $-x$, y to $-y$, $\hat{\mathbf{x}}$ to $-\hat{\mathbf{x}}$, and $\hat{\mathbf{y}}$ to $-\hat{\mathbf{y}}$, which is equivalent to a 180° azimuthal coordinate rotation about the longitudinal (z) axis (see Fig. 3.3). Therefore, the action of $\hat{\Pi}_{xy}$ on a function involving cylindrical coordinates results in the transformations $\rho \to \rho$ and $\phi \to \phi + \pi$ so that the coordinates of the HG and LG modes are acted upon as follows:

$$\hat{\Pi}_{xy}\left[\mathcal{E}_T\left(x, y, 0\right)\right] \to \mathcal{E}_T\left(-x, -y, 0\right), \tag{3.18a}$$

$$\hat{\Pi}_{xy}\left[\mathcal{E}_T\left(\rho, \phi, 0\right)\right] \to \mathcal{E}_T\left(\rho, \phi + \pi, 0\right). \tag{3.18b}$$

Substituting (3.9a) and (3.9b) into (3.18a) and (3.18b) and using (3.17) then gives the transformation properties of the HG and LG modes under the action of the 2-D parity operator $\hat{\Pi}_{xy}$:

$$\hat{\Pi}_{xy}\left|HG_{nm}\right\rangle \hat{\mathbf{u}}_\pm = -\left(-1\right)^{n+m}\left|HG_{nm}\right\rangle \hat{\mathbf{u}}_\pm, \tag{3.19a}$$

$$\hat{\Pi}_{xy}\left|LG_p^\ell\right\rangle \hat{\mathbf{u}}_\pm = -\left(-1\right)^{|\ell|}\left|LG_p^{-\ell}\right\rangle \hat{\mathbf{u}}_\pm, \tag{3.19b}$$

where $H_q\left(-u\right) = \left(-1\right)^q H_q\left(u\right)$ has again been used in (3.19a), while $e^{i\ell(\phi+\pi)} = \left(-1\right)^{|\ell|}e^{i\ell\phi}$ has been used in (3.19b). Since, as (3.19a) shows, the action of $\hat{\Pi}_{xy}$ is independent of polarization, we ignore the overall polarization transformation factor of -1 and say that $\left|HG_{nm}\right\rangle$ acts as an "even" mode under the 2-D parity flip $\hat{\Pi}_{xy}$ if $n + m$ is even, and as an "odd" mode under

$\hat{\Pi}_{xy}$ if $n + m$ is odd. Similarly, from (3.19b) it is evident that $\left| LG_p^\ell \right\rangle$ acts as an "even" mode under $\hat{\Pi}_{xy}$ if $|\ell|$ is even, and as an "odd" mode under $\hat{\Pi}_{xy}$ if $|\ell|$ is odd, regardless of the value of the radial index p. Furthermore, since $\left| LG_p^\ell \right\rangle$ is an eigenstate of the orbital angular momentum z-component operator $-i\hbar\partial_\phi$, we conclude that $\hat{\Pi}_{xy}$ acts differently upon modes with even or odd value of OAM $|\ell|$.

Parity Sorting Mach-Zehnder Interferometers

The two experimentally implemented sorter designs [23] and [46], shown in Fig. 3.4, physically implement the respective 1-D and 2-D parity operations $\hat{\Pi}_x$ and $\hat{\Pi}_{xy}$ on the transverse mode space, due to the presence of the extra mirror in one arm in the former case and the orthogonally-oriented Dove prisms [50] in the latter. For the 1-D sorter of Fig. 3.4(a), this means in particular that HG_{10} and HG_{01} input modes propagating in the x-z plane exit different ports as shown since they respectively have odd and even parity with respect to reflections about the y-axis in the transverse $(x$-$y)$ plane. On the other hand, for the the 2-D sorter of Fig. 3.4(b), input modes are distinguished on the basis of 2-D parity in the transverse plane. Therefore, conversely to the prior case, the HG_{10} and HG_{01} input modes will be sorted into the *same* port by the OAM sorter, because these modes both have odd 2-D parity. To our knowledge, no experiments were reported in which a sorter of the OAM type was employed to sort HG modes prior to our recent work [48], so that this seems to have been overlooked and the difference between the two sorters had not been previously emphasized.
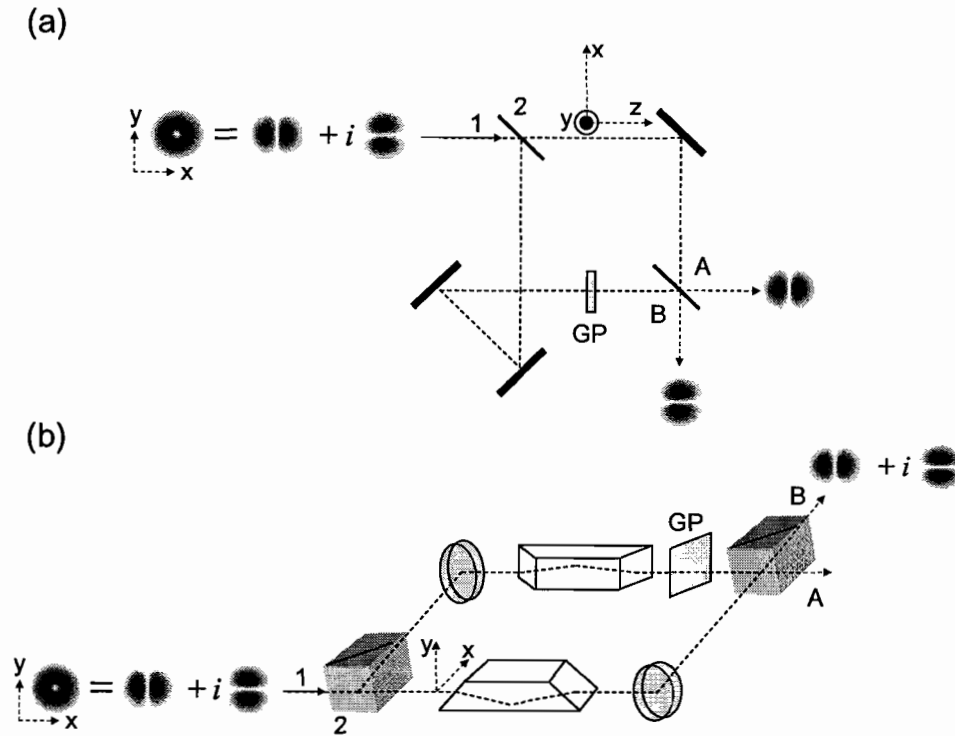
Figure 3.4. Previously realized 1-D and 2-D parity sorters of the Mach-Zehnder type, each with a tiltable phase-shifting glass plate (GP) in one arm, input ports $1, 2$ and output ports A, B. All fields are linearly polarized in the y-direction. (a) Top view of the 1-D parity sorter, which is distinguished by having an extra mirror in one arm. The thin lines represent $50 : 50$ beam splitters, while the thick lines represent mirrors. Upon entering this interferometer, an LG_0^1 mode is sorted into its constituent HG_{10} and HG_{01} components due to complete constructive and destructive interference at the output ports. (b) In contrast, the 2-D parity sorter (viewed here from the side) has a symmetric, trapezoidal Dove prism in each arm. The cubes are $50 : 50$ beam splitters, and the disks are mirrors. One of the Dove prisms is rotated 90 with respect to the other, which causes a 180 relative rotation of the two interfering beams in the transverse plane. In this case, both HG_{10} and HG_{01} modes exit the same port, so that an incident LG_0^1 mode is not decomposed. See text for further discussion.
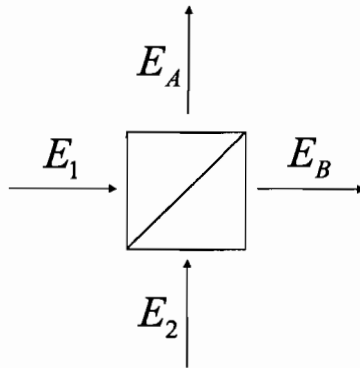
Figure 3.5. An ideal lossless beam splitter. Incident electric fields E_1 and E_2 mix at the beam splitter and give rise to output fields E_A and E_B.

In order to show that the interferometers in Fig. 3.4 indeed act as described above, we give below a theoretical treatment of their operation, which will act as a basis for the development of our phase-stable 2-D parity sorting interferometer. We therefore turn now to the task of describing the effects of the individual components of each interferometer on the input fields.

<div align="center">Beam Splitter</div>

Each of the interferometers in Fig. 3.4 sport a $50 : 50$ beam splitter at their input and output. The transformation of transverse modes due to the ideal lossless beam splitter, shown in Fig. 3.5, may be modeled by imposing conservation of energy between its input and output arms [51]. Mathematically, this requirement may be stated in terms of the linear matrix equations

$$\begin{pmatrix} E_A \\ E_B \end{pmatrix} = \begin{pmatrix} r_{1A} & t_{2A} \\ t_{1B} & r_{2B} \end{pmatrix} \begin{pmatrix} E_1 \\ E_2 \end{pmatrix} \Leftrightarrow E_{\text{out}} = \hat{U} E_{\text{in}}, \qquad (3.20)$$

along with the energy conservation constraint $|E_{\text{in}}|^2 \equiv |E_1|^2 + |E_2|^2 = |E_A|^2 + |E_B|^2 \equiv |E_{\text{out}}|^2$. Here, the input and output electric field amplitudes E_1, E_2, E_A, E_B and the beam splitter reflection and transmission coefficients r_{1A}, r_{2B}, t_{1B}, t_{2A}—all of which are in general complex—are defined via Fig. 3.5, in an obvious notation (for example, r_{1A} denotes the percentage of the field magnitude $|E_1|$ which exits port A of the beam splitter, thereby contributing to the field magnitude $|E_A|$). All input and output fields are assumed for the moment to have identical polarization states.

Together, (3.20) and the energy conservation constraint impose the following conditions on the reflection and transmission coefficients:

$$|r_{1A}|^2 + |t_{1B}|^2 = 1, \qquad (3.21a)$$

$$|r_{2A}|^2 + |t_{2B}|^2 = 1, \qquad (3.21b)$$

$$r_{1A} t_{2A}^* + t_{1B} r_{2B}^* = 0, \qquad (3.21c)$$

$$t_{2A} r_{1A}^* + r_{2B} t_{1B}^* = 0. \qquad (3.21d)$$

Writing r_{1A}, r_{2B}, t_{1B}, t_{2A} in terms of their respective complex amplitudes and phases $|r_{1A}| e^{i\phi_{1A}}$, $|r_{2B}| e^{i\phi_{2B}}$, $|t_{1B}| e^{i\phi_{1B}}$, $|t_{2A}| e^{i\phi_{2A}}$, we find that (3.21c) yields the relation

$$\frac{|r_{1A}|}{|t_{1B}|} e^{i(\phi_{1A} - \phi_{1B})} = -\frac{|r_{2B}|}{|t_{2A}|} e^{i(\phi_{2A} - \phi_{2B})}, \qquad (3.22)$$

which is satisfied only if

$$\frac{|r_{1A}|}{|t_{1B}|} = \frac{|r_{2B}|}{|t_{2A}|}, \tag{3.23a}$$

$$\phi_{1A} + \phi_{2B} - \phi_{1B} - \phi_{2A} = \pm\pi. \tag{3.23b}$$

Using (3.23a) along with (3.21a) and (3.21b) then yields

$$|r_{1A}| = |r_{2B}| \equiv R, \tag{3.24a}$$

$$|t_{2A}| = |t_{1B}| \equiv T, \tag{3.24b}$$

so that $R^2 + T^2 = 1$. Furthermore, from (3.23b) we may without loss of generality choose $\phi_{1A} = \phi_{2B} \equiv \phi_R$ and $\phi_{1B} = \phi_{2A} \equiv \phi_T$ provided $\phi_R - \phi_T = \pm\frac{\pi}{2}$ is satisfied. Using this relation, we arrive at a simplified form for the transformation $\hat{U}$ given in (3.20):

$$\hat{U} = \begin{pmatrix} Re^{i\phi_R} & Te^{i\phi_T} \\ Te^{i\phi_T} & Re^{i\phi_R} \end{pmatrix} = e^{i\phi_R} \begin{pmatrix} R & Te^{i(\phi_T - \phi_R)} \\ Te^{i(\phi_T - \phi_R)} & R \end{pmatrix} = e^{i\phi_R} \begin{pmatrix} R & iT \\ iT & R \end{pmatrix}, \quad (3.25)$$

where the convention $\phi_T - \phi_R = +\frac{\pi}{2}$ has been used in the last equality. We henceforth ignore the irrelevant overall phase factor $e^{i\phi_R}$, so that we may write $\hat{U} \equiv \begin{pmatrix} R & iT \\ iT & R \end{pmatrix}$.

For a balanced $50 : 50$ beam splitter $R = T$, so that $R^2 + T^2 = 1$ implies $R = T = \frac{1}{\sqrt{2}}$, which yields a simple expression for the balanced transformation matrix $\hat{U}_B$:
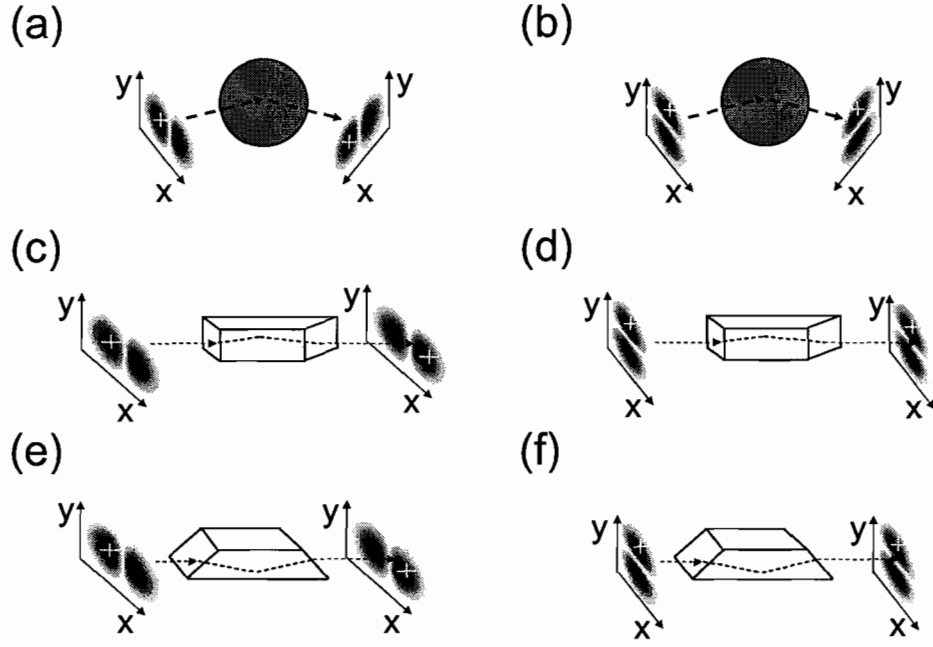
Figure 3.6. The actions of the mirrors and Dove prisms in Fig. 3.4 on $\hat{y}$-polarized HG_{10} and HG_{01} modes. The reflections in the x-z plane due to the mirrors and Dove prisms in (a)-(d) may be represented by the 1-D parity operator $\hat{\Pi}_x$, while the reflections in the y-z plane due to the Dove prisms in (e)-(f) may be represented by $\hat{\Pi}_y$. For $\hat{x}$-polarized modes, (a)-(f) must be modified so that each output mode is multiplied by a factor of -1. See text for further discussion.

$$\hat{U}_B = \frac{1}{\sqrt{2}} \begin{pmatrix} 1 & i \\ i & 1 \end{pmatrix}. \tag{3.26}$$

Interferometer Components

The actions of the mirrors and Dove prisms in Fig. 3.4 on the transverse mode space is shown in Fig. 3.6. From Figs. 3.6(a) and 3.6(b), we see that the HG_{10} and HG_{01} modes (when linearly polarized in the $\hat{y}$ direction) are respectively odd and even with respect to

a single mirror reflection in the x-z plane. This implies that such a mirror reflection is represented by the 1-D parity operator $\hat{\Pi}_x$ since by (3.15a) and (3.15b), $\hat{\Pi}_x \left| HG_{10} \right\rangle \hat{\mathbf{y}} = - \left| HG_{10} \right\rangle \hat{\mathbf{y}}$ and $\hat{\Pi}_x \left| HG_{01} \right\rangle \hat{\mathbf{y}} = + \left| HG_{01} \right\rangle \hat{\mathbf{y}}$, respectively. Conversely, it is clear due to symmetry considerations that a mirror reflection in the y-z plane is represented by $\hat{\Pi}_y$.

Since transit through each of the Dove prisms shown in Figs. 3.6(c)–3.6(f) also involves a single mirror reflection in one of these planes as shown, we may represent their action by the operators $\hat{\Pi}_x$ for 3.6(c) and 3.6(d), and $\hat{\Pi}_y$ for 3.6(e) and 3.6(f), respectively. Therefore, the appropriate mode transformations for $\hat{\mathbf{y}}$-polarized HG_{10} and HG_{01} modes are $\hat{\Pi}_x \left| HG_{10} \right\rangle \hat{\mathbf{y}} = - \left| HG_{10} \right\rangle \hat{\mathbf{y}}$, $\hat{\Pi}_x \left| HG_{01} \right\rangle \hat{\mathbf{y}} = + \left| HG_{01} \right\rangle \hat{\mathbf{y}}$, $\hat{\Pi}_y \left| HG_{10} \right\rangle \hat{\mathbf{y}} = \left| HG_{10} \right\rangle (-\hat{\mathbf{y}}) = - \left| HG_{10} \right\rangle \hat{\mathbf{y}}$, and $\hat{\Pi}_y \left| HG_{01} \right\rangle \hat{\mathbf{y}} = (-1) \left| HG_{10} \right\rangle (-\hat{\mathbf{y}}) = + \left| HG_{10} \right\rangle \hat{\mathbf{y}}$, corresponding to Figs. 3.6(c), 3.6(d), 3.6(e), and 3.6(f), respectively. For $\hat{\mathbf{x}}$-polarized modes, the above results must be modified so that each output mode is multiplied by a factor of -1.

1-D Sorter Theory

Consider now the interferometer in Fig. 3.4(a). By (3.20) and (3.26), the electric field subsequent to the input beam splitter, $\mathbf{E}_{\text{out}}$, is given by $\mathbf{E}_{\text{out}} = \hat{\mathbf{U}}_{\mathbf{B}} \mathbf{E}_{\text{in}}$, where the electric fields are displayed in bold to emphasize their vectorial nature. Since the lower and upper interferometer arms respectively involve double and single mirror reflections in the x-z plane, the appropriate operator to represent these reflections is

$$\hat{\Pi} \equiv \begin{pmatrix} \hat{\Pi}_x^2 & 0 \\ 0 & \hat{\Pi}_x \end{pmatrix} = \begin{pmatrix} 1 & 0 \\ 0 & \hat{\Pi}_x \end{pmatrix}, \qquad (3.27)$$

where $\hat{\Pi}_x^2 = 1$ has been used. Furthermore, since the glass plate may be tuned to impose an arbitrary but uniform phase shift ϕ, its matrix representation may be written as

$$\hat{\Phi} \equiv \begin{pmatrix} e^{i\phi} & 0 \\ 0 & 1 \end{pmatrix} = e^{i\frac{\phi}{2}} \begin{pmatrix} e^{i\frac{\phi}{2}} & 0 \\ 0 & e^{-i\frac{\phi}{2}} \end{pmatrix} \Leftrightarrow \begin{pmatrix} e^{i\frac{\phi}{2}} & 0 \\ 0 & e^{-i\frac{\phi}{2}} \end{pmatrix}, \qquad (3.28)$$

where the irrelevant overall phase factor $e^{i\frac{\phi}{2}}$ has been dropped in the last equality. Finally, the action of the output beam splitter is also of the form $\hat{U}_B$. From (3.20), (3.26), (3.27), and (3.28), we may therefore represent the action of the 1-D parity sorting interferometer on the input vector fields $\mathbf{E}_{\text{in}} = \begin{pmatrix} \mathbf{E_1} \\ \mathbf{E_2} \end{pmatrix} \equiv \begin{pmatrix} E_1 \hat{\mathbf{u}}_\pm \\ E_2 \hat{\mathbf{u}}_{(\pm)} \end{pmatrix}$ as

$$\mathbf{E}_{\text{out}} = \hat{\mathbf{U}}_\mathbf{B} \, \hat{\boldsymbol{\Phi}} \, \hat{\Pi} \, \hat{\mathbf{U}}_\mathbf{B} \, \mathbf{E}_{\text{in}} = \frac{1}{2} \begin{pmatrix} e^{i\frac{\phi}{2}} - e^{-i\frac{\phi}{2}}\hat{\Pi}_x & i\left(e^{i\frac{\phi}{2}} + e^{-i\frac{\phi}{2}}\hat{\Pi}_x\right) \\ i\left(e^{i\frac{\phi}{2}} + e^{-i\frac{\phi}{2}}\hat{\Pi}_x\right) & -\left(e^{i\frac{\phi}{2}} - e^{-i\frac{\phi}{2}}\hat{\Pi}_x\right) \end{pmatrix} \begin{pmatrix} E_1 \hat{\mathbf{u}}_\pm \\ E_2 \hat{\mathbf{u}}_{(\pm)} \end{pmatrix},$$
$$(3.29)$$

where the choice of polarization $\hat{\mathbf{u}}_\pm$ for mode E_1 is independent from that of mode E_2, $\hat{\mathbf{u}}_{(\pm)}$.

If we assume that the input fields $E_1 \hat{\mathbf{u}}_\pm$ and $E_2 \hat{\mathbf{u}}_{(\pm)}$ are both HG modes of the respective orders $HG_{n_1 m_1}$ and $HG_{n_2 m_2}$, then we may use (3.15) to replace $\hat{\Pi}_x E_1 \hat{\mathbf{u}}_\pm \rightarrow \pm (-1)^{n_1} E_1 \hat{\mathbf{u}}_\pm$ and $\hat{\Pi}_x E_2 \hat{\mathbf{u}}_{(\pm)} \rightarrow (\pm) (-1)^{n_2} E_2 \hat{\mathbf{u}}_{(\pm)}$ in (3.29):

$$\mathbf{E}_{\text{out}} = \begin{pmatrix} \mathbf{E_A} \\ \mathbf{E_B} \end{pmatrix} = \frac{1}{2} \begin{pmatrix} e^{i\frac{\phi}{2}} \mp (-1)^{n_1} e^{-i\frac{\phi}{2}} & i\left(e^{i\frac{\phi}{2}} (\pm)(-1)^{n_2} e^{-i\frac{\phi}{2}}\right) \\ i\left(e^{i\frac{\phi}{2}} \pm (-1)^{n_1} e^{-i\frac{\phi}{2}}\right) & -\left(e^{i\frac{\phi}{2}} (\mp)(-1)^{n_2} e^{-i\frac{\phi}{2}}\right) \end{pmatrix} \begin{pmatrix} \mathbf{E_1} \\ \mathbf{E_2} \end{pmatrix}.$$

$$(3.30)$$

Since we are interested in the case where the interferometer sorts a single input beam, we set the port 2 input beam $\mathbf{E_2}$ equal to zero, so that (3.30) simplifies to

$$\begin{pmatrix} \mathbf{E_A} \\ \mathbf{E_B} \end{pmatrix} = \begin{pmatrix} \cos\frac{\phi}{2} \, \mathbf{E_1} \\ -\sin\frac{\phi}{2} \, \mathbf{E_1} \end{pmatrix} \qquad \text{for } \mathbf{E_1} \text{ odd: } \pm(-1)^{n_1} = -1, \qquad (3.31a)$$

$$\begin{pmatrix} \mathbf{E_A} \\ \mathbf{E_B} \end{pmatrix} = \begin{pmatrix} i\sin\frac{\phi}{2} \, \mathbf{E_1} \\ i\cos\frac{\phi}{2} \, \mathbf{E_1} \end{pmatrix} \qquad \text{for } \mathbf{E_1} \text{ even: } \pm(-1)^{n_1} = +1. \qquad (3.31b)$$

When the input beam $\mathbf{E_1}$ is neither even nor odd, we may split it into its respective odd and even components $\mathbf{E_1} = \mathbf{E_1^{(o)}} + \mathbf{E_1^{(e)}}$, so that by adding (3.31a) and (3.31b) together we find that

$$\begin{pmatrix} \mathbf{E_A} \\ \mathbf{E_B} \end{pmatrix} = \frac{1}{2} \begin{pmatrix} \cos\frac{\phi}{2} \, \mathbf{E_1^{(o)}} + i\sin\frac{\phi}{2} \, \mathbf{E_1^{(e)}} \\ -\left(\sin\frac{\phi}{2} \, \mathbf{E_1^{(o)}} - i\cos\frac{\phi}{2} \, \mathbf{E_1^{(e)}}\right) \end{pmatrix}. \qquad (3.32)$$

Equation (3.32) contains two special cases which are important for applications, corresponding to $\phi = 0$ and $\phi = \frac{\pi}{2}$ (see Fig. 3.7). For $\phi = 0$, (3.32) simplifies to

$$\begin{pmatrix} \mathbf{E_A} \\ \mathbf{E_B} \end{pmatrix} = \frac{1}{2} \begin{pmatrix} \mathbf{E_1^{(o)}} \\ i\mathbf{E_1^{(e)}} \end{pmatrix}. \qquad (3.33)$$
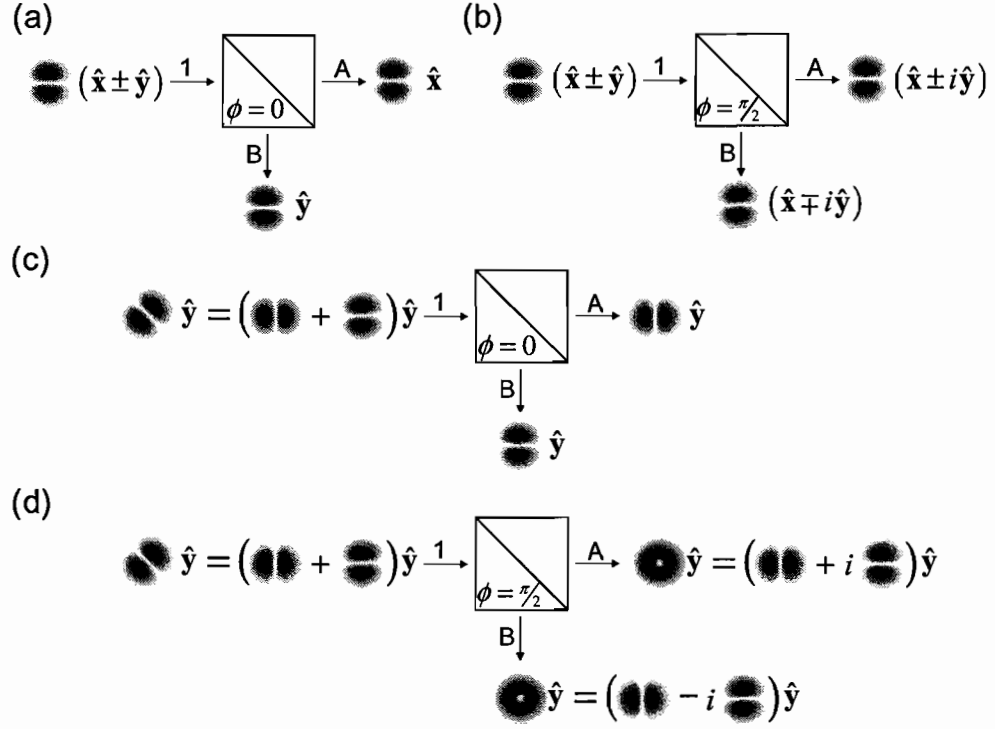
Figure 3.7. Applications of the interferometer based on 1-D parity, denoted by the slashed box. (a) For a well-defined incident HG mode, the interferometer acts as an achromatic polarizing beam splitter when $\phi = 0$ or $\phi = \pi$. (b) For a well-defined incident HG mode with $\phi = \dfrac{\pi}{2}$ or $\phi = \dfrac{3\pi}{2}$, the interferometer converts linear polarization to both right and left circular, thereby acting similarly to a achromatic quarter wave plate aligned with the coordinate axes. (c) An $HG_{+45°}$ mode, linearly polarized in either the $\hat{\mathbf{x}}$ or $\hat{\mathbf{y}}$ directions, is sorted according to 1-D parity when $\phi = 0$ or $\phi = \pi$. For this case the interferometer therefore acts as a "polarizing beam splitter" for even and odd first-order HG modes. (d) For $\phi = \dfrac{\pi}{2}$ or $\phi = \dfrac{3\pi}{2}$, an $HG_{10}^{+45°}$ mode, linearly polarized in either the $\hat{\mathbf{x}}$ or $\hat{\mathbf{y}}$ directions, is transformed into both $\left|LG_0^{+1}\right\rangle$ and $\left|LG_0^{-1}\right\rangle$ modes, thereby acting as an HG-to-LG mode converter. See text for further discussion.

from (3.33) we see explicitly that an input beam $\mathbf{E_1}$ is split by the interferometer into its respective odd and even components such that $\mathbf{E_1^{(o)}}$ exits port A and $\mathbf{E_1^{(e)}}$ exits port B. Therefore, for an input state of the form $|HG_{nm}\rangle\,(\hat{\mathbf{x}}+\hat{\mathbf{y}})$ (an HG mode linearly polarized at $45°$), the interferometer acts as an achromatic polarizing beam splitter, since the even and odd $\hat{\mathbf{y}}$ and $\hat{\mathbf{x}}$ polarizations are sorted into distinct output ports (see Fig. 3.7(a)). Furthermore, for an input state of the form $\left(|HG_{n_o m_1}\rangle + e^{i\Phi}\,|HG_{n_e m_2}\rangle\right)\hat{\mathbf{u}}_\pm$, where n_o is odd and n_e is even, the interferometer sorts the even and odd spatial modes $|HG_{n_e m}\rangle$ and $|HG_{n_o m}\rangle$ into distinct output ports (see Fig. 3.7(c)). Equation (3.33) therefore describes the 1-D parity sorter shown in Fig. 3.4(a), where this even-odd mode sorting is shown for a $\left|LG_0^{+1}\right\rangle$ mode, where $n_o = 1$, $n_e = 0$, $m_1 = 0$, $m_2 = 1$, and $\Phi = \dfrac{\pi}{2}$ (see Fig. 3.2).

For the second special case mentioned above, corresponding to $\phi = \dfrac{\pi}{2}$, (3.32) becomes

$$\begin{pmatrix} \mathbf{E_A} \\ \mathbf{E_B} \end{pmatrix} = \frac{1}{2}\begin{pmatrix} \mathbf{E_1^{(o)}} + i\mathbf{E_1^{(e)}} \\ -\left(\mathbf{E_1^{(o)}} - i\mathbf{E_1^{(e)}}\right) \end{pmatrix}. \tag{3.34}$$

Here, for the input state $|HG_{nm}\rangle\,(\hat{\mathbf{x}}+\hat{\mathbf{y}})$, the interferometer acts as an achromatic quarter wave plate with its fast and slow axes aligned with the coordinate axes, since the output polarization becomes circularly polarized (see Fig. 3.7(b)). However, the interferometer differs from a quarter wave plate in that both right and left circularly polarized beams are generated, at the cost of the total input power being split between the two output beams. For the first-order input state $|HG_{+45°}\rangle\,\hat{\mathbf{u}}_\pm = (|HG_{10}\rangle + |HG_{01}\rangle)\,\hat{\mathbf{u}}_\pm$, the interferometer outputs $\left|LG_0^{-1}\right\rangle$ and $\left|LG_0^{+1}\right\rangle$ modes to ports A and B, respectively. In this case, the interferometer acts as an achromatic mode converter which converts $|HG_{+45°}\rangle$ modes to $\left|LG_0^{\pm 1}\right\rangle$ modes,

producing LG modes of each handedness at the cost of splitting the output power (see Fig. 3.7(d)). We note here that in this case the interferometer is similar in function to the astigmatic mode converter described in [22]. Finally, we also note that as the phase shift ϕ is cycled around through π and $\dfrac{3\pi}{2}$, the interferometer again assumes the aforementioned characteristics of a parity sorter and then a mode converter, respectively, but with the output modes swapping ports. In Chapter IV we verify experimentally that this Mach-Zehnder interferometer may be used as both a parity sorter and a mode converter.

2-D Sorter Theory

Consider now the interferometer in Fig. 3.4(b). In the top arm, the beam undergoes a $\hat{\Pi}_x$ mirror reflection and then a $\hat{\Pi}_x$ Dove prism reflection as discussed in Fig. 3.6. In the bottom arm, the beam undergoes a $\hat{\Pi}_y$ Dove prism reflection followed by a $\hat{\Pi}_x$ mirror reflection. The analogous 2-D operator to the 1-D case in (3.27) is therefore

$$\hat{\Pi} \equiv \begin{pmatrix} \hat{\Pi}_x^2 & 0 \\ 0 & \hat{\Pi}_x\hat{\Pi}_y \end{pmatrix} = \begin{pmatrix} 1 & 0 \\ 0 & \hat{\Pi}_y\hat{\Pi}_x \end{pmatrix} = \begin{pmatrix} 1 & 0 \\ 0 & \hat{\Pi}_{xy} \end{pmatrix}, \tag{3.35}$$

where $\hat{\Pi}_x^2 = 1$ and (3.16) has been used. Armed with (3.35), we may now describe the action of the 2-D parity sorter on two arbitrary input vector fields analogously to (3.29), as

$$\mathbf{E}_{\text{out}} = \hat{U}_\mathbf{B}\,\hat{\Phi}\,\hat{\Pi}\,\hat{U}_\mathbf{B}\,\mathbf{E}_{\text{in}} = \frac{1}{2}\begin{pmatrix} e^{i\frac{\phi}{2}} - e^{-i\frac{\phi}{2}}\hat{\Pi}_{xy} & i\left(e^{i\left(\frac{\phi}{2}\right)} + e^{-i\frac{\phi}{2}}\hat{\Pi}_{xy}\right) \\ i\left(e^{i\frac{\phi}{2}} + e^{-i\frac{\phi}{2}}\hat{\Pi}_{xy}\right) & -\left(e^{i\frac{\phi}{2}} - e^{-i\frac{\phi}{2}}\hat{\Pi}_{xy}\right) \end{pmatrix}\begin{pmatrix} E_1\hat{\mathbf{u}}_\pm \\ E_2\hat{\mathbf{u}}_{(\pm)} \end{pmatrix}. \tag{3.36}$$

If we assume that the input fields $E_1 \hat{\mathbf{u}}_\pm$ and $E_2 \hat{\mathbf{u}}_{(\pm)}$ are both HG modes of the respective orders $HG_{n_1 m_1}$ and $HG_{n_2 m_2}$, then we may use (3.19) to replace $\hat{\Pi}_{xy} E_1 \hat{\mathbf{u}}_\pm \rightarrow -(-1)^{n_1 + m_1} E_1 \hat{\mathbf{u}}_\pm$ and $\hat{\Pi}_{xy} E_2 \hat{\mathbf{u}}_{(\pm)} \rightarrow -(-1)^{n_2 + m_2} E_2 \hat{\mathbf{u}}_{(\pm)}$ in (3.29):

$$\mathbf{E}_{\text{out}} = \begin{pmatrix} \mathbf{E_A} \\ \mathbf{E_B} \end{pmatrix} = \frac{1}{2} \begin{pmatrix} e^{i\frac{\phi}{2}} + (-1)^{n_1+m_1} e^{-i\frac{\phi}{2}} & i\left(e^{i\frac{\phi}{2}} - (-1)^{n_2+m_2} e^{-i\frac{\phi}{2}}\right) \\ i\left(e^{i\frac{\phi}{2}} - (-1)^{n_1+m_1} e^{-i\frac{\phi}{2}}\right) & -\left(e^{i\frac{\phi}{2}} + (-1)^{n_2+m_2} e^{-i\frac{\phi}{2}}\right) \end{pmatrix} \begin{pmatrix} \mathbf{E_1} \\ \mathbf{E_2} \end{pmatrix}. \tag{3.37}$$

Since we are again interested in the case where the interferometer sorts a single input beam, we set the port 2 input beam $\mathbf{E_2}$ equal to zero, so that (3.37) simplifies to

$$\begin{pmatrix} \mathbf{E_A} \\ \mathbf{E_B} \end{pmatrix} = \begin{pmatrix} i \sin\frac{\phi}{2} \mathbf{E_1} \\ i \cos\frac{\phi}{2} \mathbf{E_1} \end{pmatrix} \quad \text{for } \mathbf{E_1} \text{ odd: } (-1)^{n_1+m_1} = -1, \tag{3.38a}$$

$$\begin{pmatrix} \mathbf{E_A} \\ \mathbf{E_B} \end{pmatrix} = \begin{pmatrix} \cos\frac{\phi}{2} \mathbf{E_1} \\ -\sin\frac{\phi}{2} \mathbf{E_1} \end{pmatrix} \quad \text{for } \mathbf{E_1} \text{ even: } (-1)^{n_1+m_1} = +1. \tag{3.38b}$$

Splitting $\mathbf{E_1}$ into even and odd components $\mathbf{E_1} = \mathbf{E_1^{(O)}} + \mathbf{E_1^{(E)}}$ (with respect to 2-D parity), and adding the above equations together as in (3.32) then yields

$$\begin{pmatrix} \mathbf{E_A} \\ \mathbf{E_B} \end{pmatrix} = \frac{1}{2} \begin{pmatrix} \cos\frac{\phi}{2} \mathbf{E_1^{(E)}} + \mathbf{i}\sin\frac{\phi}{2} \mathbf{E_1^{(O)}} \\ -\left(\sin\frac{\phi}{2} \mathbf{E_1^{(E)}} - \mathbf{i}\cos\frac{\phi}{2} \mathbf{E_1^{(O)}}\right) \end{pmatrix}. \tag{3.39}$$
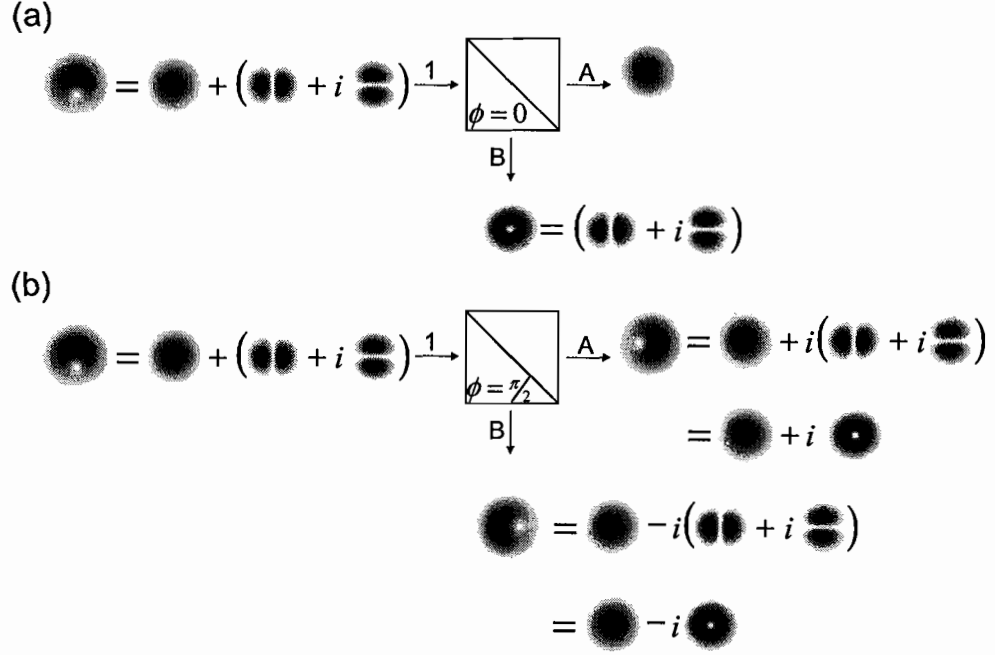
Figure 3.8. Applications of the Interferometer Based on 2-D Parity, denoted by the slashed box. (a) The interferometer acts as a 2-D parity sorter when $\phi = 0$ or $\phi = \pi$, so that even modes (with respect to 2-D parity) exit port A, while odd modes exit port B. (b) When $\phi = \dfrac{\pi}{2}$ or $\phi = \dfrac{3\pi}{2}$, the interferometer imparts both $+\dfrac{\pi}{2}$ and $-\dfrac{\pi}{2}$ phase shifts between the even $(n + m = 0)$ and odd $(n + m = 1)$ modes, at the cost of the total input power being split between the two output beams. The polarization states of the modes are not shown, since they transform trivially under the 2-D parity operation.

For the special cases $\phi = 0$ and $\phi = \dfrac{\pi}{2}$, (3.39) simplifies to the respective equations

$$\begin{pmatrix} \mathbf{E_A} \\ \mathbf{E_B} \end{pmatrix} = \frac{1}{2} \begin{pmatrix} \mathbf{E}_1^{(E)} \\ i\mathbf{E}_1^{(O)} \end{pmatrix}, \tag{3.40a}$$

$$\begin{pmatrix} \mathbf{E_A} \\ \mathbf{E_B} \end{pmatrix} = \frac{1}{2} \begin{pmatrix} \mathbf{E}_1^{(E)} + i\mathbf{E}_1^{(O)} \\ -\left(\mathbf{E}_1^{(E)} - i\mathbf{E}_1^{(O)} \right) \end{pmatrix}. \tag{3.40b}$$

For $\phi = 0$ then, we see from (3.40a) that the interferometer in (3.4)(b) acts as a 2-D parity sorter, so that each HG_{nm} mode contributing to the total input field $\mathbf{E_1}$–which obeys the constraint $n + m$ even–exits out port A, while each contributing mode satisfying $n + m$ odd exits out port B (see Fig. 3.8(a)). Furthermore, for $\phi = \dfrac{\pi}{2}$ and with an input state of the form $c_{00} |HG_{00}\rangle + c_{10} |HG_{10}\rangle + c_{01} |HG_{01}\rangle$ (where c_{00}, c_{10}, c_{01} complex amplitudes), the interferometer acts to impart a $\pm\dfrac{\pi}{2}$ phase shift between the even $(n + m = 0)$ and odd $(n + m = 1)$ modes (see Fig. 3.8(b)), analogously to (3.34). As in the case of the 1-D parity interferometer, for $\phi = \pi$ and $\phi = \dfrac{3\pi}{2}$ the 2-D interferometer respectively acts according to (3.40a) and (3.40b), but with the output modes swapping ports. The present case is simplified however by the fact that the field polarization vectors transform trivially under the action of Π_{xy} as shown in (3.17).

We will henceforth consider only the case where $\phi = 0$—the 2-D parity sorter. However, we note that the $\phi = \dfrac{\pi}{2}$ setting for this interferometer may be useful for manipulating quantum states of light in schemes utilizing entangled qutrits, c.f. [6]. For purposes of comparison, a tabulation of the action of both the 1-D and 2-D parity sorters on HG_{nm} input modes of order $n + m \leq 3$ is included as Fig. 3.9.

Phase Stable 2-D Parity Sorting Sagnac Interferometer

The two experimentally implemented sorter designs [23] and [46] shown in Fig. 3.4 share several similarities. Among these are their Mach-Zehnder character with two independent arms, and their reliance on complete constructive and destructive interference at the output

Order				Order			
$n=0$	$n=1$	$n=2$	$n=3$	$n+m=0$	$n+m=1$	$n+m=2$	$n+m=3$
HG_{00}	HG_{10}	HG_{20}	HG_{30}	HG_{00}	HG_{10}	HG_{20}	HG_{30}
HG_{01}	HG_{11}	HG_{21}			HG_{01}	HG_{02}	HG_{03}
HG_{02}	HG_{12}					HG_{11}	HG_{21}
HG_{03}							HG_{12}
A	B	A	B	A	B	A	B
Output Port				Output Port			

Figure 3.9. (a) A tabulation of the action of the the 1-D sorter upon the HG modes of order $n+m \leq 3$. The plus signs designate modal lobes which are in phase with each other and 180° out of phase with the unmarked lobes. Modes with an even value for n exit port A, while modes with odd n-value exit port B (see Fig. 3.4(a)). (b) A tabulation of the action of the the 2-D sorter upon the HG modes of order $n+m \leq 3$. The plus signs designate the relative phases of the lobes as in Fig. 3.9(a). Modes with an even value for $n+m$ exit port A, while modes with odd $n+m$-value exit port B (see Fig. 3.4(b)).

beam splitter in order to sort certain transverse spatial modes into one of two distinct output ports. Also, they both have the advantage of not relying on computer-generated holograms, which are lossy in practice, so that their sorting efficiency is limited only by the transmission and reflection coefficients of the constituent beam splitters mirrors, glass plates, and Dove prisms.

However, a major disadvantage of both the 1-D and 2-D parity sorters mentioned above is their Mach-Zehnder character, or more specifically the existence of two independent beam paths in each interferometer. This makes them subject to phase noise and drift so that in practice it is difficult to keep them aligned. Here we overcome this difficulty for the latter design by demonstrating a novel type of 2-D parity sorter in the form of an out-of-plane

Sagnac interferometer. Since the two interfering paths of the Sagnac are counter-propagating, the interferometer is automatically phase-stable. As a result, experiments involving multiple cascading interferometers are considerably more feasible when employing a Sagnac then with a Mach-Zehnder interferometer. As we will show, such cascading allows for full sorting of arbitrary superpositions of modes, including the OAM sorting schemes described in [45] and [46].

The most straightforward modification of the 2-D parity sorting Mach-Zehnder interferometer of Fig. 3.4(b) to a Sagnac interferometer is to replace the output beam splitter with a mirror, remove one of the Dove prisms, and rotate the remaining Dove prism 45° about the beam propagation axis (see Fig. 3.10(a)). With this modified setup, the split input beams propagate around the interferometer in both directions, so that the clockwise and counter-clockwise propagating beams are each rotated 90° in opposite directions by the Dove prism (see Figs. 3.10(b) and 3.10(c)). This type of Sagnac interferometer has actually been previously constructed for the purpose of direct interferometric measurement of the transverse spatial Wigner function of light in one dimension [52]. In that case, it was recognized that as the input beam was slightly laterally translated and tilted with respect to the input axis, the corresponding fluctuations in the output intensity mapped out a function of the translation distance and tilt angle proportional to the transverse Wigner function in two-dimensional phase space associated with the plane of the beam translation and tilt. This measurement scheme is based on the fact that the Wigner function may be expressed as the expectation value of the "displaced" phase space parity operator $\Pi_D(\mathbf{r}, \mathbf{p})$, which performs
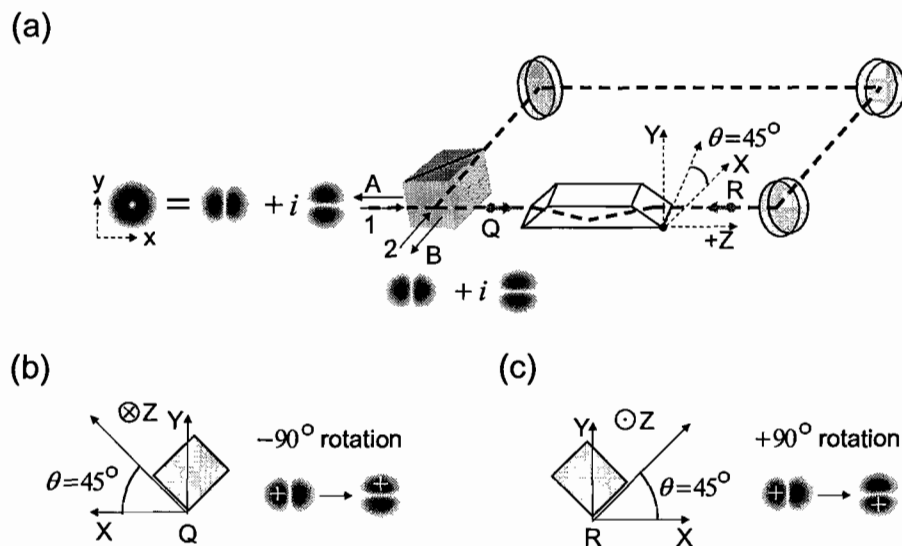
Figure 3.10. (a) The most straightforward modification of the 2-D parity sorting Mach-Zehnder interferometer of Fig. 3.4(b) to a Sagnac interferometer: an in-plane Sagnac interferometer with a single Dove prism in one arm, rotated at 45° with respect to the X axis as shown. As in the Mach-Zehnder interferometer of Fig. 3.4(b), if a superposition of HG_{10} and HG_{01} modes enters port 1, both modes exit the same port (B), so that an incident LG_0^1 mode is not decomposed. (b) A beam propagating from the vantage point of Q in (a) in the direction shown by the gray arrow (counter-clockwise around the interferometer as viewed from above) encounters the Dove prism oriented as shown, with the Z axis pointing into the page. The beam therefore undergoes a $-90°$ (clockwise) rotation, as is shown for an HG_{10} mode. (c) A beam propagating from the vantage point of R in (a) in the direction shown by the gray arrow (clockwise) encounters the Dove prism as oriented 90° with respect the clockwise propagating beam in (b), with the Z axis pointing out of the page as shown. The beam therefore undergoes a $+90°$ (counter-clockwise) rotation, shown for an HG_{10} mode.
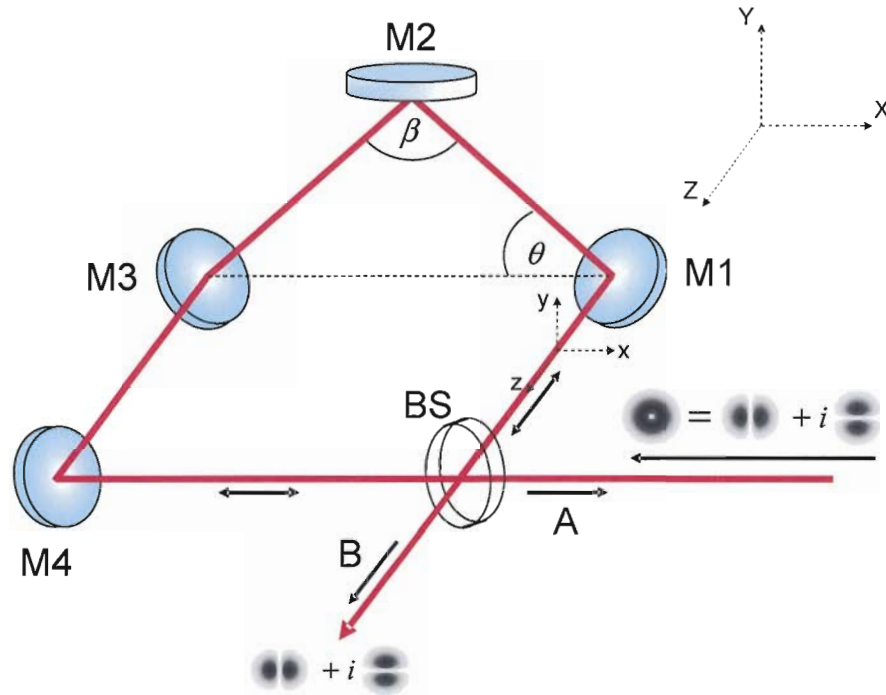
Figure 3.11. The out-of-plane 2-D parity sorting Sagnac interferometer. Mirrors M1-M3 cause the beam path to travel out of the x-z plane, tracing out two congruent sides of an isosceles triangle in the x-y plane, with congruent base angles θ and apex angle $\beta = \pi - 2\theta$. For $\beta = 90°$ (so that $\theta = 45°$), incident HG_{10} and HG_{01} modes exit the same port of this interferometer, as do LG_0^1 modes, which is also the case for the sorters in Figs. 3.10 and 3.4(b). See text for further discussion.

reflections about the phase space point $(\mathbf{r}, \mathbf{p})$ [53]. At the phase space origin $(\mathbf{r} = \mathbf{0}, \mathbf{p} = \mathbf{0})$ the operator $\Pi_D(\mathbf{r}, \mathbf{p})$ acts on transverse modes as the 2-D parity operator Π_{xy}, which provides the interpretation that a 2-D parity measurement of a transverse mode is equivalent to evaluating the transverse Wigner function of that mode at the phase space origin.

Despite its increased interferometric stability, the Sagnac interferometer with a Dove prism of Fig. 3.10 has two disadvantages: the counterpropagating beams suffer from astig-

matism of the optical wave fronts due to the internal Dove prism, and the numerical aperture of the device ($NA \approx 0.01$) is limited by the prism's relatively small cross section. Both of these disadvantages may be overcome by replacing the Dove prism and two of the mirrors inside the interferometer with three mirrors oriented in such a way that the counterpropagating beams are temporarily reflected out of the plane defined by input and output beam paths, as shown in Fig. 3.11. This type of out-of-plane Sagnac interferometer has been successfully employed to measure the transverse spatial Wigner function at the single photon level [54]. In the improved design, the image-rotation action of the Dove prism is thereby replaced by an equivalent image rotation due to the out-of-plane mirror reflections.

The Geometric Phase and Optical Image Rotation

As we will show, the reason that a rotated Dove prism acts equivalently to three mirrors with a certain out-of-plane orientation is due to a geometric (Berry) phase induced by the redirection of the wave vector (i.e., the momentum vector) of the propagating beam by the reflecting and refracting optical elements. To see this, consider first a single mirror reflection, shown in Fig. 3.12(a) for a y-polarized HG_{10} mode incident upon a mirror at angle α in the X–Y plane. As indicated in the figure, we employ capitol letters (X, Y, Z) to denote the "global" coordinate axes of the laboratory frame, while lower-case letters (x, y, z) denote "local" axes attached to the particle frame, such that the positive z axis points in the direction of particle propagation $\hat{\mathbf{k}}_c = \hat{\mathbf{z}}$.
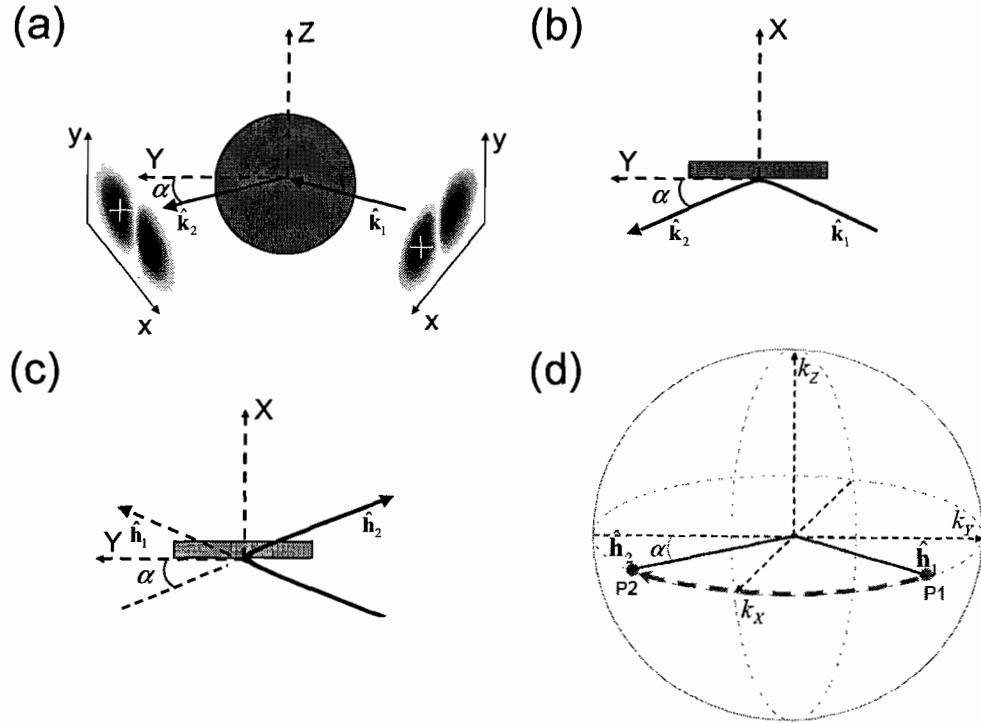
Figure 3.12. (a) A y-polarized paraxial beam in an HG_{10} transverse mode incident upon a perfectly conducting mirror at angle α in the X–Y plane of the laboratory frame (X, Y, Z). The beam is traveling in the positive z direction with respect to a local coordinate system (x, y, z) attached to the particle frame, such that the input and output wave vectors $\hat{\mathbf{k}}_1$ and $\hat{\mathbf{k}}_2$, shown as solid arrows, both point along $+z$. (b) Analogous sharply curved but continuous trajectory, defined by the solid line, with initial and final wave vectors $\hat{\mathbf{k}}_1$ and $\hat{\mathbf{k}}_2$. The viewpoint has changed to a "top view" with respect to (a), looking down at the X–Y plane. (c) "Equivalent" sharply curved trajectory, defined by the solid line, with modified initial and final wave vectors $\hat{\mathbf{h}}_1 \equiv \hat{\mathbf{k}}_1$ and $\hat{\mathbf{h}}_2 \equiv -\hat{\mathbf{k}}_2$. (d) "Equivalent" momentum-space Poincaré sphere construction corresponding to the trajectory in (c). The initial modified wave vector $\hat{\mathbf{h}}_1$ evolves rapidly to final wave vector $\hat{\mathbf{h}}_2$, thereby sweeping out a geodesic on the Poincaré sphere connecting points $P1$ and $P2$. See text for further discussion.

Recall now that any incident light beam in a wave packet with central (carrier) wave vector $\mathbf{k}_c = k_c \hat{\mathbf{z}}$ may be expressed as a linear combination of modes of the form

$$\mathbf{E}(\rho, \phi, z, t) = \mathcal{E}_T(\rho, \phi, z) \times \mathcal{E}_L(z, t)\,\hat{\mathbf{e}}, \tag{3.41}$$

where

$$\mathcal{E}_T(\rho, \phi, z) = \frac{A_p^{|\ell|}}{w(z)} \left(\frac{\rho}{w(z)}\right)^{|\ell|} L_p^{|\ell|}\left(\frac{2\rho^2}{w^2(z)}\right) e^{-\frac{\rho^2}{w^2(z)}} e^{-i\left[\ell\phi - (2p+\ell+1)\tan^{-1}\left(\frac{z}{z_0}\right) + \frac{k_c\rho^2}{2R(z)}\right]} \tag{3.42}$$

is the transverse field distribution,

$$\mathcal{E}_L(z, t) = \int \mathcal{E}(\beta)\, e^{i[(\beta - k_c)z - (\omega - \omega_c)t]} d\beta \times e^{i(k_c z - \omega_c t)} \tag{3.43}$$

is the longitudinal function, and $\hat{\mathbf{e}}$ is the unit polarization vector (cf. (3.2), (3.3), and (3.8)). We are interested in the properties of the modes (3.41) under the 1-D parity (mirror reflection) operation $\hat{\Pi}_x$ corresponding to the perfect reflection (i.e., a reflection from a perfectly conducting mirror) shown in Fig. 3.12(a). If we employ the circular basis $\hat{\mathbf{e}} \rightarrow \hat{\mathbf{e}}_\sigma = \frac{1}{\sqrt{2}}(\hat{\mathbf{x}} + i\sigma\hat{\mathbf{y}})$, the 1-D parity transformation rules (3.13) and (3.14) imply that

$$\hat{\Pi}_x \hat{\mathbf{e}}_\sigma = -\hat{\mathbf{e}}_{-\sigma}, \tag{3.44a}$$

$$\hat{\Pi}_x \mathcal{E}_T(\rho, \phi, z) = \mathcal{E}_T(\rho, -\phi, z), \tag{3.44b}$$

so that the form of the input beam $\mathbf{E}(\rho, \phi, z, t)$ is unchanged except for the replacements $\phi \rightarrow -\phi$ and $\hat{\mathbf{e}}_\sigma \rightarrow -\hat{\mathbf{e}}_{-\sigma}$: $\mathcal{E}_T(\rho, \phi, z) \times \mathcal{E}_L(z, t)\,\hat{\mathbf{e}}_\sigma \rightarrow -\mathcal{E}_T(\rho, -\phi, z) \times \mathcal{E}_L(z, t)\,\hat{\mathbf{e}}_{-\sigma}$. In other

words, the mirror reflection alters only the spin angular momentum and OAM of the beam $\mathbf{E}(\rho, \phi, z, t)$, up to a overall sign in the amplitude.

Consider now applying a (local) rotation operator $\hat{R}_y(\pi)$, representing a rotation through an angle π about the y axis, to the reflected state $-\mathcal{E}_T(\rho, -\phi, z) \times \mathcal{E}_L(z, t)\,\hat{\mathbf{e}}_{-\sigma}$. Under such a rotation, which is equivalent to changing points of view from watching a particle propagating toward the observer and watching the particle propagating away from the observer, we have $x \to -x$, $y \to y$, $z \to -z$ and $\hat{\mathbf{x}} \to -\hat{\mathbf{x}}$, $\hat{\mathbf{y}} \to \hat{\mathbf{y}}$, $\hat{\mathbf{z}} \to -\hat{\mathbf{z}}$. This is equivalent to $\phi \to -\phi$, $\hat{\mathbf{e}}_\sigma \to -\hat{\mathbf{e}}_{-\sigma}$, and $z \to -z$, so that the reflected field $\hat{\Pi}_x \mathbf{E}(\rho, \phi, z, t) = -\mathcal{E}_T(\rho, -\phi, z) \times \mathcal{E}_L(z, t)\,\hat{\mathbf{e}}_{-\sigma}$ is transformed as follows: $-\mathcal{E}_T(\rho, -\phi, z) \times \mathcal{E}_L(z, t)\,\hat{\mathbf{e}}_{-\sigma} \to +\mathcal{E}_T(\rho, \phi, -z) \times \mathcal{E}_L(-z, t)\,\hat{\mathbf{e}}_\sigma$. Therefore, we see that the rotation $\hat{R}_y(\pi)$ cancels the effect of the reflection $\hat{\Pi}_x$ on the field $\mathbf{E}(\rho, \phi, z, t)$, at the cost of a longitudinal transformation $z \to -z$. If we further assume that the beam is collimated (weakly focused) such that $z \ll z_0$ and $\rho \ll z_0$, then the original field

$$
\begin{aligned}
\mathbf{E}(\rho, \phi, z, t) = & \frac{A_p^{|\ell|}}{w(z)} \left(\frac{\rho}{w(z)}\right)^{|\ell|} L_p^{|\ell|}\left(\frac{2\rho^2}{w^2(z)}\right) e^{-\frac{\rho^2}{w^2(z)}} e^{-i\left[\ell\phi - (2p+\ell+1)\tan^{-1}\left(\frac{z}{z_0}\right)\right]} \\
& \times \int \mathcal{E}(\beta)\, e^{i[(\beta - k_c)z - (\omega - \omega_c)t]} d\beta \times e^{i\left(k_c z + \frac{k_c \rho^2}{2R(z)} - \omega_c t\right)} \hat{\mathbf{e}}_\sigma,
\end{aligned} \tag{3.45}
$$

after being reflected and rotated, may be expressed as

$$
\begin{aligned}
\hat{R}_y(\pi)\, \hat{\Pi}_x \mathbf{E}(\rho, \phi, z, t) \approx & \frac{A_p^{|\ell|}}{w_0} \left(\frac{\rho}{w_0}\right)^{|\ell|} L_p^{|\ell|}\left(\frac{2\rho^2}{w_0^2}\right) e^{-\frac{\rho^2}{w_0^2}} e^{-i\left[\ell\phi + (2p+\ell+1)\frac{z}{z_0}\right]} \\
& \times \int \mathcal{E}(\beta)\, e^{-i[(\beta - k_c)z + (\omega - \omega_c)t]} d\beta \times e^{-i\left(k_c z\left(1 + \frac{1}{2}\frac{\rho^2}{z_0^2}\right) + \omega_c t\right)} \hat{\mathbf{e}}_\sigma
\end{aligned} \tag{3.46}
$$

where $w(z) \approx w_0$, $\tan^{-1}\left(\dfrac{z}{z_0}\right) \approx \dfrac{z}{z_0}$, $\dfrac{1}{R(z)} = \dfrac{z}{z_0^2}$, and $z \to -z$ has been used. Thus, the field is unchanged under this transformation, except for a change of sign in the so-called Gouy phase term $e^{i(2p+\ell+1)\tan^{-1}\left(\frac{z}{z_0}\right)}$, and a reversal in propagation direction of the beam as is evident in the second line of (3.46), which is equivalent to $\beta \to -\beta$ and $k_c \to -k_c$. Furthermore, since $\rho \ll z_0$ implies that $\dfrac{1}{2}\dfrac{\rho^2}{z_0^2} \ll 1$, we may neglect the phase front curvature term in (3.46) to a good approximation. It follows from this that the transverse (that is, (ρ, ϕ)-dependent) part of the field $\mathbf{E}(\rho, \phi, z, t)$ is completely invariant under the transformation $\hat{R}_y(\pi)\,\hat{\Pi}_x$ up to a Gouy phase term $e^{i(2p+\ell+1)\tan^{-1}\left(\frac{z}{z_0}\right)}$, while the longitudinal part undergoes to effective transformation $\beta \to -\beta$ and $k_c \to -k_c$.

Now, it is clear that one may model the perfect mirror reflection of Fig 3.12(a) as the limiting case of a continuous trajectory with a sharp curve between input and output wave vectors $\hat{\mathbf{k}}_1$ and $\hat{\mathbf{k}}_2$ at the point of reflection, as shown in Fig 3.12(b), provided that the parity inversion operator $\hat{\Pi}_x$ is applied to the beam at the reflection point. However, in light of the above result, we have an equivalent but alternative way of describing a perfect reflection: instead of applying the parity flip $\hat{\Pi}_x$ to the beam, one may think of the "equivalent" trajectory where the output beam is transformed by the local rotation $\hat{R}_y(\pi)$, with modified input and output wave vectors $\hat{\mathbf{h}}_1 \equiv \hat{\mathbf{k}}_1$ and $\hat{\mathbf{h}}_2 \equiv -\hat{\mathbf{k}}_2$, as shown in Fig. 3.12(c). The advantage of this equivalent treatment is for a continuous path in momentum space (i.e., with no reflections $\hat{\Pi}_x$), the geometric phase formalism of Chapter II may be applied. With this in mind, we therefore construct the "equivalent" momentum-space Poincaré sphere for input and output wave vectors $\hat{\mathbf{k}}_1$ and $\hat{\mathbf{k}}_2$ using the modified wave vectors $\hat{\mathbf{h}}_1$ and $\hat{\mathbf{h}}_2$ (see Fig.

3.12(d)). Since the quickly changing direction of the wave vector $\hat{\mathbf{k}}$ at the reflection point sweeps out an angle in the X–Y plane (in the global laboratory frame), the same statement holds for the modified wave vectors $\hat{\mathbf{h}}$. Therefore, the modified momentum-space path of the vector $\hat{\mathbf{h}}$ sweeps out a geodesic (great circle) on the Poincaré sphere as is changes from $\hat{\mathbf{h}}_1$ to $\hat{\mathbf{h}}_2$, as shown in Fig. 3.12(d). It is clear from the figure that in the limiting case where the the curved path becomes infinitely sharp that $\hat{\mathbf{h}}_1$ and $\hat{\mathbf{h}}_2$ should still be connected by the unique geodesic shared by the cooresponding points $P1$ and $P2$ on the surface of the sphere.

From symmetry considerations, we conclude that the above construction is valid for mirror reflections in any plane, so that upon a second reflection involving input beam $\hat{\mathbf{k}}_2$ and output beam $\hat{\mathbf{k}}_3$, the modified output wave vector is again equal to the physical output wave vector so that $\hat{\mathbf{h}}_3 = +\hat{\mathbf{k}}_3$. Due to this cyclic behavior of the modified wave vectors, for the general case of several reflections we may therefore define the modified wave vector $\hat{\mathbf{h}}_i$ incident upon the ith mirror of the system by the simple relation

$$\hat{\mathbf{h}}_i \equiv (-1)^{i-1}\,\hat{\mathbf{k}}_i, \tag{3.47}$$

where $i - 1$ is the number of mirror reflections experienced by the beam. We note here that this modified unit wave vector has been extensively used by Galvez and Koch [55] and by Galvez and Holmes [56] in order to study the relationship between out-of-plane mirror reflections and the geometric phase, the existence of which was first pointed out by Kitano, Yabuzaki, and Ogawa [57] and formalized by Segev, Solomon, and Yariv [58].
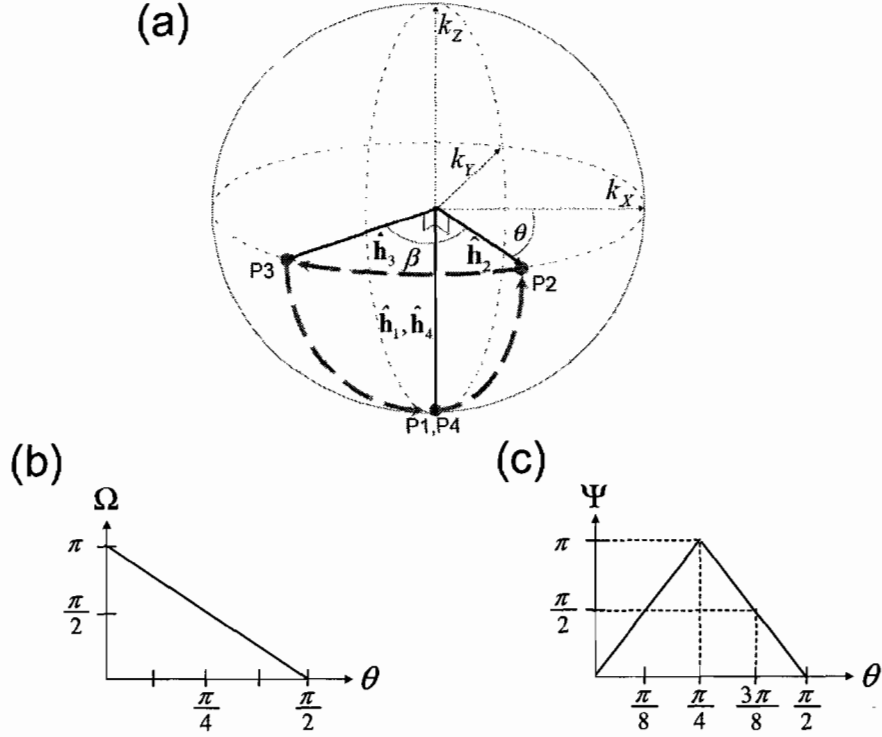
Figure 3.13. (a) The Poincaré sphere construction corresponding to the anti-clockwise propagating beam path in Fig. 3.11 as discussed in the text. The beam path angles θ and β from Fig. 3.11 define the modified wave vectors $\hat{\mathbf{h}}_1 - \hat{\mathbf{h}}_4$, which in turn define the points P1-P4 on the spherical surface as shown. The gray dashed lines denote the triangular closed loop that results from successively connecting these points with geodesic curves. Note that the axes (k_X, k_Y, k_Z) are oriented differently from the axes (X, Y, Z) of the corresponding Fig. 3.11 for ease of display. (b) Plot of the accumulated geometric phase (beam rotation angle) Ω vs. the parameter θ. (c) Plot of the relative geometric phase (rotation angle) Ψ (modulo π) of the two counter-propagating beams after propagating around the Sagnac interferometer vs. θ, emphasizing the two special cases where $\Psi = \pi$ and $\Psi = \dfrac{\pi}{2}$. These two cases correspond to the first and second cascaded interferometer stages for the OAM sorting scheme in [45]. See text for further discussion.

We now apply the aforementioned construction to the 2-D parity sorting Saganc interferometers of Figs. 3.10 and 3.11, beginning with our interferometer design of Fig. 3.11. As discussed earlier, the mirrors labeled M1-M3 in the figure are oriented such that the reflected beam path travels out of the X-Z plane, and traces out the two congruent sides of an isosceles triangle which lies completely in the X-Y plane. The action of the 50:50 beam splitter (BS in the figure) gives rise to two counter-propagating paths of equal path length, which is the reason for the phase-stability of the interferometer. We refer to the path involving reflections off of the mirrors M1-M4 in the successive order M4-M3-M2-M1 as the clockwise path, and that involving reflections of order M1-M2-M3-M4 as the anti-clockwise path.

The modified momentum-space Poincaré sphere construction corresponding to the successive reflections of the anti-clockwise path in Fig. 3.11 is given as Fig. 3.13(a). Using (3.47), we find that the beams incident upon mirrors $M1$-$M4$ in 3.11 correspond to the modified wave vectors $\hat{\mathbf{h}}_1$-$\hat{\mathbf{h}}_4$ shown in Fig. 3.13(a). These vectors in turn define four points P1-P4 on the unit sphere; however, due to the odd total number of out-of-plane reflections coupled with the fact that $\hat{\mathbf{k}}_4 = -\hat{\mathbf{k}}_1$, we have $\hat{\mathbf{h}}_1 = \hat{\mathbf{h}}_4$, which implies that $P1 = P4$, so that only three of these points are unique. Therefore, connecting in order the points P1-P4 on the spherical surface with geodesic curves (great circles) results in a triangular closed loop with an anti-clockwise orientation as shown in the figure.

As discussed previously, we may apply the geometric phase formalism developed in Chapter II to the momentum-space path defined by points $P1$-$P4$ in Fig. 3.13(a). Specifically, by

(2.48d), a photonic ($\lambda = 1$) spin-orbit wave packet of the form given in (2.12) propagating anti-clockwise around the out-of-plane Sagnac interferometer experiences a geometric phase accumulation of

$$\Phi_B = -\left(\sigma + m_\ell\right)\Omega, \tag{3.48}$$

where Ω is the solid angle subtended by the closed momentum-space curve delineated by the dashed gray line in Fig. 3.13(a). Since the Poincaré sphere is a unit sphere, Ω also equals the surface area enclosed by the closed triangular geodesic surface, which may be calculated via the following relation due to Euler [55]:

$$\cos\frac{\Omega}{2} = \frac{1 + \cos\alpha + \cos\beta + \cos\gamma}{4\cos\frac{\alpha}{2}\cos\frac{\beta}{2}\cos\frac{\gamma}{2}}, \tag{3.49}$$

In (3.49), $\alpha \equiv \hat{\mathbf{h}}_1 \cdot \hat{\mathbf{h}}_2$, $\beta \equiv \hat{\mathbf{h}}_2 \cdot \hat{\mathbf{h}}_3$, and $\gamma \equiv \hat{\mathbf{h}}_3 \cdot \hat{\mathbf{h}}_4$ are the angles between the respective helicity unit vector pairs. In our present case (cf. Figs. 3.11-3.13), $\alpha = \gamma = \dfrac{\pi}{2}$, and $\beta = \pi - 2\theta$, so that the right hand side of (3.49) simplifies to $\dfrac{1 + \cos\left(\pi - 2\theta\right)}{2\cos\left(\frac{\pi}{2} - \theta\right)}$, which is equivalent to $\sin\theta$. Therefore, we find for our design that Ω depends on θ through the simple relationship

$$\cos\frac{\Omega}{2} = \sin\theta, \tag{3.50a}$$

$$\Leftrightarrow \Omega = 2\cos^{-1}\left(\sin\theta\right), \tag{3.50b}$$

The plot of Ω vs. θ in Fig. 3.13(b), which has been composed from (3.50), shows that Ω can be tuned to any value between 0 and π by choosing the appropriate value of the

parameter θ, which ranges from $0 \leq \theta \leq \dfrac{\pi}{2}$. Now, for the clockwise traveling beam, the direction of the geodesic path of Fig. 3.13(a) is reversed, so that the accumulated geometric phase has the opposite sign with respect to that of the anti-clockwise traveling beam: $\Omega \rightarrow -\Omega$. We therefore find that the relative geometric phase accumulation Ψ between the two counter-propagating beams after one trip around the interferometer may be expressed as $\Psi = \pi - |2\Omega - \pi|$, as given through the plot of Ψ vs. θ in Fig. 3.13(c).

What are the physical consequences of the geometric phase Ω accumulated by a paraxial LG mode $\left|LG_p^{\ell}\right\rangle$? To answer this question, we note that a circularly polarized LG mode is proportional to $e^{im_{\ell}\phi}\hat{\mathbf{e}}_{\sigma}$ when expressed in the circularly polarized basis $\hat{\mathbf{e}}_{\sigma} \equiv \hat{\mathbf{x}} + i\sigma\hat{\mathbf{y}}$. Or equivalently, since equation (A.13c) in Appendix A shows that $\hat{\mathbf{e}}_{\sigma} = e^{\sigma i\phi}\left(\hat{\rho} - \sigma i\hat{\phi}\right)$, we have that

$$\left|LG_p^{\ell}\right\rangle \hat{\mathbf{e}}_{\sigma} \propto e^{i(\sigma+m_{\ell})\phi}\left(\hat{\rho} - \sigma i\hat{\phi}\right), \tag{3.51}$$

which comprises the entirety of the ϕ-dependence of the photonic state. The additional geometrical phase factor $\Phi_B = -\left(\sigma + m_{\ell}\right)\Omega$ then results in the following transformation on the state $\left|\psi\left(\mathbf{k}_c\right)\right\rangle$:

$$\left|LG_p^{\ell}\right\rangle \hat{\mathbf{e}}_{\sigma} \rightarrow \left|LG_p^{\ell}\right\rangle \hat{\mathbf{e}}_{\sigma}e^{-i(\sigma+m_{\ell})\Omega} \propto e^{i(\sigma+m_{\ell})(\phi-\Omega)}\left(\hat{\rho} - \sigma i\hat{\phi}\right). \tag{3.52}$$

From (3.52), we see that the geometric phase accumulation of $-\Omega$ is equivalent to an *azimuthal rotation* of the particle wave function in the plane perpendicular to the direction of propagation by the angle Ω (the fact that an azimuthal rotation of an LG_p^{ℓ} mode through

an angle Ω is equivalent to multiplication by a phase factor $e^{-im_\ell\Omega}$ has been previously pointed out in the context of HG–LG astigmatic mode converters [59]). This rotation affects both the transverse spatial field distribution and the (vectorial) polarization state, as can be explicitly seen in (3.52). Furthermore, since the rotation angle Ω is the same for all LG modes, any linear combination of such modes will also be rotated though angle Ω. As the LG modes form a complete basis for the transverse mode space, it follows that an arbitrary transverse beam image will be likewise rotated by the out-of-plane Saganc interferometer. As should be clear from the above treatment, this conclusion generalizes to an arbitrary series of mirror reflections: an arbitrary beam image and polarization state are rotated through an angle Ω given by the solid angle subtended by the surface defined by connecting the i modified wave vectors $\hat{\mathbf{h}}_i$ with geodesic curves (great circles) on the Poincaré sphere in momentum space.

We now construct the modified momentum-space Poincaré sphere for the case of the Sagnac interferometer with a Dove prism rotated by an angle θ in the X–Y plane, as shown in Fig. 3.14(a) for the clockwise propagating path as viewed from above in Fig. 3.10. In this case, although the beam is refracted twice, there is only a single reflection, with input and output wave vectors $\hat{\mathbf{k}}_2$ and $\hat{\mathbf{k}}_3$ as shown (we treat the beam refractions as sharp curves similarly to the case of reflections, but without a parity flip). The modified wave vectors are therefore constructed from the physical wave vectors via the relations $\hat{\mathbf{h}}_1 = \hat{\mathbf{k}}_1$, $\hat{\mathbf{h}}_2 = \hat{\mathbf{k}}_2$, $\hat{\mathbf{h}}_3 = -\hat{\mathbf{k}}_3$, and $\hat{\mathbf{h}}_4 = -\hat{\mathbf{k}}_4$. Although the resulting curve, defined by points $P1$–$P4$, is not closed, we may still apply (3.48) by closing it with a (unique) geodesic,

as has been verified experimentally in [56]. The spherical surface area enclosed by the curve is readily calculated using Fig. 3.14(a) using spherical coordinates via the surface integral $\int_0^\theta \left[\int_0^\pi \sin\theta' d\theta' \right] d\phi' = 2\theta$, so that for the clockwise propagating path the image and polarization are both rotated by angle $-\Omega_{\text{Dove}}$, where

$$\Omega_{\text{Dove}} = 2\theta. \tag{3.53}$$

Analogously to Figs. 3.13(b) and 3.13(c), we have plotted the absolute and relative geometric phase accumulations $\Omega(\theta)$ and $\Psi(\theta)$ as a function of the Dove prism tilt angle θ in Figs. 3.14(b) and 3.14(c). From 3.14(c) it is evident that both interferometers transform the transverse beam image and polarization state in an equivalent manner, as claimed at the beginning of this section.

We note here that a series of cascaded Sagnac interferometers of either the out-of-plane or tilted-Dove-prism type may be employed with different θ values to measure the OAM of a single photon to (in principle) arbitrary precision. Although a similar cascading scheme has been previously proposed and carried out [45, 46] at the single-photon level with Mach-Zehnder interferometers, such experiments are impractical when more than two or three such interferometers are involved, or when the OAM of true single photons are being measured, due to phase noise and drift. The phase-stable nature of the Sagnac interferometer overcomes these difficulties, thereby making experiments involving multiple cascading interferometers considerably more feasible. We will discuss in detail a proposed method to measure the OAM of single photon states with our out-of-plane Sagnac interferometer in Chapter IV.
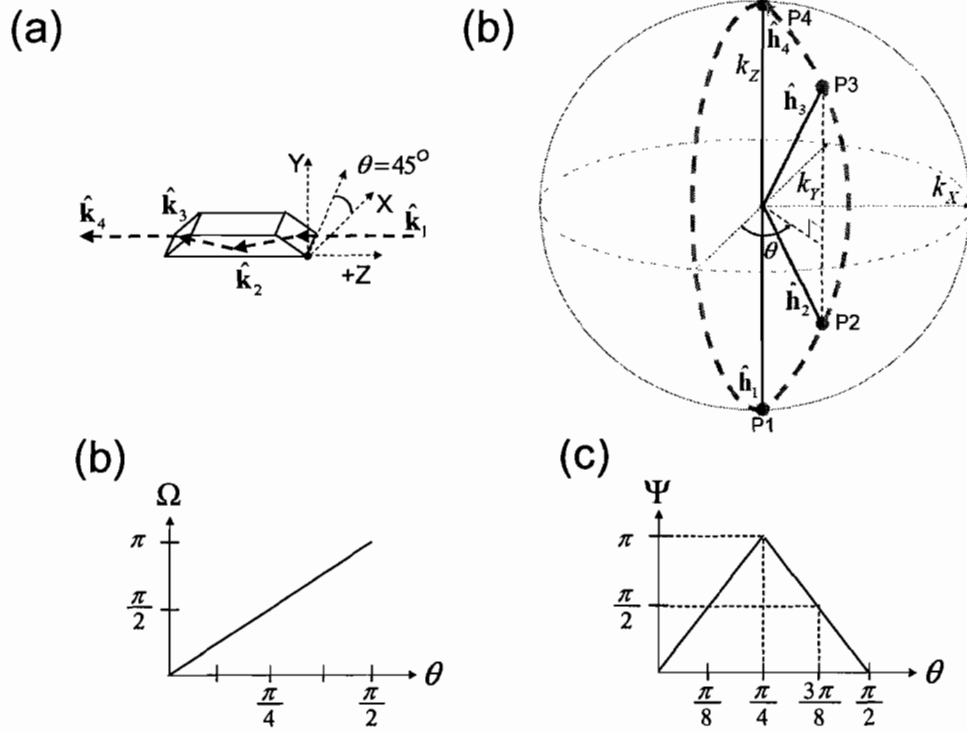
Figure 3.14. (a) The Dove prism in the Sagnac interferometer of Fig. 3.10, tilted at an angle θ with respect to the X axis. The clockwise propagating beam is deflected by the tilted Dove prism out of and back into the $Y-Z$ plane as shown, giving rise to wave vectors $\hat{\mathbf{k}}_1$–$\hat{\mathbf{k}}_4$. (b) The Poincaré sphere construction corresponding to the clockwise propagating beam path in Fig. 3.10 as discussed in the text. The Dove prism tilt angle θ defines the modified wave vectors $\hat{\mathbf{h}}_1 - \hat{\mathbf{h}}_4$, which in turn define the points P1-P4 on the spherical surface as shown. The gray dashed lines denote the wedge-shaped closed loop that results from successively connecting these points with geodesic curves. Note that the axes (k_X, k_Y, k_Z) are oriented differently from the axes (X, Y, Z) of the corresponding Fig. (a) for ease of display. (c) Plot of the accumulated geometric phase (beam rotation angle) Ω vs. the Dove prism tilt parameter θ. (d) Plot of the relative geometric phase (rotation angle) Ψ (modulo π) of the two counter-propagating beams after propagating around the Sagnac interferometer vs. θ, which yields the same result as for the out-of-plane Sagnac interferometer (see Fig. 3.13). See text for further discussion.

For the special case where the out-of-plane mirrors of our Sagnac interferometer are oriented such that $\theta = 45°$ in Fig. 3.11 such that $\beta = 90°$, the angles between the distinct helicity vectors are all $90°$ so that the area enclosed by the loop is exactly one eighth of the area of the entire sphere. This corresponds to a transverse rotation of $\Omega = \dfrac{\pi}{2}$ rads, or $90°$, as may also be calculated using (3.50). In this case ($\theta = 45°$), the out-of-plane Sagnac interferometer becomes a 2-D parity sorter for any paraxial input field, since the relative rotation between propagating and counter-propagating beams becomes $180°$ as shown in the plot of Fig. 3.13(c). In Chapter IV we employ our Sagnac with $\theta = 45°$ to present the first 2-D parity measurements of Hermite-Gauss transverse spatial modes, demonstrating experimentally the stable sorting of these modes according to their 2-D parity.

CHAPTER IV

1-D AND 2-D PARITY: EXPERIMENTS AND APPLICATIONS

Introduction

In this chapter, we present experimental results demonstrating the measurement and control of photonic transverse spatial modes, employing interferometeres based on both one-dimensional (1-D) and two-dimensional (2-D) parity as described in Chapter III. In the case of the interferometer based on 1-D parity, we observed its predicted behaviour as both a 1-D parity sorter and an Hermite-Gauss to Laguerre-Gauss (HG-to-LG) mode converter (see Figs. 3.7(c) and 3.7(d)). In the case of the interferometer based on 2-D parity, we present the first 2-D parity measurements of Hermite-Gauss transverse spatial modes, and demonstrate the stable sorting of these modes according to their 2-D parity. Additionally, we employ the 2-D sorter to sort the output modes of a "three-mode" optical fiber. We show how the 2-D sorter can be made to work at nearly 100% efficiency, and perform a detailed loss and efficiency analysis of the device. We also propose several applications of this interferometer, including its use as an alternative to holograms in spatial mode filtering, the measurement of the orbital angular momentum (OAM) of single photons, the production of Bell states entangled in first-order transverse spatial modes, and the production of heralded single photons in first-

order transverse spatial states corresponding to an arbitrary point of the first-order spatial mode Poincaré sphere [25].

The 2-D parity sorting interferometer belongs to a larger class of interferometers which differ according to the relative rotation Ψ of their constituent propagating and counter-propagating beams. For example, the 2-D sorter (with $\Psi = 180°$) can also distinguish between the zero-order (HG_{00}) and first-order (HG_{01} and HG_{10}) modes, but not between the zero-order and second-order (HG_{02}, HG_{20}, and HG_{11}) modes; conversely, a Sagnac with $\Psi = 90°$ *can* distinguish between HG_{00} and HG_{11} modes (cf. equation (3.50b) and Fig. 3.13). By orienting M1 and M3 in Fig. 3.11 in order to select the successive values $\theta = \dfrac{\pi}{4}, \dfrac{3\pi}{8}, \dfrac{7\pi}{16}, \dots$ one can achieve the relative rotations $\Psi = \pi, \dfrac{\pi}{2}, \dfrac{\pi}{4}, \dots$ required for each of the interferometer stages of the OAM sorter scheme in [45, 46]. In general, interferometers with various values of Ψ can be stably cascaded so as to sort photons with any value of their OAM, which enables the manipulation of discrete multi-dimensional qudits encoded in orbital angular momentum [6]. Furthermore, two-dimensional transverse spatial parity provides a second type of qubit encoding which is based on continuous photonic degrees of freedom, in addition to the scheme based on one-dimensional parity previously realized by [8]. Unfortunately, to our knowledge it is not possible to design a Sagnac interferometer that sorts according to 1-D parity, since the relative transverse rotation upon which our Sagnac depends treats both spatial variables on an equal footing. Therefore, it appears that encodings based on 2-D parity can be made more robust than those based on 1-D parity due to the phase-stable manipulations of qubits enabled by this work.
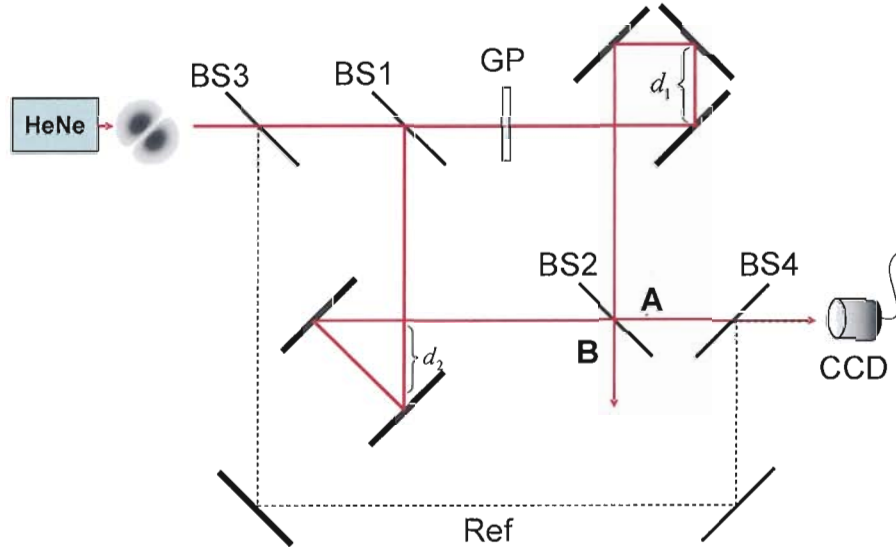
Figure 4.1. The experimental apparatus based on 1-D parity. An external-cavity helium neon laser (HeNe) produces an $HG_{45°}$ mode, whch acts at the light source. The clockwise-propagating beam encounters an odd number of mirrors and a phase-shifting glass plate (GP), while the counter-clockwise-propagating beam encounters as even number of mirrors. The additional mirrors in the clockwise-propagating path allow both interferomter path lengths to be equal so that the interferomter can function with the pulsed laser input from a mode-locked laser (the condition of equal path lengths is fulfilled when $4d_1 = \left(2 + \sqrt{2}\right) d_2$). After being split by a 50:50 beam splitter (BS1), the clockwise- and counter-clockwise-propagating beams interfere at a second beam splitter (BS2). A third beam splitter (BS3) picks off part of the source beam to use as a reference beam (Ref) which is combined with the interferometer beam via BS4 for the interferometry experiments discussed in the main text. The output field at port A was measured with a CCD camera, as well as its intensity pattern resulting from interference with the reference beam.

<u>Experiments Based on 1-D Parity</u>

Our experimental apparatus based on 1-D Parity was set up as shown in Fig. 4.1. An external-cavity helium neon laser (HeNe) produces an $HG_{45°}$ mode, whch acts at the

light source (for details on how we produced the $HG_{45°}$ mode, see the next section on 2-D parity sorting). The apparatus shown in Fig. 4.1 includes two additional 50:50 beam splitters and three additional mirrors in relation to the simplified version shown earlier in Fig. 3.4(a). The clockwise-propagating beam encounters an odd number of mirrors and a phase-shifting glass plate (GP), while the counter-clockwise-propagating beam encounters as even number of mirrors. The additional mirrors in the clockwise-propagating path allow both interferomter path lengths to be equal so that the interferomter can function with the pulsed laser input from a mode-locked laser (the condition of equal path lengths is fulfilled when $4d_1 = \left(2 + \sqrt{2}\right) d_2$). After being split by a 50:50 beam splitter (BS1), the clockwise- and counter-clockwise-propagating beams interfere at a second beam splitter (BS2). A third beam splitter (BS3) picks off part of the source beam to use as a reference beam (Ref) which is combined with the interferometer beam via BS4 for interferometry experiments as discussed below.

The output field at port A was measured with a charge-coupled device (CCD) camera (Thorlabs model number DC210), as well as its intensity pattern resulting from interference with the reference beam. A representative sample of our experimental results are presented in Fig. 4.2(a), which agree with the corresponding theoretical predictions shown in Fig. 4.2(b). In both figures, the first column indicates the input mode, while the second gives the observed/predicted intensity distribution for that mode. Column three gives the phase ϕ imparted by the glass plate, while column four gives the observed/predicted distributions

at output port A. The final column shows various observed/predicted interference patterns between the input and output modes, as discussed in detail below.

As shown in the figure, we observed the interferometer acting as both a 1-D parity sorter ($\phi = 0, \pi$) and an HG-to-LG mode converter ($\phi = \dfrac{\pi}{2}, \dfrac{3\pi}{2}$), as was derived theoretically in Figs. 3.7(c) and 3.7(d). In order to demonstrate the phase structure of the output modes, we interfered a single lobe of the reference beam with the output to port A as shown in Fig. 4.1, by steering the two beam paths together so that they were co-propagating with a slight misalignment (the other lobe of the reference beam was blocked). The resulting intensity measurements of the interference (see the final column of Fig. 4.2(a)) agree with the predicted profiles (see the final column of Fig. 4.2(b)). For $\phi = 0$ or π the interferometer acted as a 1-D parity sorter, giving rise to a uniform fringe dislocation as shown. For $\phi = \dfrac{\pi}{2}$ or $\dfrac{3\pi}{2}$ the interferometer acted as an HG-to-LG mode converter, giving rise to the characteristic "pitchfork" interference pattern associated with a mode with orbital angular momentum $\ell = 1$. Additionally, we visually observed port B of the interferometer throughout these experiments, and verified in each case that the output to port B always contained a mode orthogonal to that of the output to port A. That is, when port A output an HG_{01} mode, port B output an HG_{10} mode, while when port A ouput an LG_0^{+1} mode, port B output an LG_0^{-1} mode, etc., consistent with the theoretical predictions of Chapter III.

We note here that experiments similar to the above have been done previously with a similar 1-D parity interferometer [23]. However, by employing the reference-beam interferometry as described above, we have shown explicity the phase structure of the sorted modes,

Experiment
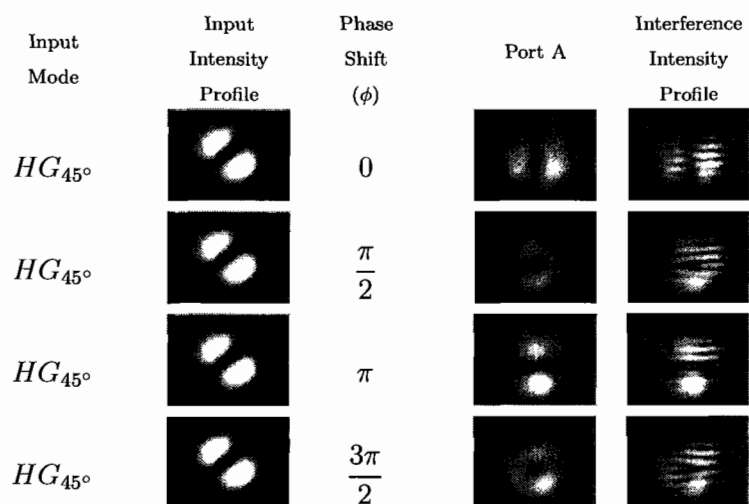
(a)

Theory
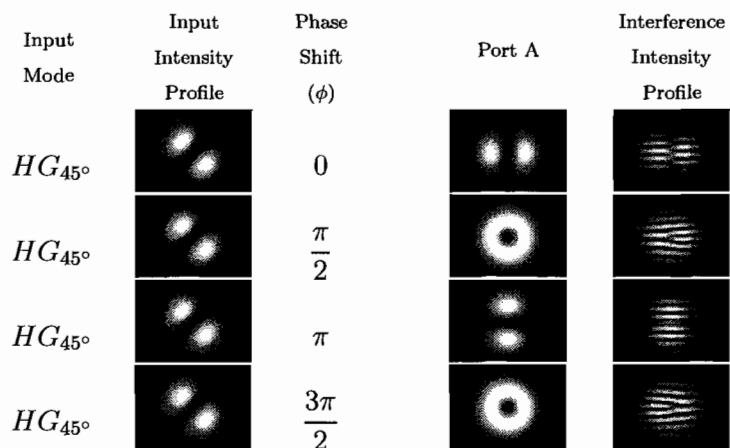
(b)

Figure 4.2. Observed (a) and predicted (b) output intensity profiles and interference patterns for the interferometer based on 1-D Parity. See text for further discussion.

which was not done in [23]. Additionally, we also employed our device to manupulate the 1-D parity degree of freedom of a pulsed (mode-locked) Titanium-Saphire laser, with results similar to that of Fig. 4.2. Due to the shorter coherence length of the mode-locked pulses, we had to match the two interferometer path lengths, which was also not attempted in the previously performed experiment [23], which exclusively used a continuous wave laser source.

Experiments Based on 2-D Parity

Our experimental apparatus based on 2-D Parity was set up as shown in Fig. 4.3. An external-cavity helium neon laser (HeNe) acts as the light source. Thin crossed metal wires (W) of diameter 50 μm were inserted into the laser cavity in order to excite higher order HG modes by suppressing lower order transverse modes which lacked a nodal point near the location of the wire. An intracavity iris (I) was then constricted in order to suppress the remaining excited modes that had a higher order than the desired mode. The Sagnac interferometer shown in Fig. 4.3 includes two Berek polarization compensators as well as two additional 50:50 beam splitters in relation to the simplified interferometer version shown in Fig. 3.11. The Berek compensators (New Focus model number 5540) were inserted into the interferometer as shown in order to improve the interference visibility by correcting for the Fresnel polarization changes due to the reflections from the dielectric mirrors M1-M3 [60, 61]. Without the compensators, the propagating and counter-propagating beams ended up with unequal elliptical polarization states upon interference at the beam splitter BS1, which led to poor interference visibility and therefore inefficient 2-D parity sorting. Since
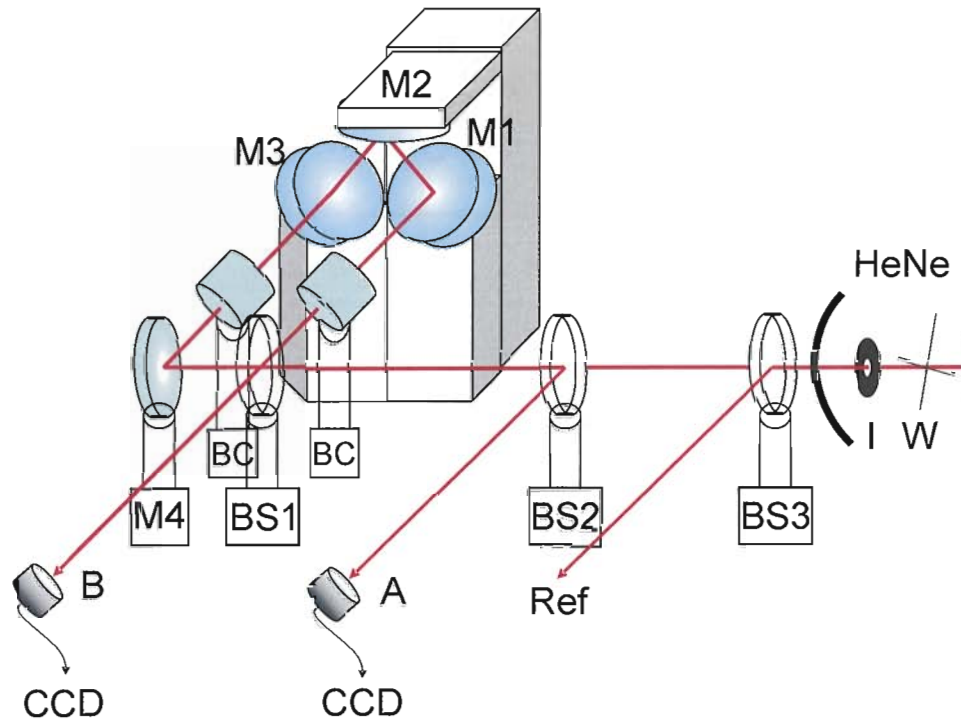
Figure 4.3. The experimental apparatus based on 2-D parity. An external-cavity helium neon laser (HeNe) acts as the light source, with thin crossed wires (W) and an iris (I) inserted into the cavity in order to select the higher order HG modes. The propagating and counter-propagating beams interfere at a 50:50 beam splitter (BS1), while a second 50:50 beam splitter (BS2) separates the backward-propagating output mode (port A) from the forward-propagating input mode. A third beam splitter (BS3) picks off part of the source beam to use as a reference beam (Ref) for the interferometry experiments discussed in the main text. Two Berek polarization compensators (BC) are placed inside the interferometer to correct for the Fresnel polarization changes due to reflections from the out-of-plane dielectric mirrors. The output fields at both port A and port B were measured with CCD cameras.
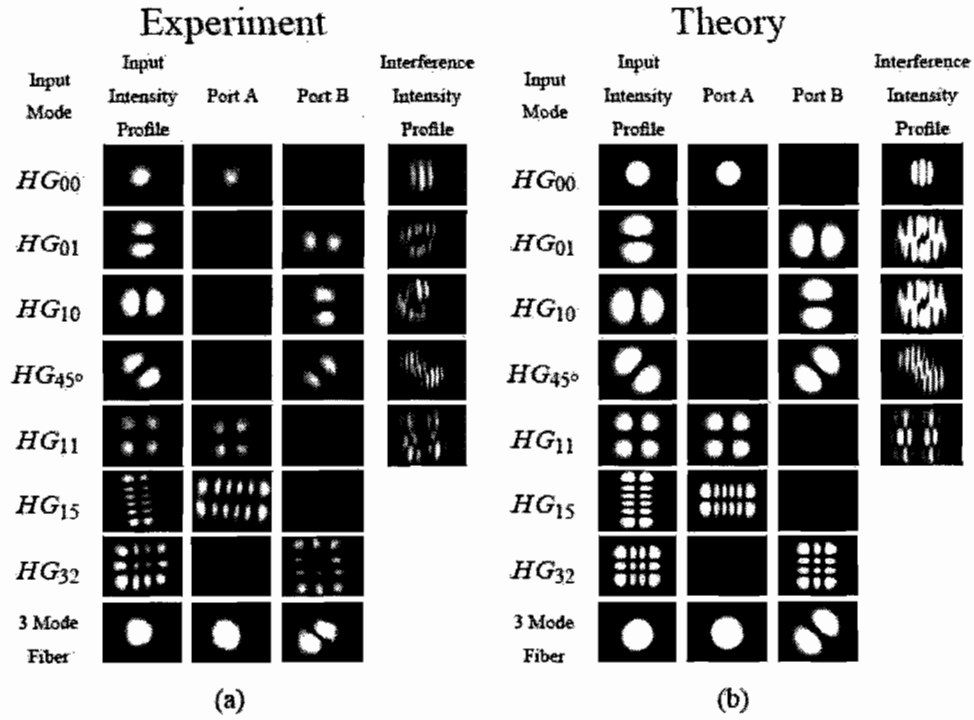
Figure 4.4. Observed (a) and predicted (b) 2-D sorter output intensity profiles and interference patterns for a given input field. See text for further discussion.

one of the interferometer's output ports (port A in Figs. 3.11 and 4.3) is counter-propagating with respect to the input beam, the addition of beam splitter BS2 acted to deflect half of the output beam from this path so that it could be imaged on a charge-coupled device (CCD) camera (Thorlabs model number DC210) as shown.

For a given input mode, we measured the output intensity profiles at both port A and port B of the interferometer using a CCD camera. A representative sample of our experimental results are presented in Fig. 4.4(a), which agree with the corresponding theoretical predictions shown in Fig. 4.4(b). In both figures, the first column indicates the input mode,

while the second gives the observed/predicted intensity distribution for that mode. Columns three and four give the observed/predicted distributions at output ports A and B, respectively. The final column shows various observed/predicted interference patterns between the input and output modes, as discussed in detail below.

Note from Fig. 4.4(a) that the HG_{00} and HG_{11} modes exit port A, while the HG_{10} and HG_{01} modes exit port B regardless of their orientation, as predicted in Fig. 4.4(b). Furthermore, the HG_{15} mode (which has even parity since $n + m = 1 + 5 = 6$) exits port A while the HG_{32} mode (which has odd parity since $n + m = 3 + 2 = 5$) exits port B. The operation of this device for such higher-order modes with higher numerical apertures demonstrates an advantage of the out-of-plane Sagnac of Fig. 3.11 over the Sagnac with a Dove prism of Fig. 3.10, whose numerical aperature is limited by the Dove prism. We sucessfully excited and sorted transverse modes with $n + m \leq 5$, being limited only by the order of the modes we were able to excite in the laser cavity due to the finite diameter of the wire.

In a second experiment, the wire and iris were removed and the light was coupled into and out of a three-mode fiber (Thorlabs SM-780) which then acted as the input source to the 2-D parity sorting interferometer. In this case, each of the HG_{00}, HG_{10}, and HG_{01}-like modes were excited in the fiber before being out-coupled and passing through the interferometer. The Saganc then sorts the fundamental (even) HG_{00} mode, which exits out of port A, from an equal superposition of (odd) HG_{10} and HG_{01} modes, which interfere together to make a diagonal HG mode which exits out of port B. In this way, our apparatus sorts the output of

a three-mode fiber into its constituent zero- and first-order mode families as shown in the last row of Figs. 4.4(a) and 4.4(b) (the theory plot is for a field composed of 85% HG_{00} and a 15% balanced superposition of first-order modes). This explicitly demonstrates the usefulness of our 2-D parity sorter as a "beam splitter" for even and odd transverse spatial modes (with respect to 2-D parity), while at the same time suggests that it can be employed as an alternative to relatively lossy holograms in spatial mode filtering, as discussed below.

In order to demonstrate the phase structure of the sorted HG modes, we employed a third beam splitter BS3 in order to "pick off" a portion of the input beam to use as a reference beam (Ref in Fig. 4.3), similarly to the 1-D parity experiment of Fig. 4.1. We then interfered the reference beam for several input modes with their corresponding parity-sorted output modes by steering the input and output beam paths together so that they were co-propagating with a slight misalignment, and recorded the resulting intensity patterns as the final column of Figs. 4.4(a) and 4.4(b). In order to interpret these results, recall that the output beam has been rotated 90° with respect to the input beam, regardless of output port. This has no effect upon the rotationally symmetric HG_{00} mode, so the familiar interference fringes of a standard Mach-Zehnder interferometer are observed. However the 90° rotation does effect the first-order modes, so that the next two rows exhibit an interference pattern resulting form the superposition of the input HG mode and its 90° rotated counterpart. Note the characteristic uniform fringe dislocation of the vertical fringes in both of these plots, which shows the nontrivial phase structure of these modes as they interfere. For the $HG_{45°}$ mode, one would expect a similar dislocated pattern, but rotated by 90°. However,

practical considerations required the presence of an extra mirror along the reference beam path in order to interfere the reference and output beams. Since an extra mirror reflection (i.e, a 1-D parity transformation) in the x-y plane transforms an $HG_{45°}$ mode into its 90° rotated counterpart, the presence of the extra mirror canceled the effect of the out-of-plane rotation, so that the resulting interference pattern (not shown) resembled that of the HG_{00} mode, which did not exhibit the phase structure of the mode. A similar issue occurs with the HG_{11} mode, which is identical to its 90° rotated counterpart up to an overall phase. In order to more clearly demonstrate the desired phase structure of the $HG_{45°}$ and HG_{11} modes, we therefore steered the output beam so that its propagation axis was *transversely shifted* with respect to the reference beam while still being (nearly) collinear with respect to it. For the case of the $HG_{45°}$ mode, the transverse shift was directed both down and to the right, while for the HG_{11} mode it was directed completely downwards. In this way, the interfering beams were only partially overlapping so that the resulting interference patterns, included in the fourth and fifth columns, clearly show the characteristic fringe dislocation effect.

Efficient 2-D Parity Sorting

Due to the 50% loss of the signal from port A from the presence of the 50:50 beam splitter BS2, the setup described above was not capable of sorting single photons with high efficiency. However, by replacing beam splitter BS2 with a Faraday isolator and appropriately adjusting the Berek polarization compensators, 100% efficiency can be obtained in principle. A Faraday isolator (shown in Fig. 4.5) consists of a piece of Faraday glass with a polarizing
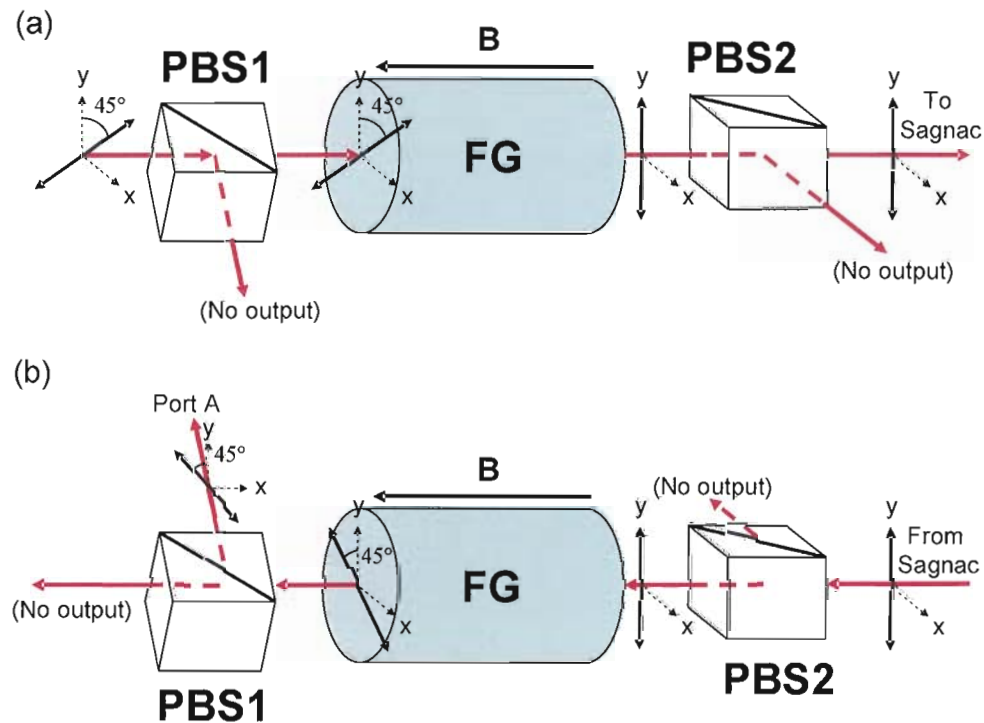
Figure 4.5. A Faraday isolator, consisting of a piece of Faraday glass (FG) with a polarizing beam splitter on each side (PBS1 and PBS2). (a) An input photon (propagating left to right) polarized at positive 45° angle with respect to the vertical is completely transmitted and becomes vertically polarized. (b) A back-propagating (from right to left) output photon from port A of the Sagnac with vertical polarization is completely transmitted through PBS2, but is subsequently completely deflected from PBS1. See text for further discussion.

beam splitter (PBS) on each side. The application of a uniform magnetic field causes the

Faraday glass to act as a polarization rotator via the Faraday effect [39]. The first PBS

(PBS1) is oriented at a positive 45° angle with respect to the vertical, such that an incoming

photon polarized along this same direction will be completely transmitted. Conversely, the

second PBS (PBS2) is oriented vertically (at a 45° angle with respect to the first), in order

to completely transmit vertically polarized photons. Therefore, the polarization state of an incoming photon initially polarized at 45° with respect to the vertical will remain unchanged as the photon is completely transmitted though PBS1, but will then be transformed to vertical polarization so that the photon is also completely transmitted through PBS2, as shown in Fig. 4.5(a). However, an arbitrarily polarized photon propagating through the isolator in the opposite direction will have its horizontally polarized component deflected by PBS2, while its vertically polarized component will be transmitted and subsequently rotated by the Faraday glass to a *negative* 45° angle with respect to the vertical, so that this remaining component is completely deflected by PBS1.

Applying this to our current problem of sorting efficiency, one finds that although our backwards-propagating beam from output port A will be completely deflected as desired upon employing a Faraday isolator, it would also in general be separated into two different paths by the two PBS's. Although one can easily recombine these beams using a half wave plate and an additional polarizing beam splitter, such a separation and recombination is undesirable as it introduces the same phase noise and drift that gives our setup an advantage over previous Mach-Zehnder-based 2-D sorter implementations. In our experiment, we can overcome this difficulty by adjusting the Berek compensators such that given a vertical input polarization, the output polarizations of both port A and port B are vertical, which we have verified is indeed possible experimentally. Therefore, with the compensators appropriately adjusted, we conclude that back-propagating photons from port A will be completely *transmitted* by PBS2 and completely *deflected* by PBS1, as shown in Fig. 4.5(b). In light of this, it is

apparent that PBS2 of Fig. 4.5 is actually unnecessary, however we have included it because of the practical consideration that Faraday isolators are readily commercially available in the form discussed above (e.g. Thorlabs model number IO-3-633-LP). We conclude that through the use of a Faraday isolator in conjunction with the Berek compensators, 100% of the output field from port A can be deflected into a single beam path that is distinct from the input path, so that our 2-D parity sorting Sagnac is in principle 100% efficient with respect to both output ports. A realistic loss analysis supporting this efficiency claim is included below, where we incorporate the effects of beam splitter imbalance and loss on the sorting and transmission efficiencies and find that both can be made to exceed 99% using readily available optics.

<div align="center">2-D Sorter Efficiency and Loss Analysis</div>

Using standard beam-splitter theory and taking into account the action of the out-of-plane mirror configuration on the nonreciprocal phase shifts of the spatial modes (see Chapter III), we find that given input fields with even and odd parity (E^{in}_{even} and E^{in}_{odd}), the output fields are

$$E^{A}_{even} = \sqrt{T}\left(tr + rt\right)E^{in}_{even} = 2\sqrt{T}trE^{in}_{even}$$

$$E^{B}_{even} = \sqrt{T}\left(t^2 - r^2\right)E^{in}_{even}$$

$$E^{A}_{odd} = \sqrt{T}\left(tr - rt\right)E^{in}_{odd} = 0$$

$$E^{B}_{odd} = \sqrt{T}\left(t^2 + r^2\right)E^{in}_{odd}, \qquad (4.1)$$

where t and r are the beam splitter transmission and reflection coefficients for the input field, while $T \leq 1$ is the round trip intensity transmission coefficient, which takes into account reflection losses in the Sagnac due to imperfections in the mirrors and Berek compensator anti-reflection (AR) coatings. Also in (4.1), E^A_{even}, E^B_{odd} and E^B_{even}, E^B_{odd} are the respective output fields associated with ports A and B.

Ideally, $T = 1$ and $t = r = \sqrt{\dfrac{1}{2}}$ for the 50:50 beam splitter which gives $E^A_{even} = E^{in}_{even}$, $E^B_{odd} = E^{in}_{odd}$, and $E^B_{even} = E^A_{odd} = 0$, so that the sorting efficiency is 100%. However, a beam splitter may be more realistically modeled by expressing the beam splitter transmission in the form $t = \sqrt{\dfrac{1}{2}}\left(1 + \dfrac{\epsilon}{2}\right)$, where $\epsilon \ll 1$ is a measure of the beam splitting ratio imbalance. Employing the standard constraint $r^2 + t^2 = 1$ yields the reflectivity as $r = \sqrt{1 - t^2} \approx \sqrt{\dfrac{1}{2}}\left(1 - \dfrac{\epsilon}{2}\right)$, where only terms first order in ϵ have been retained. Since there are four AR coatings in one Sagnac round trip (two for each Berek crystal surface) and also four additional mirror reflections involving losses comparable to that to the AR coatings, we find that $T = (1 - \delta)^8$, where δ is the loss associated with each interface. In what follows we will ignore any losses due to the beam splitter, since for AR coated beam splitters the effects casued by such losses are generally negligble in comparison to those caused by ϵ as well as the cumulative loss along the rest of the interferometer path as quantified by T.

In order to obtain an expression relating input and output intensities, we substitute the above expressions for t and r into (4.1) and square both sides, which yields

$$I^A_{even} \approx T I^{in}_{even}$$

$$I_{even}^B \approx \epsilon^2 T I_{even}^{in}$$

$$I_{odd}^A = 0$$

$$I_{odd}^B \approx T I_{odd}^{in}, \tag{4.2}$$

where $I_{even}^A \equiv \left(E_{even}^A\right)^2$, etc., and only terms of lowest order in ϵ have been retained. Armed with (4.2), we define the Sagnac sorting efficiency E_S (i.e., the sorting visibility) in terms of the ratio of the "dark" port output intensity to that of the "bright" port,

$$E_S \equiv 1 - \frac{I^{dark}}{I^{bright}} \geq 1 - \epsilon^2 \tag{4.3}$$

while expressing the total Sagnac transmission efficiency E_T in terms of the ratio of the "bright" port intensity to that of the input field,

$$E_T \equiv \frac{I^{bright}}{I^{in}} \approx T. \tag{4.4}$$

The inequality in (4.3) follows from the fact that $E_S \approx 1 - \epsilon^2$ or unity for even and odd modes respectively, while (4.4) holds approximately for both mode types. We therefore conclude that the beam splitter imbalance ϵ has the largest effect upon the sorting efficiency, while the losses associated with the transmission T do not affect E_S, but only the total photon flux through both ports.

Broadband beam splitters are readily available with splitting ratios of 55:45 or better, while AR coatings are available with losses of less than 0.1%, which imply values of about 0.1 and 0.001 for ϵ and δ respectively, thereby yielding $E_S \approx 0.99$, and $E_T \approx T \approx 0.99$ such

that the sorting and transmission efficiencies can be made to be greater than 99%. In other words, for a given input mode the "dark" port intensity can be made to be at least 100 times less intense than that of the "bright" port using standard equipment. For a precision beam splitter with splitting ratio 50.5%:49.5% this factor reaches 10^4, which corresponds to an efficiency of 99.99%, thereby supporting our claim of high efficiency in principle. In our experiments (using standard, non-precision optical equipment), we achieved better than 95% sorting effeciency E_S for all input modes. We believe the discrepency between our experimental result and our efficiency analysis is due to a lack of purity of our input modes, so that an odd input mode, for example, actually had a small even component due to imperfections in the exernal cavity laser source. Since the above analysis yields such a high effiency in principle, we conlclude that in practice polarization overlap may be the chief limiting factor in the operation of the device.

Applications of 2-D Parity Sorting

First-Order Mode Filter

One particularly useful characteristic of our Sagnac interferometer is its ability to distinguish between zero-order and first-order transverse HG modes. When used in conjunction with a three-mode optical fiber, this ability allows the Sagnac to act as a spatial mode filter that passes only the first-order HG modes while rejecting all other mode orders. To see this, consider a linearly polarized monochromatic paraxial beam with electric field $E(x, y, z) e^{-i\omega_p t}$ coupled into an optical fiber with input and output coupling lenses as shown in Fig. 4.6(a)
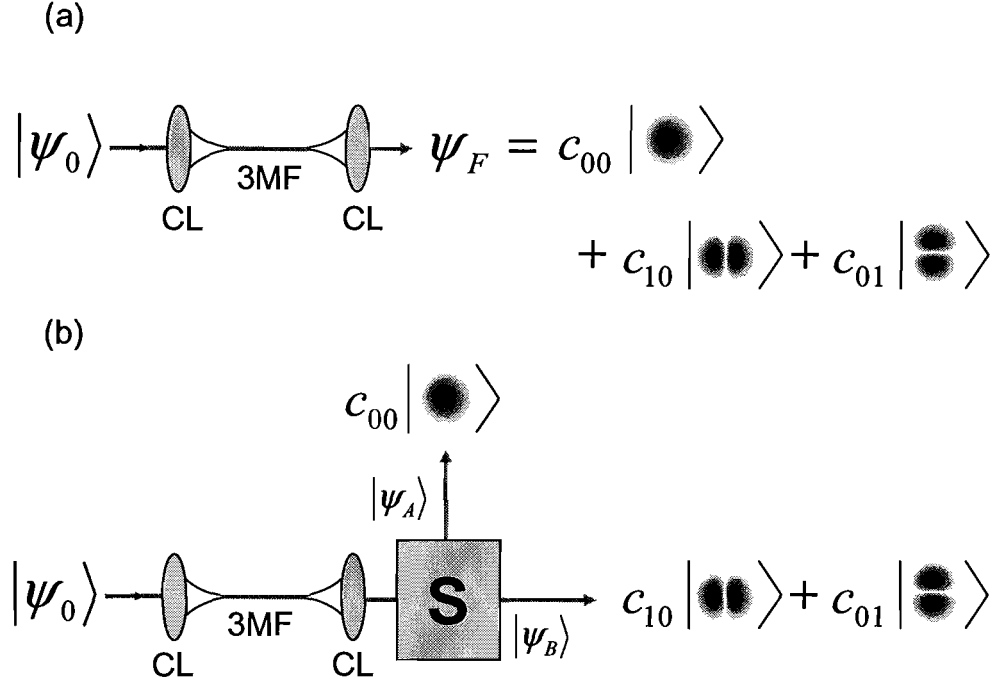
Figure 4.6. A spatial filter for zero and first-order HG modes. (a) A three-mode optical fiber (3MF) with input and output coupling lenses (CL). The fiber, which has a parabolic refractive index profile, acts as a mode filter upon an arbitrary transverse input beam $|\Psi_0\rangle = \sum_{n,m=0}^{\infty} c_{nm} |HG_{nm}\rangle$ such that upon coupling into and out of the fiber the resulting beam state is of the form $|\psi_F\rangle = c_{00} |HG_{00}\rangle + c_{10} |HG_{10}\rangle + c_{01} |HG_{01}\rangle$. (b) Inserting a 2-D Parity Sorter (S) after the fiber separates the zero and first-order modes into ports A and B, respectively.

(we align the fiber with the z-axis and place the origin at the fiber input face). Such a beam comprises a general solution to the scalar paraxial wave equation, of which the paraxial HG modes form a complete basis [49]. Employing the notation $E(x, y, z) \equiv |\psi_0\rangle$, one may therefore write

$$|\psi_0\rangle = E_0 \sum_{n,m=0}^{\infty} c_{nm} |HG_{nm}\rangle \tag{4.5}$$

where $c_{nm} \equiv \langle \psi_0 | HG_{nm}\rangle$ is the overlap integral between the incident field and the HG_{nm} mode, and the constant E_0 is the electric field magnitude. When the fiber and input coupling lens are properly aligned, the beam will be centered coaxially with the fiber, and the location of the beam waist will coincide with the plane of the fiber input face at $z = 0$. Under these conditions, the paraxial HG modes evaluated at the fiber input plane have the simplified transverse form given in equation (3.9a) of Chapter III,

$$|HG_{nm}\rangle = \frac{A_{nm}}{w_0} H_n\left(\frac{\sqrt{2}x}{w_0}\right) H_m\left(\frac{\sqrt{2}y}{w_0}\right) e^{-\frac{x^2+y^2}{w_0^2}}. \tag{4.6}$$

In comparison, the eigenmodes of an optical fiber with a parabolic refractive index profile $n(\rho) = n_0\left(1 - \Delta\frac{\rho^2}{a^2}\right)$ obeying the weakly guided condition $\Delta \ll 0$ are well approximated [62] by the linearly polarized Laguerre-Gauss modes $|LG_p^\ell\rangle$:

$$|LG_p^\ell\rangle \propto \left(\frac{\rho}{a}\right)^{|\ell|} L_q^{|\ell|}\left(V\frac{\rho^2}{a^2}\right) e^{-\frac{V}{2}\frac{\rho^2}{a^2}} e^{i\ell\phi}, \tag{4.7}$$

where a is the fiber radius, $V \equiv \frac{\omega_p n_0}{c} a\sqrt{2\Delta}$ is the normalized frequency, the $L_q^{|\ell|}$ are generalized Laguerre polynomials, and we have employed transverse cylindrical coordinates (ρ, ϕ). Furthermore, for sufficiently small a, the higher order modes will be cut off [63] so that the fiber will support only the three LG modes $|LG_0^0\rangle$, $|LG_0^{+1}\rangle$, and $|LG_0^{-1}\rangle$, or equivalently the three HG modes $|HG_{00}\rangle$, $|HG_{10}\rangle$, and $|HG_{01}\rangle$ (of course, counting the two possible orthogonal polarization states for each mode means that such a "three-mode" fiber technically

supports *six* distinct modes). Therefore, regardless of the form of the transverse input state $|\psi_0\rangle$ in equation (4.5), a weakly guided parabolic fiber will in principle filter out the higher-order HG mode contributions while transmitting the fundamental and first-order modes with high efficiency such that the remaining output state ψ_F will have the form

$$|\psi_F\rangle = c_{00}|HG_{00}\rangle + c_{10}|HG_{10}\rangle + c_{01}|HG_{01}\rangle \tag{4.8}$$

provided that the mode matching condition $w_0 = a\sqrt{\dfrac{2}{V}}$ is met. Given this fiber-filtered state, our Sagnac can then sort $|\psi_F\rangle$ such that the output modes at port A and port B are $|\psi_A\rangle = c_{00}|HG_{00}\rangle$ and $|\psi_B\rangle = c_{10}|HG_{10}\rangle + c_{01}|HG_{01}\rangle$, respectively, as shown in Fig. 4.6(b).

Measuring the OAM of Single Photons

In addition to the HG modes, an ℓth order $LG_p^{\pm\ell}$ mode is sorted by the 2-D parity-based interferometer according to whether ℓ is even or odd, which parallels the case of HG_{nm} mode sorting according to the even/odd parity of $n + m$. Because of this, the above sorting experiments on HG modes also demonstrate that stable, cascadable, single photon OAM sorting schemes corresponding to those discussed in [45, 46] are indeed feasible with our interferometer. Specifically, by orienting M1 and M3 of Fig. 3.11 in order to select the successive values $\theta = \dfrac{\pi}{4}, \dfrac{3\pi}{8}, \dfrac{7\pi}{16}, ...$ one can achieve the relative rotations $\Psi = \pi, \dfrac{\pi}{2}, \dfrac{\pi}{4}, ...$ required for each of the interferometer stages of the OAM sorter scheme in [45, 46]. As discussed in [46], a tiltable phase-shifting glass plate in one of the Mach-Zehnder arms introduces an adjustable relative phase difference between the two interferometer paths, in addition to the phase difference already introduced by the transverse spatial rotation. This

additional relative phase is needed in order to distinguish between modes possessing odd OAM values without the use of holograms [4], which are lossy in practice. Since our device is a common-path interferometer, a glass plate cannot introduce the required relative phase shift between the counter-propagating interferometer paths. However, one may surmount this difficulty by employing a device which imparts a variable phase shift that is dependent upon whether the photon is propagating forwards or backwards through it.

This device consists of of a tiltable birefringent waveplate surrounded on both sides by identical lengths of Faraday glass distinguished only by the direction of the applied magnetic fields (B) permeating them as shown in Fig 4.7. The uniform magnetic fields cause the Faraday glass to act as a polarization rotator via the Faraday effect [39], with the sense of rotation depending of the direction of the applied field. Upon entering the device from the left, a right-propagating vertically polarized photon undergoes a polarization rotation such that upon entering the waveplate the polarization is aligned with the waveplate's fast axis. The waveplate then imparts a phase shift to the photon before its polarization is returned to its original state, as shown in 4.7(a). Conversely, a vertically polarized left-propagating photon undergoes a transformation which leaves its polarization aligned with the waveplate's *slow* axis. Therefore, the left-propagating photon experiences a different phase shift than the right-propagating photon before its polarization is returned to vertical, as shown in 4.7(b). The waveplate can be tilted about its fast or slow axes in order to vary this relative phase shift, similarly to the standard method of tilting a thin glass slide. By employing one of these phase shifting devices inside our Sagnac interferometer, one may effect variable phase shifts
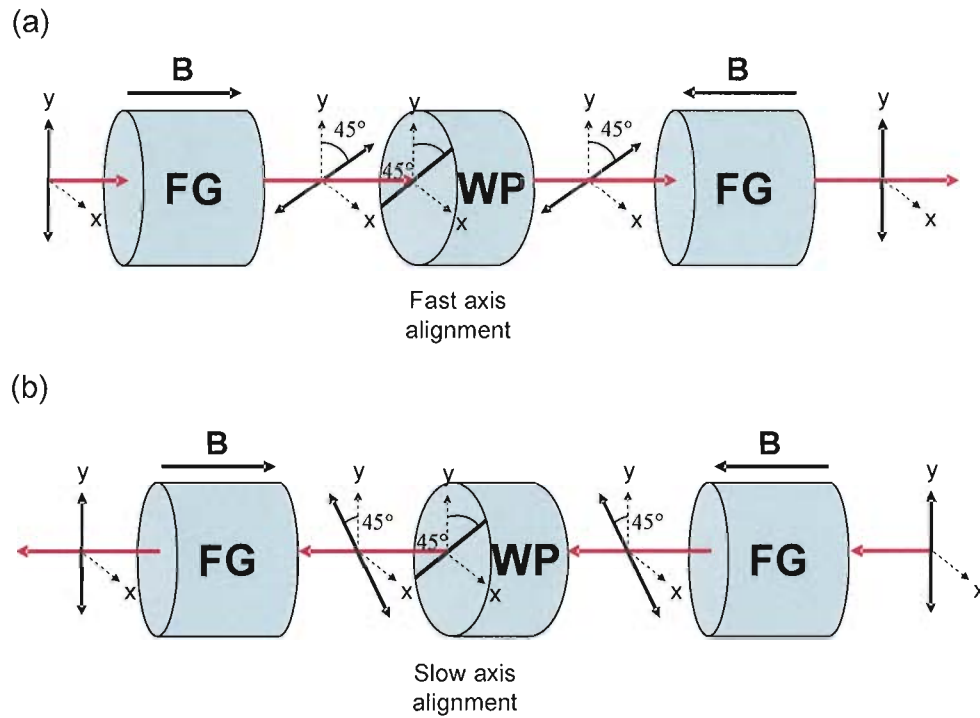
Figure 4.7. A device that imparts a relative phase shift between counter-propagating fields, consisting of a tiltable birefringent waveplate (WP) with identical lengths of Faraday glass (FG) on each side, distinguished only by the direction of the applied magnetic fields (B) permeating them. (a) A vertically polarized right-propagating photon becomes aligned with the fast axis of a birefringent waveplate (axis is denoted by the bold line), which induces a phase shift. (b) A vertically polarized left-propagating photon becomes aligned with the slow axis of the waveplate, thereby experiencing an unequal phase shift when compared to the forward-propagating beam.

between the propagating and counter-propagating beams without changing the polarization state of the light.

We conclude that our Sagnac is capable of sorting odd OAM-valued photons from one another without the use of comparatively lossy holograms. Therefore, like the device of Fig. 3.4(b), our interferometer is able to sort and measure photons possessing arbitrary absolute OAM values with 100 % efficiency in principle. Furthermore, as our Sagnac interferometer is phase-stable, it provides, for the first time, a practical way to realize a multiple-stage cascaded sorting scheme for single photon states.

Applications to Quantum Information Processing

Here we propose two applications of 2-D parity sorters to quantum information processing (QIP) with transverse spatial modes. Both make use of spontaneous parametric down conversion in addition to the first-order mode filter discussed above, as shown in Figs. 4.8(a) and 4.8(b). In both cases, a crystal with a $\chi^{(2)}$ nonlinearity is cut and oriented for Type-II collinear phase matching and pumped with a sufficiently weak cw laser in a well-defined HG mode HG_{nm}, such that the resulting state is predominantly a superposition of the vacuum and a two-photon state $|\Psi\rangle = C_1 \, ||vac\rangle\rangle + C_2 \, ||\Psi_{2ph}\rangle\rangle$, where $C_1 \gg C_2$ and the "double-ket" symbol $|| \quad \rangle\rangle$ denotes Fock-space states of the electromagnetic field [64].

When sufficiently narrowband filters centered at half the pump frequency ω_p are employed, the co-propagating two-photon state $|\Psi_{2ph}\rangle$ is frequency degenerate, and is therefore not entangled in the spectral degree of freedom. However, photons have four degrees of freedom, and $|\Psi_{2ph}\rangle$ is entangled in each of the remaining three (polarization and the two

transverse coordinates). In particular, if the appropriate birefringent phase compensators are used [2], then the biphoton mode function corresponding to the two-photon component $|\Psi_{2ph}\rangle$ of the state $|\Psi\rangle$ can be written as [2, 7]

$$|\psi_{2ph}\rangle = |\phi_{nm}\rangle \otimes \Big(|H\rangle\,|V\rangle + |V\rangle\,|H\rangle \Big) \tag{4.9}$$

where $|H\rangle$ and $|V\rangle$ denote the horizontal and vertical single-photon polarizations, and $|\phi_{nm}\rangle$ denotes the spatial portion of the biphoton mode function. In [7], $|\phi_{nm}\rangle$ was expanded in terms of the HG modes for an arbitrary HG pump beam HG_{nm}, and shown to be entangled: In terms of the HG mode functions, $|\phi_{nm}\rangle$ takes the form

$$|\phi_{nm}\rangle = \sum_{j,k,s,t=0}^{\infty} c_{jkst}^{nm} |HG_{jk}\rangle\,|HG_{st}\rangle \tag{4.10}$$

where the specific coefficients c_{jkst}^{nm} depend on the order nm of the pump beam via equation (18) of [7]. As shown there, the expansion contains an infinite number of nonzero terms, and converges slowly in general. However, many of the coefficients c_{jkst}^{nm} are zero due to selection rules. We apply this result below in two special cases.

Bell State Generation

The first QIP application we discuss is the production of Bell states entangled in first-order transverse spatial modes, as shown in Fig. 4.8(a). An HG Bell state generation experiment similar to this has been carried out by [6], which used holograms to sort and detect spatial modes. However, employing our Sagnac interferometer in the place of holograms
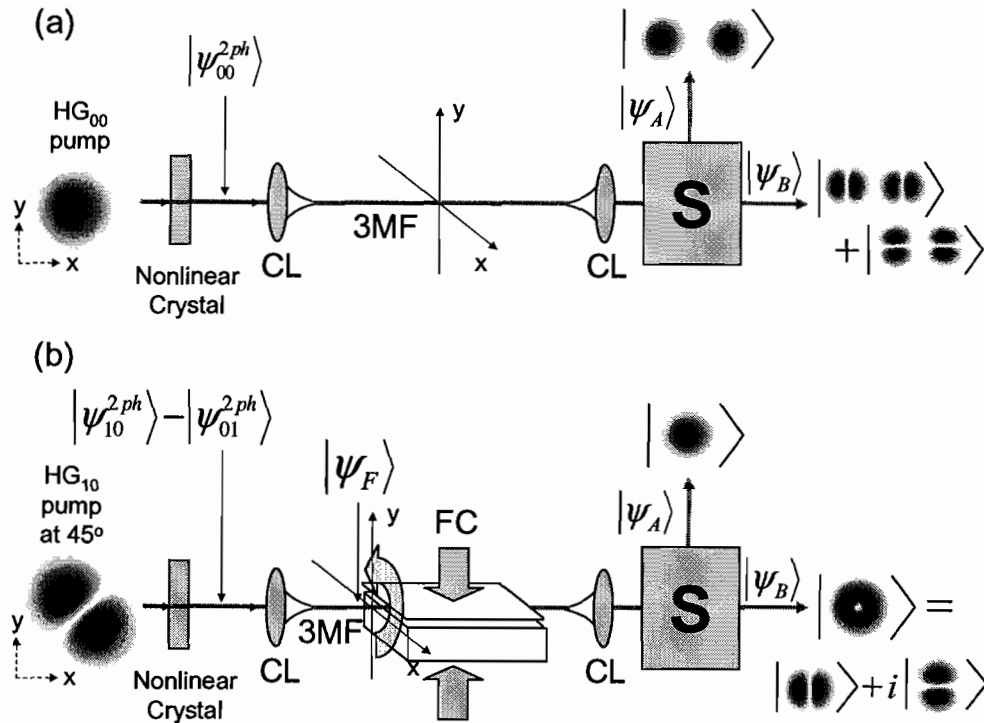
Figure 4.8. Possible applications of a 2-D parity sorter to quantum information processing. (a) Proposed scheme to produce Bell states entangled in first-order transverse spatial modes. (b) Proposed scheme to produce heralded single photons in arbitrary first-order transverse spatial states.

will provide an improvement in efficiency over standard holographic techniques. In the current setup, the pump beam is in an HG_{00} mode, and following [7] we find that the spatial part of the down converted biphoton mode function has the form

$$|\phi_{00}\rangle = c_0 |HG_{00}\rangle |HG_{00}\rangle + c_1 \Big(|HG_{10}\rangle |HG_{10}\rangle + |HG_{01}\rangle |HG_{01}\rangle \Big)$$

$$+ c_2 \Big(|HG_{00}\rangle |HG_{02}\rangle + |HG_{02}\rangle |HG_{00}\rangle \ + \ |HG_{00}\rangle |HG_{20}\rangle + |HG_{20}\rangle |HG_{00}\rangle \Big) + ...$$

$$(4.11)$$

where $c_1 = \dfrac{1}{2} c_0 \approx 0.04$, and $c_2 \approx -0.03$ under typical experimental conditions (pump beam width 0.1 mm and crystal length 1 mm), and all other coefficients of total order $j + k + s + t = 2$ are zero. The omitted terms in (4.11) all involve biphoton mode functions of total order $j + k + s + t \geq 4$. However, since each individual photonic mode is filtered by the Fiber-Sagnac combination as discussed above, the mode function in (4.11) retains only its first-order component, so that the (renormalized) mode function exiting port B is given by (4.9) and (4.11) as

$$|\psi_B\rangle = \frac{1}{\sqrt{2}} \Big(|HG_{10}\rangle |HG_{10}\rangle + |HG_{01}\rangle |HG_{01}\rangle \Big) \otimes \Big(|H\rangle |V\rangle + |V\rangle |H\rangle \Big) \qquad (4.12)$$

as shown in the figure. Thus, the filtered biphoton mode function is maximally entangled in both polarization *and* first-order spatial modes. This is a Bell state.

We note here that the two photons comprising the Bell state are co-propagating; in order to turn this source into "useful" entanglement, one must separate these photons onto two separate paths without destroying the entanglement relationship. This can be done by inserting a 50:50 beam splitter after port B, albeit with a 50% loss of the entanglement source. To obtain the HG-entangled Bell states without such a loss, one may instead use a polarizing beam splitter. The co-propagating photons are then path-separated with the cost of destroying the polarization entanglement, while the spatial mode entanglement remains.

Heralded Photons in Arbitrary Spatial Modes

We now consider the second application of our mode sorter, shown in Fig. 4.8(b). In this setup, the pump beam is a first-order HG_{10} mode rotated through an angle of 45° in the transverse plane, denoted as $HG_{45°}$. Since $HG_{45°}$ comprises an in-phase superposition of HG_{10} and HG_{01} modes, we express it in terms of these, and again employ equation (19) of [7], finding that the down-converted biphoton mode function is

$$|\phi_{45°}\rangle \equiv |\phi_{10}\rangle + |\phi_{01}\rangle = c_1 \Big(|HG_{10}\rangle |HG_{00}\rangle + |HG_{00}\rangle |HG_{10}\rangle$$
$$+ |HG_{01}\rangle |HG_{00}\rangle + |HG_{00}\rangle |HG_{01}\rangle \Big) + ... \qquad (4.13)$$

where all other coefficients of total order $j + k + s + t = 1$ are zero. Similarly to the previous case, the omitted terms in (4.13) all involve biphoton mode functions of total order $j + k + s + t \geq 3$, and are therefore filtered by the fiber. Therefore, the action of the Sagnac on the present fiber-filtered biphoton mode function is to path-separate the photons in the fundamental mode $|00\rangle$ from those in the higher modes. Thus, upon exiting the Sagnac the biphoton mode function is

$$|\psi\rangle \equiv |HG_{00}\rangle_A |HG_{45°}\rangle_B \otimes \Big(|H\rangle_A |V\rangle_B + |V\rangle_A |H\rangle_B \Big) \qquad (4.14)$$

where $|HG_{45°}\rangle \equiv |HG_{10}\rangle + |HG_{01}\rangle$ and A and B label the output ports, so that the detection of a $|HG_{00}\rangle$ photon in port A heralds a single polarization-entangled photon in the pure spatial mode $|HG_{45°}\rangle$ in port B.

In order to produce heralded single photons in *arbitrary* (first order) spatial modes, one may apply a directional compression stress on the three-mode fiber with two plates as shown in Fig 4.8(b). Such a compression breaks the cylindrical symmetry of the fiber medium which causes the non-cylindrically symmetric HG_{10} and HG_{01} modes to experience differing phase velocities as they propagate though the fiber, resulting in a nonzero relative phase at the fiber output that is controllable by the magnitude and direction of the applied stress [65]. That is, the compressor acts analogously to a fractional wave plate for polarization, with principal axes aligned parallel and perpendicular to the direction of compression, and with the degree of phase retardation proportional to the amount of stress. In the case illustrated, the biphoton mode function propagating in the fiber (before compression, but after being filtered) is $|\psi_F\rangle = |HG_{00}\rangle |HG_{45°}\rangle + |HG_{45°}\rangle |HG_{00}\rangle$, the direction of compression is along the y axis, and the magnitude is such that so that the HG_{10} and HG_{01} mode components experience a relative phase factor of $e^{i\frac{\pi}{2}} = i$. Therefore, the spatial part of the single-photon mode function $|HG_{45°}\rangle \equiv |HG_{10}\rangle + |HG_{01}\rangle$ becomes $\left|LG_0^{+1}\right\rangle \equiv |HG_{10}\rangle + i\,|HG_{01}\rangle$ after passing through the compressor, so that the heralded single-photon mode function at Sagnac output port B is both polarization entangled and in a well-defined first-order spatial mode:

$$|\psi_B\rangle = \left|LG_0^{+1}\right\rangle \otimes \Big(|H\rangle |V\rangle + |V\rangle |H\rangle \Big) \tag{4.15}$$

We note that to cover the entire Poincaré sphere of first-order transverse spatial modes [25], two such successive compressors are needed with different orientations, and with one

applying twice the amount of pressure as the other, in analogy with the requirement of a half-wave plate followed by a quarter-wave plate in order to turn linearly polarized light into light of an arbitrary polarization state. Also, the fiber compressor as shown in Fig. 4.8(b) can be used in conjunction with the setup in Fig. 4.8(a) in order to produce, for example, LG-entangled bell states. Finally, we note that the above states can also be created by pumping the crystal with the appropriate higher order mode as opposed to using fiber compressors after the fact, since our Sorter can filter our any unwanted contributions to the biphoton mode function. However, in many cases, pumping the crystal with a Gaussian mode is preferable as it can result in more efficient production of the desired mode.

CHAPTER V

SPIN-ORBIT INTERACTION FOR ELECTRONS AND PHOTONS

Introduction

As discussed in Chapter II, when an electromagnetic wave propagates in an inhomogeneous medium along a well-defined curvilinear trajectory, the evolution of its polarization state is dependent upon the path taken by the particle. This phenomenon, which was first predicted by Bortolotti [66] and explicitly calculated by Rytov [30, 67] for waves *without* orbital angular momentum (OAM), is characterized by our equation (2.48d) in Chapter II with $m_\ell = 0$ and $\lambda = 1$:

$$\Phi_B = -\sigma\Omega. \tag{5.1}$$

In (5.1), Φ_B is the (geometric) phase accumulated by a wave with well-defined helicity, $\sigma = \pm 1$ is the spin angular momentum (SAM) quantum number (representing left or right circular polarization), and Ω is the solid angle subtended by the momentum-space loop defined by the trajectory. (5.1) was first derived by Vladimirsky [68] shortly after Rytov's work. Over forty years later, prompted by the work of Berry on the general problem of geometric phase in adiabatic quantum systems [29, 69], Chiao and Wu proposed an experiment to measure

this effect of the trajectory on the polarization [70], which was subsequently carried out by Tomita and Chiao [71].

The pioneering work of Berry and the experimental confirmation of Tomita and Chiao ushered in an explosion of interest in the geometric phase. Less that a year after the experimental work, Białynicki-Birula and Białynicka-Birula extended the result (5.1) to any particle with spin propagating along a well-defined curvilinear trajectory (again without OAM) [28], resulting in the expression

$$\Phi_B = -\lambda\sigma\Omega, \tag{5.2}$$

where λ is the absolute magnitude of the particle helicity such that $\lambda = \dfrac{1}{2}$ for electrons and $\lambda = 1$ for photons ((5.2), of course, is also a special case of our equation (2.48d), with $m_\ell = 0$). That same year, Kitano, Yabuzaki, and Ogawa pointed out that geometric phase manifests itself as a transverse image rotation for a light beam undergoing out-of-plane mirror reflections [57]. This image rotation effect was subsequently studied more rigorously by Segev, Solomon, and Yariv [58], and was connected with the Poincaré sphere formalism by Galvez and Holmes [56], who also demonstrated for the first time that both the polarization and image of the light beam are rotated through the same transverse angle by any sequence of out-of-plane mirror reflections (see also [55]). This equivalence of the polarization and image rotation for light induced by the geometric phase is implicit in our fundamental equation (2.48d) for $\lambda = 1$,

$$\Phi_B = -\left(\sigma + m_\ell\right)\Omega, \tag{5.3}$$

as we showed in Chapter III (see (3.52)). Perhaps surprisingly, the connection between the geometric phase, OAM, and transverse image rotation for light was not explicitly pointed out until a few years ago by Bliokh [43], although the fact that an azimuthal rotation of an LG_p^ℓ mode through an angle Ω is equivalent to multiplication by a phase factor $e^{-im_\ell\Omega}$ was known previously [59].

Each of the aforementioned developments share a common characteristic: a particle traveling along a *curvilinear* trajectory will accumulate a geometric phase proportional to the solid angle Ω subtended by the trajectory in momentum space. However, Liberman and Zel'dovich have shown that σ and m_ℓ-dependent phase shifts reminiscent of those given in (5.3) still occur for photons propagating along a *straight* trajectory provided that the propagation medium remains inhomogeneous, as is that case in a straight optical fiber [62]. They were also the first to propose both of these distinct phase shifts as the consequence of a spin-orbit interaction (SOI) for photons (Dooghin et al. simultaneously provided the first experimental evidence for this effect [72]). Subsequently to this, several authors have further examined the connection between the geometric phase and the SOI for both electrons and photons, cf. [41–44, 73–83] and references therein. However, the majority of these studies are limited to transversely localized beams traveling along either a curved or refracted trajectory, and study the equations of motion in the semiclassical "ray" picture (the exceptions to this are [62, 73, 74], which however considered photons only). Because of this, a unified treatment

of the spin-orbit interaction for electrons and photons in the "wave function" picture, in which the full wave nature of each particle is taken into account, has not previously been given.

In this Chapter we provide such a treatment, studying the dynamics of the SOI from within a unified framework. We restrict our analysis to particle propagation in a straight cylindrically symmetric waveguide, solving both the Dirac and Maxwell equations perturbatively for this geometry. Remarkably, we find in this case that the SOI is quantitatively described by a single expression applying to either an electron or a photon. This leads to the prediction of several rotational effects for both particle types, in which the particle's spin and orbital degrees of freedom influence one another as it propagates down the waveguide. Because previous studies have been predominantly restricted to the semicalssical "ray" picture, a majority of the aforementioned rotational effects, which can be described only via the wave-function picture, were missed until our recent work on the subject [84]. As we will show, these phenomena allow for the reversible transfer of entanglement between the SAM and OAM degrees of freedom of two-particle states. The common origin of these effects in electrons and photons is a universal geometric phase associated with the interplay between either particle's spin and OAM. This implies that the SOI occurs for any particle with spin, and thereby exists independently of whether or not the particle has mass, charge, or magnetic moment.

Spin-Orbit Wave Equations

For each particle, we begin with its appropriate wave equation— i.e., the Dirac equation for electrons and Maxwell's equations for photons (Maxwell's equations are equivalent to the photon wave equation as we showed in Appendix A). From this starting point, we then show that the particle wave equation for a monoenergetic paraxial electron (photon) propagating in an inhomogeneous, cylidrically symmetric potential (permittivity) may be expressed in the form of a Schrödinger-type equation with a perturbation,

$$\hat{H}_0 \Psi_\omega + \hat{H}' \Psi_\omega = \beta^2 \Psi_\omega, \tag{5.4}$$

where Ψ_ω is the particle wave function (which has energy $\hbar\omega$), $\hat{H}_0$ is an exactly solvable portion of the Hamiltonian, $\hat{H}'$ is a small perturbation, and β is the propagation constant such that the z-dependence of the state is $\Psi_\omega \propto e^{i\beta z}$.

Electron Case

It is instructive to approach the problem of the electron spin-orbit interaction from the viewpoint of the Foldy-Wouthuysen representation of the Dirac equation, wherein the Dirac Hamiltonian has the general property that the positive energy solutions are decoupled from the negative energy solutions, so that we can describe the electron via a two-component spinor. Consider an electron with charge $-e$ moving in the presence of an electromagnetic field of nonrelativistic energy, with electric and magnetic fields $\mathbf{E}$ and $\mathbf{B}$ and scalar and vector potentials V and $\mathbf{A}$, respectively. In the presence of these fields and the corresponding

potentials, to order $\left(\frac{v}{c}\right)^4$, the Dirac Hamiltonian in the Foldy-Wouthuysen representation takes the form [85]

$$\hat{H}_\Phi = mc^2 + \frac{1}{2m}\left(\hat{\mathbf{p}} - \frac{e}{c}\mathbf{A}\right)^2 - eV - \left\{\frac{1}{2mc^2}\left(\frac{\hat{\mathbf{p}}^2}{2m}\right)^2 - \frac{e\hbar^2}{8m^2c^2}\nabla\cdot\mathbf{E}\right.$$
$$\left. -\frac{ie\hbar}{4m^2c^2}\hat{\mathbf{S}}\cdot(\nabla\times\mathbf{E}) - \frac{e}{2m^2c^2}\hat{\mathbf{S}}\cdot(\mathbf{E}\times\hat{\mathbf{p}}) + \frac{e}{mc}\hat{\mathbf{S}}\cdot\mathbf{B}\right\}$$

$$(5.5)$$

where $\hat{\mathbf{S}} \equiv \frac{\hbar}{2}\hat{\sigma}$ is the spin vector operator of 2×2 Pauli matrices, and Gaussian units have been employed. The equation $\hat{H}_\Phi\left|\Psi\right\rangle = E\left|\Psi\right\rangle$ (or equivalently $\hat{H}_\Phi\left|\Psi\right\rangle = \hbar\omega\left|\Psi\right\rangle$) contains all of the information of the Dirac equation (subject to the aforementioned constraints), and is therefore the correct wave equation for the electron. Note that we have not yet assumed anything about cylindrical symmetry and/or the specific form of the electromagnetic fields; this Hamiltonian is still quite general. We now make the assumption that the electromagnetic field is electrostatic in the laboratory frame, and assume also that the electron is traveling at a nonrelativistic speed with respect to the laboratory frame. Under these assumptions, we may take $\mathbf{B}$ and $\mathbf{A}$ equal to zero, and $\nabla\times\mathbf{E}=0$, so that after multiplying both sides by the quantity $\frac{2m}{\hbar^2}$, (5.5) becomes

$$\hat{H} \equiv \frac{2m}{\hbar^2}\hat{H}_\Phi = -\nabla^2 - \frac{2m}{\hbar^2}eV - \left\{\hat{H}_{\text{Rel}} + \hat{H}_{\text{Dar}} + \hat{H}_{\text{SO}}\right\} \tag{5.6}$$

where $\hat{H}_{\text{Rel}} = \frac{\hbar^2}{c^2}\left(\frac{\nabla^2}{2m}\right)^2$, $\hat{H}_{\text{Dar}} = -\frac{e}{4mc^2}\nabla\cdot\mathbf{E}$, and $\hat{H}_{\text{SO}} = -\frac{e}{\hbar^2 mc^2}\hat{\mathbf{S}}\cdot(\mathbf{E}\times\hat{\mathbf{p}})$, and where $\hat{\mathbf{p}} = -i\hbar\nabla$ has been used, while the constant rest mass term mc^2 has also been dropped.

Note that the first term in the curly brackets arises from the relativistic mass increase, and is independent of the form of the electric field. In the canonical case of a spherically symmetric Coulomb field (hydrogen atom), $V = \dfrac{1}{r}$ and $\mathbf{E} = -\nabla V = \dfrac{\hat{\mathbf{r}}}{r^2}$, so that the second term is known as the Darwin term, while the last term gives rise to the atomic spin-orbit interaction. Together these three terms account for all of the spectral phenomena of the hydrogen atom to order $\left(\dfrac{v}{c}\right)^4$. The spin-spin interaction between the spin magnetic moments of the proton and electron and the quantum electrodynamic Lamb shift, which are both higher order effects, are the only well-known atomic interactions for hydrogen not described by the Hamiltonian in (5.5).

Up to this point, we have yet to specify anything about $\mathbf{E}$. However, we now assume a translationally invariant (in the z direction), cylindrically symmetric potential $V(\rho)$, so that $\mathbf{E} = -\nabla V(\rho) = -\partial_\rho V(\rho)\,\hat{\rho} = -\dfrac{1}{\rho}\partial_\rho V(\rho)\,\vec{\rho}$. Given this, $\hat{H}_{\mathrm{Dar}}$ becomes

$$\hat{H}_{\mathrm{Dar}} = \frac{e}{4mc^2}\nabla^2 V(\rho) = \frac{e}{4mc^2}\left(\partial_\rho + \frac{1}{\rho}\right)(\partial_\rho V(\rho)) \tag{5.7a}$$

$$= \frac{e}{4mc^2}\left((\partial_\rho^2 V(\rho)) + (\partial_\rho V(\rho))\,\partial_\rho + \frac{1}{\rho}(\partial_\rho V(\rho))\right) \tag{5.7b}$$

where (5.7b) follows from (5.7a) since the partial derivative acts as an operator quantity, while $\hat{H}_{\mathrm{SO}}$ becomes

$$\hat{H}_{\mathrm{SO}} = \frac{e}{\hbar^2 mc^2}\frac{1}{\rho}(\partial_\rho V(\rho))\,\hat{\mathbf{S}} \cdot (\vec{\rho} \times \hat{\mathbf{p}}) \tag{5.8}$$

and $\hat{H}_{\text{Rel}}$ is unchanged. We note here that for a spherically symmetric atomic potential this spin-orbit term has the same form, but with the replacement $\rho \to r$.

The Hamiltonian $\hat{H} \equiv \dfrac{2m}{\hbar^2} \hat{H}_\Phi$ in (5.6) obeys the wave equation

$$\hat{H}\Psi = \frac{2m}{\hbar^2} E\Psi, \tag{5.9}$$

which may be more explicitly written as

$$\left(\hat{\nabla}_T^2 + k^2\left(\rho\right) \right) \Psi + \left\{ \hat{H}_{\text{Rel}} + \hat{H}_{\text{Dar}} + \hat{H}_{\text{SO}} \right\} \Psi = -\partial_z^2 \Psi. \tag{5.10}$$

where $k^2\left(\rho\right) \equiv \dfrac{2m}{\hbar^2}\left(E + eV\left(\rho\right)\right)$, and the operator ∇^2 has been decomposed into its transverse and longitudinal parts ∇_T^2 and $\partial_z{}^2$ in light of the cylindrical symmetry of the potential. Because of this translational invariance in z, for a given energy $E_0 = \hbar\omega_0$ the solutions to the full wave equation (5.10) must take the form $\Psi = \Psi\left(\rho, \phi\right) e^{i\left(\beta z - \frac{E_0}{\hbar}t\right)}$. Substituting this form into (5.10) then yields

$$\left[\nabla_T^2 + k^2\left(\rho\right) \right] \Psi + \left\{ \hat{H}_{\text{Rel}} + \hat{H}_{\text{Dar}} + \hat{H}_{\text{SO}} \right\} \Psi = \beta^2 \Psi, \tag{5.11}$$

which is an eigenvalue equation for β^2.

We would like to treat the terms in curly brackets as a perturbation of the unperturbed problem

$$\hat{H}_0 \Psi_0 = \beta_0^2 \Psi_0, \tag{5.12}$$

where $\hat{H}_0 \equiv \left(\nabla_T^2 + k^2\left(\rho\right)\right)$. The general solutions to this unperturbed, separable, "transverse Pauli equation" take the general form

$$\Psi_0 = N_{|m_\ell|}\psi_{|m_\ell|}\left(\rho\right)e^{im_\ell\phi}\hat{\mathbf{e}}_\sigma e^{i\left(\beta_0 z - \frac{E_0}{\hbar}t\right)} \equiv |m_\ell\,\sigma\rangle \tag{5.13}$$

where N is a normalization constant, $\psi_{|m_\ell|}\left(\rho\right)$ is a radial wave function determined by $k\left(\rho\right)$, and $\hat{\mathbf{e}}_\sigma \equiv \begin{pmatrix} \delta_{\sigma+} \\ \delta_{\sigma-} \end{pmatrix}$ is a two component spinor composed of Kronecker delta functions such that $\delta_{\sigma+} = 1$ if $\sigma = +1$ and $\delta_{\sigma+} = 0$ if $\sigma = -1$, etc. In expressing these wave functions, we have chosen the following complete set of commuting operators, $\{\hat{E}_0 \equiv i\hbar\partial_t,\ \hat{p}_z \equiv -i\hbar\partial_z,\ \hat{L}_z \equiv -i\hbar\partial_\phi,\ \hat{S}_z \equiv \frac{\hbar}{2}\hat{\sigma}_z\}$, which have the following respective eigenvalues, $\{\hbar\omega_0,\ \hbar\beta_0,\ \hbar m_\ell,\ \frac{\hbar}{2}\sigma\}$.

We now express the potential $V\left(\rho\right)$ in terms of a normalized potential energy $U\left(\rho\right) \equiv \dfrac{-eV\left(\rho\right)}{mc^2}$, so that without loss of generality we may write $U\left(\rho\right) = \dfrac{-eV\left(0\right)}{mc^2} + \Delta\chi\left(\rho\right)$, where $\Delta \equiv -\left(U\left(0\right) - U\left(a\right)\right) = \dfrac{eV\left(0\right) - eV\left(a\right)}{mc^2}$ and a is the effective radius of the potential. In order to guarantee transversely bound states, we assume that $V\left(\rho\right)$ is a monotonically decreasing function that becomes constant for $\rho \geq a$, such that $\chi\left(\rho\right)$ is zero at the origin and increases monotonically to one at radius a, becoming constant thereafter. This results in the perturbative terms $\hat{H}_{\text{Dar}}$ and $\hat{H}_{\text{SO}}$ taking the respective forms

$$\hat{H}_{\text{Dar}} = -\frac{\Delta}{4}\left(\left(\partial_\rho^2\chi\left(\rho\right)\right) + \left(\partial_\rho\chi\left(\rho\right)\right)\partial_\rho + \frac{1}{\rho}\left(\partial_\rho\chi\left(\rho\right)\right)\right), \tag{5.14}$$

and

$$\hat{H}_{\text{SO}} = -\frac{\Delta}{\rho} \left(\partial_\rho \chi \left(\rho \right) \right) \frac{1}{\hbar^2} \hat{\mathbf{S}} \cdot \left(\vec{\rho} \times \hat{\mathbf{p}} \right). \tag{5.15}$$

We now focus on the "vectorial" portion of $\hat{H}_{\text{SO}}$, namely the quantity $\hat{\mathbf{S}} \cdot \left(\vec{\rho} \times \hat{\mathbf{p}} \right) = \hat{\mathbf{S}} \cdot \left[\left(x\hat{\mathbf{x}} + y\hat{\mathbf{y}} \right) \times \hat{\mathbf{p}} \right]$. Since carrying out this the cross product $\left(x\hat{\mathbf{x}} + y\hat{\mathbf{y}} \right) \times \hat{\mathbf{p}}$ explicitly yields $\left(y\hat{\mathbf{x}} - x\hat{\mathbf{y}} \right) \hat{p}_z + \left(x\hat{p}_y - y\hat{p}_x \right) \hat{\mathbf{z}} = \left(y\hat{\mathbf{x}} - x\hat{\mathbf{y}} \right) \hat{p}_z + L_z \hat{\mathbf{z}}$, after the dot product with the spin vector we have

$$\hat{\mathbf{S}} \cdot \left(\vec{\rho} \times \hat{\mathbf{p}} \right) = \hat{S}_z \hat{L}_z + \left(y\hat{S}_x - x\hat{S}_y \right) \hat{p}_z, \tag{5.16a}$$

$$= \frac{\hbar^2}{2} \left(\hat{\sigma}_z \hat{\ell}_z - i\rho \left(\sin\phi \, \hat{\sigma}_x - \cos\phi \, \hat{\sigma}_y \right) \partial_z \right), \tag{5.16b}$$

where the cylindrical coordinate definitions $x = \rho \cos\phi$ and $y = \rho \sin\phi$ have been used in the last line, along with the dimensionless orbital angular momentum operator $\hat{\ell}_z \equiv \frac{\hat{L}_z}{\hbar}$. In matrix form then, (5.15) and (5.16) give

$$\hat{H}_{\text{SO}} = -\frac{\Delta}{2} \frac{1}{\rho} \left(\partial_\rho \chi \left(\rho \right) \right) \begin{pmatrix} \hat{\ell}_z & \rho e^{-i\phi} \partial_z \\ -\rho e^{i\phi} \partial_z & -\hat{\ell}_z \end{pmatrix}. \tag{5.17}$$

Furthermore, note that the matrix in (5.17) may be decomposed in the following way,

$$\begin{pmatrix} \hat{\ell}_z & \rho e^{-i\phi} \partial_z \\ -\rho e^{i\phi} \partial_z & -\hat{\ell}_z \end{pmatrix} = \begin{pmatrix} \hat{\ell}_z & 0 \\ 0 & -\hat{\ell}_z \end{pmatrix} + \rho \left[\begin{pmatrix} 0 & e^{-i\phi} \\ 0 & 0 \end{pmatrix} - \begin{pmatrix} 0 & 0 \\ e^{+i\phi} & 0 \end{pmatrix} \right] \partial_z, \tag{5.18a}$$

$$\equiv \hat{\sigma}_z \hat{\ell}_z + \rho \left[\quad \hat{\sigma}_+ \hat{\ell}_- \quad - \quad \hat{\sigma}_- \hat{\ell}_+ \quad \right] \partial_z, \tag{5.18b}$$

where $\hat{\ell}_\pm$ and $\hat{\sigma}_\pm$ are the respective raising and lowering operators for the electronic states $|m_\ell\, \sigma\rangle$, which have well-defined values for spin and orbital angular momentum, such that

$$\hat{\sigma}_\pm \hat{\ell}_\mp |m_\ell\, \mp\rangle = |m_\ell \mp 1\ \pm\rangle, \tag{5.19a}$$

$$\hat{\sigma}_\pm \hat{\ell}_\mp |m_\ell\, \pm\rangle = 0. \tag{5.19b}$$

It is most convenient to express $\hat{H}_{\text{SO}}$ in terms of these operators:

$$\hat{H}_{\text{SO}} = -\frac{\Delta}{2}\frac{1}{\rho}\left(\partial_\rho \chi\left(\rho\right)\right)\left(\hat{\sigma}_z \hat{\ell}_z + \rho\left(\hat{\sigma}_+ \hat{\ell}_- - \hat{\sigma}_- \hat{\ell}_+\right)\partial_z\right). \tag{5.20}$$

We stress here that (5.11) with $\hat{H}_{\text{Rel}} = \frac{\hbar^2}{c^2}\left(\frac{\nabla^2}{2m}\right)^2$ and $\hat{H}_{\text{Dar}}$ and $\hat{H}_{\text{SO}}$ given by (5.14) and (5.18b) is completely equivalent to (5.5) with a cylindrically symmetric electrostatic potential $v\left(\rho\right)$, so that in this sense (5.11) is "exact" (to order $\left(\frac{v}{c}\right)^4$). Furthermore, for a sufficiently weakly varying potential $V\left(\rho\right)$, we have $\Delta \ll 1$, so that $\hat{H}' \equiv \left\{\hat{H}_{\text{Rel}} + \hat{H}_{\text{Dar}} + \hat{H}_{\text{SO}}\right\}$ may be treated as a small perturbation to the unperturbed Hamiltonian $\hat{H}_0$ in (5.12). In this case, the wave equation (5.11) assumes the form (5.4) of a Schrödinger-type equation with a perturbation, as discussed at the beginning of this section.

Photon Case

We now consider a paraxial photon propagating in a non-magnetic transparent medium with constant permeability μ_0 and spatially inhomogeneous permitivity $\epsilon\left(\mathbf{r}\right)$. For monoenergetic fields $\mathbf{E}\left(\mathbf{r}, t\right) = \mathbf{E}\left(\mathbf{r}\right)e^{-i\omega t}$, $\mathbf{H}\left(\mathbf{r}, t\right) = \mathbf{H}\left(\mathbf{r}\right)e^{-i\omega t}$, $\mathbf{D}\left(\mathbf{r}, t\right) = \epsilon\left(\mathbf{r}\right)\mathbf{E}\left(\mathbf{r}, t\right)$, and $\mathbf{B}\left(\mathbf{r}, t\right) = \mu_0 \mathbf{H}\left(\mathbf{r}, t\right)$, Maxwell's equations take the well-known form [60]

$$\nabla \cdot \mathbf{D} = 0 \quad \Rightarrow \quad \epsilon\left(\mathbf{r}\right) \nabla \cdot \mathbf{E} + \nabla \epsilon\left(\mathbf{r}\right) \cdot \mathbf{E} = 0, \tag{5.21a}$$

$$\nabla \cdot \mathbf{B} = 0 \quad \Rightarrow \quad \nabla \cdot \mathbf{H} = 0, \tag{5.21b}$$

$$\nabla \times \mathbf{E} = -\partial_t \mathbf{B} \quad \Rightarrow \quad \nabla \times \mathbf{E} = i\omega\mu_0 \mathbf{H}, \tag{5.21c}$$

$$\nabla \times \mathbf{H} = \partial_t \mathbf{D} \quad \Rightarrow \quad \nabla \times \mathbf{H} = -i\omega\epsilon\left(\mathbf{r}\right)\mathbf{E}, \tag{5.21d}$$

where the identity $\nabla \cdot \epsilon\left(\mathbf{r}\right)\mathbf{E} = \epsilon\left(\mathbf{r}\right) \nabla \cdot \mathbf{E} + \nabla \epsilon\left(\mathbf{r}\right) \cdot \mathbf{E}$ has been used in 5.21a. In order to obtain an uncoupled Helmholtz-like equation for $\mathbf{E}$, we follow [63] and take the curl of both sides of (5.21c) while using the vector identity $\nabla \times \nabla \times \mathbf{E} = \nabla\left(\nabla \cdot \mathbf{E}\right) - \nabla^2 \mathbf{E}$, substituting for $\nabla \times \mathbf{H}$ using (5.21d), and employing $\nabla \cdot \mathbf{E} = -\dfrac{1}{\epsilon\left(\mathbf{r}\right)}\nabla \epsilon\left(\mathbf{r}\right) \cdot \mathbf{E} = -\nabla \ln \epsilon\left(\mathbf{r}\right) \cdot \mathbf{E}$ using (5.21a), which yields

$$\nabla^2 \mathbf{E} + \omega^2 \epsilon\left(\mathbf{r}\right) \mu_0 \mathbf{E} = -\nabla\left[\nabla \ln \epsilon\left(\mathbf{r}\right) \cdot \mathbf{E}\right]. \tag{5.22}$$

By a similar calculation [63], one may also obtain a second-order equation for $\mathbf{H}$: take the curl of (5.21d), use the vector identity $\nabla \times \epsilon\left(\mathbf{r}\right)\mathbf{E} = \epsilon\left(\mathbf{r}\right) \nabla \times \mathbf{E} + \nabla \epsilon\left(\mathbf{r}\right) \times \mathbf{E}$, and substitute for $\nabla \times \mathbf{E}$ using (5.21c) and $\nabla \cdot \mathbf{H}$ using (5.21d), which yields

$$\nabla^2 \mathbf{H} + \omega^2 \epsilon\left(\mathbf{r}\right) \mu_0 \mathbf{H} = i\omega\left[\nabla \epsilon\left(\mathbf{r}\right) \times \mathbf{E}\right]. \tag{5.23}$$

We will henceforth focus on equation (5.22), for which the electric field $\mathbf{E}$ and magnetic field $\mathbf{H}$ are uncoupled, since $\mathbf{H}$ may be determined through (5.23) once $\mathbf{E}$ is known.

Specializing now to the case of a cylindrically symmetric medium, we employ cylindrical coordinates (ρ, ϕ, z), while constraining the permitivity $\epsilon(\mathbf{r}) \to \epsilon(\rho)$ to be a function of ρ only and therefore translationally invariant with respect to the z axis. Imposing this condition along with the monoenergetic field assumption constrains the z and t dependence of the fields such that $\mathbf{E}$ assumes traveling wave form

$$\mathbf{E} = \left[\mathbf{E}_T(\rho, \phi) + E_z(\rho, \phi)\,\hat{\mathbf{z}}\right] e^{i(\beta z - \omega t)}. \tag{5.24}$$

where we have also split $\mathbf{E}$ up into transverse and longitudinal parts $\mathbf{E}_T(\rho, \phi)$ and $E_z(\rho, \phi)\,\hat{\mathbf{z}}$ in order to exploit the cylindrical symmetry of the medium. Inserting (5.24) into (5.22) then yields the following two equations involving the transverse and longitudinal fields [63],

$$\left[\nabla_T^2 - \beta^2 + \omega^2 \epsilon(\rho)\,\mu_0\right] \mathbf{E}_T = -\nabla_T\left[\nabla_T \ln \epsilon(\rho) \cdot \mathbf{E}_T\right], \tag{5.25a}$$

$$\left[\nabla_T^2 - \beta^2 + \omega^2 \epsilon(\rho)\,\mu_0\right] E_z = -i\beta\left[\nabla_T \ln \epsilon(\rho) \cdot \mathbf{E}_T\right], \tag{5.25b}$$

where the relation $\nabla\left[\nabla \ln \epsilon(\rho) \cdot \mathbf{E}(\rho, \phi)\right] = \nabla_T\left[\nabla_T \ln \epsilon(\rho) \cdot \mathbf{E}\right] = \nabla_T\left[\nabla_T \ln \epsilon(\rho) \cdot \mathbf{E}_T\right] + i\beta\left[\nabla_T \ln \epsilon(\rho) \cdot \mathbf{E}_T\right]$ has been used, with $\nabla_T \equiv \nabla - \partial_z \hat{\mathbf{z}}$ and $\nabla_T^2 \equiv \nabla^2 - \partial_z^2$.

Note that the exact equation (5.25a) involves $\mathbf{E}_T$ alone, while in (5.25b) $\mathbf{E}_T$ and E_z are coupled. (5.25a) may therefore be used to generate complete and exact solutions to Maxwell's equations, since a solution of (5.25a) for the transverse field $\mathbf{E}_T$ may be substituted into (5.25b) to generate the complete filed $\mathbf{E}$, which may then be substituted into (5.23) to

generate $\mathbf{H}$. In this way, the problem of finding the electromagnetic fields $\mathbf{E}$ and $\mathbf{H}$ is reduced to solving (5.25a) for the transverse electric field.

Since Maxwell's equations constitute the proper wave equation for the photon [26, 27], we now replace the transverse field vector $\mathbf{E}_T$ with the suggestive wave function notation Ψ, while defining $k^2(\rho) \equiv \omega^2 \epsilon(\rho) \mu_0$ and $\hat{H}'\Psi \equiv \nabla_T [\nabla_T \ln \epsilon(\rho) \cdot \mathbf{E}_T]$, thereby arriving at a compact expression for (5.25a) in the form of a two-component Schrödinger-type equation:

$$\left[\nabla_T^2 + k^2(\rho)\right]\Psi + \hat{H}'\Psi = \beta^2 \Psi. \tag{5.26}$$

This eigenvalue equation for β is similar in form to the analogous electron equation (5.11).

Similarly to the electron case, we would like to treat the $\hat{H}'$ term as a perturbation of the unperturbed problem

$$\hat{H}_0 \Psi_0 = \beta_0^2 \Psi_0, \tag{5.27}$$

where $\hat{H}_0 \equiv \left(\hat{\nabla}_T^2 + k^2(\rho)\right)$. The general solutions to this unperturbed, separable equation take a general form similar to (5.13)

$$\Psi_0 = N_{|m_\ell|}\psi_{|m_\ell|}(\rho) e^{im_\ell \phi}\hat{\mathbf{e}}_\sigma e^{i(\beta_0 z - \omega t)} \equiv |m_\ell \, \sigma\rangle. \tag{5.28}$$

However, for the photon case $\hat{\mathbf{e}}_\sigma \equiv \dfrac{1}{\sqrt{2}}(\hat{\mathbf{x}} + i\sigma\hat{\mathbf{y}})$ is a unit vector denoting the photon's circular polarization (helicity) state with respect to the z axis, as determined by the SAM quantum number $\sigma = \pm 1$.

It is worth noting here that although (5.26) generates complete and exact solutions to Maxwell's equations for an inhomogeneous permitivity $\epsilon(\rho)$, for the limiting special case of a *homogeneous* permitivity, $\epsilon(\rho) \to \epsilon$, this statement no longer holds. This deficiency stems from (5.22) and (5.23), from which (5.26) was derived. These equations, which become the homogeneous vector Helmholtz equations under the replacement $\epsilon(\mathbf{r}) \to \epsilon$, are still necessary but are no longer sufficient conditions for the fields $\mathbf{E}$ and $\mathbf{H}$ to be solutions to Maxwell's equations (5.21), as is well known. In order to obtain a complete description of the solutions to Maxwell's equations in this homogeneous limit we must therefore use an alternative approach.

In Appendix A, we develop this alternative treatment for free-space fields by applying (5.21) to the solutions of the homogeneous vector Helmholtz equations, (i.e., (5.22) and (5.23) with the terms containing a permitivity gradient $\nabla \ln \epsilon(\mathbf{r})$ set to zero). Armed with the proper free-space solutions for the monoenergetic fields, we then define and employ the paraxial limit, which has not been assumed up to this point so that the above equations (5.22)–(5.26) apply even to *non*-paraxial monoenergetic fields. We find that for beams propagating paraxially in free space, Maxwell's equations (5.21) may be reduced to a single equation for the transverse electric field (see (A.24)),

$$\left[\nabla_T^2 + k^2\right] \mathbf{E}_T = \beta^2 \mathbf{E}_T, \tag{5.29a}$$

$$\Leftrightarrow \hat{H}_0 \Psi = \beta^2 \Psi, \tag{5.29b}$$

where $k^2 \equiv \omega^2 \epsilon \mu_0$, and the photon wave function notation has been used in (5.29b). Since

(5.26) reduces to (5.29b) in the free-space limit where $\hat{H}' \Psi_\omega \to 0$ and $k(\rho) \to k$, we conclude that (5.26) does indeed provide a complete description of the free-space electromagnetic field in the paraxial limit.

Our present goal is to express $\hat{H}'$ of (5.26) in such a way that the photonic spin-orbit interaction is manifest. With this in view, we note that $\nabla_T \ln \epsilon(\rho) = \partial_\rho \ln \epsilon(\rho) \hat{\rho}$ so that $\hat{H}'$ simplifies to

$$\nabla_T [\nabla_T \ln \epsilon(\rho) \cdot \mathbf{E}_T] = \nabla_T [f(\rho) E_\rho]$$

$$= [(\nabla_T f(\rho)) + f(\rho) \nabla_T] E_\rho$$

$$= (\nabla_T f(\rho)) E_\rho + f(\rho) \nabla_T E_\rho \qquad (5.30)$$

where $f(\rho) \equiv \partial_\rho \ln \epsilon(\rho)$, and where $E_\rho(\rho, \phi) \equiv \mathbf{E}_T \cdot \hat{\rho}$ is the radial component of the field. In the circularly polarized basis, we have the results $\nabla_T = \hat{\mathbf{e}}_+ \nabla_+ + \hat{\mathbf{e}}_- \nabla_-$ with $\nabla_\pm \equiv \frac{1}{\sqrt{2}} e^{\mp i\phi} \left(\partial_\rho \mp \frac{i}{\rho} \partial_\phi \right)$, and $E_\rho = \frac{1}{\sqrt{2}} \left(e^{+i\phi} E_+ + e^{-i\phi} E_- \right)$ with $E_\pm \equiv \mathbf{E} \cdot \hat{\mathbf{e}}_\pm^*$. Substituting these relations into the right-hand side of (5.30), using $\nabla_\pm f(\rho) = \frac{1}{\sqrt{2}} e^{\mp i\phi} (\partial_\rho f(\rho))$, and employing the column vector notation $\mathbf{E}_T = E_+ \hat{\mathbf{e}}_+ + E_- \hat{\mathbf{e}}_- \equiv \begin{pmatrix} E_+ \\ E_- \end{pmatrix}$ readily yields the first line of the following succession of expressions:

$$\hat{H}'\mathbf{E}_T =$$

$$\frac{1}{2}\left[\begin{array}{cc} (\partial_\rho f) + fe^{-i\phi}\left(\partial_\rho - \dfrac{i}{\rho}\partial_\phi\right)e^{+i\phi} & (\partial_\rho f)\,e^{-2i\phi} + fe^{-i\phi}\left(\partial_\rho - \dfrac{i}{\rho}\partial_\phi\right)e^{-i\phi} \\ (\partial_\rho f)\,e^{+2i\phi} + fe^{+i\phi}\left(\partial_\rho + \dfrac{i}{\rho}\partial_\phi\right)e^{+i\phi} & (\partial_\rho f) + fe^{+i\phi}\left(\partial_\rho + \dfrac{i}{\rho}\partial_\phi\right)e^{-i\phi} \end{array}\right]\left(\begin{array}{c} E_+ \\ E_- \end{array}\right) \tag{5.31a}$$

$$=\left[\begin{array}{cc} \hat{g} + he^{-i\phi}\hat{\ell}_z e^{+i\phi} & \hat{g}e^{-2i\phi} + he^{-i\phi}\hat{\ell}_z e^{-i\phi} \\ \hat{g}e^{+2i\phi} - he^{+i\phi}\hat{\ell}_z e^{+i\phi} & \hat{g} - he^{+i\phi}\hat{\ell}_z e^{-i\phi} \end{array}\right]\left(\begin{array}{c} E_+ \\ E_- \end{array}\right) \tag{5.31b}$$

$$=\left\{\left[\hat{g} + h\hat{\sigma}_z\mathbf{Q}\hat{\ell}_z\mathbf{Q}\right] + \left[\hat{g}\mathbf{N} + h\hat{\sigma}_z\mathbf{Q}\hat{\sigma}_x\hat{\ell}_z\mathbf{Q}\right]\right\}\left(\begin{array}{c} E_+ \\ E_- \end{array}\right) \tag{5.31c}$$

$$=\left\{\left[\hat{g}_+ + h\hat{\sigma}_z\hat{\ell}_z\right] + \left[\hat{g}_+ + h\hat{\sigma}_z\hat{\ell}_z\right]\mathbf{N}\right\}\left(\begin{array}{c} E_+ \\ E_- \end{array}\right). \tag{5.31d}$$

The spin-orbit interaction is explicitly manifest in the $h\hat{\sigma}_z\hat{\ell}_z$ term of (5.31d); the steps (5.31a)-(5.31c) are presented to clarify its derivation: In (5.31b), we have identified the (dimensionless) OAM z-component operator $(-i\partial_\phi) \equiv \hat{\ell}_z$ in (5.31a) while adopting the shorthand notation

$$\hat{g} \equiv \frac{1}{2}\left[\left(\partial_\rho f\left(\rho\right)\right) + f\left(\rho\right)\partial_\rho\right], \tag{5.32a}$$

$$h \equiv \frac{1}{2}\frac{f\left(\rho\right)}{\rho} \tag{5.32b}$$

where $\hat{g}$ has a "hat" to emphasize its character as a differential operator. In (5.31c), we have

written the resulting expression (5.31b) in terms of the following simple matrix,

$$\mathbf{Q} \equiv \begin{pmatrix} 0 & e^{-i\phi} \\ e^{+i\phi} & 0 \end{pmatrix}, \tag{5.33}$$

with $\hat{\sigma}_x$ and $\hat{\sigma}_z$ being the Pauli matrices, and

$$\mathbf{N} \equiv \mathbf{Q}\hat{\sigma}_x\mathbf{Q} = \begin{pmatrix} 0 & e^{-2i\phi} \\ e^{+2i\phi} & 0 \end{pmatrix}. \tag{5.34}$$

Also in (5.31c), $\hat{H}'$ has been explicitly split up into its diagonal and anti-diagonal parts, so

that the first term in square brackets (which we will denote as $\hat{H}'_\mathrm{D}$) is purely diagonal while,

the second term ($\hat{H}'_\mathrm{AD}$) is anti-diagonal. Finally, in order to make the SOI explicitly manifest

we use the operator identities $\hat{\ell}_z\mathbf{Q} = \mathbf{Q}\hat{\sigma}_z + \mathbf{Q}\hat{\ell}_z$, $\mathbf{Q}^2 = \hat{\sigma}_z^2 = \hat{\sigma}_0$, $\hat{\sigma}_x\hat{\ell}_z = \hat{\ell}_z\hat{\sigma}_x$, $\mathbf{Q}\hat{\sigma}_z = -\hat{\sigma}_z\mathbf{Q}$,

and $\hat{\sigma}_z\mathbf{N} = -\mathbf{N}\hat{\sigma}_z$ in order to simplify the matrix products in the diagonal and anti-diagonal

terms of (5.31c),

$$\hat{\sigma}_z\mathbf{Q}\hat{\ell}_z\mathbf{Q} = \hat{1} + \hat{\sigma}_z\hat{\ell}_z$$

$$\hat{\sigma}_z\mathbf{Q}\hat{\sigma}_x\hat{\ell}_z\mathbf{Q} = \left(\hat{1} + \hat{\sigma}_z\hat{\ell}_z\right)\mathbf{N}. \tag{5.35}$$

Defining $\hat{g}_+ \equiv \hat{g} + h = \frac{1}{2}\left[(\partial_\rho f(\rho)) + f(\rho)\partial_\rho + \frac{f(\rho)}{\rho}\right]$ then yields the final result given in (5.31d).

The perturbation Hamiltonian (5.31d) turns out to have a very similar form as compared to the electron Hamiltonian. To see this, we assume that the permitivity $\epsilon(\rho)$ is a monotonically decreasing function that becomes constant for $\rho \geq a$, where a is again an effective radius. Given these constraints, $\epsilon(\rho)$ can without loss of generality be written in the form

$$\epsilon(\rho) \equiv \epsilon_0 n_0^2\Big(1 - \Delta\chi(\rho)\Big). \tag{5.36}$$

which is similar in form to the normalized potential energy in the electron case. In (5.36), $\Delta \equiv \frac{\epsilon(0) - \epsilon(a)}{\epsilon(0)} = \frac{n_0^2 - n_a^2}{n_0^2}$, where $\epsilon(0) \equiv \epsilon_0 n(0)^2$ and $\epsilon(a) \equiv \epsilon_0 n(a)^2$ are the respective values of the permitivity at $\rho = 0$ and $\rho = a$, with n_0 and n_a denoting the refractive index at those points. Also in (5.36), $\chi(\rho)$ is zero at the origin and increases monotonically to one at radius a, becoming constant thereafter. Using the above form of the permitivity gives

$$f(\rho) \equiv \partial_\rho \ln\epsilon(\rho) = \frac{-\Delta}{1 - \Delta\chi(\rho)}(\partial_\rho\chi(\rho)), \tag{5.37}$$

so that

$$\hat{g}_+ = \frac{-1}{1 - \Delta\chi(\rho)}\frac{\Delta}{2}\left[(\partial_\rho^2\chi(\rho)) + (\partial_\rho\chi(\rho))\partial_\rho + \frac{1}{\rho}(\partial_\rho\chi(\rho)) + \Delta\frac{(\partial_\rho\chi(\rho))^2}{1 - \Delta\chi(\rho)}\right], \tag{5.38}$$

where $(\partial_\rho f(\rho)) = \frac{-1}{1 - \Delta\chi(\rho)}\Delta\left[(\partial_\rho^2\chi(\rho)) + \Delta\frac{(\partial_\rho\chi(\rho))^2}{1 - \Delta\chi(\rho)}\right]$ has been used. Substitution of (5.38) and (5.37) into (5.31d) then yields the following form for the perturbation term $\hat{H}'$:

$$\hat{H}' = \frac{-1}{1 - \Delta\chi(\rho)}\frac{\Delta}{2}$$
$$\times \left[\left(\partial_\rho^2\chi(\rho)\right) + \left(\partial_\rho\chi(\rho)\right)\partial_\rho + \frac{1}{\rho}\left(\partial_\rho\chi(\rho)\right) + \frac{1}{\rho}\left(\partial_\rho\chi(\rho)\right)\hat{\sigma}_z\hat{\ell}_z + \Delta\frac{\left(\partial_\rho\chi(\rho)\right)^2}{1 - \Delta\chi(\rho)} \right](1 + \mathbf{N})$$

$$(5.39a)$$

$$\equiv \hat{H}_{\mathrm{Dar}} + \hat{H}_{\mathrm{SO}} + \hat{H}_\gamma. \tag{5.39b}$$

In (5.39b),

$$\hat{H}_{\mathrm{Dar}} \equiv \frac{-1}{1 - \Delta\chi(\rho)}\frac{\Delta}{2}\left(\left(\partial_\rho^2\chi(\rho)\right) + \left(\partial_\rho\chi(\rho)\right)\partial_\rho + \frac{1}{\rho}\left(\partial_\rho\chi(\rho)\right) \right)(1 + \mathbf{N}) \tag{5.40}$$

is analogous to the Darwin term (5.14) in the electron case, while

$$\hat{H}_{\mathrm{SO}} \equiv \frac{-1}{1 - \Delta\chi(\rho)}\frac{\Delta}{2}\frac{1}{\rho}\left(\partial_\rho\chi(\rho)\right)\hat{\sigma}_z\hat{\ell}_z(1 + \mathbf{N}) \tag{5.41}$$

is analogous to the electronic spin orbit term (5.17), and the final term

$$\hat{H}_\gamma \equiv \frac{-1}{1 - \Delta\chi(\rho)}\frac{\Delta^2}{2}\frac{\left(\partial_\rho\chi(\rho)\right)^2}{1 - \Delta\chi(\rho)}(1 + \mathbf{N}) \tag{5.42}$$

appears only in the photon case.

The portion $\hat{\sigma}_z\hat{\ell}_z(1 + \mathbf{N})$ of the photon spin-orbit Hamiltonian $\hat{H}_{\mathrm{SO}}$ may be decomposed in a form similar to (5.18):

$$
\begin{pmatrix} \hat{\ell}_z & \hat{\ell}_z e^{-2i\phi} \\ -\hat{\ell}_z e^{+2i\phi} & -\hat{\ell}_z \end{pmatrix} = \begin{pmatrix} \hat{\ell}_z & 0 \\ 0 & -\hat{\ell}_z \end{pmatrix} + \hat{\ell}_z \left[\begin{pmatrix} 0 & e^{-2i\phi} \\ 0 & 0 \end{pmatrix} - \begin{pmatrix} 0 & 0 \\ e^{+2i\phi} & 0 \end{pmatrix} \right], \quad (5.43\text{a})
$$

$$
\equiv \quad \hat{\sigma}_z \hat{\ell}_z \quad + \hat{\ell}_z \left[\quad \hat{\sigma}_+^2 \hat{\ell}_-^2 \quad - \quad \hat{\sigma}_-^2 \hat{\ell}_+^2 \quad \right], \quad (5.43\text{b})
$$

where $\hat{\sigma}_\pm^2$ and $\hat{\ell}_\pm^2$ are the respective raising and lowering operators for the *photonic* states $|m_\ell \, \sigma\rangle$, which have well-defined values for the photonic spin and orbital angular momentum such that

$$
\hat{\sigma}_\pm^2 \hat{\ell}_\mp^2 |m_\ell \mp\rangle = |m_\ell \mp 2 \; \pm\rangle, \quad (5.44\text{a})
$$

$$
\hat{\sigma}_\pm^2 \hat{\ell}_\mp^2 |m_\ell \pm\rangle = 0. \quad (5.44\text{b})
$$

(i.e., $\hat{\sigma}_\pm^2$ and $\hat{\ell}_\pm^2$ raise and lower the SAM and OAM by a quantity of $2\hbar$). As in the electron case, it is most convenient to express $\hat{H}_{\text{SO}}$ in terms of these operators:

$$
\hat{H}_{\text{SO}} = \frac{-1}{1 - \Delta\chi(\rho)} \frac{\Delta}{2} \frac{1}{\rho} \left(\partial_\rho \chi(\rho) \right) \left(\hat{\sigma}_z \hat{\ell}_z + \hat{\ell}_z \left(\hat{\sigma}_+^2 \hat{\ell}_-^2 - \hat{\sigma}_-^2 \hat{\ell}_+^2 \right) \right). \quad (5.45)
$$

We stress here that (5.26) with $\hat{H}'$ given by (5.39b) is completely equivalent to Maxwell's equations (5.21) in the sense that (5.26) generates complete and exact solutions to (5.21) with a cylindrically symmetric permitivity $\epsilon(\rho)$. Furthermore, for a sufficiently weakly varying permitivity $\epsilon(\rho)$, we have $\Delta \ll 1$, analogously to the aforementioned case of a weakly varying potential for electrons. In this case we may treat $\hat{H}'$ as a small perturbation to the unperturbed Hamiltonian $\hat{H}_0$ in (5.27), so that the photon wave equation (5.26) assumes the

form (5.4), as is also the case for electrons. Finally, we note that a Hamiltonian reminiscent of (5.39) and including the spin-orbit term $\hat{H}_{\mathrm{SO}}$ has been given previously in [74]. However, in that work the Hamiltonian was only derived in the non-exact, weakly-guiding approximation, with the result that the $\hat{H}_\gamma$ term and the $\dfrac{1}{1 - \Delta\chi(\rho)}$ prefactor in the exact equation (5.39a) are absent in the approximate treatment [74].

<div align="center">Unperturbed Wave Functions</div>

In the last two sections we showed that both the electron and photon wave equations assume the form

$$\left[\nabla_T^2 + k^2(\rho)\right]\Psi + \hat{H}'\Psi = \beta^2\Psi, \tag{5.46}$$

for an electron (photon) propagating in a cylindrically symmetric potential (permitivity), cf. (5.11) and (5.26). The associated unperturbed equation has the form

$$\left[\nabla_T^2 + k^2(\rho)\right]\Psi_0 = \beta_0^2\Psi_0, \tag{5.47}$$

for both particles, cf. (5.12) and (5.27). Substituting the general form for the unperturbed electron solutions (5.13) (or the unperturbed photon solutions (5.28)) into (5.47) yields the "radial" equation

$$\hat{R}\psi_{|m_\ell|}(\rho) \equiv \left(\partial_\rho^2 + \frac{1}{\rho}\partial_\rho - \frac{m^2}{\rho^2} + k^2(\rho)\right)\psi_{|m_\ell|}(\rho) = \beta_0^2\psi_{|m_\ell|}(\rho), \tag{5.48}$$

where $\hat{R}$ has been introduced as the "radial" operator, and $\nabla_T = \partial_\rho^2 + \dfrac{1}{\rho}\partial_\rho$ has been used.

Since the equation (5.48) may be put into Sturm Liouville form, its eigenfunctions are orthonormal with real eigenvalues $\left(\beta_0^2\right)_n$ with $n = 0, 1, 2, ...$, such that the nth eigenfunction $\psi_{n|m_\ell|}(\rho)$ has n zeros in the interval $0 < \rho < \infty$. As a result of this, n plays the role of a "radial" quantum number, analogously to that of the spherically symmetric Hydrogenic atom. We henceforth choose to express our analysis in terms of the following complete set of commuting operators, $\{\hat{\omega}_0, \hat{R}, \hat{\ell}_z, \hat{\sigma}_z\}$, which are associated with the following respective quantum numbers, $\{\omega_0, n, m_\ell, \sigma\}$. For a given particle frequency (energy) ω_0, the unperturbed state of the electron or photon is completely determined by the three discrete quantum numbers n, m_ℓ, σ. In what follows we therefore adopt the ket notation $|n\,m_\ell\,\sigma\rangle \equiv N_{n|m_\ell|}\psi_{n|m_\ell|}(\rho)\,e^{im_\ell\phi}\hat{\mathbf{e}}_\sigma e^{i(\beta_0 z - \omega t)}$ in order to denote an unperturbed monoenergetic particle state, where we have made explicit the dependence of the normalization factor N and the radial wave function $\psi(\rho)$ on the radial quantum number n.

Perturbation Hamiltonians

In preparation for our perturbative treatment, we now reexpress the perturbation Hamiltonian $\hat{H}'$ for both particles in a form amenable to the application of perturbation theory. As we will show in the next section, it is convenient to separate $\hat{H}'$ into its respective diagonal and anti-diagonal parts:

$$\hat{H}' = \hat{H}^{(\text{D})} + \hat{H}^{(\text{AD})}. \tag{5.49}$$

For electrons then, we have

$$\hat{H}^{(\mathrm{D})} = \hat{H}_{\mathrm{Rel}} + \hat{H}_{\mathrm{Dar}} + \hat{H}_{\mathrm{SO}}^{(\mathrm{D})}, \tag{5.50a}$$

$$\hat{H}^{(\mathrm{AD})} = \hat{H}_{\mathrm{SO}}^{(\mathrm{AD})}, \tag{5.50b}$$

where

$$\hat{H}_{\mathrm{Rel}} = \frac{\hbar^2}{c^2} \left(\frac{\hat{\nabla}^2}{2m} \right)^2, \tag{5.51a}$$

$$\hat{H}_{\mathrm{Dar}} = -\frac{\Delta}{4} \left(\left(\partial_\rho^2 \chi \left(\rho \right) \right) + \left(\partial_\rho \chi \left(\rho \right) \right) \partial_\rho + \frac{1}{\rho} \left(\partial_\rho \chi \left(\rho \right) \right) \right), \tag{5.51b}$$

and with

$$\hat{H}_{\mathrm{SO}}^{(\mathrm{D})} = -\frac{\Delta}{2} \frac{1}{\rho} \left(\partial_\rho \chi \left(\rho \right) \right) \hat{\sigma}_z \hat{\ell}_z \tag{5.52a}$$

$$\hat{H}_{\mathrm{SO}}^{(\mathrm{AD})} = -\frac{\Delta}{2} \frac{1}{\rho} \left(\partial_\rho \chi \left(\rho \right) \right) \rho \left(\hat{\sigma}_+ \hat{\ell}_- - \hat{\sigma}_- \hat{\ell}_+ \right) \partial_z \tag{5.52b}$$

being the respective diagonal and anti-diagonal parts of the spin-orbit operator $\hat{H}_{\mathrm{SO}}$ (see (5.6), (5.14), and (5.18)–(5.20)).

For photons, the Darwin-like term $\hat{H}_{\mathrm{Dar}}$, spin-orbit term $\hat{H}_{\mathrm{SO}}$, and photon term $\hat{H}_\gamma$ each have the respective diagonal and anti-diagonal parts (see (5.39)–(5.42) and (5.45)),

$$\hat{H}_{\text{Dar}}^{(D)} = \frac{-1}{1 - \Delta\chi(\rho)} \frac{\Delta}{2} \left(\left(\partial_\rho^2 \chi(\rho) \right) + \left(\partial_\rho \chi(\rho) \right) \partial_\rho + \frac{1}{\rho} \left(\partial_\rho \chi(\rho) \right) \right), \tag{5.53a}$$

$$\hat{H}_{\text{SO}}^{(D)} = \frac{-1}{1 - \Delta\chi(\rho)} \frac{\Delta}{2} \frac{1}{\rho} \left(\partial_\rho \chi(\rho) \right) \hat{\sigma}_z \hat{\ell}_z, \tag{5.53b}$$

$$\hat{H}_{\gamma}^{(D)} = \frac{-1}{1 - \Delta\chi(\rho)} \frac{1}{2} \Delta^2 \frac{\left(\partial_\rho \chi(\rho) \right)^2}{1 - \Delta\chi(\rho)}, \tag{5.53c}$$

$$\hat{H}_{\text{Dar}}^{(AD)} = \frac{-1}{1 - \Delta\chi(\rho)} \frac{\Delta}{2} \left(\left(\partial_\rho^2 \chi(\rho) \right) + \left(\partial_\rho \chi(\rho) \right) \partial_\rho + \frac{1}{\rho} \left(\partial_\rho \chi(\rho) \right) \right) \left(\hat{\sigma}_+^2 \hat{\ell}_-^2 + \hat{\sigma}_-^2 \hat{\ell}_+^2 \right), \tag{5.53d}$$

$$\hat{H}_{\text{SO}}^{(AD)} = \frac{-1}{1 - \Delta\chi(\rho)} \frac{\Delta}{2} \frac{1}{\rho} \left(\partial_\rho \chi(\rho) \right) \hat{\sigma}_z \hat{\ell}_z \left(\hat{\sigma}_+^2 \hat{\ell}_-^2 + \hat{\sigma}_-^2 \hat{\ell}_+^2 \right), \tag{5.53e}$$

$$\hat{H}_{\gamma}^{(AD)} = \frac{-1}{1 - \Delta\chi(\rho)} \frac{1}{2} \Delta^2 \frac{\left(\partial_\rho \chi(\rho) \right)^2}{1 - \Delta\chi(\rho)} \left(\hat{\sigma}_+^2 \hat{\ell}_-^2 + \hat{\sigma}_-^2 \hat{\ell}_+^2 \right), \tag{5.53f}$$

where $\mathbf{N} = \hat{\sigma}_+^2 \hat{\ell}_-^2 + \hat{\sigma}_-^2 \hat{\ell}_+^2$ has been used, so that

$$\hat{H}^{(D)} = \hat{H}_{\text{Dar}}^{(D)} + \hat{H}_{\text{SO}}^{(D)} + \hat{H}_{\gamma}^{(D)}, \tag{5.54}$$

and

$$\hat{H}^{(AD)} = \hat{H}_{\text{Dar}}^{(AD)} + \hat{H}_{\text{SO}}^{(AD)} + \hat{H}_{\gamma}^{(AD)}. \tag{5.55}$$

Taking one more step, we further separate out the spin-orbit contribution from the diagonal Hamiltonians $\hat{H}^{(D)}$ for both particles, so that

$$\hat{H}^{(D)} = \hat{H}_0^{(D)} + \hat{H}_{\text{SO}}^{(D)}, \tag{5.56}$$

where $\hat{H}_0^{(D)} = \hat{H}_{\text{Rel}} + \hat{H}_{\text{Dar}}$ for electrons and $\hat{H}_0^{(D)} = \hat{H}_{\text{Dar}}^{(D)} + \hat{H}_{\gamma}^{(D)}$ for photons, while $\hat{H}_{\text{SO}}^{(D)}$ for both particles is given above in (5.52a) and (5.53b), respectively. Our desired form for

the perturbation Hamiltonian is thence expressed as the sum of a diagonal "base" term, a diagonal spin-orbit term, and an anti-diagonal term:

$$\hat{H}' = \hat{H}_0^{(D)} + \hat{H}_{SO}^{(D)} + \hat{H}^{(AD)}. \tag{5.57}$$

Although this form for $\hat{H}'$ is still exact, it is readily amenable to perturbative techniques in the regime where $\Delta \ll 1$.

Perturbative Treatment

For both electrons and photons, the condition $\Delta \ll 1$ is the criterion for the waveguide to be weakly guiding, from which it follows that the guided modes are nearly paraxial. For the remainder of this section, we will henceforth assume that $\Delta \ll 1$ holds so that we may apply perturbation theory to the wave electron and photons wave equations, which each have the form (5.4). In this weakly guiding regime, the photon prefactors $\dfrac{1}{1 - \Delta\chi(\rho)}$ in equations (5.53a)–(5.53f) are approximately equal to unity (to first order in Δ), and the photon terms $\hat{H}_\gamma^{(D)}$ and $\hat{H}_\gamma^{(AD)}$, which are second order in Δ, are approximately zero to the same order. The photon Hamiltonian $\hat{H}' = \hat{H}_0^{(D)} + \hat{H}_{SO}^{(D)} + \hat{H}^{(AD)}$ thereby simplifies somewhat under the approximation $\Delta \ll 1$, such that $\hat{H}_0^{(D)} \to \hat{H}_{Dar}^{(D)}$ and $\hat{H}^{(AD)} \to \hat{H}_{Dar}^{(AD)} + \hat{H}_{SO}^{(AD)}$, with

$$\hat{H}_{Dar}^{(D)} \to -\frac{\Delta}{2}\left((\partial_\rho^2 \chi(\rho)) + (\partial_\rho \chi(\rho))\,\partial_\rho + \frac{1}{\rho}(\partial_\rho \chi(\rho)) \right) \tag{5.58a}$$

$$\hat{H}_{SO}^{(D)} \to -\frac{\Delta}{2}\frac{1}{\rho}(\partial_\rho \chi(\rho))\,\hat{\sigma}_z \hat{\ell}_z, \tag{5.58b}$$

$$\hat{H}_{\mathrm{Dar}}^{(\mathrm{AD})} \to -\frac{\Delta}{2} \left(\left(\partial_\rho^2 \chi(\rho)\right) + \left(\partial_\rho \chi(\rho)\right) \partial_\rho + \frac{1}{\rho}\left(\partial_\rho \chi(\rho)\right) \right) \left(\hat{\sigma}_+^2 \hat{\ell}_-^2 + \hat{\sigma}_-^2 \hat{\ell}_+^2 \right), \tag{5.58c}$$

$$\hat{H}_{\mathrm{SO}}^{(\mathrm{AD})} \to -\frac{\Delta}{2}\frac{1}{\rho} \left(\partial_\rho \chi(\rho)\right) \hat{\sigma}_z \hat{\ell}_z \left(\hat{\sigma}_+^2 \hat{\ell}_-^2 + \hat{\sigma}_-^2 \hat{\ell}_+^2 \right). \tag{5.58d}$$

In preparation for the application of perturbation theory, we now proceed to explicitly evaluate the matrix elements of the perturbation operator $\hat{H}'$ in the monoenergetic unperturbed states $|\Psi_0\rangle = |n\, m_\ell\, \sigma\rangle$ for both particles.

Electron Case

We begin by focusing on $\hat{H}_{\mathrm{Rel}}$ (see (5.51a)) and noting that the unperturbed wave equation (5.12) may be equivalently expressed as

$$\nabla^2 \Psi_0 = -\frac{2m}{\hbar^2}\left(E + eV(\rho)\right)\Psi_0 \tag{5.59}$$

where $E = \hbar\omega$, and the replacement $\beta_0^2 \to -\partial_z^2$ has been made. Employing (5.59) and the previously defined ket notation $\Psi_0 = |n\, m_\ell\, \sigma\rangle$ we find that the matrix elements of $\hat{H}_{\mathrm{Rel}}$ are

$$\left\langle \hat{H}_{\mathrm{Rel}} \right\rangle = \langle n'\, m_\ell'\, \sigma'|\, \hat{H}_{\mathrm{Rel}}\, |n\, m_\ell\, \sigma\rangle = \frac{E_0^2}{\hbar^2 c^2} \langle n'\, m_\ell'\, \sigma'| \left(1 + \frac{eV(\rho)}{E_0}\right)^2 |n\, m_\ell\, \sigma\rangle. \tag{5.60}$$

Letting $\mathcal{E}_0 \equiv \dfrac{E_0}{mc^2}$ so that $\dfrac{eV(\rho)}{E_0} = \dfrac{1}{\mathcal{E}_0}\dfrac{eV(\rho)}{mc^2} = \dfrac{1}{\mathcal{E}_0}\left(\dfrac{eV(0)}{mc^2} - \Delta\chi(\rho)\right)$, and fixing the arbitrary "zero-point" potential according to $V(0) = 0$, we find that

$$\langle n'\, m_\ell'\, \sigma'|\, \hat{H}_{\mathrm{Rel}}\, |n\, m_\ell\, \sigma\rangle = \frac{E_0^2}{\hbar^2 c^2} \langle n'\, m_\ell'\, \sigma'| \left(1 - \frac{\Delta}{\mathcal{E}_0}\chi(\rho)\right)^2 |n\, m_\ell\, \sigma\rangle. \tag{5.61}$$

Since the inner product denotes integration in the transverse ρ and ϕ variables, and the integrand depends only on ρ, we find that the explicit form of the inner product in (5.61) is

$$\left\langle \hat{H}_{\text{Rel}} \right\rangle = \frac{E_0^2}{\hbar^2 c^2} \left(\delta_{n'n} - 4\pi \frac{\Delta}{\mathcal{E}_0} \int \rho d\rho \chi(\rho) N_{n'|m_\ell|} N_{n|m_\ell|} \psi_{n'|m_\ell|}(\rho) \psi_{n|m_\ell|}(\rho) \right.$$

$$\left. + 2\pi \left(\frac{\Delta}{\mathcal{E}_0} \right)^2 \int \rho d\rho \chi^2(\rho) N_{n'|m_\ell|} N_{n|m_\ell|} \psi_{n'|m_\ell|}(\rho) \psi_{n|m_\ell|}(\rho) \right) \delta_{m'_\ell m_\ell} \delta_{\sigma'\sigma}, \qquad (5.62a)$$

$$\equiv F^{(\text{Rel})}_{n'n|m_\ell|} \delta_{m'_\ell m_\ell} \delta_{\sigma'\sigma}. \qquad (5.62b)$$

We now proceed to evaluate $\left\langle \hat{H}_{\text{Dar}} \right\rangle$ (see (5.51b)):

$$\left\langle \hat{H}_{\text{Dar}} \right\rangle = -\frac{\Delta}{4} \left(\langle n' m'_\ell \sigma' | \left(\partial_\rho^2 \chi(\rho) \right) | n m_\ell \sigma \rangle \right.$$

$$\left. + \langle n' m'_\ell \sigma' | \left(\partial_\rho \chi(\rho) \right) \partial_\rho | n m_\ell \sigma \rangle + \langle n' m'_\ell \sigma' | \frac{1}{\rho} \left(\partial_\rho \chi(\rho) \right) | n m_\ell \sigma \rangle \right), \quad (5.63a)$$

$$= -\Delta \frac{\pi}{2} N_{n'|m_\ell|} N_{n|m_\ell|} \left(\int \rho d\rho \left(\partial_\rho^2 \chi(\rho) \right) \psi_{n'|m_\ell|}(\rho) \psi_{n|m_\ell|}(\rho) \right.$$

$$\left. + \int d\rho \left[\rho \left(\partial_\rho \chi(\rho) \right) \psi_{n'|m_\ell|} \partial_\rho \psi_{n|m_\ell|}(\rho) + \left(\partial_\rho \chi(\rho) \right) \psi_{n'|m_\ell|}(\rho) \psi_{n|m_\ell|}(\rho) \right] \right) \delta_{m'_\ell m_\ell} \delta_{\sigma'\sigma},$$

$$(5.63b)$$

$$= \Delta \frac{\pi}{2} N_{n'|m_\ell|} N_{n|m_\ell|} \left(\int \rho d\rho \left(\partial_\rho \chi(\rho) \right) \psi_{n'|m_\ell|}(\rho) \partial_\rho \psi_{n|m_\ell|}(\rho) \right) \delta_{m'_\ell m_\ell} \delta_{\sigma'\sigma}, \qquad (5.63c)$$

$$\equiv F^{(\text{Dar})}_{n'n|m_\ell|} \delta_{m'_\ell m_\ell} \delta_{\sigma'\sigma}, \qquad (5.63d)$$

where integration by parts has been performed on the first term in (5.63b), which cancels the remaining terms, leaving (5.63c). This result leads us to define a simpler *effective* Darwin Hamiltonian term $\hat{H}_{\text{Dar}}^{(\text{Eff})}$,

$$\hat{H}_{\text{Dar}}^{(\text{Eff})} \equiv \frac{\Delta}{4} \left(\partial_\rho \chi \left(\rho \right) \right) \partial_\rho, \tag{5.64}$$

whose inner product yields the correct result (5.63d):

$$\left\langle \hat{H}_{\text{Dar}}^{(\text{Eff})} \right\rangle = \langle n' \, m'_\ell \, \sigma' | \, \frac{\Delta}{4} \left(\partial_\rho \chi \left(\rho \right) \right) \partial_\rho \, | n \, m_\ell \, \sigma \rangle = F_{n'n|m_\ell|}^{(\text{Dar})} \delta_{m'_\ell m_\ell} \delta_{\sigma'\sigma}. \tag{5.65}$$

We now evaluate the matrix elements of the diagonal part $\hat{H}_{\text{SO}}^{(\text{D})}$ of the spin-orbit term $\hat{H}_{\text{SO}}$ (see (5.52a)):

$$\left\langle \hat{H}_{\text{SO}}^{(\text{D})} \right\rangle = -\frac{\Delta}{2} \langle n' \, m'_\ell \, \sigma' | \, \frac{1}{\rho} \left(\partial_\rho \chi \left(\rho \right) \right) \hat{\sigma}_z \hat{\ell}_z \, | n \, m_\ell \, \sigma \rangle, \tag{5.66a}$$

$$= -\Delta \pi N_{n'|m_\ell|} N_{n|m_\ell|} \sigma m_\ell \left(\int d\rho \left(\partial_\rho \chi \left(\rho \right) \right) \psi_{n'|m_\ell|} \left(\rho \right) \psi_{n|m_\ell|} \left(\rho \right) \right) \delta_{m'_\ell m_\ell} \delta_{\sigma'\sigma}, \tag{5.66b}$$

$$\equiv -\sigma \mu F_{n'n|m_\ell|}^{(\text{SO})} \delta_{m'_\ell m_\ell} \delta_{\sigma'\sigma}, \tag{5.66c}$$

where $\mu \equiv \dfrac{m_\ell}{|m_\ell|}$ is designated the absolute sign of the OAM quantum number m_ℓ.

Finally, we evaluate the matrix elements of the the anti-diagonal term $\hat{H}^{(\text{AD})}$ of the perturbation operator $\hat{H}'$ (see (5.18b)), which involves a calculation similar to that of (5.66):

$$\left\langle \hat{H}^{(\text{AD})} \right\rangle = -\frac{\Delta}{2} \langle n' \, m'_\ell \, \sigma' | \left(\partial_\rho \chi \left(\rho \right) \right) i\beta_0 \left(\hat{\sigma}_+ \hat{\ell}_- - \hat{\sigma}_- \hat{\ell}_+ \right) | n \, m_\ell \, \sigma \rangle, \tag{5.67a}$$

$$= -i\beta \Delta \pi N_{n'|m_\ell|} N_{n|m_\ell|}$$

$$\times \left(\int \rho d\rho \left(\partial_\rho \chi \left(\rho \right) \right) \psi_{n'|m_\ell|} \left(\rho \right) \psi_{n|m_\ell|} \left(\rho \right) \right) \left(\delta_{m'_\ell m_\ell - 1} \delta_{\sigma'\sigma + 1} - \delta_{m'_\ell m_\ell + 1} \delta_{\sigma'\sigma - 1} \right),$$

$$\tag{5.67b}$$

$$\equiv -iF_{n'n|m_\ell|}^{(\mathrm{AD})} \left(\delta_{m_\ell' m_\ell - 1} \delta_{\sigma' \sigma + 1} - \delta_{m_\ell' m_\ell + 1} \delta_{\sigma' \sigma - 1} \right). \tag{5.67c}$$

By (5.62b), (5.63d), (5.66c), and (5.67c), the matrix elements of the complete Hamiltonian $\hat{H}' = \hat{H}_0^{(\mathrm{D})} + \hat{H}_{\mathrm{SO}}^{(\mathrm{D})} + \hat{H}^{(\mathrm{AD})}$ in the unperturbed electronic states may therefore be written as

$$\left\langle \hat{H}' \right\rangle = \left(F_{n'n|m_\ell|}^{(0)} - \sigma\mu F_{n'n|m_\ell|}^{(\mathrm{SO})} \right) \delta_{m_\ell' m_\ell} \delta_{\sigma'\sigma} - iF_{n'n|m_\ell|}^{(\mathrm{AD})} \left(\delta_{m_\ell' m_\ell - 1} \delta_{\sigma'\sigma+1} - \delta_{m_\ell' m_\ell + 1} \delta_{\sigma'\sigma-1} \right), \tag{5.68}$$

where $F_{n'n|m_\ell|}^{(0)} \equiv F_{n'n|m_\ell|}^{(\mathrm{Rel})} + F_{n'n|m_\ell|}^{(\mathrm{Dar})}$. It is instructive to express the matrix elements of the inner product (5.68) (for arbitrary n and n') in explicit matrix form:

$$\langle n' \, m_\ell' \, \sigma' | \, \hat{H}' \, | n \, m_\ell \, \sigma \rangle =$$

$$
\begin{pmatrix}
 & |n\,0\,+\rangle & |n\,0\,-\rangle & |n\,{-}1\,+\rangle & |n\,1\,-\rangle & |n\,1\,+\rangle & |n\,{-}1\,-\rangle & \cdots \\
|n'\,0\,+\rangle & F_{n'n0+}^{(\mathrm{D})} & 0 & 0 & 0 & -iF_{n'n1}^{(\mathrm{AD})} & 0 \\
|n'\,0\,-\rangle & 0 & F_{n'n0-}^{(\mathrm{D})} & 0 & 0 & 0 & iF_{n'n1}^{(\mathrm{AD})} \\
|n'\,{-}1\,+\rangle & 0 & 0 & F_{n'n\,{-}1+}^{(\mathrm{D})} & 0 & 0 & 0 \\
|n'\,1\,-\rangle & 0 & 0 & 0 & F_{n'n1-}^{(\mathrm{D})} & 0 & 0 \\
|n'\,1\,+\rangle & iF_{n'n1}^{(\mathrm{AD})} & 0 & 0 & 0 & F_{n'n1+}^{(\mathrm{D})} & 0 \\
|n'\,{-}1\,-\rangle & 0 & -iF_{n'n1}^{(\mathrm{AD})} & 0 & 0 & 0 & F_{n'n\,{-}1-}^{(\mathrm{D})} \\
\vdots & & & & & & & \ddots
\end{pmatrix}, \tag{5.69}
$$

where $F_{n'nm_\ell\sigma}^{(\mathrm{D})} \equiv F_{n'n|m_\ell|}^{(0)} - \sigma\mu F_{n'n|m_\ell|}^{(\mathrm{SO})}$. From (5.68) and (5.69) we see that the matrix $\langle n' \, m_\ell' \, \sigma' | \, \hat{H}' \, | n \, m_\ell \, \sigma \rangle$ is diagonal within each subspace block labeled by $|m_\ell|$ (i.e., each subspace spanned by the vectors $\{|n \, +|m_\ell| \, +\rangle, |n \, -|m_\ell| \, -\rangle, |n \, +|m_\ell| \, -\rangle, |n \, -|m_\ell| \, +\rangle\}$).

Photon Case

For the photon case, the four terms (5.58) which contribute to $\hat{H}'$ are similar to the electron terms above, so that their matrix elements are readily evaluated by following (5.63), (5.66), and (5.67):

$$
\begin{aligned}
\left\langle \hat{H}' \right\rangle = {} & \left(F^{(0)}_{n'n|m_\ell|} - \sigma\mu F^{(SO)}_{n'n|m_\ell|} \right) \delta_{m'_\ell m_\ell} \delta_{\sigma'\sigma} \\
& + F^{(0)}_{n'n|m_\ell|} \left((m_\ell - 2)\, \delta_{m'_\ell m_\ell - 2}\delta_{\sigma'\sigma+2} - (m_\ell + 2)\, \delta_{m'_\ell m_\ell + 2}\delta_{\sigma'\sigma-2} \right) \\
& - F^{(SO)}_{n'n|m_\ell|} \left(\delta_{m'_\ell m_\ell - 2}\delta_{\sigma'\sigma+2} + \delta_{m'_\ell m_\ell + 2}\delta_{\sigma'\sigma-2} \right) \qquad\qquad (5.70)
\end{aligned}
$$

where $F^{(0)}_{n'n|m_\ell|} \equiv 2F^{(Dar)}_{n'n|m_\ell|}$, and where the coefficients $F^{(Dar)}_{n'n|m_\ell|}$ and $F^{(SO)}_{n'n|m_\ell|}$ are given in (5.63d) and (5.66c). Expressing the matrix elements of the inner product (5.70) (for arbitrary n and n') in explicit matrix form then yields

$$\langle n'\, m'_\ell\, \sigma'|\,\hat{H}'\,|n\, m_\ell\, \sigma\rangle =$$

$$
\begin{pmatrix}
 & |n\,0\,+\rangle & |n\,0\,-\rangle & |n\,{-1}\,+\rangle & |n\,1\,-\rangle & |n\,1\,+\rangle & |n\,{-1}\,-\rangle & |n\,{-2}\,+\rangle & \cdots \\
|n'\,0\,+\rangle & F^{(D)}_{n'n\,0\,+} & 0 & 0 & 0 & 0 & 0 & -F^{(2)}_{n'n\,2} & \\
|n'\,0\,-\rangle & 0 & F^{(D)}_{n'n\,0\,-} & 0 & 0 & 0 & 0 & 0 & \ddots \\
|n'\,{-1}\,+\rangle & 0 & 0 & F^{(D)}_{n'n\,{-1}\,+} & -F^{(1)}_{n'n\,1} & 0 & 0 & 0 & \\
|n'\,1\,-\rangle & 0 & 0 & -F^{(1)}_{n'n\,1} & F^{(D)}_{n'n\,1\,-} & 0 & 0 & 0 & \\
|n'\,1\,+\rangle & 0 & 0 & 0 & 0 & F^{(D)}_{n'n\,1\,+} & 0 & 0 & \\
|n'\,{-1}\,-\rangle & 0 & 0 & 0 & 0 & 0 & F^{(D)}_{n'n\,{-1}\,-} & 0 & \\
|n'\,{-2}\,+\rangle & -F^{(2)}_{n'n\,2} & 0 & 0 & 0 & 0 & 0 & F^{(D)}_{n'n\,2\,-} & \\
|n'\,2\,-\rangle & 0 & -F^{(2)}_{n'n\,2} & 0 & 0 & 0 & 0 & 0 & \ddots \\
|n'\,2\,+\rangle & 0 & 0 & 0 & 0 & 0 & 0 & 0 & \\
|n'\,{-2}\,-\rangle & 0 & 0 & 0 & 0 & 0 & 0 & 0 & \\
\vdots & & & & & & & \vdots & \ddots
\end{pmatrix},
$$

$$(5.71)$$

where $F^{(1)}_{n'n\,1} \equiv F^{(0)}_{n'n\,1} + F^{(SO)}_{n'n\,1}$ and $F^{(2)}_{n'n\,1} \equiv 2F^{(0)}_{n'n\,1} + F^{(SO)}_{n'n\,1}$. In contrast to the electron case, we see from (5.71) that the matrix $\langle n'\, m'_\ell\, \sigma'|\,\hat{H}'\,|n\, m_\ell\, \sigma\rangle$ is *not* diagonal within the $|m_\ell| = 1$ subspace block. However, the $|m_\ell| = 1$ subspace proves to be the sole exception, as it follows from inspection of (5.70) that $\langle n\, m_\ell\, \sigma|\,\hat{H}'\,|n\, m_\ell\, \sigma\rangle$ is diagonal within all other $|m_\ell|$-dependent subspace blocks. As this property proves to be important for the application of perturbation

theory, we exclude for photons the $|m_\ell| = 1$ block from consideration for the remainder of this chapter.

Perturbation Theory

Armed with (5.69) and (5.71), we are now in a position to apply perturbation theory to both the electron and photon cases. We henceforth assume that the eigenvalues $\left(\beta_0^2\right)_{n|m_\ell|}$ of the monoenergetic states $|n\, m_\ell\, \sigma\rangle$ are sufficiently distinct such that $\left|\langle n'\, m'_\ell\, \sigma'|\, \hat{H}'\, |n\, m_\ell\, \sigma\rangle\right| \ll \left(\beta_0^2\right)_{n|m_\ell|} - \left(\beta_0^2\right)_{n'|m'_\ell|}$ for all values of n, n', $|m_\ell|$, and $|m'_\ell|$ (this assumption, which we have shown to be true for the specific case where $\chi\left(\rho\right)$ is a step function, may reasonably be expected to hold for arbitrary $\chi\left(\rho\right)$). According to first-order quantum-mechanical degenerate perturbation theory [86], under this assumption all off-diagonal terms which lie outside the $|m_\ell|$-dependent subspace blocks may be neglected to first order in Δ when calculating the first-order shift in the quantity β_0^2. Specifically, this means that to first order in Δ, the final term in (5.68) is negligible for electrons, while for photons the last two lines of (5.70) may be neglected (with the sole exception of the off-diagonal terms in the the photonic $|m_\ell| = 1$ block, which we exclude from our analysis as previously stated). Therefore, for the purposes of first-order perturbation theory the matrix elements $\langle n'\, m'_\ell\, \sigma'|\, \hat{H}'\, |n\, m_\ell\, \sigma\rangle$ take the same basic diagonal form for both particles,

$$\left\langle \hat{H}' \right\rangle = \left(F_{n'n|m_\ell|}^{(0)} - \sigma\mu F_{n'n|m_\ell|}^{(SO)} \right) \delta_{m'_\ell m_\ell}\delta_{\sigma'\sigma}, \tag{5.72}$$

where $F_{n'n|m_\ell|}^{(0)} \equiv F_{n'n|m_\ell|}^{(Rel)} + F_{n'n|m_\ell|}^{(Dar)}$ for electrons and $F_{n'n|m_\ell|}^{(0)} \equiv 2F_{n'n|m_\ell|}^{(Dar)}$ for photons, while

$F_{n'n|m_\ell|}^{(SO)}$ has the same form for both particles. From (5.72), one may extract the effective Hamiltonian for calculating the shifts to the quantity β_0^2, to first order in Δ:

$$\hat{H}_{\text{Eff}} = \frac{\hbar^2}{c^2}\left(\frac{\hat{\nabla}^2}{2m}\right)^2 + \frac{\Delta}{2}\left(\partial_\rho\chi\left(\rho\right)\right)\left(\frac{1}{2}\partial_\rho - \frac{1}{\rho}\hat{\sigma}_z\hat{\ell}_z\right) \tag{5.73}$$

for electrons, and

$$\hat{H}_{\text{Eff}} = \frac{\Delta}{2}\left(\partial_\rho\chi\left(\rho\right)\right)\left(\partial_\rho - \frac{1}{\rho}\hat{\sigma}_z\hat{\ell}_z\right) \tag{5.74}$$

for photons.

Since the effective Hamiltonians (5.73) and (5.74) are completely diagonal in the $|n\,m_\ell\,\sigma\rangle$ basis (with the exception of the $|m_\ell| = 1$ block for photons) first-order degenerate perturbation theory [86] gives the following formula for the first-order shifts $\delta\left(\beta^2\right)$ to the quantity β_0^2, which is valid for both particles:

$$\delta\left(\beta^2\right) = \langle n\,m_\ell\,\sigma|\,\hat{H}_{\text{Eff}}\,|n\,m_\ell\,\sigma\rangle, \tag{5.75a}$$

$$= F_{nn|m_\ell|}^{(0)} - \sigma\mu F_{nn|m_\ell|}^{(SO)}, \tag{5.75b}$$

where (5.72) has been used. Substituting the definitions of $F_{nn|m_\ell|}^{(0)}$ and $F_{nn|m_\ell|}^{(SO)}$ into (5.75b) (or equivalently, employing (5.73) and (5.74)) thereby yields an explicit expression for the shifts to β_0^2, to first order in Δ:

$$\delta\left(\beta^2\right) = \frac{N_{n|m_\ell|}^2 E_0^2}{\hbar^2 c^2}\left(\frac{1}{N_{n|m_\ell|}^2} - 4\pi\frac{\Delta}{\mathcal{E}_0}\int\rho d\rho\chi\left(\rho\right)\psi_{n|m_\ell|}^2\left(\rho\right)\right)$$

$$+ \Delta\frac{\pi}{2}N_{n|m_\ell|}^2\int\rho d\rho\left(\partial_\rho\chi\left(\rho\right)\right)\psi_{n|m_\ell|}\left(\rho\right)\partial_\rho\psi_{n|m_\ell|}\left(\rho\right)$$

$$- \sigma m_\ell\Delta\pi N_{n|m_\ell|}^2\int d\rho\left(\partial_\rho\chi\left(\rho\right)\right)\psi_{n|m_\ell|}^2\left(\rho\right) \tag{5.76}$$

for electrons, and

$$\delta\left(\beta^2\right) = \Delta\pi N_{n|m_\ell|}^2\int\rho d\rho\left(\partial_\rho\chi\left(\rho\right)\right)\psi_{n|m_\ell|}\left(\rho\right)\partial_\rho\psi_{n|m_\ell|}\left(\rho\right)$$

$$- \sigma m_\ell\Delta\pi N_{n|m_\ell|}^2\int d\rho\left(\partial_\rho\chi\left(\rho\right)\right)\psi_{n|m_\ell|}^2\left(\rho\right) \tag{5.77}$$

for photons. It is remarkable that the expressions for the two particles are nearly identical, with the exceptions of an extra term resulting from the relativistic mass increase of the massive electron, and a factor of two difference between the electron and photon "Darwin" terms.

Spin-Orbit Interaction

The first two terms of the electronic Hamiltonian (5.73) and the first term of the photonic Hamiltonian (5.74) each have matrix elements which are proportional to the identity matrix within each $|m_\ell|$-dependent subspace block, as may be verified by inspection of the $F_{n'n|m_\ell|}^{(0)}$ term of (5.72), which depends only upon the absolute value $|m_\ell|$ of the OAM quantum number. As a result of this, the degeneracy in the states $|n\,m_\ell\,\sigma\rangle$ with respect to the SAM

quantum number σ and the sign $\mu \equiv \dfrac{m_\ell}{|m_\ell|}$ of the OAM quantum number m_ℓ is not lifted by these terms, so that they do not contribute to the spin-orbit splitting of β_0^2. Since we are interested primarily in spin-orbit effects, we henceforth neglect the contributions due to these non spin-orbit terms. This leads to a simple form for the effective Hamiltonian governing the spin-orbit interaction for both particles,

$$\hat{H}_{SO}^{(Eff)} = -\frac{\Delta}{2}\frac{1}{\rho}\left(\partial_\rho \chi\left(\rho\right)\right)\hat{\sigma}_z\hat{\ell}_z, \tag{5.78}$$

and a correspondingly simple form for the first-order shifts $\delta\left(\beta^2\right)$,

$$\delta\left(\beta^2\right) = \left\langle \hat{H}_{SO}^{(Eff)} \right\rangle = -\sigma\mu F_{nn|m_\ell|}^{(SO)}, \tag{5.79a}$$

$$= -\sigma m_\ell \Delta \pi N_{n|m_\ell|}^2 \int d\rho \left(\partial_\rho \chi\left(\rho\right)\right)\psi_{n|m_\ell|}^2\left(\rho\right). \tag{5.79b}$$

It is remarkable that the effective spin-orbit Hamiltonian $\hat{H}_{SO}^{(Eff)}$ and therefore also the expression for the first-order spin-orbit shifts $\delta\left(\beta^2\right)$ are identical in form for both electrons and photons.

Spin-Orbit Correction to the Propagation Constant

So far we have calculated the first-order corrections to the *square* of the unperturbed propagation constant, $\delta\left(\beta^2\right)$. However, as can be seen from (5.13) and (5.28), it is the *first* power of β_0 which appears in the phase of the electron and photon wave functions. We are therefore actually interested in the correction to first power of β_0, which we denote as $\delta\beta$. To extract this quantity from (5.79), we write the first-order equation $\beta_1 = \beta_0 + \delta\beta$ (where

β_1 contains the first-order corrections to β_0), square both sides of this relation, neglect the term second order in $\delta\beta$, and rearrange which yields $\beta_1^2 - \beta_0^2 \approx 2\beta_0\delta\beta$. Since by definition we also have $\beta_1^2 - \beta_0^2 \equiv \delta\left(\beta^2\right)$, we conclude that

$$\delta\beta = \frac{\delta\left(\beta^2\right)}{2\beta_0}. \tag{5.80}$$

From (5.79), we then conclude that the first-order corrections $\delta\beta$ to the unperturbed propagation constant β_0 are given by

$$\delta\beta = \frac{1}{2\beta_0}\left\langle \hat{H}_{\text{SO}}^{(\text{Eff})}\right\rangle = -\sigma m_\ell \Delta \frac{\pi}{2\beta_0} N_{n|m_\ell|}^2 \int d\rho\,\left(\partial_\rho \chi\left(\rho\right)\right)\psi_{n|m_\ell|}^2\left(\rho\right). \tag{5.81}$$

We conclude that the propagation constant β_0 is split by the spin-orbit interaction such that the correction $\delta\beta$ is negative when the quantity σm_ℓ is positive, and positive when σm_ℓ is negative. Note however that β_0 is related to the particle's unperturbed phase velocity $v_p^{(0)}$ via $v_p^{(0)} \equiv \frac{\omega}{\beta_0}$, so that the effect of the spin-orbit interaction on $v_p^{(0)}$ is to shift it according to

$$v_p = v_p^{(0)} + \delta v_p = \frac{\omega}{\beta_0} - \frac{\omega}{\beta_0^2}\delta\beta, \tag{5.82}$$

which is valid to first-order in Δ. Noting also that the signs of the SAM and OAM quantum numbers σ and m_ℓ describe the orientation of their associated spin and orbital angular momentum vectors as parallel or anti-parallel with respect to the quantization axis, we arrive at a more physical interpretation for the cylindrical spin-orbit interaction: the phase velocity shifts upwards when the SAM and OAM vectors are oriented parallel with respect to one another, while it experiences a downward shift when the SAM and OAM are oriented in

an anti-parallel manner. In terms of the total angular momentum (TAM) quantum number $m_j \equiv m_\ell + \sigma$, we find that states with higher absolute TAM $|m_j|$ (i.e., parallel states) shift the phase velocity upwards, while states lower $|m_j|$ (anti-parallel states), shift the phase velocity downwards.

Spin and Orbital Rotation Effects

The effect of the cylindrical spin-orbit interaction (to first order in Δ) on a monoenergetic state $|n\, m_\ell\, \sigma\rangle$ is to impart a phase factor of the form $e^{-i\sigma\mu|\delta\beta|}$ to the state as it propagates through a distance z down the waveguide:

$$|n\, m_\ell\, \sigma\rangle \rightarrow e^{-i\sigma\mu|\delta\beta|z}\, |n\, m_\ell\, \sigma\rangle, \tag{5.83}$$

where $|\delta\beta| = \Delta\dfrac{\pi\,|m_\ell|}{2\beta_0}N^2_{n|m_\ell|}\displaystyle\int d\rho\, (\partial_\rho\chi(\rho))\,\psi^2_{n|m_\ell|}(\rho)$, as can be seen from (5.13), (5.28), and (5.81). Armed with, (5.83), we may derive the spin and orbital rotational effects mentioned in the introduction to this chapter in a unified manner.

Orbit-Controlled Spin Rotation

We begin by noting that for both electrons and photons an arbitrary particle spin (polarization) state $|\hat{e}\rangle$ may be described by a complex superposition of the two basis spinors (vectors) $\{\hat{e}_+, \hat{e}_-\}$. Since such a superposition corresponds to the state of a two-level quantum system, we may follow Bloch and parametrize the spin (polarization) state as follows:
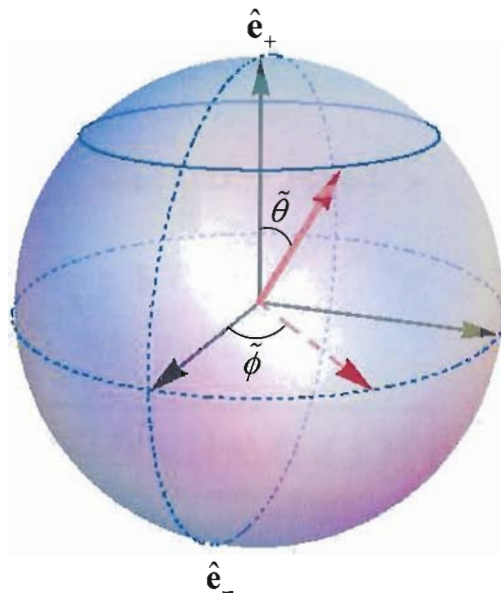
Figure 5.1. The Bloch sphere representing the complex spin-polarization superposition state $|\hat{\mathbf{e}}\rangle$. The angles $\tilde{\theta}$ and $\tilde{\phi}$ parameterizing the superposition in (5.84) correspond to the spherical polar angles of the Bloch vector, shown as the bold red arrow. The dashed red arrow is the projection of the Bloch vector into the azimuthal plane. The "north" and "south" poles of the Bloch sphere correspond respectively to the spin-polarization states $\hat{\mathbf{e}}_+$ and $\hat{\mathbf{e}}_-$. The SOI causes a Bloch vector initially oriented at angles $\tilde{\theta}$ and $\tilde{\phi}$ to precess in the azimuthal ($\hat{\phi}$) direction, thereby tracing out the path given by the solid blue line. In the special case illustrated, $\tilde{\theta} = \dfrac{\pi}{4}$ and $\tilde{\phi} = \dfrac{\pi}{4}$. See text for further discussion.

$$|\hat{\mathbf{e}}\rangle = \cos\left(\frac{\tilde{\theta}}{2}\right)e^{-i\frac{\tilde{\phi}}{2}}\,\hat{\mathbf{e}}_+ + \sin\left(\frac{\tilde{\theta}}{2}\right)e^{i\frac{\tilde{\phi}}{2}}\,\hat{\mathbf{e}}_-, \tag{5.84}$$

where $\tilde{\theta}$ and $\tilde{\phi}$ may be represented geometrically as the spherical polar angles of the so-called

"Bloch vector", which uniquely determine a point on the spin-polarization Bloch sphere (see

Fig. 5.1). In light of this, we consider an arbitrary spin-polarization superposition of the

states $|n\, m_\ell\, \sigma\rangle$, such that the superposition state retains well-defined values of its OAM and radial quantum numbers m_ℓ and n, which by (5.13) and (5.28) may be written as

$$|\phi_0\,(m_\ell,\, n)\rangle \equiv \cos\left(\frac{\tilde{\theta}}{2}\right)e^{-i\frac{\tilde{\phi}}{2}}\,|n\, m_\ell +\rangle + \sin\left(\frac{\tilde{\theta}}{2}\right)e^{i\frac{\tilde{\phi}}{2}}\,|n\, m_\ell -\rangle. \qquad (5.85)$$

According to (5.83), as the state (5.85) propagates a distance z down the waveguide, each of the two components pick up a phase factor from the spin-orbit interaction, the sign of which depends upon the sign of product $\sigma\mu$:

$$|\phi\,(m_\ell,\, n)\rangle = \cos\left(\frac{\tilde{\theta}}{2}\right)e^{-i\frac{\tilde{\phi}}{2}}e^{-i\mu|\delta\beta|z}\,|n\, m_\ell +\rangle + \sin\left(\frac{\tilde{\theta}}{2}\right)e^{i\frac{\tilde{\phi}}{2}}e^{i\mu|\delta\beta|z}\,|n\, m_\ell -\rangle, \qquad (5.86a)$$

$$= N_{n|m_\ell|}\psi_{n|m_\ell|}\,(\rho)\,e^{i(m_\ell\phi+\beta_0 z-\omega t)}\left[\cos\left(\frac{\tilde{\theta}}{2}\right)e^{-i\mu\left(|\delta\beta|z+\mu\frac{\tilde{\phi}}{2}\right)}\hat{\mathbf{e}}_+ + \sin\left(\frac{\tilde{\theta}}{2}\right)e^{i\mu\left(|\delta\beta|z+\mu\frac{\tilde{\phi}}{2}\right)}\hat{\mathbf{e}}_-\right].$$

$$(5.86b)$$

The spin-polarization portion (in square brackets) of the propagating state (5.86b) has the same general form as (5.84), however the azimuthal Bloch vector angle $\tilde{\phi}$ in (5.84) is transformed by the SOI according to $\dfrac{\tilde{\phi}}{2} \to \mu\left(|\delta\beta|\,z + \mu\dfrac{\tilde{\phi}}{2}\right)$. This implies that the SOI causes a Bloch vector with initial spherical polar angles $\tilde{\theta}, \tilde{\phi}$ to precess in the azimuthal ($\hat{\phi}$) direction with a precession rate of $|\delta\beta|$ per unit z, with the direction of precession controlled by the absolute sign μ of the OAM (see Fig. 5.1).

For electrons, this Bloch vector precession in the two-level state space corresponds to a similar precession of the expectation value of the spin vector in three-dimensional real space:

$$\left\langle \hat{\mathbf{S}} \right\rangle = \left\langle \hat{S}_x \right\rangle \hat{\mathbf{x}} + \left\langle \hat{S}_y \right\rangle \hat{\mathbf{y}} + \left\langle \hat{S}_z \right\rangle \hat{\mathbf{z}}, \tag{5.87a}$$

$$= \hbar \cos\left(\frac{\tilde{\theta}}{2}\right) \sin\left(\frac{\tilde{\theta}}{2}\right) \left[\cos\left(2\left|\delta\beta\right| z + \mu\tilde{\phi}\right)\hat{\mathbf{x}} + \mu \sin\left(2\left|\delta\beta\right| z + \mu\tilde{\phi}\right)\hat{\mathbf{y}} \right] + \frac{\hbar}{2} \cos\left(\tilde{\theta}\right)\hat{\mathbf{z}}. \tag{5.87b}$$

As can be seen from (5.87b), the average spin vector tilts at angle $\tilde{\theta}$ with respect to the z axis and precesses around it with increasing z, such that the direction of precession is controlled by the absolute sign μ of the OAM, similarly to the Bloch vector. However, the precession rate per unit z of the spin vector is $2\left|\delta\beta\right|$, which is twice that of the Bloch vector. For photons, the polarization state may also be expressed directly in terms of the Cartesian unit vectors $\hat{\mathbf{x}}$ and $\hat{\mathbf{y}}$ as an alternative to the Bloch vector representation:

$$\hat{\mathbf{e}} = \frac{1}{\sqrt{2}} \left[\sin\left(\frac{\tilde{\theta}}{2}\right) e^{i\mu\left(\left|\delta\beta\right|z + \mu\frac{\tilde{\phi}}{2}\right)} + \cos\left(\frac{\tilde{\theta}}{2}\right) e^{-i\mu\left(\left|\delta\beta\right|z + \mu\frac{\tilde{\phi}}{2}\right)} \right] \hat{\mathbf{x}}$$
$$- \frac{i}{\sqrt{2}} \left[\sin\left(\frac{\tilde{\theta}}{2}\right) e^{i\mu\left(\left|\delta\beta\right|z + \mu\frac{\tilde{\phi}}{2}\right)} - \cos\left(\frac{\tilde{\theta}}{2}\right) e^{-i\mu\left(\left|\delta\beta\right|z + \mu\frac{\tilde{\phi}}{2}\right)} \right] \hat{\mathbf{y}}. \tag{5.88}$$

It is instructive to consider the special case of an initial spin-polarization state in a balanced superposition, such that $\tilde{\theta} = \dfrac{\pi}{2}$ (although it is not necessary, we also set $\tilde{\phi} = 0$ without loss of generality). In this case, (5.87b) becomes

$$\left\langle \hat{\mathbf{S}} \right\rangle = \frac{\hbar}{2} \left[\cos\left(2\left|\delta\beta\right| z\right)\hat{\mathbf{x}} + \mu \sin\left(2\left|\delta\beta\right| z\right)\hat{\mathbf{y}} \right], \tag{5.89}$$

while (5.88) reduces to
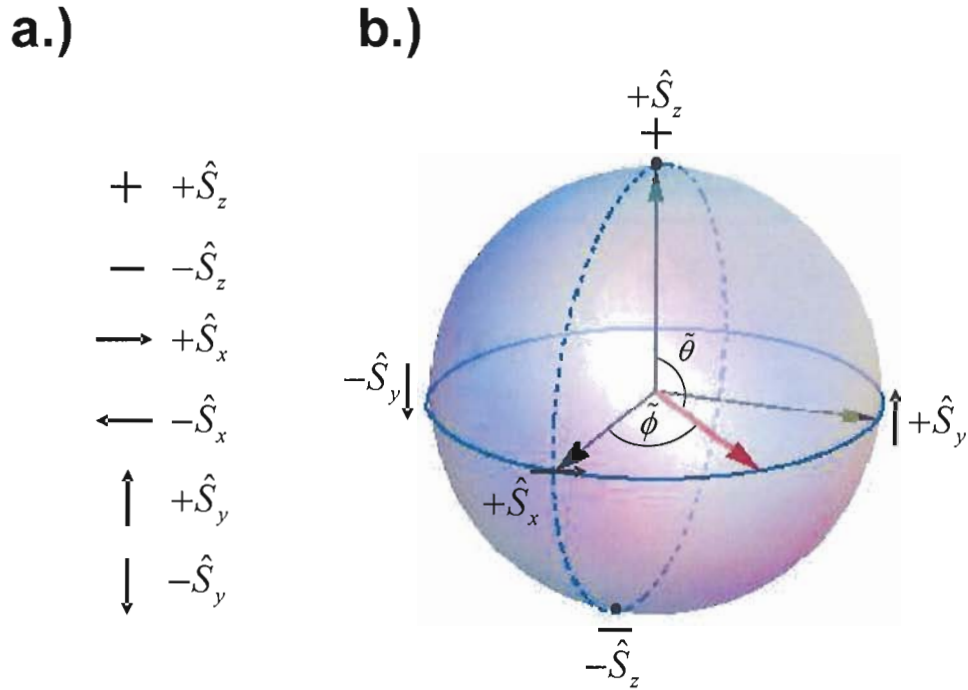
Figure 5.2. (a) Representation of various electronic spin states: $+$ and $-$ stand for spin up and spin down along the z axis (i.e., eigenstates of $\hat{S}_z$ with positive and negative eigenvalues), $\rightarrow$ and $\leftarrow$ for eigenstates of $\hat{S}_x$ with positive and negative eigenvalues, and $\uparrow$ and $\downarrow$ for eigenstates of $\hat{S}_y$ with positive and negative eigenvalues. (b) The evolution of the expectation value of the electron spin vector $\left\langle \hat{\mathbf{S}} \right\rangle$ in real three-dimensional space due to the SOI, for the special case of a balanced superposition where $\tilde{\theta} = \dfrac{\pi}{2}$. The long black arrows represent the x, y, z coordinate axes which correspond respectively to the spin states $\rightarrow$, $\uparrow$, and $+$, while the red arrow represents the spin vector. The spin vector lies entirely in the x–y plane and precesses around the z axis, alternating between eigenstates of $\hat{S}_x$ and $\hat{S}_y$ and thereby tracing out the path given by the solid blue line.

$$\hat{\mathbf{e}} = \cos\left(|\delta\beta|\, z\right)\hat{\mathbf{x}} + \mu \sin\left(|\delta\beta|\, z\right)\hat{\mathbf{y}}. \tag{5.90}$$

From (5.89), we see that under these conditions the electron spin expectation vector lies entirely in the x–y plane and precesses around the z axis, as shown in Fig. 5.2. Similarly,
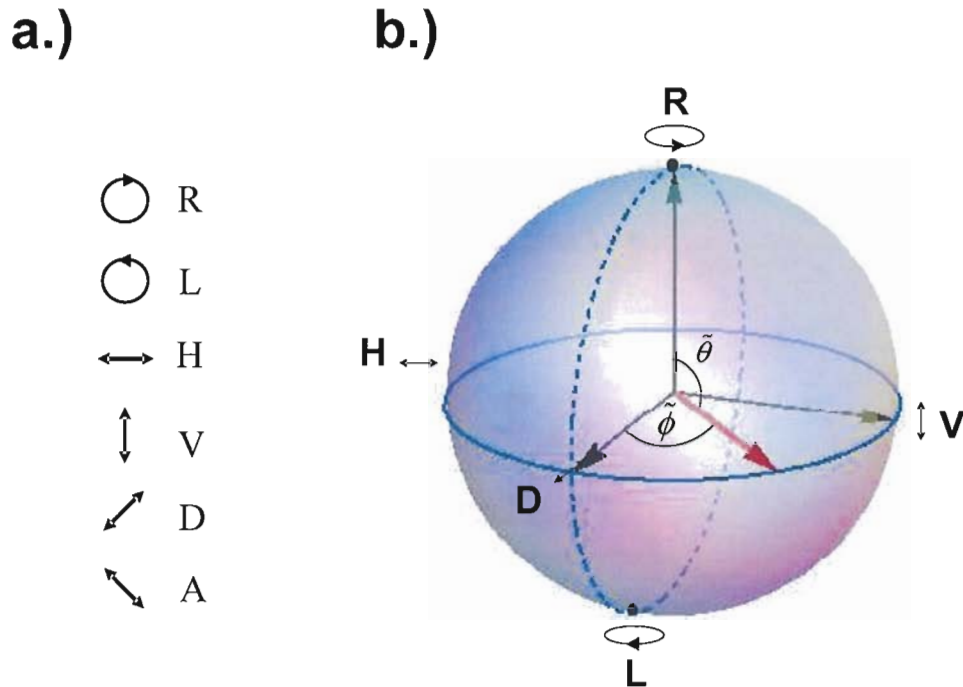
Figure 5.3. (a) Representation of various photonic polarization states: R and L stand for right and left circular polarization, H and V for horizontal and vertical linear polarization, and D and A for diagonal and anti-diagonal linear polarization. (b) The evolution of the photon polarization vector $|\hat{e}\rangle$ on the polarization Bloch sphere due to the SOI, for the special case of a balanced superposition where $\tilde{\theta} = \frac{\pi}{2}$. The long black arrows represent coordinate axes which correspond to the respective polarization states D, V, and R, while the red arrow represents the polarization Bloch vector. The Bloch vector lies entirely in the equatorial plane of the Bloch sphere and precesses about its pole, alternating between states of linear polarization in the $\hat{x}$ and $\hat{y}$ directions and thereby tracing out the path given by the solid blue line.

while from (5.90), the photon polarization Bloch vector lies entirely in the "equatorial" plane and precesses around the "polar" axis of the Bloch sphere, as shown in Fig. 5.3. The electron spin vector therefore undergoes periodic oscillation, alternating between eigenstates of $\hat{S}_x$ and $\hat{S}_y$ (see Fig. 5.2), while the photon polarization remains linear and rotates in the

x–y plane of real space, periodically alternating between states of linear polarization in the $\hat{\mathbf{x}}$ and $\hat{\mathbf{y}}$ directions (see Fig. 5.3).

The result that the electron spin expectation precession rate $2\,|\delta\beta|$ is double that of the photon polarization precession rate $|\delta\beta|$ is consistent with the fact that the SOI phase factor in (5.83) acts on the electron spin state $\hat{\mathbf{e}}$ as a *spinorial* rotation transformation through an angle ψ about the z axis, while it acts on the photon polarization state as the corresponding *vectorial* rotation transformation through angle ψ. A spinorial rotation as expressed in the spin-z basis acts upon the initial spinor superposition $\hat{\mathbf{e}} = \dfrac{1}{\sqrt{2}}\begin{pmatrix} 1 \\ 1 \end{pmatrix}$ via the spinorial matrix representation [87],

$$\frac{1}{\sqrt{2}}\begin{pmatrix} e^{-i\frac{\psi}{2}} & 0 \\ 0 & e^{i\frac{\psi}{2}} \end{pmatrix}\begin{pmatrix} 1 \\ 1 \end{pmatrix}. \tag{5.91}$$

By (5.83) the spinorial rotation due to the SOI may also be expressed in the similar form,

$$\frac{1}{\sqrt{2}}\begin{pmatrix} e^{-i\mu|\delta\beta|z} & 0 \\ 0 & e^{i\mu|\delta\beta|z} \end{pmatrix}\begin{pmatrix} 1 \\ 1 \end{pmatrix}. \tag{5.92}$$

Equating these two matrices and solving for the rotation angle ψ then yields the factor of two: $\psi = 2\mu\,|\delta\beta|\,z$. In contrast to the electron case, a vectorial rotation as expressed in the Cartesian (x, y, z) basis acts upon the initial polarization vector $\hat{\mathbf{e}} = \begin{pmatrix} 1 \\ 0 \\ 0 \end{pmatrix}$ (which represents the helicity superposition $(\hat{\mathbf{e}}_+ + \hat{\mathbf{e}}_-) \propto \hat{\mathbf{x}}$) via the vectorial matrix representation,

$$
\begin{pmatrix} \cos\psi & \sin\psi & 0 \\ -\sin\psi & \cos\psi & 0 \\ 0 & 0 & 1 \end{pmatrix} \begin{pmatrix} 1 \\ 0 \\ 0 \end{pmatrix}. \tag{5.93}
$$

By (5.83), the vectorial rotation may also be expressed in the similar form,

$$
\begin{pmatrix} \cos\mu\,|\delta\beta|\,z & \sin\mu\,|\delta\beta|\,z & 0 \\ -\sin\mu\,|\delta\beta|\,z & \cos\mu\,|\delta\beta|\,z & 0 \\ 0 & 0 & 1 \end{pmatrix} \begin{pmatrix} 1 \\ 0 \\ 0 \end{pmatrix}, \tag{5.94}
$$

so that equating these two matrices and solving for ψ results in $\psi = \mu\,|\delta\beta|\,z$, with the factor of two now absent.

We call the effect embodied in equations (5.86)-(5.90) orbit-controlled spin rotation, since the direction and rate of the rotational precession of spin-polarization Bloch vector are respectively controlled by the absolute sign and magnitude of the OAM quantum number. We have illustrated the special case of a balanced spin-polarization superposition state for $n = 0$ and $|m_\ell| = 2$ (see equations (5.86), (5.89), and (5.90), and Figs. 5.2 and 5.3) and its associated spin-polarization rotation effect in Figs. 5.4(a) and 5.4(c).

<div align="center">Spin-Controlled Orbital Rotation</div>

In addition to the spin-polarization rotation effect described above, the SOI is also responsible for an effect in which involves the directional control of the azimuthal rotation of the particle's *transverse spatial wave function* (i.e., its "orbital" state) by the sign of the SAM quantum number. We call this distinct but related effect spin-controlled orbital rota-
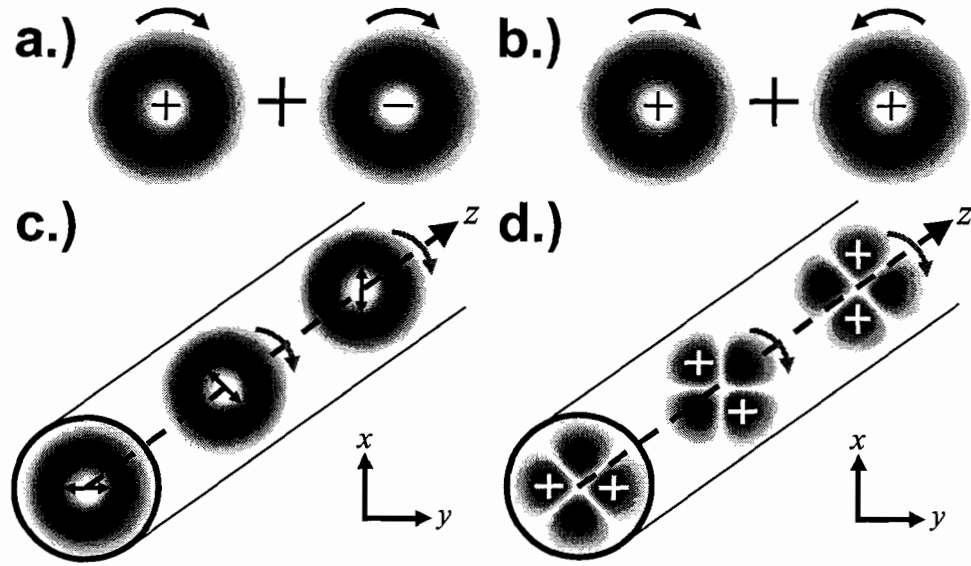
Figure 5.4. (a) An OAM eigenstate with $|m_\ell| = 2$ in a balanced superposition of $+$ and $-$ SAM states. The $\pm$ signs contained within the transverse spatial profiles indicate the SAM of the contributing state, while the arrows indicate its OAM handedness. (b) A SAM eigenstate in a balanced superposition of right and left-handed OAM states with $|m_\ell| = 2$. When states (a) and (b) propagate down a straight waveguide, the spin-polarization vector of the state in (a) (see equations (5.89) and (5.90)) and the transverse spatial profile of the state in (b) (see equation (5.97)) exhibit azimuthal rotation, as shown in (c) and (d), with the sense of rotation controlled by the sign of the OAM and SAM quantum numbers, respectively. The straight arrows in (c) denote the orientation of the state's spin (polarization) vector, while the white plus signs in (d) represent relative transverse phase.

tion. In analogy with the arbitrary *spin* angular momentum superposition with well-defined values of m_ℓ and n considered above in (5.85), we now consider an arbitrary superposition of *orbital* angular momentum states with constant absolute OAM value $|m_\ell|$, and with well-defined values of its *spin* angular momentum and radial quantum numbers σ and n. By (5.13) and (5.28) such a superposition may be written as

$$|\phi_0(\sigma, n)\rangle \equiv \cos\left(\frac{\tilde{\theta}}{2}\right)e^{-i\frac{\tilde{\phi}}{2}}|n + |m_\ell| \; \sigma\rangle + \sin\left(\frac{\tilde{\theta}}{2}\right)e^{i\frac{\tilde{\phi}}{2}}|n - |m_\ell| \; \sigma\rangle. \tag{5.95a}$$

$$= N_{n|m_\ell|}\psi_{n|m_\ell|}(\rho)\,\hat{\mathbf{e}}\left[\cos\left(\frac{\tilde{\theta}}{2}\right)e^{i\left(|m_\ell|\phi-\frac{\tilde{\phi}}{2}\right)} + \sin\left(\frac{\tilde{\theta}}{2}\right)e^{-i\left(|m_\ell|\phi-\frac{\tilde{\phi}}{2}\right)}\right]. \tag{5.95b}$$

According to (5.83), as the state (5.95) propagates a distance z down the waveguide, each of the two components pick up a phase factor from the spin-orbit interaction, the sign of which depends upon the sign of product $\sigma\mu$:

$$|\phi(\sigma, n)\rangle = \cos\left(\frac{\tilde{\theta}}{2}\right)e^{-i\frac{\tilde{\phi}}{2}}e^{-i\sigma|\delta\beta|z}|n + |m_\ell| \; \sigma\rangle + \sin\left(\frac{\tilde{\theta}}{2}\right)e^{i\frac{\tilde{\phi}}{2}}e^{i\sigma|\delta\beta|z}|n - |m_\ell| \; \sigma\rangle, \tag{5.96a}$$

$$= N_{n|m_\ell|}\psi_{n|m_\ell|}(\rho)$$
$$\left[\cos\left(\frac{\tilde{\theta}}{2}\right)e^{i\left(|m_\ell|\phi-\sigma\left(|\delta\beta|z+\sigma\frac{\tilde{\phi}}{2}\right)\right)} + \sin\left(\frac{\tilde{\theta}}{2}\right)e^{-i\left(|m_\ell|\phi-\sigma\left(|\delta\beta|z+\sigma\frac{\tilde{\phi}}{2}\right)\right)}\right]e^{i(\beta_0 z-\omega t)}\hat{\mathbf{e}}_\sigma. \tag{5.96b}$$

This equation is the OAM analogue to (5.86), which describes the evolution of an arbitrary spin superposition under the SOI. In full analogy with equation 5.84, one may define an "orbital" (OAM) Bloch sphere associated with the two-level system defined by the basis states $|n + |m_\ell|\sigma\rangle$ and $|n - |m_\ell|\sigma\rangle$, as shown in Fig. 5.5. Although the special case of $n = 0$, $|m_\ell| = 1$ is shown in the figure, an orbital Bloch sphere may be defined for all n and $|m_\ell|$ values. Note however that for the special case of $|m_\ell| = 1$ (for any n value) photons do not experience the same spin-orbit interaction as explained previously, so that this model applies only to electrons in that case.
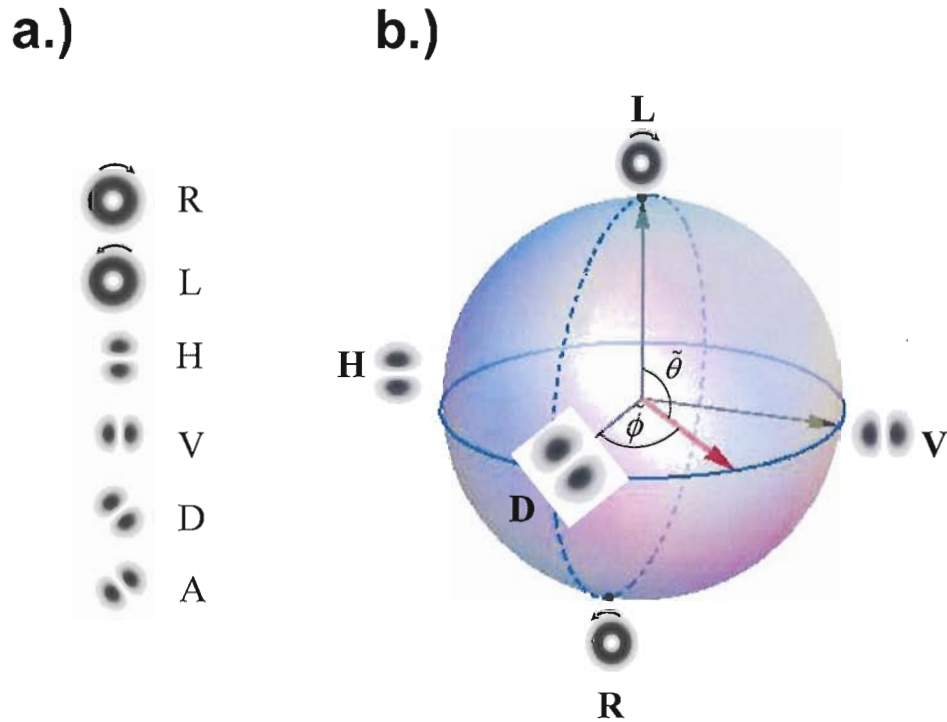
Figure 5.5. (a) Representation of various superpositions of photonic transverse spatial modes with $n = 0$ and $|m_\ell| = 1$: R and L stand for the right handed and left handed states $|n +1\,\sigma\rangle$ and $|n -1\,\sigma\rangle$, H and V for the "horizontal" and "vertical" superposition states $|n +1\,\sigma\rangle \pm |n -1\,\sigma\rangle$, and D and A for the "diagonal" and "anti-diagonal" superpositions $|n +1\,\sigma\rangle \pm i |n -1\,\sigma\rangle$. (b) The evolution of the OAM Bloch vector on the OAM Bloch sphere due to the SOI, for the special case of a balanced superposition where $\tilde{\theta} = \dfrac{\pi}{2}$. The long black arrows represent coordinate axes which correspond to the respective orbital states D, V, and R, while the red arrow represents the OAM Bloch vector. The Bloch vector lies entirely in the equatorial plane of the Bloch sphere and precesses about its pole, alternating between "horizontal" and "vertical" orbital states and thereby tracing out the path given by the solid blue line. See text for further discussion.

The "orbital" portion (in square brackets) of the propagating state (5.96b) has the same general form as the square-bracket orbital term in (5.95b), however the azimuthal OAM Bloch vector angle $\tilde{\phi}$ in (5.95b) is transformed by the SOI according to $\dfrac{\tilde{\phi}}{2} \rightarrow \sigma\left(|\delta\beta|\, z + \sigma\dfrac{\tilde{\phi}}{2}\right)$. This implies that the SOI causes an OAM Bloch vector with initial spherical polar angles $\tilde{\theta}, \tilde{\phi}$ to precess in the azimuthal ($\hat{\phi}$) direction with a precession rate of $|\delta\beta|$ per unit z, with the direction of precession controlled by the absolute sign σ of the SAM, in full analogy with Fig. 5.1. This OAM Bloch vector precession (shown in Fig. 5.5) corresponds physically to the azimuthal rotation of the particle's *transverse wave function* at a rate of $|\delta\beta|$ rads per unit z, as we will presently show below for the special case of a balanced superposition.

For balanced states, where $\tilde{\theta} = \dfrac{\pi}{2}$ (we also set $\tilde{\phi} = 0$ without loss of generality), (5.96b) reduces to

$$|\phi\left(\sigma,\, n\right)\rangle = N_{n|m_\ell|}\psi_{n|m_\ell|}\left(\rho\right)\frac{\sqrt{2}}{2}\left[e^{i(|m_\ell|\phi - \sigma|\delta\beta|z)} + e^{-i(|m_\ell|\phi - \sigma|\delta\beta|z)}\right]e^{i(\beta_0 z - \omega t)}\hat{\mathbf{e}}_\sigma. \qquad (5.97\text{a})$$

$$= N_{n|m_\ell|}\psi_{n|m_\ell|}\left(\rho\right)\sqrt{2}\cos\left(|m_\ell|\,\phi - \sigma\,|\delta\beta|\,z\right)e^{i(\beta_0 z - \omega t)}\hat{\mathbf{e}}_\sigma. \qquad (5.97\text{b})$$

From the $\cos\left(m_\ell\phi - \sigma\,|\delta\beta|\,z\right)$ term in (5.97b), it is clearly evident that the particle's transverse wave function undergoes azimuthal rotation analogously to the spin-polarization rotation phenomenon described in (5.89) and (5.90). However, in the present case the direction of rotation is controlled by the sign of the SAM quantum number σ. We have illustrated this special case of a balanced orbital superposition state for $n = 0$ and $|m_\ell| = 2$ (see equations (5.96) and (5.97), and Fig. 5.5) and its associated orbital rotation effect in Figs. 5.4(b) and 5.4(d).

Temporal Spin and Orbital Rotation Effects

Each of the spin and orbital rotational effects described above may occur in two distinct contexts: the rotation may occur in either space (i.e., as a function of the distance z propagated down the waveguide as already shown) or in time. We now turn to the description of the temporal manifestation of the SOI effects. Considering again the unperturbed states $|n\,m_\ell\,\sigma\rangle \equiv N_{n|m_\ell|}\psi_{n|m_\ell|}\left(\rho\right)e^{im_\ell\phi}\hat{\mathbf{e}}_\sigma e^{i(\beta_0 z - \omega t)}$ we now build the following spin and orbital superpositions,

$$\cos\left(\frac{\tilde{\theta}}{2}\right)e^{-i\frac{\tilde{\phi}}{2}}\left|n\,m_\ell\,+\right\rangle e^{i\mu(|\delta\beta|z-|\delta\omega|t)} + \sin\left(\frac{\tilde{\theta}}{2}\right)e^{i\frac{\tilde{\phi}}{2}}\left|n\,m_\ell\,-\right\rangle e^{-i\mu(|\delta\beta|z-|\delta\omega|t)}, \tag{5.98a}$$

$$\cos\left(\frac{\tilde{\theta}}{2}\right)e^{-i\frac{\tilde{\phi}}{2}}\left|n\,+|m_\ell|\,\sigma\right\rangle e^{i\sigma(|\delta\beta|z-|\delta\omega|t)} + \sin\left(\frac{\tilde{\theta}}{2}\right)e^{i\frac{\tilde{\phi}}{2}}\left|n\,-|m_\ell|\,\sigma\right\rangle e^{-i\sigma(|\delta\beta|z-|\delta\omega|t)}, \tag{5.98b}$$

where $|\delta\omega| \equiv v_p^{(0)}|\delta\beta|$, with $v_p^{(0)} \equiv \dfrac{\omega}{\beta_0}$ being the particle's unperturbed phase velocity. The new basic states making up these superpositions remain solutions to the unperturbed electron and photon wave equations (5.12) and (5.27), albeit with new propagation constants $\beta' = \beta_0 \pm \mu|\delta\beta|$ and angular frequencies $\omega' = \omega \mp \mu|\delta\omega|$.

As discussed previously, each component of the above superposition picks up a $\sigma\mu$-dependent phase factor from the SOI as the particle propagates down the waveguide as given by (5.83): the states in (5.98a) pick up factors of the form $e^{\pm i\mu|\delta\beta|z}$, while the states in (5.98b) pick up factors $e^{\pm i\sigma|\delta\beta|z}$, such that the resulting superposition states are

$$\cos\left(\frac{\tilde{\theta}}{2}\right)e^{-i\frac{\tilde{\phi}}{2}}e^{-i\mu|\delta\omega|t}\,|n\,m_\ell\,+\rangle + \sin\left(\frac{\tilde{\theta}}{2}\right)e^{i\frac{\tilde{\phi}}{2}}e^{i\mu|\delta\omega|t}\,|n\,m_\ell\,-\rangle$$

$$= N_{n|m_\ell|}\psi_{n|m_\ell|}\left(\rho\right)e^{i(m_\ell\phi+\beta_0 z-\omega t)}\left[\cos\left(\frac{\tilde{\theta}}{2}\right)e^{-i\mu\left(|\delta\omega|t+\mu\frac{\tilde{\phi}}{2}\right)}\hat{\mathbf{e}}_+ + \sin\left(\frac{\tilde{\theta}}{2}\right)e^{i\mu\left(|\delta\omega|t+\mu\frac{\tilde{\phi}}{2}\right)}\hat{\mathbf{e}}_-\right],$$

$$(5.99)$$

and

$$\cos\left(\frac{\tilde{\theta}}{2}\right)e^{-i\frac{\tilde{\phi}}{2}}e^{-i\sigma|\delta\omega|t}\,|n\,+|m_\ell|\,\sigma\rangle + \sin\left(\frac{\tilde{\theta}}{2}\right)e^{i\frac{\tilde{\phi}}{2}}e^{i\sigma|\delta\omega|t}\,|n\,-|m_\ell|\,\sigma\rangle$$

$$= N_{n|m_\ell|}\psi_{n|m_\ell|}\left(\rho\right)$$

$$\times\left[\cos\left(\frac{\tilde{\theta}}{2}\right)e^{i\left(|m_\ell|\phi-\sigma\left(|\delta\omega|t+\sigma\frac{\tilde{\phi}}{2}\right)\right)} + \sin\left(\frac{\tilde{\theta}}{2}\right)e^{-i\left(|m_\ell|\phi-\sigma\left(|\delta\omega|t+\sigma\frac{\tilde{\phi}}{2}\right)\right)}\right]e^{i(\beta_0 z-\omega t)}\hat{\mathbf{e}}_\sigma.$$

$$(5.100)$$

Since the respective equations (5.99) and (5.100) are identical in form to (5.86) and (5.96) under the substitution $|\delta\beta|\,z \leftrightarrow |\delta\omega|\,t$, we conclude that azimuthal precession of the spin and orbital Bloch vectors as derived above will occur with a temporal precession rate of $|\delta\omega|$ per unit t. Furthermore, all of the subsequently derived results (see (5.87)-(5.90) and (5.97)) also hold under the same replacement.

In comparison with the spatial manifestation of the SOI, the temporal manifestation is perhaps less natural: in the former case, a monoenergetic superposition state with an initially well-defined value for β_0 evolves under the SOI into a monoenergetic superposition state whose components have different propagation constants $\beta_0 \pm \delta\beta$ (see (5.86) and (5.96)).

Conversely, in the latter (temporal) case, the initial superposition components have different values for both their propagation constant and angular frequency, with the SOI *causing* a degeneracy in β so that only the frequencies remain distinct (see (5.99) and (5.100)). Nevertheless, transverse modes of light with temporal rotational characteristics reminiscent of the present SOI effect (so-called "optical ferris wheels") have been realized experimentally and have applications in the field of atom trapping [88]. Additionally, even more closely related free-space effects have been proposed in [89].

Applications

The spin and orbital rotation phenomena described in (5.89)-(5.90) and (5.97) each act as so-called Hadamard transformations on their associated subspaces. For the spin-polarization case, defining the qubits $|0\rangle \equiv \frac{1}{\sqrt{2}}\Big(|n\,m_\ell\,+\rangle + |n\,m_\ell\,-\rangle\Big)$ and $|1\rangle \equiv \frac{1}{\sqrt{2}}\Big(|n\,m_\ell\,+\rangle - |n\,m_\ell\,-\rangle\Big)$, we find that under the SOI an initial qubit state $|0\rangle$ evolves into the final qubit state $|\mu\rangle \equiv \frac{1}{\sqrt{2}}(|0\rangle + \mu\,|1\rangle)$ after propagating though a distance $z = \frac{1}{|\delta\beta|}\frac{\pi}{4\,|m_\ell|}$. Similarly, for the orbital case, defining qubits $|0\rangle \equiv \frac{1}{\sqrt{2}}\Big(|n\,+|m_\ell|\,\sigma\rangle + |n\,-|m_\ell|\,\sigma\rangle\Big)$ and $|1\rangle \equiv \frac{1}{\sqrt{2}}\Big(|n\,+|m_\ell|\,\sigma\rangle - |n\,-|m_\ell|\,\sigma\rangle\Big)$ leads to the evolution of initial state $|0\rangle$ into final state $|\sigma\rangle \equiv \frac{1}{\sqrt{2}}(|0\rangle + \sigma\,|1\rangle)$ when $z = \frac{1}{|\delta\beta|}\frac{\pi}{4\,|m_\ell|}$.

Because these spin and orbital Hadamard transformations (see Figs. 5.4(c) and 5.4(d)) are respectively controlled by the particle's OAM and SAM quantum numbers, the effects allow for the reversible transfer of entanglement between the SAM and OAM degrees of freedom of two-particle states. We demonstrate this here for the special case where

$|m_\ell| = 2$, for concreteness. Denoting the single-particle state in (5.97b) for $|m_\ell| = 2$ and

$z = 0$ as $|\sigma\ HG_{11}\rangle$, we consider a purely polarization-entangled Bell state with two pho-

tons in spatially separated HG_{11} (Hermite-Gauss-like) spatial modes, $|+\ HG_{11}\rangle\,|-\ HG_{11}\rangle -$

$|-\ HG_{11}\rangle\,|+\ HG_{11}\rangle$. In the product ket notation, the first ket represents the quantum state

of one particle, while the second ket represents that of the other, with each particle of the

two-particle entangled state propagating in a separate waveguide. According to (5.97b),

for $z = \dfrac{\pi}{8\,|\delta\beta|}$ (i.e., for $|\delta\beta|\,z = 22.5°$) this two-particle state will evolve under the SOI

to $|+\ HG_{11}^{+}\rangle\,|-\ HG_{11}^{-}\rangle - |-\ HG_{11}^{-}\rangle\,|+\ HG_{11}^{+}\rangle$, where the single-photon state $|\sigma\ HG_{11}^{\pm}\rangle$ de-

notes a photon whose transverse spatial wave function has been rotated $\pm22.5°$ from that of

the state $|\sigma\ HG_{11}\rangle$. By employing wave plates and spatial mode converters [90], it is pos-

sible to transform this state into $|D\ LG_{+2}\rangle\,|A\ LG_{-2}\rangle - |A\ LG_{-2}\rangle\,|D\ LG_{+2}\rangle$, where D and

A stand for 'diagonal' and 'anti-diagonal' (oriented at $\pm45°$) linear polarization (see Fig.

5.3), and $LG_{\pm2}$ stands for an OAM (Laguerre-Gauss-like) eigenstate with $m_\ell = \pm2$. Finally,

the complementary SOI interaction described by (5.89) and/or (5.90) evolves the state into

$|H\ LG_{+2}\rangle\,|H\ LG_{-2}\rangle - |H\ LG_{-2}\rangle\,|H\ LG_{+2}\rangle$, where H stands for horizontal polarization (see

Fig. 5.3).

Since we are left with a purely OAM-entangled Bell state, we have therefore demonstrated

the ability of the spin-orbit interaction to transfer entanglement between the spin and orbital

degrees of freedom of a two-particle state. Although we have used the polarization notation

here (D, A, H, etc.) the above results apply equally to electrons. Furthermore, by reversing

the order of the above operations, the entanglement may be restored to the spin degree of

freedom, so that this entanglement transfer is a reversible process. Finally, we note that when used in conjunction with a one-dimensional parity sorter (which can be made to act analogously to a polarizing beam splitter, but on the photonic transverses mode space, see Chapter III), the spin-controlled orbital rotation effect (which acts analogously to how a half wave plate acts on the photonic polarization state) may be used to construct transverse spatial mode-entangled cluster states for purposes of quantum information processing [91].

CHAPTER VI

SPIN-ORBIT INTERACTION AS A GEOMETRIC PHASE

In Chapter V, we showed that both electrons and photons exhibit a spin-orbit interaction (SOI) when propagating in a cylindrically symmetric medium by solving their respective wave equations perturbatively. We found that the Hamiltonians for both particles had analogous forms, leading to a single expression which describes the SOI for both particle types. However, the physical reason behind this similarity of the SOI between electrons and photons is not made transparent by using this direct approach. On the one hand, the origin of the SOI for electrons has a clear and direct physical interpretation, since electrons are massive charged particles which posses a spin magnetic moment: an electron traveling with a nonzero velocity with respect to an inhomogeneous electrostatic field will experience an effective magnetic field due to relativistic effects, which in turn interacts with the particle's spin magnetic moment. On the other hand, photons are both massless and chargeless and have no appreciable magnetic moment, but still behave analogously to electrons with respect to the SOI.

In this Chapter, we show that the common origin of the SOI effects in electrons and photons is a universal geometric phase associated with the interplay between either particle's spin angular momentum (SAM) and orbital angular momentum (OAM). This implies that the SOI occurs for any particle with spin, and thereby exists independently of whether or

not the particle has mass, charge, or magnetic moment. For simplicity, we focus on the special case of a step profile for the electron potential or photon permittivity, such that $\chi(\rho) = \theta_H(\rho)$ in the notation of Chapter V, with $\theta_H(\rho)$ being the Heaviside step function. To elucidate the aforementioned problem of the physical interpretation of the SOI, we first describe the SOI for electrons using a heuristic approach which relies on the existence of the electronic properties of mass, charge and magnetic moment. We then proceed to the geometric phase approach in which we arrive at a unified interpretation of the SOI for both electrons and photons, starting from the fundamental equation (2.48d). Finally, we compare the results of the geometric phase-based approach with the wave equation results derived in Chapter V.

Electronic Model of the Spin-Orbit Interaction

For the case of the electron, consider a cylindrically symmetric potential which can be modeled by two concentric cylindrical surfaces with nearly equal radii a and $a + \delta a$ (see Fig. 6.1). The inner cylinder is uniformly positively charged (as observed in the laboratory frame), and the outer cylinder is uniformly negatively charged, in such a way that overall the waveguide is neutral. The electric field is zero inside the inner cylinder and outside the outer cylinder, but is nonzero (and approximately constant) in the region between the cylinders, such that

$$\mathbf{E} = \mathcal{E}_0 \frac{a}{\rho} \Theta(\rho) \hat{\rho} \approx \mathcal{E}_0 \Theta(\rho) \hat{\rho}, \tag{6.1}$$
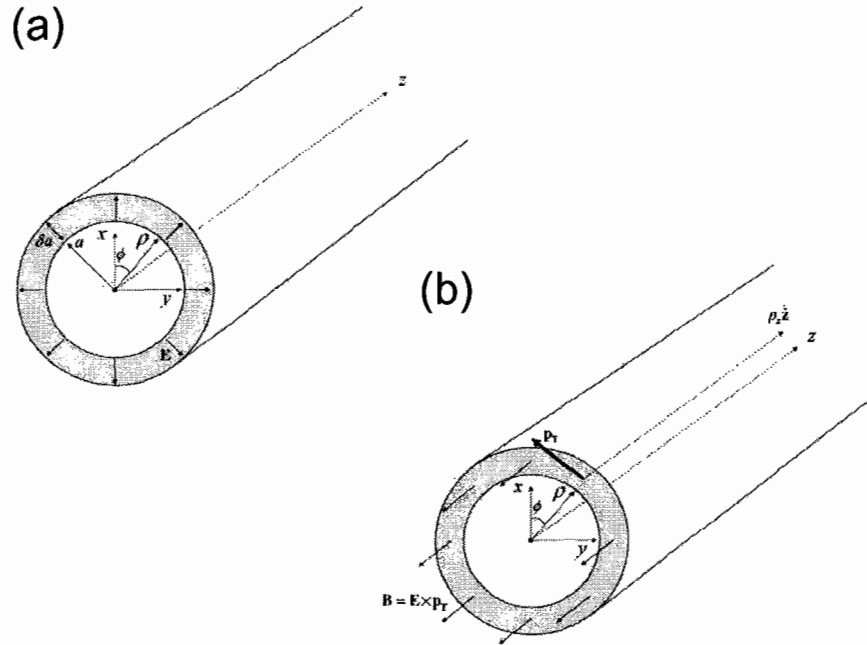
Figure 6.1. (a) Two concentric cylindrical surfaces with nearly equal radii a and $a +$ δa. The inner (outer) cylinder is positively (negatively) charged, thereby giving rise to an approximately constant electric field pointing radially outward between the cylinders, as expressed in equation (6.1). The electric field is zero elsewhere. (b) The magnetic field contribution due to an electron propagating paraxially between the cylinders of the waveguide with nonzero p_ϕ, as experienced in the electron's rest frame. As discussed in the main text, we ignore the contribution due to p_z (represented by the dotted arrow in the figure), so that the field shown in the figure is that due only to the transverse component of momentum $\mathbf{p}_T$ (represented by the bold arrow in the figure). This effective magnetic field points in the negative-z direction for anti-clockwise p_ϕ (as shown above), and in the positive-z direction for clockwise p_ϕ.

where $\Theta\left(\rho\right) \equiv \theta_H\left(\rho - a\right) - \theta_H\left(\rho - \left(a + \delta a\right)\right)$ with θ_H being the Heaviside step function and ρ the radial distance in cylindrical coordinates, and where $\hat{\rho}$ is the radial unit vector. The approximation on the right hand side of (6.1) is valid in the regime where $\delta a \ll a$. The magnetic field is zero everywhere in the laboratory frame.

We are interested in the case of an electron traveling down the cylinder with magnetic moment $\vec{\mu}$ and nonzero orbital angular momentum z-component $L_z = \rho p_\phi$ with respect to the cylinder axis (we presently treat the electron as a classical particle, and will subsequently quantize the problem). We also assume that the electron is moving paraxially with respect to the cylinder axis such that $|\mathbf{p}_T| \ll |\mathbf{p}_z|$, where $\mathbf{p}_z \equiv p_z\hat{z}$ and $\mathbf{p}_T \equiv p_\rho\hat{\rho} + p_\phi\hat{\phi}$ are the electron's longitudinal and transverse momenta in cylindrical coordinates, respectively. We will show that when such an electron is present in the region with nonzero electric field, the electronic motion gives rise to a spin-orbit interaction between its magnetic moment z-component μ_z and OAM L_z.

The standard theory of the electronic SOI is summarized in [92]. The magnetic field in the (primed) rest frame of the electron is

$$\mathbf{B}' = -\gamma\frac{\mathbf{v}}{c} \times \mathbf{E} \approx -\frac{\mathbf{v}}{c} \times \mathbf{E}, \tag{6.2}$$

where v is the electron velocity in the laboratory frame, and the Lorentz factor $\gamma \approx 1$ for sufficiently low v, which we will assume throughout this derivation. Also in (6.2), we have employed Gaussian units, following [92]. The presence of the electron's magnetic moment $\vec{\mu}$ in such a field gives rise to a magnetic dipole interaction energy $H' = -\vec{\mu} \cdot \mathbf{B}'$. After

accounting for the relativistic Thomas precession effect [92], which effectively contributes a factor of $\frac{1}{2}$, this energy becomes

$$H' = \tfrac{1}{2}\vec{\mu} \cdot \left(\frac{\mathbf{v}}{c} \times \mathbf{E}\right) = -\frac{1}{2mc}\vec{\mu} \cdot \left(\mathbf{E} \times (p_z\hat{z} + \mathbf{p}_T)\right), \tag{6.3}$$

where $\mathbf{p} = p_z\hat{z} + \mathbf{p}_T$ is the electron momentum in the laboratory frame. The SOI Hamiltonian therefore contains two parts in our present case with respective forms $\vec{\mu} \cdot (\mathbf{E} \times p_z\hat{z})$ and $\vec{\mu} \cdot (\mathbf{E} \times \mathbf{p}_T)$. As the former term depends on the longitudinal momentum p_z only, and therefore does not involve the electron's transverse OAM, we henceforth disregard it as a candidate for SOI. Upon employing (6.1), however, it is evident that the latter term involves a magnetic field vector proportional to $\mathbf{E} \times \mathbf{p}_T = \mathcal{E}_0 p_\phi \Theta(\rho)\,\hat{\mathbf{z}}$, which points either *parallel* or *anti-parallel* with the z-axis according to the sign of $p_\phi = \dfrac{1}{\rho}L_z$ (see Fig. 6.1). From (6.3), this results in a SOI energy contribution of

$$H_{\mathrm{SOI}} \approx -\frac{1}{2mc}\frac{\mathcal{E}_0}{a}\mu_z L_z \Theta(\rho), \tag{6.4}$$

where $\rho \approx a$ has been used. From (6.4) it is evident that when the electron is in the region $a \le \rho \le a + \delta a$, it experiences a SOI energy shift proportional to the *product* of μ_z and L_z. In other words, the *sign* of the spin-orbit energy shift depends upon whether μ_z and L_z are pointing *parallel* or *anti-parallel* to each other.

We quantize (6.4) by letting $\mu_z \to -\dfrac{e}{mc}\hat{S}_z = -\dfrac{e\hbar}{2mc}\hat{\sigma}_z$ and $L_z \to -i\hbar\partial_\phi \equiv \hbar\hat{\ell}_z$ ($\hat{\sigma}_z$ is the Pauli matrix), so that the quantized Hamiltonian is

$$\hat{H}_{\text{SOI}} = \frac{e}{4mc^2} \frac{\mathcal{E}_0 \hbar^2}{ma} \hat{\sigma}_z \hat{\ell}_z \Theta\left(\rho\right), \tag{6.5}$$

where $e = |e|$ is the elementary charge.

The Hamiltonian in (6.5) is analogous to that which arises from an electron orbiting around a proton in a hydrogen atom—the canonical example for SOI. In that case, the electric field can be written as $\mathbf{E} = \frac{1}{r}\mathcal{E}_0^{Coulomb}\mathbf{r}$, where $\mathcal{E}_0^{Coulomb} = \frac{e}{r^2}$ is the Coulomb field due to the proton, so that the Hamiltonian in (6.3) gives rise to the well-known atomic spin-orbit coupling Hamiltonian for a Coulomb potential [37]:

$$\hat{H}_{\text{Coulomb}} = \frac{e}{4mc^2} \frac{\mathcal{E}_0^{Coulomb} \hbar^2}{mr} \hat{\sigma} \cdot \hat{\ell}, \tag{6.6}$$

where $\hat{\sigma} \equiv \frac{\hat{\mathbf{S}}}{\hbar}$ and $\hat{\ell} \equiv \frac{\hat{\mathbf{L}}}{\hbar}$ are the dimensionless SAM and OAM vector operators.

Though the Hamiltonians in (6.5) and (6.6) have similar forms and in both cases the SOI arises from the same Hamiltonian (6.3), the difference between the spherical and cylindrical geometries has significant physical consequences. In particular, for the cylinder case the spin and orbital quantum angular momentum operators corresponding to the quantities μ_z and L_z *commute* with the Hamiltonian, while for the atomic interaction this is not the case, so that one must use the *total* angular momentum operator $\hat{J}^2$ and the z-component of total angular momentum $\hat{J}_z$ in the place of these. Therefore, while the total angular momentum quantum numbers j and m_j are good quantum numbers for the hydrogen atom, the spin and OAM quantum numbers σ and m_ℓ are not. Conversely, σ, m_ℓ and m_j are *all* good

quantum numbers for the cylinder case (though j is not, due to the breaking of the spherical symmetry), so that states with well-defined σ and m_ℓ are energy eigenstates.

In order to compare the heuristically derived Hamiltonian (6.5) with our previous (more rigorous) results, we note that the Hamiltonian $\hat{H}_{SOI}$ acts as a perturbation to the *energy* of the electron as opposed to its propagation constant β_0. In order to render (6.5) comparable to our effective Hamiltonian (5.78) in Chapter V, we must multiply it by a factor $-\dfrac{2m}{\hbar^2}$, so that the effective spin-orbit Hamiltonian becomes

$$\hat{H}_{\text{SO}}^{\text{(Heuristic)}} = -\frac{\Delta}{2}\frac{\Theta\left(\rho\right)}{a}\hat{\sigma}_z\hat{\ell}_z, \tag{6.7}$$

where $\mathcal{E}_0 \approx V\left(0\right) - V\left(a\right)$ and $\Delta \equiv \dfrac{e\left(V\left(0\right) - V\left(a\right)\right)}{mc^2}$ have been used (the negative sign in the factor $-\dfrac{2m}{\hbar^2}$ arises from the electronic dispersion relation as we have demonstrated in a previous paper [93]). Substituting the Heaviside step function such that $\chi\left(\rho\right) \to \theta_H\left(\rho - a\right)$ in the rigorously derived equation (5.78) yields

$$\hat{H}_{\text{SO}}^{\text{(Eff)}} = -\frac{\Delta}{2}\frac{\delta\left(\rho - a\right)}{\rho}\hat{\sigma}_z\hat{\ell}_z, \tag{6.8}$$

where $\partial_\rho\theta_H\left(\rho - a\right) = \delta\left(\rho - a\right)$ has been used, with $\delta\left(\rho - a\right)$ being the Dirac delta function. We conclude that our heuristic derivation yields the correct result, since the function $\Theta\left(\rho\right)$ plays a similar role as $\delta\left(\rho - a\right)$ in the Hamiltonian by setting $\rho \approx a$ upon the evaluation of any expectation values.

Note however that the derivation of (6.7) relied on the interaction of the spin magnetic moment of the electron with the effective magnetic field $\mathbf{B}'$, cf. (6.2)–(6.4). Because of

this there is no clear way to arrive at an analogous heuristic derivation of the spin-orbit interaction for the photon, which lacks a magnetic moment. We presently overcome this difficulty by analyzing the SOI from the viewpoint of the geometric phase.

Spin-Orbit Interaction as a Geometric Phase

Consider an electron or photon in a spin-orbit wave packet (see (2.12f)) with $m_\ell = 0$, propagating along the well-defined (semiclassical) trajectory of a circular helix with constant radius a and pitch angle θ, such that the helix pitch is $h_z = \dfrac{2\pi a}{\tan(\theta)}$ as pictured in Figs. 2.3 and 2.1. As we showed in Chapter II, in a single helical cycle such an electron or photon will accumulate a geometric phase as given by (2.49), which is a special case of the general equation (2.48d),

$$\Phi_B = -\lambda\sigma\Omega = -\lambda\sigma 4\pi\sin^2\frac{\theta}{2}. \tag{6.9}$$

In (6.9), λ is the particle helicity magnitude, σ is the SAM quantum number of the spin-orbit wave packet, $\Omega = 4\pi\sin^2\dfrac{\theta}{2}$ is the total solid angle subtended by the particle's momentum-space curve C as seen from the origin, and the (intrinsic) OAM quantum number m_ℓ of the wave packet has been set to zero. If the handedness of the above helical path is reversed, so is the orientation of the closed surface bounded by C, so that the accumulated Berry phase is still given by (6.9) but with $\Omega \to -\Omega$. In order to take into account this sign dependence of the Berry phase Φ_B on the handedness of the helical path, we introduce the sign factor $\mu_h = \pm 1$ in (6.9). Furthermore, in order to extend the result to an arbitrary number of

helical cycles we multiply Φ_B by $\dfrac{z}{h_z}$, where z is the axial particle position. In this way, the total accumulated geometric phase γ may be written as a function of both the helix handedness μ_h and the axial particle position z:

$$\gamma = -\lambda\sigma\mu_h\frac{\Omega}{h_z}z. \tag{6.10}$$

We now apply (6.10) to the case of an electron (photon) traveling in a helical path along the cylindrical surface of a waveguide with a step profile for the potential (permittivity), such that the helix pitch angle is θ. We further assume that the dimensionless waveguide parameter Δ (defined in Chapter V) obeys the weakly-guiding (paraxial) condition $\Delta \ll 1$, so that the pitch angle θ approaches the critical angle for total internal reflection of the wave fronts of the electron (photon) wave function. In such a case, we have $\theta \ll 1$ such that $\theta \approx \sqrt{\Delta}$ (cf. [63]), so that

$$\Omega = 4\pi\sin^2\frac{\theta}{2} \approx \pi\theta^2 \approx \pi\Delta, \tag{6.11}$$

and

$$h_z \approx \frac{2\pi a}{\theta}, \tag{6.12}$$

which yields

$$\gamma \approx -\lambda\sigma\mu_h\frac{\Delta}{2a}\theta z. \tag{6.13}$$

Furthermore, in this paraxial regime we may equate the magnitude λ of the particle helicity with the magnitude s of the particle spin along the z axis, and the sign of the helix handedness μ_h with the sign of the OAM quantum number μ, so that $\lambda \to s$ and $\mu_h \to \mu$, respectively. With these replacements, the accumulated geometric phase γ then gives rise to the effective propagation constant shift $\delta\beta_{\text{geo}} = \dfrac{\gamma}{z}$,

$$\delta\beta_{\text{geo}} = -s\sigma\mu\frac{\Delta}{2a}\theta. \tag{6.14}$$

Equation (6.14) is our desired equation for the effective propagation constant shift due to the accumulated geometric phase of an electron or photon propagating in a cylindrical medium; it gives $\delta\beta$ in terms of the magnitude of the particle spin s, the signs σ and μ of the SAM and OAM quantum numbers, and the geometric parameters Δ, a, and θ associated with the waveguide.

Comparison of the Berry Phase and Wave Equation Results

Here we compare the geometric result (6.14) with the wave equation results for the first-order propagation constant shifts $\delta\beta$ as calculated in equation (5.81) of Chapter V:

$$\delta\beta = -\sigma m_\ell \Delta \frac{\pi}{2\beta_0} N^2_{n|m_\ell|} \int d\rho \, (\partial_\rho \chi(\rho)) \, \psi^2_{n|m_\ell|}(\rho). \tag{6.15}$$

As already calculated above, $\partial_\rho \chi(\rho) \to \delta(\rho - a)$ for the special case of step profile which we are considering here, so that the above integral is easily evaluated as

$$\int d\rho \delta \left(\rho - a \right) \psi_{n|m_\ell|}^2 \left(\rho \right) = \psi_{n|m_\ell|}^2 \left(a \right). \tag{6.16}$$

Furthermore, the unperturbed electron and photon wave equations (5.12) and (5.27) each reduce to the following equation in the step profile case,

$$\hat{\nabla}_T^2 \Psi_{n|m_\ell|\sigma} = - \left(k^2 - \beta_0^2 \right) \Psi_{n|m_\ell|\sigma} \equiv -\kappa^2 \Psi_{n|m_\ell|\sigma}, \tag{6.17}$$

where $k^2 \left(\rho \right)$ is a piecewise constant function of ρ such that

$$k^2 \left(\rho \right) = \frac{2m}{\hbar^2} \left(E + eV \left(0 \right) \left(1 - \frac{V \left(0 \right) - V \left(a \right)}{V \left(0 \right)} \theta_H \left(\rho \right) \right) \right) \tag{6.18}$$

for electrons and

$$k^2 \left(\rho \right) = \omega^2 \mu_0 \epsilon \left(0 \right) \left(1 - \frac{\epsilon \left(0 \right) - \epsilon \left(a \right)}{\epsilon \left(0 \right)} \theta_H \left(\rho \right) \right) \tag{6.19}$$

for photons, and we have defined $\Psi_{n|m_\ell|\sigma} \equiv N_{n|m_\ell|} \psi_{n|m_\ell|} \left(\rho \right) e^{im_\ell\phi} e^{i(\beta_0 z - \omega t)} \hat{\mathbf{e}}_\sigma$ and $\kappa^2 \equiv k^2 - \beta_0^2$ for both particles.

Upon substitution of the monoenergetic wave function $\Psi_{n|m_\ell|\sigma}$ into (6.17), this step-profile wave equation leads to the following radial equation (cf. (5.48)),

$$\left(\partial_\rho^2 + \frac{1}{\rho} \partial_\rho - \frac{m^2}{\rho^2} + \kappa^2 \right) \psi_{n|m_\ell|} \left(\rho \right) = 0. \tag{6.20}$$

This is Bessel's differential equation, with solutions

$$\psi_{n|m_\ell|}(\rho) = J_{|m_\ell|}\left(\kappa_{n|m_\ell|}\rho\right) \tag{6.21}$$

for $\rho \leq a$, and

$$\psi_{n|m_\ell|}(\rho) = K_{|m_\ell|}\left(\tilde{\kappa}_{n|m_\ell|}\rho\right), \tag{6.22}$$

for $\rho \geq a$. Here, $J_{|m_\ell|}\left(\kappa_{n|m_\ell|}a\right)$ is an m_ℓ^{th}-order Bessel function of the first kind, and $K_{|m_\ell|}\left(\tilde{\kappa}_{n|m_\ell|}\rho\right)$ is an m_ℓ^{th}-order modified Bessel function of the second kind. The coefficients $\kappa_{n|m_\ell|}$ and $\tilde{\kappa}_{n|m_\ell|}$ are determined by requiring the radial wave function $\psi_{n|m_\ell|}(\rho)$ and its first derivative $\partial_\rho\psi_{n|m_\ell|}(\rho)$ to be continuous at the step boundary where $\rho = a$, which leads to the following characteristic equation,

$$\kappa_{n|m_\ell|}a\frac{J_{|m_\ell|+1}\left(\kappa_{n|m_\ell|}a\right)}{J_{|m_\ell|}\left(\kappa_{n|m_\ell|}a\right)} = \tilde{\kappa}_{n|m_\ell|}a\frac{K_{|m_\ell|+1}\left(\tilde{\kappa}_{n|m_\ell|}a\right)}{K_{|m_\ell|}\left(\tilde{\kappa}_{n|m_\ell|}a\right)}, \tag{6.23}$$

where the Bessel identities $\partial_\rho Z_{|m_\ell|}\left(\kappa_{n|m_\ell|}\right) = \frac{\kappa_{n|m_\ell|}}{2}\left(Z_{|m_\ell|-1}\left(\kappa_{n|m_\ell|}\right) - Z_{|m_\ell|+1}\left(\kappa_{n|m_\ell|}\right)\right)$ and $Z_{|m_\ell|+1}\left(\kappa_{n|m_\ell|-1}\right) = \frac{2m_\ell}{\kappa_{n|m_\ell|}a}\left(Z_{|m_\ell|}\left(\kappa_{n|m_\ell|}\right) - Z_{|m_\ell|+1}\left(\kappa_{n|m_\ell|}\right)\right)$ have been used, with Z standing in for either the J or the K Bessel function.

Equation (6.23) yields a distinct characteristic equation for each value of of the OAM quantum number m_ℓ and radial quantum number n, with each characteristic equation consisting of a single equation in the two dimensionless unknowns $\kappa_{n|m_\ell|}a$ and $\tilde{\kappa}_{n|m_\ell|}a$. In order to find a second equation in these variables, we construct the quantity

$$k^2(a) - k^2(0) = \left(\tilde{\kappa}_{n|m_\ell|} - \kappa_{n|m_\ell|}\right)a \equiv V^2 \tag{6.24}$$

(see (6.18) and (6.19)), so that $\kappa_{n|m_\ell|}a$ and $\tilde{\kappa}_{n|m_\ell|}a$ may be calculated by substituting (6.24) in to (6.23) and numerically solving the resulting transcendental equation. Note also that for a given value of m_ℓ, a solution of (6.23) exists for all values of n up to an m_ℓ-dependent maximum threshold value of n above which no further solutions to (6.23) exist for that value of m_ℓ. Furthermore, there also exists a threshold value for m_ℓ above which there is no value for n which solves (6.23), so that the allowed values for m_ℓ and n are always finite.

It follows from the above considerations that for $\rho \leq a$ the "radial" wave functions $\psi_{n|m_\ell|}^2 (a)$ may be expressed as

$$\psi_{n|m_\ell|}^2 (a) \to J_{|m_\ell|}^2 \left(\kappa_{n|m_\ell|}a \right), \tag{6.25}$$

in a step-profile medium, so that from (6.15) and (6.16) the propagation constant shifts become

$$\delta\beta = -\sigma\mu\frac{\Delta}{2}\frac{|m_\ell|}{\beta_0}\pi N_{n|m_\ell|}^2 J_{|m_\ell|}^2 \left(\kappa_{n|m_\ell|}a \right), \tag{6.26}$$

where $m_\ell \equiv \mu |m_\ell|$ has been used, and the normalization factor $N_{n|m_\ell|}^2$ may be readily evaluated from (5.13) and (5.28) with (6.21) and (6.22):

$$
N_{n|m_\ell|}^2 = \frac{1}{\pi a^2} \frac{1}{J_{|m_\ell|}^2 \left(\kappa_{n|m_\ell|}a \right)}
$$
$$
\times \left\{ \frac{K_{|m_\ell|-1} \left(\tilde{\kappa}_{n|m_\ell|}a \right) K_{|m_\ell|+1} \left(\tilde{\kappa}_{n|m_\ell|}a \right)}{K_{|m_\ell|}^2 \left(\tilde{\kappa}_{n|m_\ell|}a \right)} - \frac{J_{|m_\ell|-1} \left(\kappa_{n|m_\ell|}a \right) J_{|m_\ell|+1} \left(\kappa_{n|m_\ell|}a \right)}{J_{|m_\ell|}^2 \left(\kappa_{n|m_\ell|}a \right)} \right\}^{-1}.
$$
$$\tag{6.27}$$

From (6.26) and (6.27), we may then write an explicit formula for the propagation constant shifts,

$$
\delta\beta = -\sigma\mu\frac{\Delta}{2a}\frac{|m_\ell|}{\beta_0 a}
$$
$$
\times \left\{ \frac{K_{|m_\ell|-1}\left(\tilde{\kappa}_{n|m_\ell|}a\right)K_{|m_\ell|+1}\left(\tilde{\kappa}_{n|m_\ell|}a\right)}{K^2_{|m_\ell|}\left(\tilde{\kappa}_{n|m_\ell|}a\right)} - \frac{J_{|m_\ell|-1}\left(\kappa_{n|m_\ell|}a\right)J_{|m_\ell|+1}\left(\kappa_{n|m_\ell|}a\right)}{J^2_{|m_\ell|}\left(\kappa_{n|m_\ell|}a\right)} \right\}^{-1}.
$$

$$(6.28)$$

Although the geometric phase result (6.14) does not coincide exactly with the more accurate perturbative result (6.28), their forms are seen to be strikingly similar when it is recognized that the factor in curly brackets in (6.28) is of order one when $|m_\ell|$ is near its maximal allowed (threshold) value. Furthermore, for waveguides with a relatively large radius a such that $V^2 \gg 1$, one may define a "semiclassical" limit of large OAM ($|m_\ell| \gg 1$), which corresponds to a helical path near the interface of the waveguide. Since most of the electron or photon wave function is well-localized near the fiber radius a in this limit, we would expect agreement with our geometric phase model in which we have assumed a helix radius equal to the fiber radius a. Upon performing a numerical analysis involving the solution of (6.23) and (6.24), we find that in this semiclassical limit the term in curly brackets in (6.28) approaches unity, while $\frac{m_\ell}{\beta_0 a} \to \theta$. Equations (6.14) and (6.28) are therefore in complete agreement for photons, where $s = 1$. For electrons however, $s = \frac{1}{2}$, for which (6.14) yields half of the shift given by the more rigorous perturbative calculation. This apparent discrepancy can be explained by recalling that in deriving the result (6.14) we *required* the parallel transport of the spin for both particles (cf. Appendix B). Although

this assumption is consistent with our result for photons, our effective SOI Hamiltonian $\hat{H}_{SO}^{(Eff)}$ in (5.78) actually causes the electron spin vector $\langle \hat{\mathbf{S}} \rangle$ to precess at *twice* the rate of the photon polarization vector (cf. (5.87b) and (5.89) in Chapter V and the subsequent discussion). One therefore expects the accumulated phase due to the electron spin evolution to be precisely double the amount predicted by (6.14), as we reported in [84].

As was shown explicitly in Chapter V through the derivation of (5.86) and (5.96), it is the SAM and OAM Bloch vectors of the electron and photon which evolve analogously under the SOI, as opposed to the electron spin and the photon polarization vectors. It is therefore these more abstract quantities which undergo parallel transport due to the spin-orbit interaction according to (5.86) and (5.96) resulting in the SOI rotational effects discussed in in Chapter V. We therefore conclude that the spin-orbit interaction dynamics of the electron and photon are identical to first order in perturbation theory and have a common geometric origin, with the role of the electron's potential energy $U(\rho)$ being played by the permittivity $\epsilon(\rho)$ in the photon case.

CHAPTER VII

CONCLUSIONS

In this dissertation, we have presented experimental and theoretical techniques for the measurement and control of transverse photonic degrees of freedom. In Chapter II we presented a general theory of a quantum "spin-orbit" wave packet with well-defined values of intrinsic spin angular momentum (SAM) and orbital angular momentum (OAM), propagating in a weakly inhomogeneous medium with a cyclically varying momentum. We found that a particle (either an electron or a photon) in such a wave packet exhibits a geometric phase which depends upon both the spin and orbital quantum numbers, as well the magnitude of the particle helicity and the geometric properties of the particle trajectory as given in (2.48d):

$$\Phi_B = - \left(\lambda \sigma + m_\ell \right) \Omega. \tag{7.1}$$

Here, λ is the particle helicity magnitude, σ and m_ℓ are the respective SAM and OAM quantum numbers of the spin-orbit wave packet, and Ω is the momentum-space solid angle subtended by a cyclical loop.

Equation (7.1) has two contributions; the $-\lambda\sigma\Omega$ term, which is different for electrons and photons by a factor of one-half, and the $-m_\ell\Omega$ term, which is the same for both particles. Since both terms are connected with geometric properties of the curvilinear particle trajec-

tory (i.e., the particle's "orbit") through the Ω term, we conclude that the spin-dependent $-\lambda\sigma\Omega$ term plays the role of a semiclassical "spin-orbit" interaction, while the intrinsic OAM-dependent $-\lambda m_\ell\Omega$ term plays the role of a semiclassical "orbit-orbit" interaction in which the intrinsic OAM and the semiclassical extrinsic orbital motion interact via the geometric phase. For photons (where $\lambda = 1$), the symmetry between the spin-dependent term and the OAM-dependent term has the consequence that the polarization state of a linearly polarized beam-like light field rotates at the same rate as the transverse image carried by the field due to this semiclassical geometric phase effect. As a consequence, any series of out-of-plane mirror reflections will have the same transverse rotational effect on polarization as is does on beam image.

In Chapter III, we presented theoretically the properties of interferometric devices based on both one-dimensional and two-dimensional transverse mode parity of photons. We showed how the interferometer based on one-dimensional parity can be made to act as a polarizing beam splitter (Fig. 3.7(a)), or a linear-to-circular polarization converter (Fig. 3.7(b)) for well-defined Hermite-Gauss (HG) modes, and a one-dimensional (1-D) parity sorter (Fig. 3.7(c)) or an Hermite-Gauss to Laguerre-Gauss (HG-to-LG) mode converter (Fig. 3.7(d)) for modes with well-defined (vertical or horizontal) linear polarization states. In the former pair of cases, the action of the interferometer on the polarization state depended upon the parity properties of the input transverse spatial mode, while in the latter pair, the action on the spatial mode depended on the input polarization state. In this sense, the 1-D parity interferometer couples the spin and orbital degrees of freedom of photons, even though as

an in-plane device it does not operate according to any geometric phase-based interactions in the sense of (7.1). For the interferometer based on two-dimensional (2-D) parity, we showed how it can be made to act as a 2-D parity sorter (Fig. 3.8(a)) or a device which imparts a positive (negative) phase shift to modes which are even (odd) with respect to their 2-D parity (Fig. 3.8(b)). We introduced a new type of phase-stable interferometric 2-D parity sorter, an out-of-plane Sagnac interferometer whose sorting capabilities are based on the geometric phase effect of (7.1). Two-dimensional transverse spatial parity provides a second, type of qubit encoding that is based on continuous photonic degrees of freedom in addition to previously realized schemes based on one-dimensional parity. This new type of encoding can be made more robust than the 1-D case due to the stability of our Sagnac interferometer.

In Chapter IV, we experimentally verified predictions made in Chapter III. We observed the predicted behavior of the 1-D parity interferometer as both a 1-D parity sorter and an HG-to-LG mode converter, and of the 2-D parity interferometer as a 2-D parity sorter. In doing so, we realized the first 2-D parity measurements of Hermite-Gauss transverse spatial modes, and demonstrated the stable sorting of these modes according to their 2-D parity. Additionally, we employed the 2-D sorter to sort the output modes of a "three-mode" optical fiber. Although we observed port B of our interferometer (see Fig. 4.3) as operating at 95% or better efficiency for all input modes, a detailed loss and efficiency analysis of the device allowed us to conclude that it can be realistically made to work at nearly 100% efficiency. We also discussed several applications of this interferometer, including its use

as an alternative to holograms in spatial mode filtering, the measurement of the OAM of single photons, the production of Bell states entangled in first-order transverse spatial modes, and the production of heralded single photons in first-order transverse spatial states corresponding to an arbitrary point of the first-order spatial mode Poincaré sphere.

In Chapter V, we provided the first unified treatment of the spin-orbit interaction (SOI) for both electrons and photons in the "wave function" picture, in which the full wave nature of each particle is taken into account. Solving both the Dirac and Maxwell equations perturbatively in a straight cylindrical waveguide, we showed that the effective SOI Hamiltonian has the same form for both electrons and photons. As a consequence of this, we found that the SOI is quantitatively described by a single expression applying to either an electron or a photon, which predicts that either particle picks up a phase Φ due to the SOI of the general form

$$\Phi \propto \sigma m_\ell z, \tag{7.2}$$

where z is the distance the particle has propagated down the waveguide.

Using this expression, we predicted the possibility of four distinct spatio-temporal spin and orbital rotational effects for each particle, in which the particle's spin and orbital degrees of freedom influence one another due to the SOI as it propagates down the waveguide. Specifically, we found that the SOI can cause the particle's spin/polarization Bloch vector, with initial spherical polar angles $\tilde{\theta}, \tilde{\phi}$, to precess in the azimuthal ($\hat{\phi}$) direction with a precession rate of $|\delta\beta|$ per unit z, with the direction of precession controlled by the absolute

sign μ of the OAM (see Fig. 5.1). Conversely, the SOI can additionally cause the particle's OAM Bloch vector to precess in the azimuthal direction with the same precession rate $|\delta\beta|$, with the direction of precession controlled by the absolute sign σ of the SAM. We conclude that the spin/polarization and OAM Bloch sphere dynamics are the same for both electrons and photons with respect to the SOI, although the precession rate of the average electron spin vector is twice the rate of that of the photon polarization vector due to the geometric differences between spinors and vector dynamics. Employing these rotation effects, we also demonstrated theoretically that these rotational phenomena allow for the reversible transfer of entanglement between the SAM and OAM degrees of freedom of two-particle states.

Finally, in Chapter VI, we focused on the special case of SOI in a waveguide with a step-profile for the electronic potential or the photonic permittivity, and used (7.1) to show that the common origin of the SOI effects in electrons and photons is a universal geometric phase associated with the parallel transport of each particle's SAM and OAM Bloch vectors. Recent numerical studies carried out by us for arbitrary waveguide parameter V suggest a conincidence between the strength of the SOI for a particle with average radial position ρ_{Avg} as calculated by (6.28), and the magnitude of the geometric phase as calculated by (6.14), with the radius of the semiclassical helical trajectory chosen according to $a \to \rho_{\mathrm{Avg}}$ and with $s \to 1$. This suggests that the geometric phase analogy may be carried at least approximately beyond the semiclassical limit of large, "near-threshold" OAM.

Final Remarks

The research presented in this dissertation makes possible several future directions that could prove fruitful for the measurement and control of transverse spatial states of light. Consider first the transverse spatial parity-based interferometers discussed in Chapter III. Although our focus was primarily upon the 2-D parity sorter due to its superior phase stability as compared to the interferometer based on 1-D parity, the latter interferometer may also be productively used to manipulate the transverse spatial output of a biphoton state from spontaneous parametric down conversion. Furthermore, since the 1-D parity interferometer (unlike its 2-D counterpart) allows for nontrivial interaction between the spin and orbital photonic degrees of freedom, employing a sufficiently stable version could open up fruitful new avenues toward the engineering of biphoton states.

A second direction involves further study of the photonic spin-orbit interaction in other geometries besides that of the cylindrically symmetric case. For example, to the author's knowledge the SOI effects for a spherically symmetric permittivity remains an open question for the photonic case, although the electronic analogue is, of course, the well-known textbook problem of a hydrogenic atom (i.e., an electron in a spherically symmetric electrostatic potential). Do the photon and electron exhibit analogous physical characteristics in the spherical case, as they have been found to do under cylindrical symmetry? Although this particular question does not seem to have been discussed in the literature, the coupling of photons into micron-scale glass microspheres is a well-studied and experimentally accessible

field [94]. Further study of such a spherically symmetric "photonic hydrogen" system has the potential to be of both pedagogical and practical value. Pedagogically speaking, in solving the electronic and photonic versions of a similar problem in tandem leads to a deeper understanding of how both particles behave, as we have already seen in the cylindrical case. Practically speaking, with a functional photonic analogue of the hydrogen atom in hand, one could bring to bear 100 years of collective experience in atomic physics in order to probe the physics of the photon, thereby informing the study of photons with electrons, and vice versa.

A major theme throughout this thesis is an emphasis on treating both electrons and photons on an analogous footing, as quantum particles obeying their respective relativistic wave equations. From this perspective, we derived a "semiclassical" spin-orbit Berry phase as proportional to the sum of the helicity and OAM quantum numbers: $\lambda\sigma + m_\ell$. In contrast, the "quantum" Berry phase for a particle in a straight waveguide is proportional not to the *sum* of σ and m_ℓ, but their *product* σm_ℓ. Although these interactions therefore seem to have different forms, we have arrived at a semiclassical limit of the latter expression via direct application of the former, by identifying the extrinsic OAM associated with the semiclassical orbital path with the intrinsic OAM for a quantum particle in a straight waveguide. Since the full details of the connection between the geometric phase and the spin-orbit interaction in the wave function picture remain unclear, what is clear is the need for further study along these lines.

APPENDIX A

THE PHOTON WAVE EQUATION AND THE PARAXIAL LIMIT

In this appendix we derive and solve an exact three-component Schrödinger-type wave equation for a monoenergetic beam-like photon propagating in free space, and then take the paraxial limit of this wave equation and its solutions.

We begin with Maxwell's equations in free space, which for monoenergetic electromagnetic fields $\mathbf{E}(\mathbf{r}, t) = \mathbf{E}(\mathbf{r}) e^{-i\omega t}$ and $\mathbf{H}(\mathbf{r}, t) = \mathbf{H}(\mathbf{r}) e^{-i\omega t}$ may be written as [60]

$$\nabla \cdot \mathbf{E} = 0, \tag{A.1a}$$

$$\nabla \cdot \mathbf{H} = 0, \tag{A.1b}$$

$$\nabla \times \mathbf{E} = i\omega\mu_0\mathbf{H}, \tag{A.1c}$$

$$\nabla \times \mathbf{H} = -i\omega\epsilon_0\mathbf{E}, \tag{A.1d}$$

Multiplying (A.1a) and (A.1c) by the factor $\dfrac{1}{\sqrt{2\mu_0}}$, multiplying (A.1b) and (A.1d) by the factor $\dfrac{\Sigma i}{\sqrt{2\epsilon_0}}$ (with $\Sigma = \pm 1$), and adding (A.1a) to (A.1b) and (A.1c) to (A.1d) yields the respective equations

$$\nabla \cdot \mathbf{F}_\Sigma = 0, \tag{A.2a}$$

$$\nabla \times \mathbf{F}_\Sigma = \Sigma k \mathbf{F}, \tag{A.2b}$$

where $\mathbf{F}_\Sigma \equiv \dfrac{1}{\sqrt{2}} \left(\sqrt{\epsilon_0}\mathbf{E} + \Sigma i \sqrt{\mu_0}\mathbf{H} \right)$ is known as the Riemann-Silberstein vector, and $k = \omega\sqrt{\epsilon_0\mu_0}$ has been used. The Riemann-Silberstein vector $\mathbf{F}_\Sigma$, which may be thought of as the wave function for the photon [26, 27, 95], therefore obeys the wave equation (A.2b), with (A.2a) playing the role of an auxiliary condition on $\mathbf{F}_\Sigma$.

For a specific value of Σ, $\mathbf{F}_\Sigma$ may be thought of as a component of a photon wave function with helicity Σ, so that a complete six-component photon wave function $\mathcal{F}$ may be constructed by composing Riemann-Silberstein vectors of positive and negative helicity:

$$\mathcal{F} = \frac{1}{\sqrt{2}} \begin{pmatrix} (\sqrt{\epsilon_0}\mathbf{E} + i\sqrt{\mu_0}\mathbf{H}) \\ (\sqrt{\epsilon_0}\mathbf{E} - i\sqrt{\mu_0}\mathbf{H}). \end{pmatrix} \tag{A.3}$$

In (A.3), the upper and lower components, which are three dimensional vectors, respectively transform according to the irreducible representations $(1,0)$ and $(0,1)$ of the proper Lorentz group. In this sense, the object (A.3) stands in complete analogy with the spinor wave function for massless spin-$\dfrac{1}{2}$ particles which obeys the Weyl equation, and whose upper and lower spinorial components transform according to the irreducible representations $\left(\dfrac{1}{2},0\right)$ and $\left(0,\dfrac{1}{2}\right)$ of the proper Lorentz group. In contrast to wave functions for massive particles, the bilinear product $\mathcal{F}^\dagger\mathcal{F}$ is an energy density as opposed to a probability density, so that the volume integral $\mathcal{F}^\dagger\mathcal{F}'$ of two distinct photon wave functions $\mathcal{F}$ and $\mathcal{F}'$ cannot be interpreted as the probability amplitude for finding a photon in the state $\mathcal{F}$, when it is known to be in state $\mathcal{F}'$ [96]. However, for a photon described by a given wave function $\mathcal{F}$, the product $\mathcal{F}^\dagger\mathcal{F}$ is related to the probability for a photon-counting detector to detect the photon [95],

and in this way a somewhat looser analogy with massive particle wave functions may still be made.

In the case when a photon propagates in an inhomogeneous medium, the upper and lower components of $\mathcal{F}$ couple to one another [27], and the mathematical treatment becomes much more complicated. In free space, however, the components of $\mathcal{F}$ are decoupled, so that we use the two independent equations (A.2b) (one for each value of Σ) and the single three-component vector $\mathbf{F}$ to describe the evolution of the photon wave function. We may derive from (A.2b) a Helmholtz-like equation for $\mathbf{F}_\Sigma$ by taking the curl of both sides of that equation, which yields

$$-\nabla^2 \mathbf{F}_\Sigma = k^2 \mathbf{F}_\Sigma, \tag{A.4a}$$

$$\Leftrightarrow \left[\nabla^2 + k^2\right] \mathbf{F}_\Sigma = 0, \tag{A.4b}$$

where the vector identity $\nabla \times \nabla \times \mathbf{F}_\Sigma = \nabla\left(\nabla \cdot \mathbf{F}_\Sigma\right) - \nabla^2 \mathbf{F}_\Sigma$ and (A.2b) have been used on the left hand side of (A.4a), while (A.2a) has been used on the right.

We are interested in monoenergetic beam-like photons whose wave functions propagate in a well-defined direction with phase velocity $\dfrac{\omega}{\beta}$, where β is known as the propagation constant. Taking the propagation direction to be the z-direction, the photon wave function takes on the traveling-wave form

$$\mathbf{F}_{\omega\beta\Sigma} = \mathbf{F}\left(\rho, \phi, z\right) e^{i(\beta z - \omega t)}, \tag{A.5}$$

where we have used cylindrical coordinates (ρ, ϕ, z), and we have labeled Riemann-Silberstein vector with its respective frequency and propagation constant quantum numbers ω and β, in addition to the helicity quantum number Σ. Furthermore, without loss of generality we may assume that $\mathbf{F}(\rho, \phi, z) \to \mathbf{F}(\rho, \phi)$ is independent of z, since the resulting non-diffracting beams (the so-called Bessel beams, cf. [35, 36]) form a complete basis set for an arbitrary diffracting wave $\mathbf{F}(\rho, \phi, z)$. With this assumption, substituting (A.5) into (A.4b) yields

$$\left[\nabla_T^2 + k^2\right] \mathbf{F}_{\omega\beta\Sigma} = \beta^2 \mathbf{F}_{\omega\beta\Sigma}. \tag{A.6}$$

This equation, known as the vector Helmholtz equation, is essentially three independent copies of Bessel's partial differential equation. Its solutions assume the form

$$\mathbf{F}_{\omega\beta\Sigma} = \left(F_+ \hat{\mathbf{e}}_+ + F_- \hat{\mathbf{e}}_- + F_z \hat{\mathbf{z}}\right) e^{i\beta z - \omega t}, \tag{A.7}$$

where

$$F_+ = J_{m_+}(\kappa\rho) e^{im_+ \phi}, \tag{A.8a}$$

$$F_- = J_{m_-}(\kappa\rho) e^{im_- \phi}, \tag{A.8b}$$

$$F_z = J_{m_z}(\kappa\rho) e^{im_z \phi}. \tag{A.8c}$$

In (A.7), we have employed a "circularly polarized" basis for $\mathbf{F}$ such that $\hat{\mathbf{e}}_\sigma \equiv \dfrac{1}{\sqrt{2}} (\hat{\mathbf{x}} + i\sigma\hat{\mathbf{y}})$, where $\sigma = \pm 1$. To avoid confusion, we stress that σ is a label for the basis vectors in the plane transverse to the wave propagation, and is therefore distinct from the helicity quantum

number $\Sigma = \pm 1$ defined earlier for the photon wave function, although as we will show these quantities do correspond in the paraxial limit. In (A.8), $J_{m_i}(\kappa\rho)$ is a Bessel function of the first kind of order m_i, with $\kappa \equiv \sqrt{k^2 - \beta^2}$ being the transverse wave number.

The vector Helmholtz equation (A.6) is a necessary but not sufficient condition for the $\mathbf{E}$ and $\mathbf{H}$ fields contained in $\mathbf{F}$ to be solutions of Maxwell's equations (A.1), as is well known. Therefore, in order to completely account for the physical constraints placed upon $\mathbf{F}_{\omega\beta\Sigma}$, we must again use the fundamental photon wave equation (A.2b). In view of this, following a method due to Kapany and Burke [97], we decompose the ∇ operator into the circularly polarized basis:

$$\nabla = \partial_x \hat{\mathbf{x}} + \partial_y \hat{\mathbf{y}} + \partial_z \hat{\mathbf{z}} = \frac{1}{2} [\partial_x - i\partial_y] (\hat{\mathbf{x}} + i\hat{\mathbf{y}}) + \frac{1}{2} [\partial_x + i\partial_y] (\hat{\mathbf{x}} - i\hat{\mathbf{y}}) + \partial_z \hat{\mathbf{z}}$$

$$\frac{1}{\sqrt{2}} [\partial_x - i\partial_y] \hat{\mathbf{e}}_+ + \frac{1}{\sqrt{2}} [\partial_x + i\partial_y] \hat{\mathbf{e}}_- + \partial_z \hat{\mathbf{z}}$$

$$\equiv \nabla_+ \hat{\mathbf{e}}_+ + \nabla_- \hat{\mathbf{e}}_- + \partial_z \hat{\mathbf{z}}. \tag{A.9}$$

Using (A.7) and (A.9), (A.2b) may then be written as

$$(\nabla_+ \hat{\mathbf{e}}_+ + \nabla_- \hat{\mathbf{e}}_- + \partial_z \hat{\mathbf{z}}) \times (F_+ \hat{\mathbf{e}}_+ + F_- \hat{\mathbf{e}}_- + F_z \hat{\mathbf{z}}) = \Sigma k (F_+ \hat{\mathbf{e}}_+ + F_- \hat{\mathbf{e}}_- + F_z \hat{\mathbf{z}}) \tag{A.10}$$

To simplify (A.10) we use the following identities,

$$\hat{\mathbf{e}}_\sigma \times \hat{\mathbf{e}}_\sigma = 0, \tag{A.11a}$$

$$\hat{\mathbf{e}}_\sigma \times \hat{\mathbf{e}}_{-\sigma} = -\sigma i \hat{\mathbf{z}}, \tag{A.11b}$$

$$\hat{\mathbf{e}}_\sigma \times \hat{\mathbf{z}} = -\hat{\mathbf{z}} \times \hat{\mathbf{e}}_\sigma = \sigma i \hat{\mathbf{e}}_\sigma, \tag{A.11c}$$

$$\partial_z F_i = i\beta F_i, \tag{A.11d}$$

so that the coupled vector equation (A.10) breaks down into three coupled scalar partial differential equations:

$$\hat{\mathbf{e}}_+ : \quad +i\nabla_+ F_z + \beta F_+ = \Sigma k F_+, \tag{A.12a}$$

$$\hat{\mathbf{e}}_- : \quad -i\nabla_- F_z - \beta F_- = \Sigma k F_-, \tag{A.12b}$$

$$\hat{\mathbf{z}} : \quad -i\nabla_+ F_- + i\nabla_- F_+ = \Sigma k F_z. \tag{A.12c}$$

The equations (A.12) may be easily solved once it is recognized that the operators ∇_σ act as quantum mechanical raising and lowering operators on the solutions (A.8). To see this, we must express these operators in terms of cylindrical polar coordinates:

$$\nabla_\sigma \equiv \frac{1}{\sqrt{2}}\left(\partial_x - \sigma i \partial_y\right) = \frac{1}{\sqrt{2}}\left(\hat{\mathbf{x}} - \sigma i \hat{\mathbf{y}}\right) \cdot \left(\hat{\mathbf{x}}\partial_x + \hat{\mathbf{y}}\partial_y\right) = \frac{1}{\sqrt{2}}\,\hat{\mathbf{e}}_{-\sigma} \cdot \nabla_T, \tag{A.13a}$$

$$\nabla_T \to \hat{\rho}\partial_\rho + \frac{1}{\rho}\hat{\phi}\partial_\phi, \tag{A.13b}$$

$$\hat{\mathbf{e}}_{-\sigma} = \hat{\mathbf{x}} - \sigma i\hat{\mathbf{y}} = \cos\phi\,\hat{\rho} - \sin\phi\,\hat{\phi} - \sigma i\left(\sin\phi\,\hat{\rho} + \cos\phi\,\hat{\phi}\right) = e^{-\sigma i\phi}\left(\hat{\rho} - \sigma i\hat{\phi}\right), \tag{A.13c}$$

$$\Rightarrow \nabla_\sigma = \frac{1}{\sqrt{2}}\,\hat{\mathbf{e}}_{-\sigma} \cdot \nabla_T = \frac{e^{-\sigma i\phi}}{\sqrt{2}}\left(\hat{\rho} - \sigma i\hat{\phi}\right) \cdot \left(\hat{\rho}\partial_\rho + \frac{1}{\rho}\hat{\phi}\partial_\phi\right) = \frac{e^{-\sigma i\phi}}{\sqrt{2}}\left(\partial_\rho - \sigma\frac{i}{\rho}\partial_\phi\right),$$
$$\tag{A.13d}$$

where (A.13b) and (A.13c) have been substituted into (A.13a) to obtain (A.13d). Using (A.13d), we find that application of ∇_σ on the wave function components F_i, which have the general form $f_m \equiv J_m\left(\kappa\rho\right)e^{im\phi}$, results in

$$\nabla_\sigma f_m = \frac{1}{\sqrt{2}} e^{-\sigma i\phi}\left(\partial_\rho - \sigma\frac{i}{\rho}\partial_\phi\right) J_m\left(\kappa\rho\right)e^{im\phi}, \tag{A.14a}$$

$$= \frac{1}{\sqrt{2}}\left(\partial_\rho + \sigma\frac{m}{\rho}\right) J_m\left(\kappa\rho\right)e^{i(m-\sigma)\phi}, \tag{A.14b}$$

$$= \frac{\sigma\kappa}{\sqrt{2}} J_{m-\sigma}\left(\kappa\rho\right)e^{i(m-\sigma)\phi}, \tag{A.14c}$$

$$= \frac{\sigma\kappa}{\sqrt{2}} f_{m-\sigma}, \tag{A.14d}$$

where the Bessel function identity $\left(\partial_\rho + \sigma\frac{m}{\rho}\right) J_m\left(\kappa\rho\right) = \sigma\kappa J_{m-\sigma}\left(\kappa\rho\right)$ has been used in (A.14c). From this we see that $\nabla_\sigma f_m \propto f_{m-\sigma}$, so that ∇_σ acts as raising and lowering operators on the solutions (A.8), as was previously claimed.

It now follows from inspection of equations (A.12) using $\nabla_\sigma f_m \propto f_{m-\sigma}$ that the effect of (A.12) is to constrain the relationship between quantum numbers m_+, m_-, m_z to $m_\sigma = m_z - \sigma$, so that (letting $m_z \equiv m$) we may write

$$F_+ = A_+ f_{m-1}, \tag{A.15a}$$

$$F_- = A_- f_{m+1}, \tag{A.15b}$$

$$F_z = A_z f_m, \tag{A.15c}$$

where A_+, A_-, and A_z are as yet undetermined constants. Substituting (A.15) back into

(A.12) then turn the three coupled partial differential equations into three algebraic equations,

$$\hat{e}_+ : \quad \frac{i\kappa}{\sqrt{2}}A_z + \beta A_+ = \Sigma k A_+, \tag{A.16a}$$

$$\hat{e}_- : \quad \frac{i\kappa}{\sqrt{2}}A_z - \beta A_- = \Sigma k A_-, \tag{A.16b}$$

$$\hat{e}_z : \quad -\frac{i\kappa}{\sqrt{2}}\left(A_+ + A_-\right) = \Sigma k A_z, \tag{A.16c}$$

Only two of these equations are linearly independent, so we may choose to solve (A.16a) and (A.16b) for of A_z:

$$A_+ = \frac{i\kappa}{\sqrt{2}}\frac{1}{\Sigma k - \beta}A_z, \tag{A.17a}$$

$$A_- = \frac{i\kappa}{\sqrt{2}}\frac{1}{\Sigma k + \beta}A_z, \tag{A.17b}$$

$$\tag{A.17c}$$

which may be alternatively expressed in the more compact form

$$A_\sigma = \frac{i\kappa}{\sqrt{2}}\frac{1}{\Sigma k - \sigma\beta}A_z = \frac{i\kappa}{\sqrt{2}}\frac{\Sigma k + \sigma\beta}{k^2 - \beta^2}A_z \tag{A.18a}$$

$$= \frac{i}{\sqrt{2}}\frac{\beta}{\kappa}\left(\Sigma\sqrt{1 + \frac{\kappa^2}{\beta^2}} + \sigma\right)A_z \tag{A.18b}$$

$$\equiv \frac{i}{\sqrt{2}}\frac{1}{\delta}\left(\Sigma\sqrt{1 + \delta^2} + \sigma\right)A_z, \tag{A.18c}$$

where $k^2 = \beta^2 + \kappa^2$ has been used in (A.18b), and $\delta \equiv \dfrac{\kappa}{\beta}$ in (A.18c). Substituting (A.18c) into (A.15), and (A.15) into (A.7) and (A.8) then gives the exact form of the beam-like photon wave function in free space,

$$
\begin{aligned}
\mathbf{F}_{\omega\beta\Sigma m} = F_0 \Bigg[&\frac{1}{2} \left(\Sigma\sqrt{1+\delta^2} + 1 \right) J_{m-1}\left(\kappa\rho\right) e^{i(m-1)\phi} \hat{\mathbf{e}}_+ \\
&+ \frac{1}{2} \left(\Sigma\sqrt{1+\delta^2} - 1 \right) J_{m+1}\left(\kappa\rho\right) e^{i(m+1)\phi} \hat{\mathbf{e}}_- - \frac{i}{\sqrt{2}} \delta J_m\left(\kappa\rho\right) e^{im\phi} \hat{\mathbf{z}} \Bigg] e^{i\beta z - \omega t}, \quad \text{(A.19)}
\end{aligned}
$$

where $F_0 \equiv \dfrac{i\sqrt{2}A}{\delta}$. The subscripts $(\omega\,\beta\,\Sigma\,m)$ of $\mathbf{F}$, along with the relation $\omega^2\epsilon_0\mu_0 = \beta^2 + \kappa^2$, completely determine the form of $\mathbf{F}_{\omega\beta\Sigma m}$.

We are now in a position to take the paraxial limit of the wave function (A.19), which is defined as the regime where the particle momentum is directed predominantly along the propagation axis of the wave function, so that $\kappa \ll \beta$, or equivalently, $\delta \ll 1$. The paraxial limit of the free space photon wave function is therefore the limit where $\delta \to 0$ in (A.19):

$$
\begin{aligned}
\mathbf{F}_{\omega\beta\Sigma m} &\to \mathbf{F}^{\text{parax}}_{\omega\beta\Sigma m_\ell} \\
&= F_0 \left[\frac{1}{2} \left(\Sigma + 1 \right) J_{m-1}\left(\kappa\rho\right) e^{i(m-1)\phi} \hat{\mathbf{e}}_+ + \frac{1}{2} \left(\Sigma - 1 \right) J_{m+1}\left(\kappa\rho\right) e^{i(m+1)\phi} \hat{\mathbf{e}}_- \right] e^{i\beta z - \omega t}, \\
&= \Sigma F_0 J_{m-\Sigma}\left(\kappa\rho\right) e^{i(m-\Sigma)\phi} \hat{\mathbf{e}}_\Sigma e^{i\beta z - \omega t}, \quad \text{(A.20)}
\end{aligned}
$$

The paraxial non-diffracting beams of (A.20) (including the small z-component given in (A.19)) have been previously derived in [98] as a special case of the general solution to the vector Helmholtz wave equation (cf. their example of a "circularly polarized beam"). This

stands in contrast to our approach which has derived (A.20) as the paraxial limit of the exact solutions to Maxwell's equations, which more clearly brings out the role of the helicity quantum number Σ in taking this limit.

Comparing (A.19) and (A.20) we see that in the paraxial regime, the longitudinal (z) component of the photon wave function is negligible, and either its $\hat{\mathbf{e}}_+$ or $\hat{\mathbf{e}}_-$ component must vanish for a given well-defined helicity Σ. Because of this, a wave function $\mathbf{F}_{\omega\beta\Sigma m}$ which is paraxial has well-defined values for its spin angular momentum (SAM, or circular polarization in the transverse plane) and its orbital angular momentum (OAM), with respective quantum numbers Σ and $m_\ell \equiv m - \Sigma$, which contrasts with the general case (A.19) in which $\mathbf{F}_{\omega\beta\Sigma m}$ is an eigenstate of neither SAM nor OAM. In light of this, in the paraxial regime we may identify the quantum number $m \equiv m_j$ as the z-component of total angular momentum, and replace $m \rightarrow m_\ell + \Sigma$ in (A.20), which yields the wave function $\mathbf{F}^{\mathrm{parax}}_{\omega\beta\Sigma m_\ell}$ of a paraxial photon in term of its SAM and OAM quantum numbers Σ and m_ℓ:

$$\mathbf{F}^{\mathrm{parax}}_{\omega\beta\Sigma m_\ell} = \Sigma F_0 J_{m_\ell}\left(\kappa\rho\right) e^{im_\ell\phi}\hat{\mathbf{e}}_\Sigma e^{i\beta z - \omega t} \tag{A.21a}$$

$$= (-1)^{m_\ell}\,\Sigma F_0 J_{|m_\ell|}\left(\kappa\rho\right) e^{im_\ell\phi}\hat{\mathbf{e}}_\Sigma e^{i\beta z - \omega t} \tag{A.21b}$$

$$\equiv N J_{|m_\ell|}\left(\kappa\rho\right) e^{im_\ell\phi}\hat{\mathbf{e}}_\Sigma e^{i\beta z - \omega t} \tag{A.21c}$$

where $J_{m_\ell}\left(\kappa\rho\right) = (-1)^{m_\ell}\,J_{|m_\ell|}$ has been used in (A.21b), and N is a normalization constant.

From (A.21c), we conclude that the helicity quantum number $\Sigma = \pm 1$ appears only in the circularly polarized basis vectors $\hat{\mathbf{e}}_{\pm 1}$, so that the helicity Σ and the circularly polarization quantum number σ do correspond in the paraxial limit, so that we may equivalently write

$$\mathbf{F}_{\omega \beta \Sigma m_\ell}^{\text{parax}} = N J_{|m_\ell|}\left(\kappa \rho\right) e^{i m_\ell \phi} \hat{\mathbf{e}}_\sigma e^{i \beta z - \omega t} \tag{A.22}$$

We will make extensive use throughout this dissertation of the form (A.22) for the paraxial photon wave function.

Finally, we note that the paraxial wave function in (A.22) has the general form given by (A.7) and (A.8) (i.e., the solutions to (A.6)), but with $F_z = 0$ and only one of F_+ or F_- nonzero. It follows from this that the transverse part of (A.6) is sufficient to derive the photon wave function in the paraxial limit, so that the wave equation for paraxial photons takes the form

$$\left[\nabla_T^2 + k^2\right] \mathbf{F}_T = \beta^2 \mathbf{F}_T, \tag{A.23}$$

where the subscript T emphasizes that the photon wave function is entirely transverse ($F_z = 0$), and where the quantum number subscripts (ω, β, σ, m_ℓ) have been suppressed. Therefore, in the paraxial limit, the transverse Helmholtz equation (A.23) is both a necessary and sufficient condition for the photon wave function to be a solution to Maxwell's equation, which is not true generally. Furthermore, since in free space the electric field $\mathbf{E}$ uniquely determines the magnetic field $\mathbf{H}$, we may choose at our convenience to consider only the real part of (A.23), which takes the form

$$\left[\nabla_T^2 + k^2\right] \mathbf{E}_T = \beta^2 \mathbf{E}_T, \tag{A.24}$$

since the real part of the Riemann-Silberstein vector $\mathbf{F}_\Sigma \equiv \dfrac{1}{\sqrt{2}} \left(\sqrt{\epsilon_0}\mathbf{E} + \Sigma i \sqrt{\mu_0}\mathbf{H}\right)$ is $\sqrt{\dfrac{\epsilon_0}{2}}\mathbf{E}$ ($\mathbf{E}_T$ is the transverse electric field). We use (A.24) as the starting point in our discussion of the free-space wave equation for a monoenergetic beam-like photon in Chapter II (see equation (2.4)).

APPENDIX B

GAUGE POTENTIAL IN MOMENTUM SPACE

In this appendix, we derive the forms of the momentum-space gauge potential (connection) associated with an electron or photon propagating with well-defined momentum $\mathbf{p}$ along a curvilinear path. Throughout this appendix, scalar matrix operators are generally denoted by capitol letters with hats (e.g. $\hat{U}$), while unit vectors are denoted as lower case bold letters with hats (e.g. $\hat{\mathbf{x}}$). Vectorial matrix operators are denoted with bold capitol letters with hats (e.g. $\hat{\mathbf{A}}$).

Electron Gauge Potential

We begin with the case of an electron, which is described by the Pauli equation. In the absence of external fields, the Pauli equation reduces to the form [37]

$$i\hbar\partial_t \left|\psi\right\rangle = \frac{p^2}{2m} \left(\hat{\sigma}\cdot\hat{\mathbf{p}}\right)^2 \left|\psi\right\rangle, \tag{B.1}$$

which may also be expressed in terms of the electron spin operator $\hat{\mathbf{S}} \equiv \frac{\hbar}{2}\hat{\sigma}$ as

$$i\hbar\partial_t \left|\psi\right\rangle = \frac{2k^2}{m} \left(\hat{\mathbf{S}}\cdot\hat{\mathbf{p}}\right)^2 \left|\psi\right\rangle. \tag{B.2}$$

In (B.1) and (B.2), $\hat{\mathbf{S}} \equiv \frac{\hbar}{2}\hat{\sigma} = \frac{\hbar}{2}\left(\hat{\sigma}_x\hat{\mathbf{x}} + \hat{\sigma}_y\hat{\mathbf{y}} + \hat{\sigma}_z\hat{\mathbf{z}}\right)$ is the Pauli spin operator, $\hat{\mathbf{p}} \equiv \frac{\mathbf{p}}{p}$ is the unit momentum vector, and $p = \hbar k$ has been used.

The helicity operator $\hat{\mathbf{S}} \cdot \hat{\mathbf{p}}$ contained in (B.2) has the following explicit matrix form:

$$\hat{\mathbf{S}} \cdot \hat{\mathbf{p}} = \frac{\hbar}{2} \frac{1}{p} \begin{pmatrix} p_z & p_x - ip_y \\ p_x + ip_y & -p_z \end{pmatrix}. \tag{B.3}$$

$\hat{\mathbf{S}} \cdot \hat{\mathbf{p}}$ may therefore be diagonalized by the momentum-dependent unitary (gauge) transformation [28] $\hat{U}(\mathbf{p})^{-1} \left(\hat{\mathbf{S}} \cdot \hat{\mathbf{p}} \right) \hat{U}(\mathbf{p})$, where

$$\hat{U}(\mathbf{p}) \equiv \frac{1}{\sqrt{p(p + p_z)}} \begin{pmatrix} p + p_z & p_x - ip_y \\ -(p_x + ip_y) & p + p_z \end{pmatrix}, \tag{B.4}$$

as can be readily checked by direct matrix multiplication. The explicit result is

$$\hat{U}(\mathbf{p})^{-1} \left(\hat{\mathbf{S}} \cdot \hat{\mathbf{p}} \right) \hat{U}(\mathbf{p}) = \begin{pmatrix} \dfrac{1}{2} & 0 \\ 0 & -\dfrac{1}{2} \end{pmatrix} \equiv \lambda \hat{\sigma}_z, \tag{B.5}$$

where $\lambda = \dfrac{1}{2}$ is the magnitude of the electron helicity.

As is well known, in diagonalizing the helicity operator, the gauge transformation $\hat{U}(\mathbf{p})^{-1} \left(\hat{\mathbf{S}} \cdot \hat{\mathbf{p}} \right) \hat{U}(\mathbf{p})$ gives rise to a gauge covariant derivative (i.e., a gauge connection) $\hat{\mathbf{A}}(\mathbf{p})$ which determines the parallel transport of the electron spin as it propagates along the curvilinear path (cf. [42]). This gauge connection is calculated by the expression

$$\hat{\mathbf{A}}(\mathbf{p}) \equiv i\hat{U}(\mathbf{p})^{-1} \partial_{\mathbf{p}} \hat{U}(\mathbf{p}), \tag{B.6}$$

where the vectorial directional derivative $\partial_{\mathbf{p}} \equiv \partial_{p_x} \hat{\mathbf{p}}_x + \partial_{p_y} \hat{\mathbf{p}}_y + \partial_{p_y} \hat{\mathbf{p}}_z$ acts on each element of the matrix $\hat{U}(\mathbf{p})$. Direct calculation of $\hat{\mathbf{A}}(\mathbf{p})$ using (B.6) and (B.4) yields

$$\hat{\mathbf{A}}\left(\mathbf{p}\right) = \frac{1}{2p\left(p+p_z\right)}\Bigg[\left(ip_x\hat{\sigma}_0 + \left(p+p_z\right)\hat{\sigma}_y + p_y\hat{\sigma}_z\right)\hat{\mathbf{x}}$$

$$+ \left(ip_y\hat{\sigma}_0 + \left(p+p_z\right)\hat{\sigma}_x - p_x\hat{\sigma}_z\right)\hat{\mathbf{y}}$$

$$+ \left(2ip_z\hat{\sigma}_0 + p_y\hat{\sigma}_x - p_x\hat{\sigma}_y\right)\hat{\mathbf{z}}\Bigg], \tag{B.7}$$

where $\hat{\sigma}_0$ is the 2×2 identity matrix.

We are interested in the case where the electron undergoes sufficiently adiabatic changes in its momentum such that its helicity σ does not undergo a transition from σ to $-\sigma$. This assumption is equivalent to neglecting the off-diagonal elements of $\hat{\mathbf{A}}\left(\mathbf{p}\right)$, as has been shown in a general mathematical context in [42, 99, 100]. The diagonal part of $\hat{\mathbf{A}}\left(\mathbf{p}\right)$ is found simply by setting all terms proportional to $\hat{\sigma}_x$ and $\hat{\sigma}_y$ to zero in (B.7):

$$\hat{\mathbf{A}}_{\mathrm{D}}\left(\mathbf{p}\right) = \frac{1}{2p\left(p+p_z\right)}\Bigg[\left(ip_x\hat{\sigma}_0 + p_y\hat{\sigma}_z\right)\hat{\mathbf{x}} + \left(ip_y\hat{\sigma}_0 - p_x\hat{\sigma}_z\right)\hat{\mathbf{y}} + 2ip_z\hat{\sigma}_0\hat{\mathbf{z}}\Bigg], \tag{B.8a}$$

$$= \Bigg[\frac{1}{2p\left(p+p_z\right)}\left(ip_x\hat{\mathbf{x}} + ip_y\hat{\mathbf{y}} + 2ip_z\hat{\mathbf{z}}\right)\hat{\sigma}_0 + \frac{1}{2p\left(p+p_z\right)}\left(p_y\hat{\mathbf{x}} - p_x\hat{\mathbf{y}}\right)\hat{\sigma}_z\Bigg], \tag{B.8b}$$

$$\equiv \hat{\mathbf{A}}_{\hat{\sigma}_0}\left(\mathbf{p}\right)\hat{\sigma}_0 + \hat{\mathbf{A}}_{\hat{\sigma}_z}\left(\mathbf{p}\right)\hat{\sigma}_z. \tag{B.8c}$$

Now, since $\hat{\mathbf{A}}_{\mathrm{D}}\left(\mathbf{p}\right)$ is a matrix-valued vector field in momentum space, it has a well-defined (matrix-valued) curl. Taking the curl of $\hat{\mathbf{A}}_{\mathrm{D}}\left(\mathbf{p}\right)$ via (B.8c) yields

$$\nabla \times \hat{\mathbf{A}}_{\mathrm{D}}\left(\mathbf{p}\right) = \left(\nabla \times \hat{\mathbf{A}}_{\hat{\sigma}_0}\left(\mathbf{p}\right)\right)\hat{\sigma}_0 + \left(\nabla \times \hat{\mathbf{A}}_{\hat{\sigma}_z}\left(\mathbf{p}\right)\right)\hat{\sigma}_z, \tag{B.9a}$$

$$= i \frac{p_T^2 - 2pp_z}{p^3 \left(p + p_z\right)^2} \left(p_y \hat{\mathbf{x}} - p_x \hat{\mathbf{y}}\right) \hat{\sigma}_0 - \frac{\hat{\mathbf{p}}}{p^2} \hat{\sigma}_z, \tag{B.9b}$$

where $p_T^2 \equiv p_x^2 + p_y^2$. Furthermore, in the paraxial regime where $\delta_x \equiv \dfrac{p_x}{p_z} \ll 1$, $\delta_y \equiv \dfrac{p_y}{p_z} \ll 1$, and $p_z \approx p$, (B.9b) approximately reduces to

$$\nabla \times \hat{\mathbf{A}}_{\mathrm{D}}\left(\mathbf{p}\right) = \frac{-i}{2p^2} \left(\delta_y \hat{\mathbf{x}} - \delta_x \hat{\mathbf{y}}\right) \hat{\sigma}_0 - \frac{\hat{\mathbf{p}}}{p^2} \hat{\sigma}_z. \tag{B.10}$$

Therefore, in the paraxial limit where $\delta_x, \delta_y \to 0$, the term proportional to $\hat{\sigma}_0$ vanishes so that

$$\nabla \times \hat{\mathbf{A}}_{\mathrm{D}}\left(\mathbf{p}\right) = -\frac{\hat{\mathbf{p}}}{p^2} \hat{\sigma}_z, \tag{B.11}$$

or, since $\hat{\sigma}_z$ is diagonal, we may express this 2×2 matrix equation as two independent 1×1 equations via the helicity quantum number σ:

$$\nabla \times \hat{\mathbf{A}}_{\mathrm{D}}\left(\mathbf{p}\right) = -\sigma \frac{\hat{\mathbf{p}}}{p^2}. \tag{B.12}$$

From this, it is evident that we may define an *effective* gauge connection $\hat{\mathbf{A}}_{\mathrm{eff}}\left(\mathbf{p}\right)$ whose curl gives the result $-\dfrac{\hat{\mathbf{p}}}{p^2}$, such that $\nabla \times \hat{\mathbf{A}}_{\mathrm{D}}\left(\mathbf{p}\right) = \sigma \nabla \times \hat{\mathbf{A}}_{\mathrm{eff}}\left(\mathbf{p}\right)$ in the adiabatic and paraxial limits. Upon comparing (B.12) with (B.7), we see that $\hat{\mathbf{A}}_{\mathrm{eff}}\left(\mathbf{p}\right)$ is given by (B.7) with all terms proportional to $\hat{\sigma}_0$, $\hat{\sigma}_x$, and $\hat{\sigma}_y$ set equal to zero, and $\hat{\sigma}_z$ set equal to 1:

$$\hat{\mathbf{A}}_{\mathrm{eff}}\left(\mathbf{p}\right) = \frac{1}{2p \left(p + p_z\right)} \left(p_y \hat{\mathbf{x}} - p_x \hat{\mathbf{y}}\right). \tag{B.13}$$

The 1×1 vector gauge connection $\hat{\mathbf{A}}_{\text{eff}}(\mathbf{p})$ plays a role analogous to that of the vector potential $\mathbf{A}$ in magnetostatics, whose curl gives rise to the magnetic field ($\mathbf{B} = \nabla \times \mathbf{A}$). Applying this analogy to the present case, the "magnetic field" associated with $\hat{\mathbf{A}}_{\text{eff}}(\mathbf{p})$ is that of a "magnetic monopole" $\frac{\hat{\mathbf{p}}}{p^2}$ in momentum space with "charge" -1. For this reason, $\hat{\mathbf{A}}_{\text{eff}}(\mathbf{p})$ is sometimes called a gauge (or monopole) potential.

Recalling now the definition (B.6) of the the gauge connection $\hat{\mathbf{A}}(\mathbf{p})$, we are led to the definition of the effective gauge potential $\hat{\mathbf{A}}_{\text{eff}}(\mathbf{p})$:

$$\hat{\mathbf{A}}_{\text{eff}}(\mathbf{p}) \equiv \hat{U}_{\text{eff}}(\mathbf{p})^{-1} i\partial_{\mathbf{p}} \hat{U}_{\text{eff}}(\mathbf{p}), \tag{B.14}$$

where the unitary transformation $\hat{U}_{\text{eff}}(\mathbf{p})$ now takes the form of a 1×1 momentum-dependent unitary matrix, which thereby has the general form

$$\hat{U}_{\text{eff}}(\mathbf{p}) = e^{i\phi(\mathbf{p})}. \tag{B.15}$$

Using (B.15) and (B.14) implies that $\hat{\mathbf{A}}_{\text{eff}}(\mathbf{p})$ may be expressed as

$$\hat{\mathbf{A}}_{\text{eff}}(\mathbf{p}) = e^{-i\phi(\mathbf{p})} i\partial_{\mathbf{p}} e^{i\phi(\mathbf{p})}, \tag{B.16}$$

which has the same form as the integrand of (2.45) in Chapter II. Letting $\mathbf{p} \to \mathbf{k}_c$ in (B.16), we have thereby shown for electrons that the quantity $e^{-i\phi(\mathbf{k}_c)} i\partial_{\mathbf{k}_c} e^{i\phi(\mathbf{k}_c)}$ has the form of a momentum-dependent vector potential $\mathbf{A}(\mathbf{k}_c)$ with curl $\nabla \times \mathbf{A}(\mathbf{k}_c) = -\frac{\hat{\mathbf{k}}_c}{k_c^2}$, as claimed in Chapter II.

Photon Gauge Potential

The photon case proceeds analogously to the electron case above. Photon evolution is described by the photon wave equation, which for monoenergetic photons has the free-space form

$$i\hbar\partial_t \mathbf{F}_\sigma = \sigma c\nabla \times \mathbf{F}_\sigma, \tag{B.17}$$

where the Riemann-Silberstein vector $\mathbf{F}_\sigma \equiv \dfrac{1}{\sqrt{2}} \left(\sqrt{\epsilon_0}\mathbf{E} + \sigma i\sqrt{\mu_0}\mathbf{H}\right)$ plays the role of the photon wave function as discussed in Appendix A. Letting $\mathbf{F}_\sigma \to |\psi\rangle$, equation (B.17) may alternatively be written in a form analogous to the Pauli wave equation for electrons (B.2),

$$i\hbar\partial_t |\psi\rangle = \sigma ck\hat{\mathbf{S}} \cdot \hat{\mathbf{p}} |\psi\rangle, \tag{B.18}$$

where $\hat{\mathbf{S}} \equiv \hbar \left(\hat{\mathbf{s}}_x + \hat{\mathbf{s}}_y + \hat{\mathbf{s}}_z\right)$ is the spin operator for particles of spin one, with

$$\hat{\mathbf{s}}_x = \begin{pmatrix} 0 & 0 & 0 \\ 0 & 0 & -i \\ 0 & i & 0 \end{pmatrix}, \quad \hat{\mathbf{s}}_y = \begin{pmatrix} 0 & 0 & i \\ 0 & 0 & 0 \\ -i & 0 & 0 \end{pmatrix}, \text{ and } \hat{\mathbf{s}}_z = \begin{pmatrix} 0 & -i & 0 \\ i & 0 & 0 \\ 0 & 0 & 0 \end{pmatrix}. \tag{B.19}$$

For photons, the helicity operator $\hat{\mathbf{S}} \cdot \hat{\mathbf{p}}$ contained in (B.18) has the following explicit matrix form:

$$\hat{\mathbf{S}} \cdot \hat{\mathbf{p}} = \frac{i\hbar}{p} \begin{pmatrix} 0 & -p_z & p_y \\ p_z & -0 & -p_x \\ -p_y & p_x & 0 \end{pmatrix}. \tag{B.20}$$

As in the electron case, $\hat{\mathbf{S}} \cdot \hat{\mathbf{p}}$ may be diagonalized by a unitary gauge transformation [28] $\hat{U}(\mathbf{p})^{-1} \left(\hat{\mathbf{S}} \cdot \hat{\mathbf{p}} \right) \hat{U}(\mathbf{p})$, where

$$\hat{U}(\mathbf{p}) \equiv \frac{1}{p p_T} \begin{pmatrix} p_x p_z - i p p_y & p_x p_z + i p p_y & p_x p_T \\ p_y p_z + i p p_x & p_y p_z - i p p_x & p_y p_T \\ -p_T^2 & -p_T^2 & p_z p_T \end{pmatrix}, \tag{B.21}$$

where $p_T \equiv \sqrt{p_x^2 + p_y^2}$. The explicit result is

$$\hat{U}(\mathbf{p})^{-1} \left(\hat{\mathbf{S}} \cdot \hat{\mathbf{p}} \right) \hat{U}(\mathbf{p}) = \begin{pmatrix} 1 & 0 & 0 \\ 0 & -1 & 0 \\ 0 & 0 & 0 \end{pmatrix} \equiv \lambda \hat{\Sigma}_z, \tag{B.22}$$

as can be checked by direct matrix multiplication, where $\lambda = 1$ is the magnitude of the electron helicity, and $\hat{\Sigma}_z$ is the diagonal 3×3 "Pauli" spin z-component matrix for a spin one particle as given in (B.22).

The photon gauge connection $\hat{\mathbf{A}}(\mathbf{p})$ may then be directly calculated via (B.6), yielding

$$
\hat{\mathbf{A}}(\mathbf{p}) = \frac{1}{2p^2 p_T^2}
\begin{pmatrix}
ip_x \left(p^2 + p_z^2\right) - 2pp_y p_z & -ip_x p_T^2 & p_T \left(-pp_y + ip_x p_z\right) \\
-ip_x p_T^2 & ip_x \left(p^2 + p_z^2\right) + 2pp_y p_z & p_T \left(pp_y + ip_x p_z\right) \\
2p_T \left(-pp_y + ip_x p_z\right) & 2p_T \left(pp_y + ip_x p_z\right) & 2ip_x p_T^2
\end{pmatrix} \hat{\mathbf{x}}
$$

$$
+ \frac{1}{2p^2 p_T^2}
\begin{pmatrix}
ip_y \left(p^2 + p_z^2\right) + 2pp_x p_z & -ip_y p_T^2 & p_T \left(pp_x + ip_y p_z\right) \\
-ip_y p_T^2 & ip_y \left(p^2 + p_z^2\right) - 2pp_x p_z & p_T \left(-pp_x + ip_y p_z\right) \\
2p_T \left(pp_x + ip_y p_z\right) & 2p_T \left(-pp_x + ip_y p_z\right) & 2ip_y p_T^2
\end{pmatrix} \hat{\mathbf{y}}
$$

$$
+ \frac{i}{2p^2}
\begin{pmatrix}
p_z & p_z & -p_T \\
p_z & p_z & -p_T \\
2p_T & 2p_T & 2p_z
\end{pmatrix} \hat{\mathbf{z}},
\tag{B.23}
$$

Furthermore, in the paraxial limit $\hat{\mathbf{A}}(\mathbf{p}) \to \hat{\mathbf{A}}_{\text{Parax}}(\mathbf{p})$, we may neglect the terms in (B.23) which are second and third order in the small quantities p_x, p_y, or p_T in comparison with the dominating terms which have only one factor of p_x, p_y, or p_T:

$$
\hat{\mathbf{A}}_{\text{Parax}}(\mathbf{p}) = \frac{1}{2p^2 p_T^2}
\begin{pmatrix}
ip_x \left(p^2 + p_z^2\right) - 2pp_y p_z & 0 & 0 \\
0 & ip_x \left(p^2 + p_z^2\right) + 2pp_y p_z & 0 \\
0 & 0 & 0
\end{pmatrix} \hat{\mathbf{x}}
$$

$$+ \frac{1}{2p^2p_T^2} \begin{pmatrix} ip_y\left(p^2+p_z^2\right)+2pp_xp_z & 0 & 0 \\ 0 & ip_y\left(p^2+p_z^2\right)-2pp_xp_z & 0 \\ 0 & 0 & 0 \end{pmatrix} \hat{\mathbf{y}} + \frac{i}{2p^2} \begin{pmatrix} p_z & p_z & 0 \\ p_z & p_z & 0 \\ 0 & 0 & 2p_z \end{pmatrix} \hat{\mathbf{z}},$$

$$(\text{B.24})$$

Simplifying (B.24) and letting $\delta \equiv \dfrac{p_T}{p_z}$, then gives

$$\hat{\mathbf{A}}_{\text{Parax}}\left(\mathbf{p}\right) = \frac{i\left(1+\delta^{-2}\right)}{2p^2}\left(p_x\hat{\mathbf{x}}+p_y\hat{\mathbf{y}}\right) \begin{pmatrix} 1 & 0 & 0 \\ 0 & 1 & 0 \\ 0 & 0 & 0 \end{pmatrix} + \frac{ip_z}{2p^2}\hat{\mathbf{z}} \begin{pmatrix} 1 & 1 & 0 \\ 1 & 1 & 0 \\ 0 & 0 & 2 \end{pmatrix}$$

$$+ \frac{\delta^{-1}}{pp_T}\left(-p_y\hat{\mathbf{x}}+p_x\hat{\mathbf{y}}\right) \begin{pmatrix} 1 & 0 & 0 \\ 0 & -1 & 0 \\ 0 & 0 & 0 \end{pmatrix}, \qquad (\text{B.25})$$

where $\left(p^2+p_z^2\right) = \left(p_T^2+2p_z^2\right)$ has been used. Since $\delta \ll 1$ in the paraxial limit, the δ^{-2} and

δ^{-1} terms dominate in (B.25), such that $\hat{\mathbf{A}}_{\text{Parax}}\left(\mathbf{p}\right) \to \hat{\mathbf{A}}_{\text{D}}\left(\mathbf{p}\right)$ is approximately diagonal,

$$\hat{\mathbf{A}}_{\text{D}}\left(\mathbf{p}\right) = \frac{i\delta^{-2}}{2p^2}\left(p_x\hat{\mathbf{x}}+p_y\hat{\mathbf{y}}\right)\hat{\Sigma}_0 + \frac{\delta^{-1}}{pp_T}\left(-p_y\hat{\mathbf{x}}+p_x\hat{\mathbf{y}}\right)\hat{\Sigma}_z, \qquad (\text{B.26a})$$

$$\equiv \hat{\mathbf{A}}_{\hat{\Sigma}_0}\left(\mathbf{p}\right)\hat{\Sigma}_0 + \hat{\mathbf{A}}_{\hat{\Sigma}_z}\left(\mathbf{p}\right)\hat{\Sigma}_z, \qquad (\text{B.26b})$$

where $\hat{\Sigma}_0\left(\hat{\Sigma}_z\right)$ is a 3×3 matrix consisting of the 2×2 identity (Pauli matrix σ_z) and a

third row of zeros as shown in (B.25). The diagonal form $\hat{\mathbf{A}}_{\text{D}}\left(\mathbf{p}\right)$ in (B.26) for photons is

analogous to (B.8) in the electron case.

We now take the curl of $\hat{\mathbf{A}}_{\mathrm{D}}(\mathbf{p})$ as before, which by (B.26b) results in

$$\nabla \times \hat{\mathbf{A}}_{\mathrm{D}}(\mathbf{p}) = \left(\nabla \times \hat{\mathbf{A}}_{\hat{\Sigma}_0}(\mathbf{p})\right)\hat{\Sigma}_0 + \left(\nabla \times \hat{\mathbf{A}}_{\hat{\Sigma}_z}(\mathbf{p})\right)\hat{\Sigma}_z, \tag{B.27a}$$

$$= -i\frac{2p_z}{p^4}\left(p_y\hat{\mathbf{x}} - p_x\hat{\mathbf{y}}\right)\hat{\Sigma}_0 - \frac{\hat{\mathbf{P}}}{p^2}\hat{\Sigma}_z. \tag{B.27b}$$

Again using $\delta_x \equiv \dfrac{p_x}{p_z} \ll 1$, $\delta_y \equiv \dfrac{p_y}{p_z} \ll 1$, and $p_z \approx p$, we find that the paraxial equation (B.27) may be written as

$$\nabla \times \hat{\mathbf{A}}_{\mathrm{D}}(\mathbf{p}) \approx -i\frac{2}{p^2}\left(\delta_y\hat{\mathbf{x}} - \delta_x\hat{\mathbf{y}}\right)\hat{\Sigma}_0 - \frac{\hat{\mathbf{P}}}{p^2}\hat{\Sigma}_z, \tag{B.28}$$

so that once more we find that the $\hat{\Sigma}_z$ term dominates in the paraxial limit:

$$\nabla \times \hat{\mathbf{A}}_{\mathrm{D}}(\mathbf{p}) \approx -\frac{\hat{\mathbf{P}}}{p^2}\hat{\Sigma}_z, \tag{B.29}$$

Therefore, since $\hat{\sigma}_z = \hat{\Sigma}_z$ in the 2×2 subspace we conclude that in the paraxial limit, for both electrons and photons, the curl of the gauge connection takes the form

$$\nabla \times \hat{\mathbf{A}}_{\mathrm{D}}(\mathbf{p}) \approx -\frac{\hat{\mathbf{P}}}{p^2}\hat{\sigma}_z, \tag{B.30}$$

which is consistent with the result first reported in [28]. It then follows from (B.11)–(B.16) that for both electrons and photons, the quantity $e^{-i\phi(\mathbf{k}_c)}i\partial_{\mathbf{k}_c}e^{i\phi(\mathbf{k}_c)}$ has the form of a momentum-dependent vector potential $\mathbf{A}(\mathbf{k}_c)$ with curl $\nabla \times \mathbf{A}(\mathbf{k}_c) = -\dfrac{\hat{\mathbf{k}}_c}{k_c^2}$, as claimed in Chapter II.

BIBLIOGRAPHY

[1] A. Einstein, B. Podolsky, and N. Rosen, Phys. Rev. **47**, 777 (1935).

[2] P. G. Kwiat, K. Mattle, H. Weinfurter, A. Zeilinger, A. V. Sergienko, and Y. Shih, Phys. Rev. Lett. **75**, 4337 (1995).

[3] P. G. Kwiat, E. Waks, A. G. White, I. Appelbaum, and P. H. Eberhard, Phys. Rev. A **60**, R773 (1999).

[4] A. Mair, A. Vaziri, G. Weihs, and A. Zeilinger, Nature **412**, 313 (2001).

[5] S. P. Walborn, A. N. de Oliveira, R. S. Thebaldi, and C. H. Monken, Phys. Rev. A **69**, 023811 (2004).

[6] N. K. Langford, R. B. Dalton, M. D. Harvey, J. L. O'Brien, G. J. Pryde, A. Gilchrist, S. D. Bartlett, and A. G. White, Phys. Rev. Lett. **93**, 053601 (2004).

[7] S. P. Walborn, S. Pádua, and C. H. Monken, Phys. Rev. A **71**, 053812 (2005).

[8] T. Yarnall, A. F. Abouraddy, B. E. A. Saleh, and M. C. Teich, Phys. Rev. Lett. **99**, 250502 (2007).

[9] T. Yarnall, A. F. Abouraddy, B. E. A. Saleh, and M. C. Teich, Phys. Rev. Lett. **99**, 170408 (2007).

[10] J. T. Barreiro, N. K. Langford, N. A. Peters, and P. G. Kwiat, Phys. Rev. Lett. **95**, 260501 (2005).

[11] S. P. Walborn, A. N. de Oliveira, S. Pádua, and C. H. Monken, Phys. Rev. Lett. **90**, 143601 (2003).

[12] T. B. Pittman, Y. H. Shih, D. V. Strekalov, and A. V. Sergienko, Phys. Rev. A **52**, R3429 (1995).

[13] P. Walther, K. J. Resch, T. Rudolph, E. Schenck, H. Weinfurter, V. Vedral, M. Aspelmeyer, and A. Zeilinger, Nature **434**, 169 (2005).

[14] N. Kiesel, C. Schmid, U. Weber, G. Tóth, O. Gühne, R. Ursin, and H. Weinfurter, Phys. Rev. Lett. **95**, 210502 (2005).

[15] C.-Y. Lu, X.-Q. Zhou, O. Gühne, W.-B. Gao, J. Zhang, Z.-S. Yuan, A. Goebel, T. Yang, and J.-W. Pan, Nat. Phys. **3**, 91 (2007).

[16] C.-Y. Lu, X.-Q. Zhou, O. Gühne, W.-B. Gao, J. Zhang, Z.-S. Yuan, A. Goebel, T. Yang, and J.-W. Pan, Nat. Phys. (2010).

[17] K. Chen, C.-M. Li, Q. Zhang, Y.-A. Chen, A. Goebel, S. Chen, A. Mair, and J.-W. Pan, Phys. Rev. Lett. **99**, 120503 (2007).

[18] P. J. Mosley, J. S. Lundeen, B. J. Smith, P. Wasylczyk, A. B. U'Ren, C. Silberhorn, and I. A. Walmsley, Phys. Rev. Lett. **100**, 133601 (2008).

[19] P. J. Mosley, J. S. Lundeen, B. J. Smith, and I. A. Walmsley, New Journ. Phys. **10**, 093011 (2008).

[20] S. Ramelow, L. Ratschbacher, A. Fedrizzi, N. K. Langford, and A. Zeilinger, Phys. Rev. Lett. **103**, 253601 (2009).

[21] E. Nagali, F. Sciarrino, F. De Martini, L. Marrucci, B. Piccirillo, E. Karimi, and E. Santamato, Phys. Rev. Lett. **103**, 013601 (2009).

[22] L. Allen, M. W. Beijersbergen, R. J. C. Spreeuw, and J. P. Woerdman, Phys. Rev. A **45**, 8185 (1992).

[23] H. Sasada and M. Okamoto, Phys. Rev. A **68**, 012323 (2003).

[24] L. Marrucci, C. Manzo, and D. Paparo, Phys. Rev. Lett. **96**, 163905 (2006).

[25] S. J. van Enk, Opt. Commun. **102**, 59 (1993).

[26] I. Bialynicki-Birula, Acta Phys. Pol. A **86**, 97 (1994).

[27] I. Bialynicki-Birula, in *Progress in Optics XXXVI*, edited by E. Wolf (Elsevier, Amsterdam, 1996), pp. 245–294.

[28] I. Bialynicki-Birula and Z. Bialynicka-Birula, Phys. Rev. D **35**, 2383 (1987).

[29] M. V. Berry, Proc. R. Soc. London A **392**, 45 (1984).

[30] S. M. Rytov, Dokl. Akad. Nauk. SSSR **18**, 2 (1938).

[31] S. Pancharatnam, Proc. Ind. Acad. Sci. **44**, 247 (1956).

[32] Y. Aharonov and D. Bohm, Phys. Rev. **115**, 485 (1959).

[33] Y. Aharonov and J. Anandan, Phys. Rev. Lett. **58**, 1593 (1987).

[34] J. Samuel and R. Bhandari, Phys. Rev. Lett. **60**, 2339 (1988).

[35] J. Durnin, J. Opt. Soc. Am. A **4**, 651 (1987).

[36] J. Durnin, J. J. Miceli, and J. H. Eberly, Phys. Rev. Lett. **58**, 1499 (1987).

[37] R. Shankar, *Principles of Quantum Mechanics* (Springer, Berlin, 1994), 2nd ed.

[38] I. S. Gradshteyn and I. M. Ryzhik, *Table of Integrals, Series, and Products* (Academic Press, San Deigo, 1994), 5th ed.

[39] B. E. A. Saleh and T. M. Carl, *Fundamentals of Photonics* (Wiley-Interscience, New York, 1991).

[40] J. J. Sakurai, *Modern Quantum Mechanics* (Addison Wesley, Reading, MA, 1994).

[41] K. Y. Bliokh and V. D. Freilikher, Phys. Rev. B **72**, 035108 (2005).

[42] K. Y. Bliokh and Y. P. Bliokh, Ann. Phys. **319**, 13 (2005).

[43] K. Y. Bliokh, Phys. Rev. Lett. **97**, 043901 (2006).

[44] K. Y. Bliokh, Y. P. Bliokh, S. Savel'ev, and F. Nori, Phys. Rev. Lett. **99**, 190404 (2007).

[45] J. Leach, M. J. Padgett, S. M. Barnett, S. Franke-Arnold, and J. Courtial, Phys. Rev. Lett. **88**, 257901 (2002).

[46] H. Wei, X. Xue, J. Leach, M. J. Padgett, S. M. Barnett, S. Franke-Arnold, E. Yaoc, and J. Courtial, Opt. Commun. **223**, 117 (2003).

[47] X. Xue, H. Wei, and A. G. Kirk, Opt. Lett. **26**, 1746 (2001).

[48] C. C. Leary, L. A. Baumgardner, and M. G. Raymer, Opt. Express **17**, 2435 (2009).

[49] A. E. Siegman, *Lasers* (University Science Books, Sausalito, CA, 1986).

[50] D. W. Swift, Opt. Laser Technol. **4**, 175 (1972).

[51] Z. Y. Ou and L. Mandel, Am. J. Phys. **57**, 66 (1989).

[52] E. Mukamel, K. Banaszek, I. A. Walmsley, and C. Dorrer, Opt. Lett. **28**, 1317 (2003).

[53] A. Royer, Phys. Rev. A **15**, 449 (1977).

[54] B. J. Smith, B. Killett, M. G. Raymer, I. A. Walmsley, and K. Banaszek, Opt. Lett. **30**, 3365 (2005).

[55] E. J. Galvez and P. M. Koch, J. Opt. Soc. Am. A **14**, 3410 (1997).

[56] E. J. Galvez and C. D. Holmes, J. Opt. Soc. Am. A **16**, 1981 (1999).

[57] M. Kitano, T. Yabuzaki, and T. Ogawa, Phys. Rev. Lett. **58**, 523 (1987).

[58] M. Segev, R. Solomon, and A. Yariv, Phys. Rev. Lett. **69**, 590 (1992).

[59] A. T. O'Neil and J. Courtial, Opt. Commun. **181**, 35 (2000).

[60] J. D. Jackson, *Classical Electrodynamics* (Wiley, New York, 1999), 3rd ed.

[61] M. Born and E. Wolf, *Principles of Optics* (Pergamon, Oxford, 1970), 4th ed.

[62] V. S. Liberman and B. Y. Zel'dovich, Phys. Rev. A **46**, 5199 (1992).

[63] A. W. Snyder and J. D. Love, *Optical Waveguide Theory* (Kluwer Academic Publishers, Norwell, MA, 1983), 1st ed.

[64] C. K. Hong and L. Mandel, Phys. Rev. A **31**, 2409 (1985).

[65] D. McGloin, N. B. Simpson, and M. J. Padgett, App. Opt. **37**, 469 (1998).

[66] E. Bortolotti, Atti R. Accad. Naz. Lincei Rend Cl. Sci. Fis. Mat. Nat. **4**, 552 (1926).

[67] S. M. Rytov, Tr. Fiz. Inst. Akad. Nauk. SSSR **2**, 1 (1940).

[68] V. V. Vladimirsky, Dokl. Akad. Nauk. SSSR **21**, 222 (1941).

[69] M. V. Berry, in *Fundamental Aspects of Quantum Theory*, edited by V. Gorini and A. Frigerio (Plenum, New York, 1986), pp. 267–268.

[70] R. Y. Chiao and Y. Wu, Phys. Rev. Lett. **57**, 933 (1986).

[71] A. Tomita and R. Y. Chiao, Phys. Rev. Lett. **57**, 937 (1986).

[72] A. V. Dooghin, N. D. Kundikova, V. S. Liberman, and B. Y. Zel'dovich, Phys. Rev. A **45**, 8204 (1992).

[73] A. V. Volyar, V. Z. Zhilaitis, T. A. Fadeeva, and V. G. Shvedov, Pis'ma Zh. Tekh. Fiz. **24**, 83 (1998).

[74] A. V. Volyar, V. Z. Zhilaitis, and V. G. Shvedov, Zh. Tekh. Fiz. **24**, 87 (1998).

[75] K. Bliokh and Y. Bliokh, Phys. Lett. A **333**, 181 (2004).

[76] M. Onoda, S. Murakami, and N. Nagaosa, Phys. Rev. Lett. **93**, 083901 (2004).

[77] K. Y. Bliokh, Europhys. Lett. **72**, 7 (2005).

[78] A. Brard and H. Mohrbach, Phys. Lett. A **352**, 190 (2006).

[79] A. Brard, H. Mohrbach, J. Lages, P. Gosselin, Y. Grandati, H. Boumrar, and M. F., J. Phys.: Conf. Ser. **70**, 012004 (2007).

[80] P. Gosselin, A. Brard, and H. Mohrbach, Euro. Phys. J. B **58**, 137 (2007).

[81] K. Y. Bliokh, A. Niv, V. Kleiner, and E. Hasman, Nat. Photon. **2**, 748 (2008).

[82] O. Hosten and P. Kwiat, Science **319**, 787 (2008).

[83] K. Y. Bliokh and A. S. Desyatnikov, Phys. Rev. A **79**, 011807 (2009).

[84] C. C. Leary, M. G. Raymer, and S. J. van Enk, Phys. Rev. A **80**, 061804 (2009).

[85] W. Greiner, *Relativistic Quantum Mechanics: Wave Equations* (Springer-Verlag, Berlin, 1997).

[86] E. Merzbacher, *Quantum Mechanics* (Wiley, New York, 1997), 3rd ed.

[87] M. Carmeli, *Group Theory and General Relativity* (World Scientific, Singapore, 1977).

[88] S. Franke-Arnold, J. Leach, M. J. Padgett, V. E. Lembessis, D. Ellinas, A. J. Wright, J. M. Girkin, P. Ohberg, and A. A. S., Opt. Express **15**, 8619 (2007).

[89] S. J. van Enk and G. Nienhuis, Phys. Rev. A **76**, 053825 (2007).

[90] M. W. Beijersbergen, L. Allen, H. E. L. O. van der Veen, and J. P. Woerdman, Opt. Commun. **96**, 123 (1993).

[91] D. E. Browne and T. Rudolph, Phys. Rev. Lett. **95**, 010501 (2005).

[92] M. E. Rose, *Relativistic Electron Theory* (Wiley, New York, 1961).

[93] C. C. Leary, D. Reeb, and M. G. Raymer, New Journ. Phys. **10**, 103022 (2008).

[94] S. M. Lacey, Ph.D. thesis, University of Oregon (2003).

[95] B. J. Smith and M. G. Raymer, New Journ. Phys. **9**, 414 (2007).

[96] B. J. Smith, Ph.D. thesis, University of Oregon (2007).

[97] N. S. Kapany and J. J. Burke, *Optical Waveguides* (Academic Press, New York, 1972).

[98] Z. Bouchal and M. Olivik, Journ. Mod. Opt. **42**, 1555 (1995).

[99] K. Y. Bliokh, J. Math. Phys. **43**, 25 (2002).

[100] K. Y. Bliokh, J. Math. Phys. **43**, 5624 (2002).